

4

GL-TR-90-0033(I)
ENVIRONMENTAL RESEARCH PAPERS, NO. 1053

AD-A220 381

Atmospheric Density and Aerodynamic Drag
Models for Air Force Operations

Proceedings of Workshop Held at AFGL
20-22 October 1987

EDITOR:

FRANK A. MARCOS



13 February 1990



Approved for public release; distribution unlimited.

IONOSPHERIC PHYSICS DIVISION PROJECT 4643
GEOPHYSICS LABORATORY
WANSKOM AFB, MA 01731-5000

REPORT DOCUMENTATION PAGE

Form Approved
OMB No 0704-0188

This report is the property of the Department of Information Systems and is loaned to you for review only. It is to be returned to the Department of Information Systems and is not to be distributed outside the Department. If you have any comments regarding the burden estimates or any other aspect of this report, including suggestions for reducing the burden, please write to Washington Headquarters Services, Directorate for Information Operations and Reports, 1215 Jefferson Davis Highway, Suite 1204, Arlington, VA 22202-4302, and to the Office of Management and Budget, Paperwork Reduction Project (0704-0188), Washington, DC 20503.

1. AGENCY USE ONLY (Leave blank)		2. REPORT DATE 13 February 1990	3. REPORT TYPE AND DATES COVERED Scientific Interim	
4. TITLE AND SUBTITLE Atmospheric Density and Aerodynamic models for Air Force Operations			5. FUNDING NUMBERS PE 62101F PR4643 TA14 WU01	
6. AUTHOR(S) Frank A. Marcos (ED)			8. PERFORMING ORGANIZATION REPORT NUMBER GL-TR-90-0033(I) ERP. No. 1053	
7. PERFORMING ORGANIZATION NAME(S) AND ADDRESS(ES) Geophysics Laboratory (LIS) Hanscom AFB, MA 01731-5000			10. SPONSORING / MONITORING AGENCY REPORT NUMBER	
9. SPONSORING / MONITORING AGENCY NAME(S) AND ADDRESS(ES) Same as Above			11. SUPPLEMENTARY NOTES Volume I consists of pages 1 - 1 through 4 - 196. Volume II consists of pages 5 - 1 through 9 - 10.	
12a. DISTRIBUTION / AVAILABILITY STATEMENT Approved for public release; Distribution unlimited			12b. DISTRIBUTION CODE	
13. ABSTRACT (Maximum 200 words) This report contains papers presented at a Workshop on Atmospheric Density and Aerodynamic Drag Models for Air Force Operations held at the Air Force Geophysics Laboratory from 20-22 Oct 87. The major objective was to assess the capability for significant improvement in models of absolute density, winds, temperature and composition. Emphasis was focused on the altitude region 80-250 Km. Papers were presented in the following areas: Air Force requirements, physics of density and drag variability, empirical models, thermospheric general circulation models, new density and drag measurement techniques (direct and remote sensing), aerodynamic drag coefficients, and solar and magnetospheric inputs. A set of recommendations for improved modeling capabilities was developed by the participants.				
14. SUBJECT TERMS Upper Atmosphere Density; Models of Upper Atmosphere; Neutral Density; Density Specification; Density Forecasting; Satellite Drag			15. NUMBER OF PAGES 338	
			16. PRICE CODE	
17. SECURITY CLASSIFICATION OF REPORT UNCLASSIFIED	18. SECURITY CLASSIFICATION OF THIS PAGE UNCLASSIFIED	19. SECURITY CLASSIFICATION OF ABSTRACT UNCLASSIFIED	20. LIMITATION OF ABSTRACT SAR	

CONTENTS

1. Overview

- 1.1 Introduction
- 1.2 Meeting Agenda

2. Air Force Requirements

- 2.1 Air Weather Service's Neutral Atmospheric Model
- 2.2 Point Density Specification
- 2.3 X-30 National Aero-space Plane (NASP) Environmental Support
- 2.4 Atmospheric Density Models in Operational Systems

3. Physics of Density and Drag Variability

- 3.1 Mesosphere-Thermosphere Coupling
- 3.2 Atmospheric Gravity Waves
- 3.3 Tidal Effects on Thermospheric Circulation, Densities and Temperatures
- 3.4 Thermosphere Dynamics and Its Influence on Atmospheric Density: The Dynamics Explorer Experience
- 3.5 Thermosphere Dynamics: Recent Contributions from Dynamics Explorer-2

4. New Density and Drag Measurements

- 4.1 AFGL Lidar Facility**
- 4.2 Lidar and Rocket Measurements of Atmospheric Structure Properties**
- 4.3 Gravity Wave Density Variations Inferred from Ground-Based Radar Measurements of Winds in the Lower Thermosphere**
- 4.4 Incoherent Scatter Density**
- 4.5 Incoherent Scatter Measurements of High-Latitude Lower Thermospheric Density and Dynamics**
- 4.6 Remote Measurement of Upper Atmospheric Density**
- 4.7 Determination of Atomic Oxygen Density and Temperature of the Thermosphere By Remote Sensing**
- 4.8 Atmospheric Density Measurements with the Remote Atmospheric and Ionospheric Detection System (RAIDS)**
- 4.9 The Atmospheric Density Specification Satellite (ADS)**
- 4.10 Accelerometer Measurements of Density and Winds for ADS**
- 4.11 ADS Mass Spectrometer Absolute Density**
- 4.12 In Situ Measurements of the Neutral Wind and Their Application to the ADS Mission**
- 4.13 Fabry-Perot Interferometer for ADS**
- 4.14 Shuttle Reentry Density Measurements (Between 60 and 160 km)**

5. Empirical Models

- 5.1 MSIS-86 Empirical Model Status and Future Directions**
- 5.2 Atmospheric Structure Between 80 and 120 km**
- 5.3 GRAM Model and Various NASA Density Measurement Projects**
- 5.4 Accuracy of Satellite Drag Models**

6. Thermospheric General Circulation Models

- 6.1 Modeling the Global Structure of the Thermosphere: Circulation, Temperature and Density**
- 6.2 Numerical Computation of Thermospheric Density, Using Coupled Ionospheric/Thermospheric Codes and Parameterised Solar and Geomagnetic Inputs**
- 6.3 Developing an Operational Version of Thermosphere General Circulation Models**
- 6.4 Future Thermospheric General Circulation Model (TGCM) Needs**
- 6.5 Thermosphere-Ionosphere-Magnetosphere Coupling**
- 6.6 Ionospheric Coupling With Thermosphere General Circulation Models**
- 6.7 Global Thermospheric Specifications and Forecasting**

7. Drag Coefficients

- 7.1 High Altitude Drag Coefficients**
- 7.2 Direct Simulation Monte Carlo (DSMC) Drag Predictions**
- 7.3 Satellite Drag and Lift Deduced From Measured Gas-Surface Interaction at 5 eV**

7.4 Variability in the Satellite Drag Coefficient, CD

7.5 Satellite Drag Coefficient Variability

7.6 Drag Coefficients-Remarks

8. Solar and Magnetospheric Inputs

8.1 Solar X-Ray, EUV and UV Flux

8.2 Solar Flares and the Solar EUV Flux

8.3 Ground-Based Solar Coronal Observations as a Possible Input to Atmospheric Models

8.4 Taking the First Steps in Real-Time EUV Monitoring for Drag: the Series of USAF-NOAA Solar X-Ray Imagers (SXIs) on GOES

8.5 Solar Activity Measurements Experiment (SAMEX) on the High Resolution Solar Observatory (HRSO)

8.6 SIMPL

8.7 Absolute Extreme Ultraviolet Solar Spectral Irradiance Monitor (AESSIM)

8.8 The Geomagnetic Activity Outlook for 1987-1997 (Cycle 22)

8.9 Magnetospheric Convection and DMSP

8.10 Particles and Joule Energy Input

8.11 Solar and Magnetospheric Inputs/ Summary

9. Summary and Conclusions

Attendance List

1. OVERVIEW

.

.

.

.

1.1 INTRODUCTION

Earth's neutral atmosphere affects many aspects of Air Force operations. These include satellite tracking, lifetime and reentry prediction, design and operation of aerospace systems and the specification of absolute density for point analysis. Requirements for knowledge of absolute density and aerodynamic drag variations within 5-10% are not met by current models. Evaluations of models above 150 km have shown that despite improvements in our morphological description of the atmosphere, model accuracies for drag variability have remained at about $\pm 15\%$ (one sigma) during the past two decades. This plateau has been dubbed "the 15% barrier".

The objective of this workshop was to assess our capability to significantly improve models of density, winds, temperature and composition. Emphasis was focussed on the altitude region 80-250 km where there continues to be a lack of coordinated neutral density programs. The meeting format was similar to that initiated at NOAA's Satellite Drag Workshop in 1982 and followed at the NASA MSFC Drag Workshop in 1985. There was an extremely strong response to this meeting from the scientific and user community. The 103 registered participants, listed at the end of this report, included representatives from 22 Government agencies, 7 Universities, 6 research centers and 7 private organizations.

Section 1.2 gives the meeting agenda. Papers submitted by workshop speakers are in Sections 2-8. Some of the titles differ from those in the agenda and a few papers were not received. Through presentation and discussion, the three-day meeting provided extensive coverage of the following areas: Air Force relevance, atmospheric physics, empirical and theoretical models, measurement techniques, drag coefficients and solar influences. A meeting summary is given in Section 9. It was concluded that significant improvements in our 80-250 km modeling capability are achievable. A team approach to this multi-faceted problem was recommended. The major requirement is to obtain a comprehensive data base of accurate neutral atmosphere measurements and associated forcings to extensively test and improve formulations in thermospheric general circulation models.

(Received for publication 23 January 1990)



**AIR FORCE GEOPHYSICS LABORATORY
IONOSPHERIC PHYSICS DIVISION**



WORKSHOP

**ATMOSPHERIC DENSITY AND AERODYNAMIC DRAG
MODELS FOR AIR FORCE OPERATIONS**

20-22 OCTOBER 1987

**HOLZMAN SEMINAR ROOM
BUILDING 1105A
AIR FORCE GEOPHYSICS LABORATORY
HANSCOM AFB, MA 01731-5000**

- **MAJOR OBJECTIVE IS TO ASSESS CAPABILITY FOR
SIGNIFICANT IMPROVEMENT IN MODELS OF DENSITY,
WINDS, TEMPERATURE AND COMPOSITION
-- FOCUS ON ALTITUDE REGION 80-250 km**

- **FINAL AGENDA, SCHEDULE AND AREA INFORMATION
ARE ATTACHED**

- **ORGANIZER: FRANK A. MARCOS
IONOSPHERIC PHYSICS DIVISION, AFGL
TELEPHONE. (617) 377-3037**

FINAL AGENDA

WORKSHOP ON ATMOSPHERIC DENSITY AND AERODYNAMIC DRAG

MODELS FOR AIR FORCE OPERATIONS

AIR FORCE GEOPHYSICS LABORATORY

20-22 OCT 87

** TUESDAY, 20 OCTOBER 1987 **

I. INTRODUCTION

TIME: 0900-1000

- CHAIR: F. A. Marcos (AFGL)

1. Welcoming Address

Col. J. R. Kidd
Commander, AFGL

2. Meeting Overview and Objectives

H. Carlson (AFGL/LIS)

II. AIR FORCE REQUIREMENTS

TIME: 1000-1145

- CHAIR: (Capt. T. Schott, HQAWS)

1. Air Weather Service's Neutral
Density Model

Capt. T. Schott (HQAWS)

2. Point Density Specification

C. Schaaf (AFGL/LYA)

3. National Aerospace Plane

Lt. S. Johnson (ASD/WE)

4. Issues on Atmospheric Drag

J. Liu (SPACECMD)

Models in Operational Systems

5. Ionosphere-Thermosphere System

H. Carlson (AFGL/LIS)

LUNCH: 1145-1315

III. PHYSICS OF DENSITY AND DRAG VARIABILITY

TIME: 1315-1450

- CHAIR: R. G. Roble (NCAR)

- | | |
|--|----------------------------------|
| 1. Mesosphere - Lower Therm. Coupling | J. Forbes (Boston Univ.) |
| 2. Gravity Waves in Mesosphere-Therm. | R. Walterscheid (Aerospace Corp) |
| 3. Tidal Effects on Thermospheric
Circulation, Temperature and
Density Structure | C. Fesen (Univ. Colo) |
| 4. Thermosphere Dynamics and the
Influence on Atmospheric Density:
The LE Experience | T Killeen (Univ. Mich) |
| 5. Session Summary | R. Roble (NCAR) |

BREAK: 1450-1510

IV. NEW DENSITY AND DRAG MEASUREMENTS/REMOTE SENSING

A. GROUND-BASED

TIME: 1510-1655

- CHAIR: P. B. Hays (Univ. of Michigan)

- | | |
|------------------------------------|-------------------------------|
| 1. AFGL Lidar Facility | D. Sipler (AFGL/LID) |
| 2. Lidar Density Measts | C. R. Philbrick (AFGL/LID) |
| 3. Radar Winds/Gravity Waves | R. Vincent (Univ. Adelaide) |
| 4. Incoherent Scatter Density | W. Oliver (MIT Haystack Obs.) |
| 5. High Lat. Lower Therm. Dynamics | R. Johnson (SRI Int'l) |

EVENING: Lidar Facility Tour

(D. Sipler, AFGL/LID)

** WEDNESDAY, 21 OCTOBER 1987 **

IV. NEW DENSITY AND DRAG MEASUREMENTS/REMOTE SENSING (Cont'd)

TIME: 0830-1000

- CHAIR: P. B. Hays (Univ. of Mich)

B. SATELLITE REMOTE SENSING

- | | |
|---|------------------------|
| 1. Density 80-120 Km | P. Hays (Univ. Mich) |
| 2. Determination of Atomic Oxygen
Density and Temperature of the
Thermosphere by Remote Sensing | R. Sharma (AFGL/LSI) |
| 3. RAIDS | R. McCoy (NRL) |
| C. COUPLED ENERGETICS AND DYNAMICS
ATMOSPHERIC RESEARCH | W. Sharp (Univ. Mich.) |

- Session Summary

P. Hays (Univ. Mich)

BREAK: 1000-1020

V. EMPIRICAL MODELS

TIME: 1020-1140, 1310-1340

- CHAIR: T. L. Killeen (U. of Michigan)

- | | |
|---|-------------------------------|
| 1. MSIS 86 Empirical Model, Status
and Future Directions | A. Hedin (NASA/GSFC) |
| 2. Model Evaluations from AFGL
Accelerometer Data | F. Marcos (AFGL/LIS) |
| 3. CIRA 86, 80-120 KM | G. Groves (Univ. Coll. Lond.) |

LUNCH: 1125-1310

- | | |
|--------------------|----------------------------------|
| 4. GRAM Model | D. Johnson/G. Fichtl (NASA/MSFC) |
| 5. Session Summary | T. Killeen (Univ. Mich) |

VI. GENERAL CIRCULATION MODELS

TIME: 1340-1505, 1525-1615

- CHAIR: J. M. Forbes (Boston Univ.)

- | | |
|---|----------------------------|
| 1. NCAR TGCM | R. Roble (NCAR) |
| 2. Operational TGCM's | T. Killeen (Univ. Mich) |
| 3. Global Thermospheric Specifications
and Forecasting | Capt. C. Tschan (HQ AWS) |
| 4. U. Coll. Lond. TGCM | D. Rees (Univ. Coll. Lond) |

BREAK: 1505-1525

- | | |
|-----------------------------------|----------------------------|
| 5. Future TGCM Needs | R. Schunk (Utah St. Univ.) |
| 6. Coupled Thermo-Ionosphere TGCM | D. Anderson (AFGL/LIS) |
| 7. Session Summary | J. Forbes (Boston Univ.) |

** THURSDAY, 22 OCTOBER 1987 **

VII. DRAG COEFFICIENTS

TIME: 0800-0935

- CHAIR: Blanchard (NASA/LaRC)

- | | |
|--|--------------------------------|
| 1. Aerodynamic Drag Calculations and the
Effects of Surface Reflection
Uncertainties | G. Bird (Univ. of Sydney) |
| 2. Direct Simulation Monte Carlo Drag
Predictions | J. Moss (NASA/LaRC) |
| 3. In-Orbit Measurements of Atom Scattering
for Drag Calculations | J. Gregory/G. Karr (NASA/MSFC) |
| 4. Satellite Drag Coefficient Variability | K. Tobiska (Univ. of Colo.) |

BREAK: 0935-1150

VIII. NEW DENSITY AND DRAG MEASUREMENTS/DIRECT SENSING

TIME: 0955-1150

- CHAIR: H. C. Carlson (AFGL/LIS)

- | | |
|---|----------------------------|
| 1. Atmospheric Density
Specification Satellite (ADS) | F. Marcos (AFGL/LIS) |
| 2. ADS Mass Spec., Absolute Density | J. Ballenthin (AFGL/LID) |
| 3. ADS Mass Spec., Winds | D. Kayser (Aerospace Corp) |
| 4. ADS FPI and Feasibility | T. Killeen (Univ. Mich) |
| 5. Shuttle Accel. Density Results | R. Blanchard (NASA/LaRC) |
| 6. Session Summary | H. Carlson (AFGL/LIS) |

LUNCH: 1150-1300

IX. SOLAR AND MAGNETOSPHERIC INPUTS

TIME: 1300-1500

- CHAIR: N. C. Maynard (AFGL/PHG)

- | | |
|--|---------------------------------------|
| 1. Solar Flux | R. Donnelly (NOAA) |
| 2. Solar Flares and UV Inputs | S. Keil (AFGL/PHS) |
| 3. Gd-based Solar Coronal Observations
as a Possible Input to Atmospheric
Models | R. Alrock (AFGL/PHS) |
| 4. Future Solar and Solar Wind
Measurements | |
| a. GOES Solar X-ray Imager | W. Wagner (NOAA) |
| b. SAMEX | S. Keil (AFGL/PHS) |
| c. SIMPL | M. Shea (AFGL/PHP) |
| d. EUV Calibration | W. Parkinson (SAO) |
| 5. Geomagnetic Predictions | J. Joselyn (NOAA) |
| 6. Magnetospheric Convection
and DMSP | N. Maynard/F. Rich (AFGL/PHG) |
| 7. Particle and Joule Energy
Dissipation from DMSP | F. Rich/S. Gussenhoven/
(AFGL/PHP) |
| 8. Evans Index | D. Evans (NOAA) |

BREAK: 1500-1520

X. SUMMARY/CONCLUSIONS

TIME: 1520-1620

- CHAIR: F. A. Marcos (AFGL)

- | | |
|--|----------|
| 1. Absolute Density | Chairmen |
| 2. Winds, Composition, Temperature, Drag | Chairmen |

ADJOURN: 1620

2. AIR FORCE REQUIREMENTS

AWS' NEUTRAL ATMOSPHERIC MODEL

by

Capt Tom Schott

AWS/DNXP

Scott AFB, IL 62225-5008

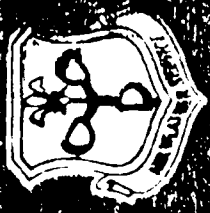
(618)-256-4781

(AV576-4781)

OVERVIEW

- **Background on AWS' Space Environmental Support System (SESS)**
- **AWS Space Research Requirements**
- **AWS' Neutral Atmospheric Model**

CHARTER

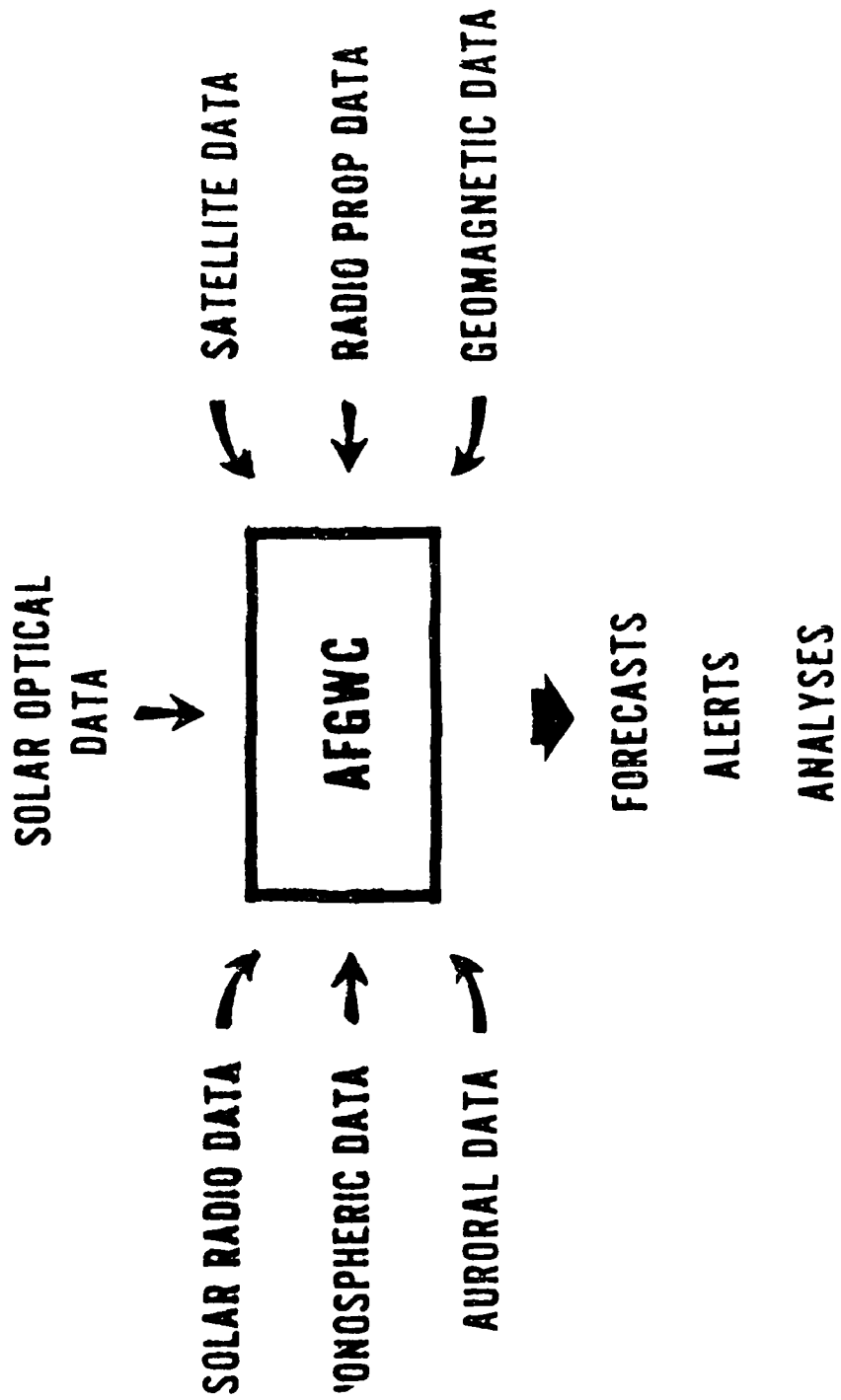


"AFWS WILL PROVIDE . . . (THOSE) STAFF AND OPERATIONAL FUNCTIONS REQUIRED TO ACQUIRE, PRODUCE, AND PROVIDE INFORMATION ON THE . . . STATE OF THE AEROSPACE ENVIRONMENT. THESE FUNCTIONS INCLUDE . . . SPACE ENVIRONMENT OBSERVATIONS AND FORECASTS."

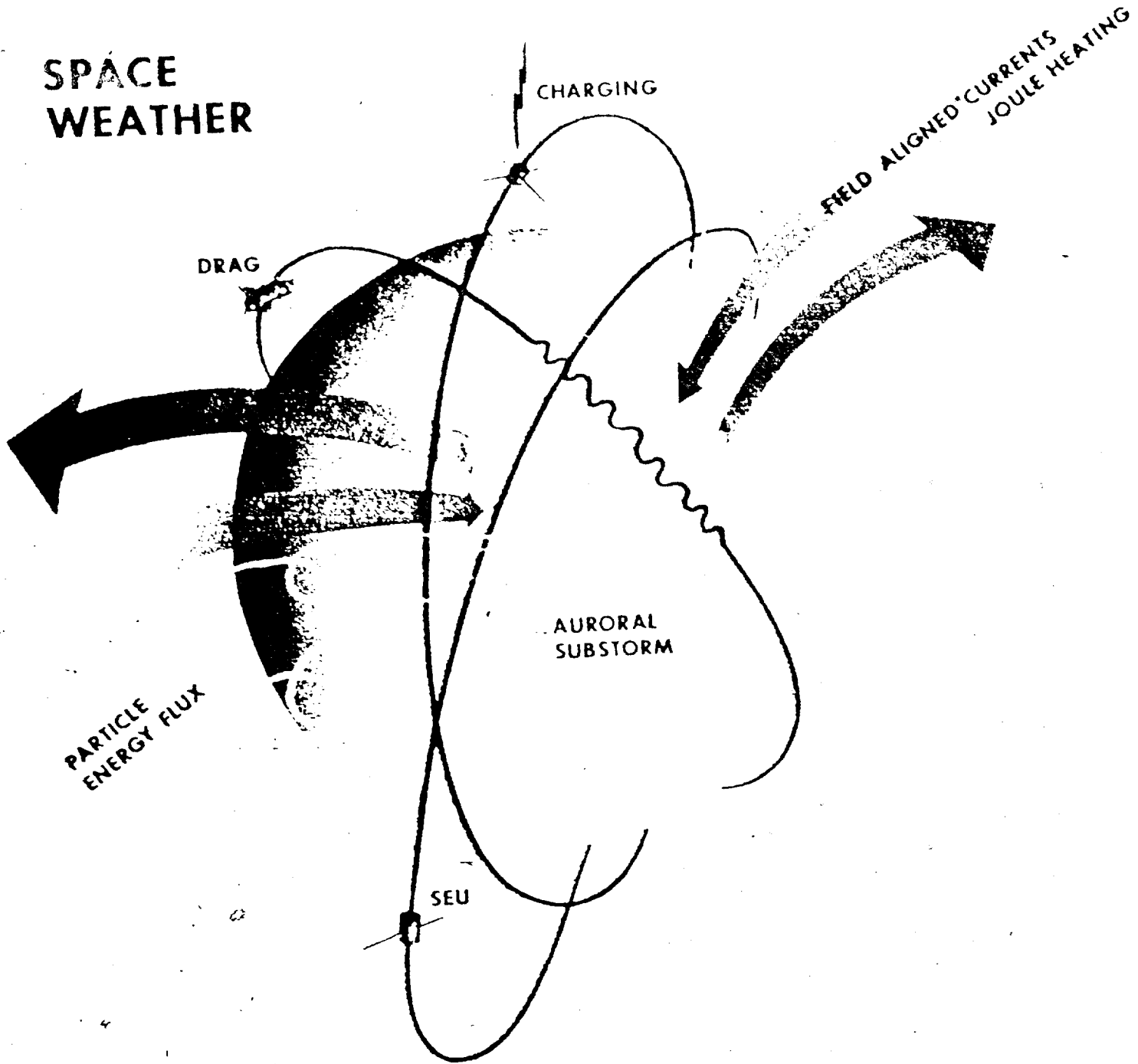
- AFR 23-31

15548 BX

SESS PRODUCTION CENTER



SPACE WEATHER



2-7

SESS RESEARCH AREAS

AWS GEOPHYSICAL REQUIREMENTS

- IONOSPHERIC MODELING
- MAGNETOSPHERIC MODELING
- SOLAR MONITORING AND PREDICTION
- NEUTRAL DENSITY ATMOSPHERIC MODELING

AWS RESEARCH OBJECTIVES

- SOLAR ACTIVITY AND INTERPLANETARY FIELD
- ATMOSPHERIC AND NEAR EARTH SPACE ENVIRONMENT

NEUTRAL ATMOSPHERIC MODEL

- Global specification and prediction from 100 - 1000 km

- Parameters

-- Neutral density

-- Neutral Wind

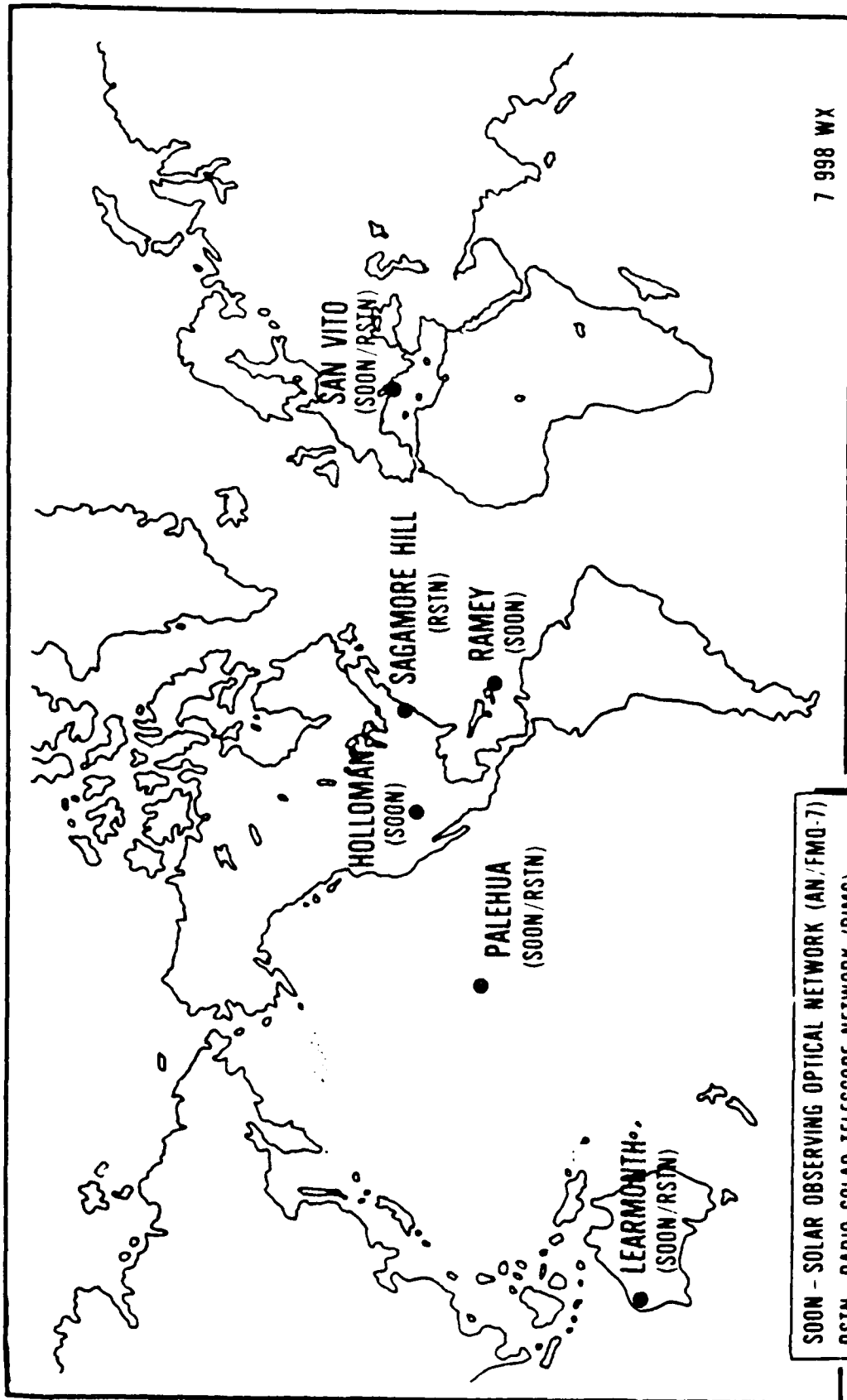
-- Temperature

-- Atmospheric composition

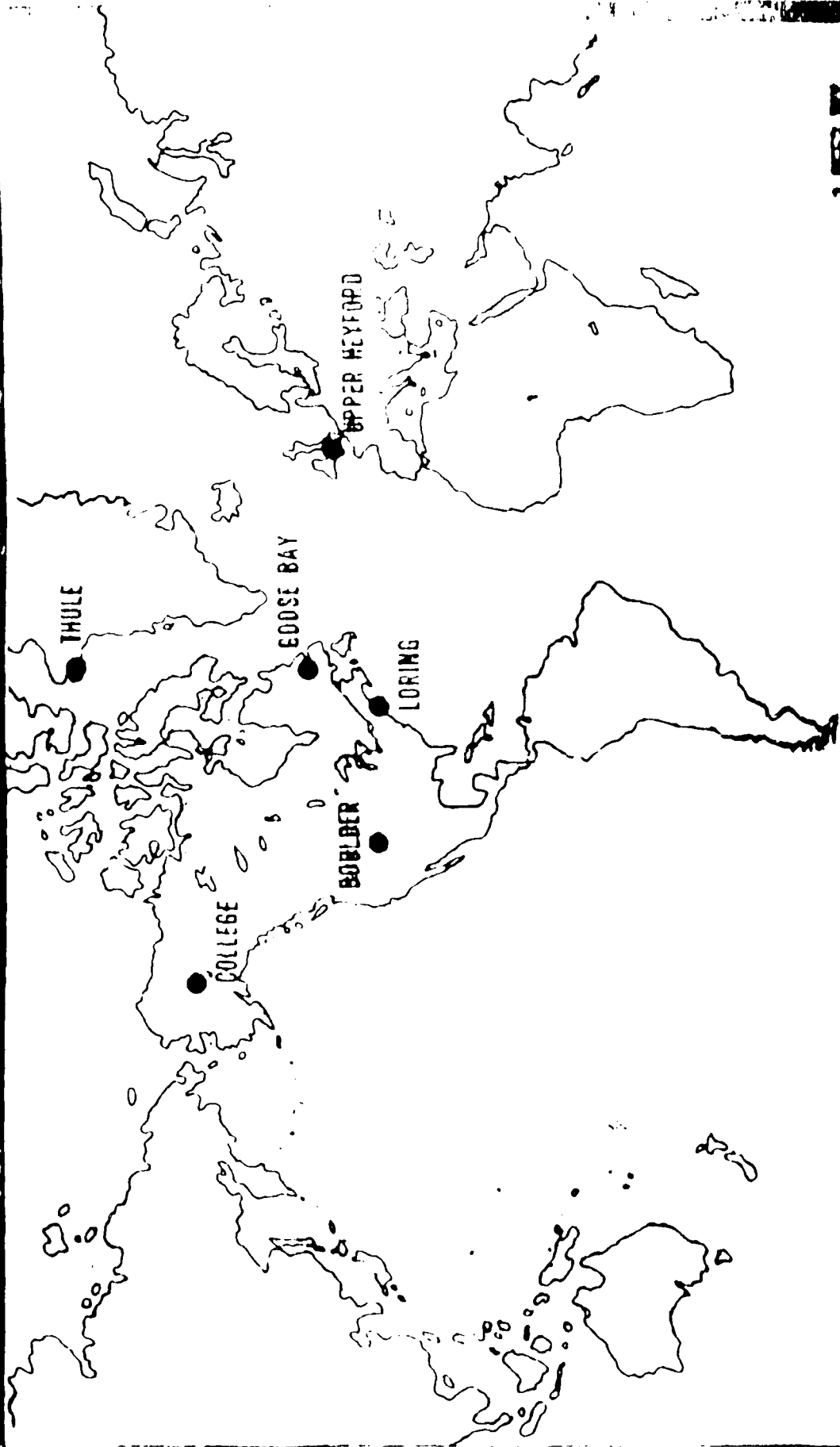
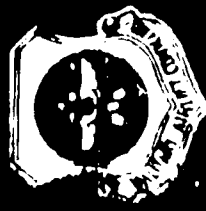
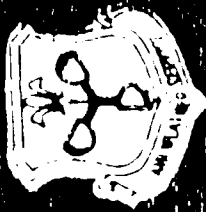
MODELING LIMITATIONS

- **AWS' operational model must be responsive**
 - Can not be time consuming
 - Must consider AWS computer limitations
- **Model must make use of real-time data sources**
 - New sensors

AWS SOLAR OBSERVATORIES



MAGNETOMETERS



1 553 17

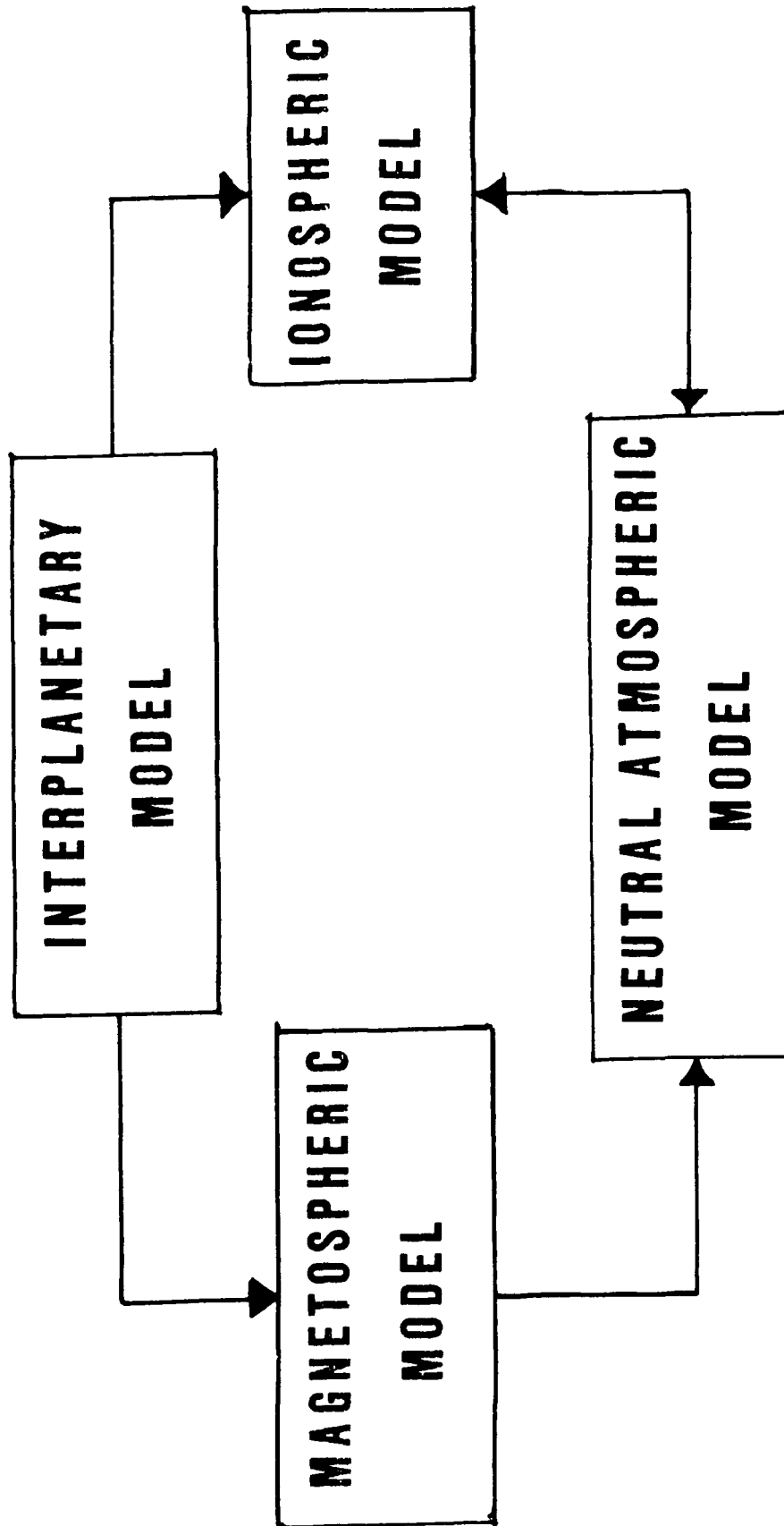
SATELLITE-BASED OBSERVATIONS

**- DMSP - AURORAL IMAGERY, PRECIPITATING PARTICLES,
IN-SITU PLASMA DENSITY**

**- CIVILIAN GEOSTATIONARY - SOLAR X-RAYS,
ENERGETIC PARTICLES**

- DOD GEOSTATIONARY - ENERGETIC PARTICLES

INTEGRATED SPACE ENVIRONMENTAL MODELING SYSTEM (ISEMS)



POINT DENSITY SPECIFICATION

Crystal L.B. Schaaf

AFGL/LYA

The IMPROVED POINT ANALYSIS MODEL (IPAM) is a new Air Force Global Weather Central operational model that *describes the atmosphere above and around a given point on the earth's surface for a specific time*. This new model, which will be operational in the fall of 1988, will represent a significant improvement in the quality of point analyses and an expansion in the delivery of customer required parameters. However, there are still a number of areas where enhancements will be needed. AFGL, under guidance from AWS, is undertaking a variety of research efforts aimed at further improving IPAM. As techniques, algorithms, or models are developed, emphasis will then be placed on successfully transitioning the technology from AFGL researchers to AWS personnel who can then implement the ideas at Global Weather Central.

IPAM will provide its customers with a listing of the atmospheric conditions at and around a requested point. A *pseudo-surface observation* will be deduced from any and all available meteorological surface information. A cloud depiction will be provided, extracted from the Real-Time Nephanalysis (Fye, 1978). Information will be produced describing the atmosphere and choosing the appropriate default inputs needed to run LOWTRAN (Kneizys, *et al.*, 1983 -- LOWTRAN is a separate model that calculates atmospheric transmittance and radiance over a given path). Finally a vertical profile of the atmosphere will be provided. Below 100,000 ft, this profile is based on RAOB, ROCOB, satellite soundings, aircraft reports, and cloud-tracked winds and is produced using optimum interpolation techniques. Above 100,000 ft, the profile merely depends on Groves Model (Groves, 1985) linked to MSIS83 (Hedin, 1983) in a fashion similar to that described by Groves (1987).

There is a requirement to improve the specification of temperature, pressure, and relative humidity to 120 km and density to 200 km. Both vertical and line-of-sight profiles are needed. Suggestions and techniques discussed at this workshop will be used to enhance and expand the capabilities of IPAM.

Fye, F.K., 1978; The AFGWC automated cloud analysis model. AFGWC Tech. Memo. 78-002, 97p.

Groves, G.V., 1985; A global reference atmosphere from 18 to 80 km. Air Force Surveys in Geophysics, no. 448, AFGL-TR-85-0129, 121p, AD A162499.

_____, 1987; Modeling of atmospheric structure: 70 - 130 km. AFGL-TR-87-0226, AD A201077.

Hedin, A., 1983; A revised thermospheric model based on mass spectrometer and incoherent scatter data. *J. Geophys. Res.*, 88, p. 10170.

Kneizys, F.X., Shettle, E.P., Gallery, W.O., Chetwynd, J.H., Abreu, L.W., Selby, J.E.A., Clough, S.A., and Fenn, R.W., 1983; Atmospheric transmittance/radiance computer code LOWTRAN 6. Environmental Research Papers, no. 846. AFGL-TR-83-0187, 200p, AD A137786.

POINT PAPER

on

X-30 National Aero-Space Plane (NASP) Environmental Support

Lt. Steven Johnson

DET 1, 2WS, Wright Patterson AFB

Presented at the Atmospheric Density and Aerodynamic Drag Models for Air Force Operations Workshop, Air Force Geophysics Laboratory, Hanscom AFB, 20 Oct 87.

DISCUSSION

- Program organization and goal.
 - Joint DOD (DARPA, Air Force, Navy, and SDIO) and NASA program.
 - Joint Program Office (JPO) located at Wright-Patterson AFB.
 - As of 1 Nov Program Manager will be Dr Robert Barthelemy.
 - 1Lt Steve Johnson (Det 1, 2 WS) provides support to the JPO.
 - Program goal is to demonstrate the technologies required for hypersonic cruise and single-stage-to-orbit (SSTO) capabilities.
 - X-30 is a research vehicle not being designed with any specific mission or with mass production in mind.
- Flight envelope.
 - Limited time in the troposphere.
 - Stratosphere is the primary flight regime.
 - Hypersonic cruise: Mach 8-12 at altitudes 100,000 to 150,000 ft.
 - Acceleration to high Mach numbers for orbital insertion here.
 - Above 50 km NASP will fly an orbital insertion trajectory.
 - Above 80 km NASP is essentially spacecraft.
 - Powered by rocket motor, speeds near escape velocity.
 - Ascent trajectory very different from Space Shuttle.
 - NASP accelerates within the atmosphere.
 - Descent trajectory similar to Space Shuttle.
 - Ultimately to obtain a low Earth orbit.

- Desired environmental data.
 - The most current reference atmosphere above 90 km.
 - Standard deviation data desired for flight control system design.
 - Applicability of data under varying solar conditions.
 - Identify spectrum of gravity waves to be encountered.
 - An as yet undefined crucial magnitude to vehicle design fully understood.
 - Wave sources known and forecastable.
 - A characterization of turbulent extremes near the turbopause is needed.
 - Effects of breaking gravity waves quantified.
 - Effects of solar tides.
 - Changes in density/drag with diurnal and semidiurnal tides.
 - Areal extent at varying latitudes.
 - Test flights are set to begin in 1993.
 - Sunspot cycle places mid 1990's in period of increased solar activity.
- Conclusions.
 - Phase 2 work now beginning.
 - Engine and airframe contracts have been awarded.
 - Emphasis shifting from conceptual design to technology development.
 - More accurate data desired.
 - Means and perturbations both important to vehicle design.
 - Atmospheric models applicable over a wide range of conditions.
 - Test flights scheduled for the mid 1990's.

1Lt Steven Johnson/Det 1, 2 WS/AUTOVON 785-2208

**OFFICE OF THE
STAFF
METEOROLOGIST**



BRIEFER: LT STEVE JOHNSON

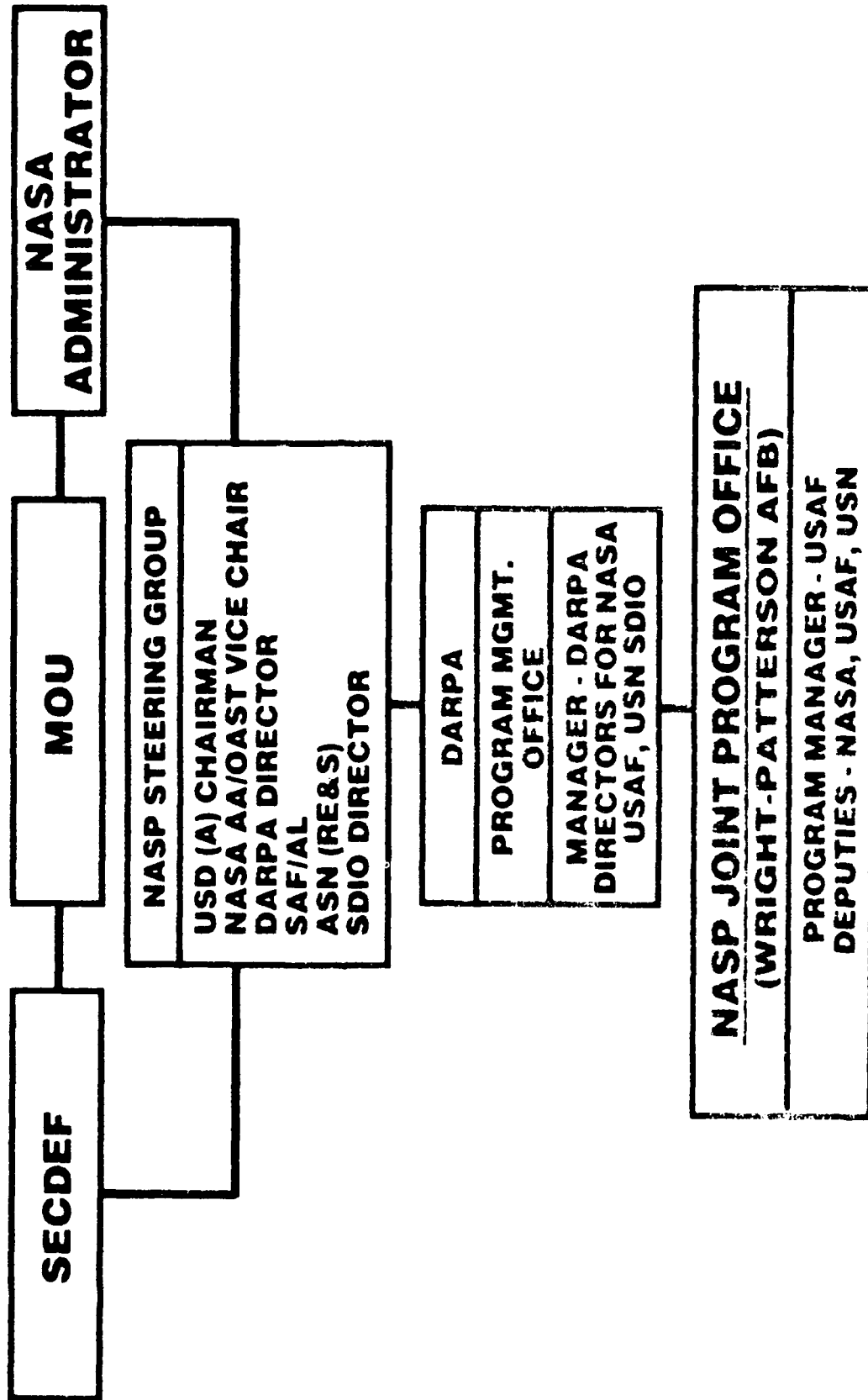


OVERVIEW

- PROGRAM ORGANIZATION AND GOAL
- FLIGHT ENVELOPE
- DESIRED ENVIRONMENTAL DATA
- CONCLUSIONS



DOD/NASA NATIONAL AEROSPACE PLANE PHASE 2 ORGANIZATION





FLIGHT ENVELOPE

- LIMITED TIME IN TROPOSPHERE
- STRATOSPHERE PRIMARY FLIGHT REGIME
 - HYPERSONIC CRUISE
 - ACCELERATION TO HIGH MACH NUMBERS
- ORBITAL INSERTION TRAJECTORY ABOVE 50 Km



FLIGHT ENVELOPE

- ABOVE 80 Km
- SPEED AT ESCAPE VELOCITY
- POWERED BY ROCKET MOTOR
- ASCENT TRAJECTORY VERY DIFFERENT FROM SPACE SHUTTLE
 - NASP ACCELERATES IN THE ATMOSPHERE ($\leq 150,000$ FT)
- DESCENT TRAJECTORY SIMILAR TO SPACE SHUTTLE
- LOW EARTH ORBIT



DESIRED ENVIRONMENTAL DATA

- MOST CURRENT REFERENCE ATMOSPHERE ABOVE 90 Km
- STANDARD DEVIATION DATA DESIRED
- APPLICABILITY UNDER VARYING SOLAR CONDITIONS
- SPECTRUM OF GRAVITY WAVES IDENTIFIED
- CRUCIAL MAGNITUDE FULLY UNDERSTOOD
- SOURCES KNOWN AND FORECASTABLE



DESIRED ENVIRONMENTAL DATA

- CHARACTERIZATION OF TURBULENT EXTREMES NEAR TURBOPAUSE
 - BREAKING OF GRAVITY WAVES
- EFFECTS OF THE SOLAR TIDES
 - DIURNAL AND SEMIDIURNAL
 - AREAL EXTENT AT VARYING LATITUDE
- TEST FLIGHTS SCHEDULED FOR MID-1990s
 - PERIOD OF INCREASED SOLAR ACTIVITY



CONCLUSIONS

- PHASE 2 WORK NOW BEGINNING
 - EMPHASIS MOVING FROM CONCEPTUAL TO TECHNOLOGY DEVELOPMENT
- MORE ACCURATE DATA DESIRABLE
 - MEANS AND PERTURBATIONS
 - ATMOSPHERIC MODELS APPLICABLE OVER A WIDE RANGE OF CONDITIONS
- TEST FLIGHTS IN THE MID-1990s

2.4

ATMOSPHERIC DENSITY MODELS
IN OPERATIONAL SYSTEMS

BY

JOSEPH J F LIU
SPACE DIVISION/DOA
HQ AFSPACECOM

VGS PREPARED FOR

WORKSHOP ON ATMOSPHERIC DENSITY AND AERODYNAMIC DRAG MODELS FOR
AIR FORCE OPERATIONS

20-22 OCTOBER 1987

AFGL

OPS REQUIREMENTS ON SATELLITE DYNAMICS

- ACCURACY OF NEUTRAL DENSITY
- PARAMETER PREDICTABILITY
SHORT-TERM/LONG-TERM
- ALTITUDE RANGE
- COMPUTATIONAL EFFICIENCY
- IMPROVEMENTS OVER EXISTING MODEL
- COMPATIBILITY ISSUES
- ADDITIONAL FEATURES:
WIND, CHARGE "DRAG",
NEW/ADDITIONAL PARAMETERS, ETC.

ATMOSPHERIC DENSITY MODELS IN USE

- ANALYTIC MODELS
 - EXPONENTIAL MODELS
 - BASIC MODEL
 - MODIFIED AND IMPROVED MODELS
 - POWER FUNCTION MODELS
 - BASIC MODEL
 - MODIFIED AND IMPROVED MODELS
- EMPIRICAL MODELS
 - DENSEL
 - HARRIS-PRIESTER
 - JACCHIA MODELS AND DERIVATIVES
 - JACCHIA 64, 70, 71, 77
 - JACCHIA-BASS 77
 - WALKER 64
 - LAFONTAINE'S ANALYTIC MODEL
 - BARLIER MODEL
 - MASS SPECTROMETER AND INCOHERENT SCATTER DATA MODELS

OPS PROBLEMS RELATING TO DENSITY MODELS

- NO SIGNIFICANT IMPROVEMENTS ON NEUTRAL DENSITY
- NO RELIABLE PARAMETER PREDICTION CAPABILITY
- NO IMPROVEMENT ON EFFICIENCY
- PROLIFERATION & COMPATIBILITY PROBLEMS

PROJECTS REQUIRE BETTER ATM MODEL

- TIP
- COMBO
- LASER CLEARINGHOUSE
- SPACE SHUTTLE
- SENSOR CALIBRATION
- MILITARY APPLICATIONS
- OTHERS

SPADOC EPHEMERIS MODELS USING ATM DENSITY MODEL

- GENERAL PERTURBATIONS THEORIES: SGP4, HANDE
- SEMI-ANALYTIC THEORY: SALT
- SPECIAL PERTURBATIONS THEORY: SP

NOTE: ACROSS-THE-BOARD EFFECTS ON ALL OPS APPLICATIONS

OPS & SCIENCES COOPERATION

- INITIATE OPS & SCIENCES WORKING GROUP
 - TIME: WEEK OF 15 FEB 1988
 - LOCATION: AFSPACECOM
- IDENTIFY MUTUAL NEEDS
 - EMPHASIZE TEAM WORK & COMPATIBILITY
- SET OPS REQUIREMENTS AND R&D GOALS
 - SHORT-TERM & LONG-TERM
- ASSESS IMPACTS & PRIORITIES
- CONSOLIDATE RESOURCES
- ESTABLISH FEASIBLE ACTION ITEMS

NUMERICAL EXAMPLE 1

ORBITAL CHARACTERISTICS

SEMI-MAJOR AXIS = 7000 KM, ECCENTRICITY = .0667
INCLINATION = 50 DEG, EPOCH ALTITUDE = 650 KM
BALLISTIC COEF = $-.00213 \text{ M}^{**2}/\text{KG}$, EPOCH: 1970 136

DAYS SINCE EPOCH	PROPAGATION ERRORS (KM)			
	5%	10%	15%	20%
1	5	10	15	20
2	21	43	64	86
5	119	237	356	474
10	540	1080	1616	2151

NUMERICAL EXAMPLE 2

ORBITAL CHARACTERISTICS

SEMI-MAJOR AXIS = 6718 KM, ECCENTRICITY = .0293
INCLINATION = 50 DEG, EPOCH ALTITUDE = 466 KM
BALLISTIC COEF = -.0018, EPOCH: 1970 220

DAYS SINCE EPOCH	PROPAGATION ERRORS (KM)			
	5%	10%	15%	20%
1	11	22	33	43
2	46	91	137	182
5	280	559	839	1120
10	1261	2516	3750	5000

NUMERICAL EXAMPLE 3

ORBITAL CHARACTERISTICS

SEMI-MAJOR AXIS = 6600 KM, ECCENTRICITY = .0012
INCLINATION = 32 DEG, EPOCH ALTITUDE = 217 KM
BALLISTIC COEF = -.0286, EPOCH: 1978 258

HRS SINCE EPOCH	PROPAGATION ERRORS (KM)			
	5%	10%	15%	20%
12	20	40	60	80
24	108	215	320	430
32	260	530	800	1100
38	550	1000	1400	1750

RECOMMENDED REQUIREMENTS

ALTITUDE	AVERAGE NEUTRAL DENSITY ERROR
< 200 KM	5%
500-700 KM	10%
> 700 KM	15%

SLIDE 1

SPACE OPERATIONS WORKSHOP III

AFSPACECOM DO PANEL: TOPIC 4 - ASTRODYNAMIC STANDARDS

PLAN FOR ASTRODYNAMIC STANDARDS

1. Assess the Need for Astrodynamic Standards
2. Identify the Areas that Require Standards
3. Quantify Operational Impact
4. Prioritize Standard Elements
5. Develop Recommendations

SPACE OPERATIONS WORKSHOP III

AFSPACECOM DO PANEL: TOPIC 4 - ASTRODYNAMIC STANDARDS

JUSTIFICATIONS FOR ASTRODYNAMIC STANDARDS

1. Ensure the Integrity of Operational Systems
2. Optimize the Communication between Centers and Users
3. Provide Baseline for Future Systems
4. Enhance Compatibility and Inter-operability

3. PHYSICS OF DENSITY AND DRAG VARIABILITY

3.1

MESOSPHERE-THERMOSPHERE COUPLING

Jeffrey M. Forbes

**Department of Electrical, Computer, and Systems
Engineering
Boston University, Boston, MA 02215**

**Workshop on
Atmospheric Density and Aerodynamic Drag
Models for Air Force Operations
Air Force Geophysics Laboratory
20 - 22 October 1987**

1. MESOPAUSE-REGION PROCESSES

The mesopause is the minimum in the earth's atmospheric temperature vertical profile near 90 km (Figure 1), and as such represents the boundary between the mesosphere (a region of negative temperature gradient, ca. 50 - 90 km) and the thermosphere (a region of positive temperature gradient, ca. 90 - 500 km). A schematic summary of the important interactions which take place in the height region around the mesopause is provided in Figure 2. The primary sources of heat input into the lower thermosphere include absorption of EUV and UV radiation, Joule dissipation of ionospheric currents, particle precipitation, and dissipation of wave and turbulent energy. The primary heat sink between 100 and 140 km is downward heat conduction. Below 100 km the densities and collision frequencies of polyatomic molecules CO_2 , O_3 , H_2O , and NO are sufficiently great that heat loss by infrared radiation plays a significant role in determining the thermal structure. Differential heating in latitude tends to set up a large-scale (geostrophic) circulation, as it does in the stratosphere. However, upward propagating gravity waves can achieve convective instability at these heights, leading to a momentum flux divergence which effectively causes a force imbalance, sometimes called a 'wave drag', in the mean eastward momentum equation. The force imbalance induces a mean meridional circulation, and thereby a Coriolis torque opposing the drag and adiabatic heating/cooling, giving rise to a reversed meridional temperature gradient in the region of the mesopause (Figure 1 inset).

Gravity waves are thought to originate in such tropospheric sources as storms and topographic excitation. In addition to depositing momentum, dissipating gravity waves induce turbulent mixing which strongly influences the transport and distributions of long-lived chemical species such as NO . Molecular diffusion, as its efficiency increases with decreasing density, usually becomes faster than turbulent diffusion rates above about 100 km, the level sometimes referred to as the 'turbopause'. It is well known that the level of the turbopause is a major factor controlling the composition and hence the total mass density in the thermosphere.

Similarly, tidal oscillations of 24-hour ('diurnal') and 12-hour ('semidiurnal') periods are generated by H_2O and O_3 insolation absorption in the

troposphere and stratosphere and propagate through the mesopause into the lower thermosphere (Figure 3). Tides represent a major source of temperature and wind variability in the mesopause region, and are also capable of generating turbulence and depositing mean momentum and heat above 85 km. In addition, interactions with the magnetoplasma at higher levels induce important redistributions of ionization both directly and through the electric fields generated via dynamo action. These effects feed back via the ion drag mechanism to affect the neutral dynamics and density variations.

Within this workshop session the subject of gravity waves is addressed by Dr. R.L. Walterscheid, and that of the penetration of tidal waves above 100 km and their consequences above about 120 km, by Dr. C.G. Fesen. This paper, therefore, will concentrate on tidal oscillations between 80 and 120 km and their contributions to density variability within this height regime.

2. THE STATUS OF ATMOSPHERIC TIDES RESEARCH

Atmospheric tides represent one obvious mechanism for dynamically coupling the lower atmosphere with the upper atmosphere and ionosphere. Semidiurnal and diurnal tidal oscillations are excited by H_2O and O_3 insolation absorption in the troposphere, stratosphere, and mesosphere, and propagate upwards into the lower and upper thermosphere. In the mesosphere mode coupling occurs via interactions with the mean wind field to modify the mixture of modes driven directly by thermal excitation. The shorter wavelength modes dissipate and deposit mean momentum and heat at the base of the thermosphere. The longer wavelength modes penetrate to upper levels and combine with oscillations excited in-situ to produce the total observed diurnal variation of winds, temperatures, densities, and pressures at any given height and latitude.

Quantitatively, the degree to which tides of lower atmospheric origin affect the diurnal and latitudinal structure of the thermosphere as a function of height, season, and solar cycle is still not well known. Certainly, the

effects are expected to become more prominent as the EUV excitation diminishes with declining solar activity. Insofar as modelling is concerned, a major uncertainty in thermospheric general circulation models (TGCMs) is specification of tidal-period oscillations at the lower boundary near 95 km. This can be greatly aided by global observations available from MST, meteor wind, and medium-frequency radars (Figures 4 and 5), combined with spectral model results for the height regime below 100 km. The spectral models as they now exist must be upgraded to incorporate more realistic specifications of heating rates, turbulent diffusivities, and mean winds on at least a monthly basis. Modelling and observational efforts must be directed both along the lines of 'climatology' and 'weather'; that is, while it is important to understand seasonal and global trends, other efforts must focus on transient phenomena such as equinox transitions or stratwarm effects.

In addition, further work is required to understand the physics of gravity wave/tidal interactions, related implications with regard to the interpretation of observations, and how such effects can be parameterized in models which simulate tides. For instance, work by D. Fritts, R. Vincent, and R. Walterscheid shows that tides can induce a daily variation in the momentum, heat, and turbulence deposition by dissipating gravity waves. The accompanying wind, temperature, and density fluctuations, which at this point in time can only be speculated on, would be expected to occur at higher levels as well as in-situ.

3. DENSITY VARIATIONS DUE TO TIDES

Numerical models typically solve a reduced set of equations, either cast in terms of the perturbation geopotential, or the three velocity components and temperature, depending on how diffusion is parameterized. Assuming the tidal temperature perturbations δT are small compared with the mean background temperature T_0 , one can derive an approximate expression for the relative variation in total mass density:

$$\frac{\delta \rho}{\rho_0} \approx \left\{ 1 - \frac{\delta T}{T_0} \right\} \exp\{x_m\} - 1$$

where

$$x_m = \frac{-g\bar{M}}{R^*} \int_0^z \frac{\delta T}{T_0^2} dz'$$

Using the numerical simulations by Forbes (J. Geophys. Res., 87, p. 5222 - 5252, 1982), tidal variations in density as illustrated in Figures 6 and 7 can be computed. The estimated variations of 5 - 20 percent between 80 and 120 km ought to be important for aerospace operations in this height regime.

4. THE LOWER THERMOSPHERE COUPLING STUDY

The subject of mesosphere-thermosphere coupling is the focus for the Lower Thermosphere Coupling Study (LTCS) of the CEDAR (Coupled Energetics and Dynamics of the Atmospheric Regions) and WITS (World Ionosphere - Thermosphere Study) Programs. The LTCS (Figure 8), which began in 1986, is a coordinated investigation of the lower thermosphere (80 - 180 km) combining observational and numerical modelling efforts with the ultimate goal of better understanding the dynamic and electrodynamic processes coupling the mesosphere, lower thermosphere, and upper thermosphere regions. Primary emphasis is placed on neutral winds and temperatures, and electric fields and currents, as these are among the parameters of main scientific interest, and there is a need to keep the study as narrowly focused as possible. Nevertheless, the better understanding of physical phenomena and improved modelling capabilities likely to emerge from the study will enhance the capability to specify total mass density as well.

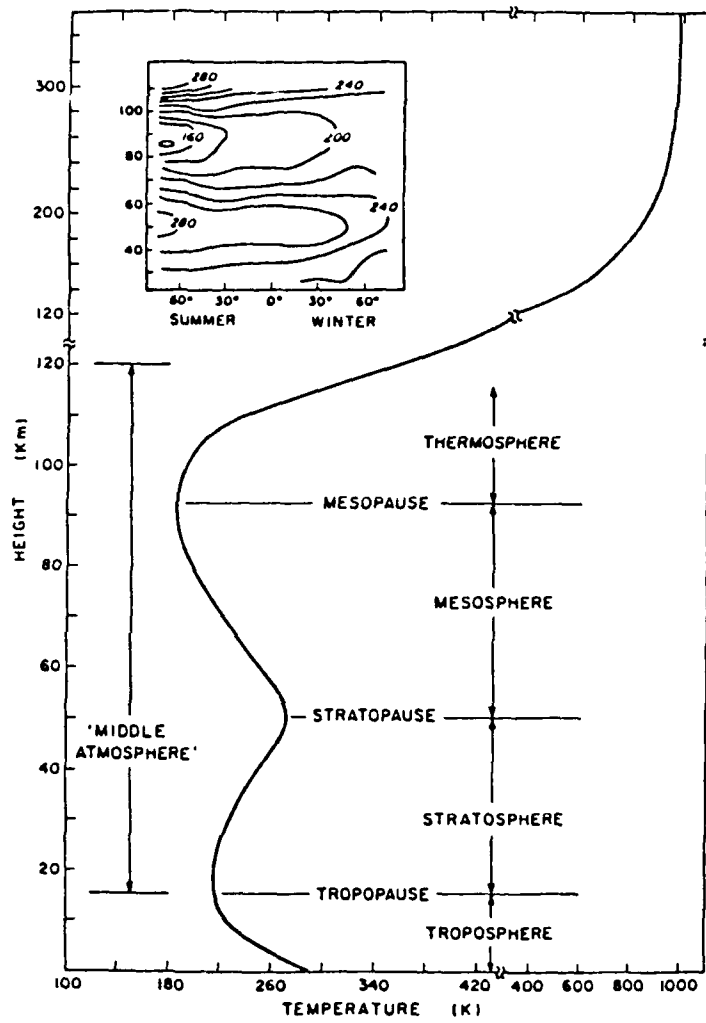


Figure 1. Average midlatitude vertical temperature structure (based on U.S. Standard Atmosphere, 1976) and (inset) zonally-averaged height-latitude temperature structure during solstice conditions (based on Cospar International Reference Atmosphere, 1972).

MESOPAUSE REGION PROCESSES

THERMAL STRUCTURE DYNAMICAL STRUCTURE

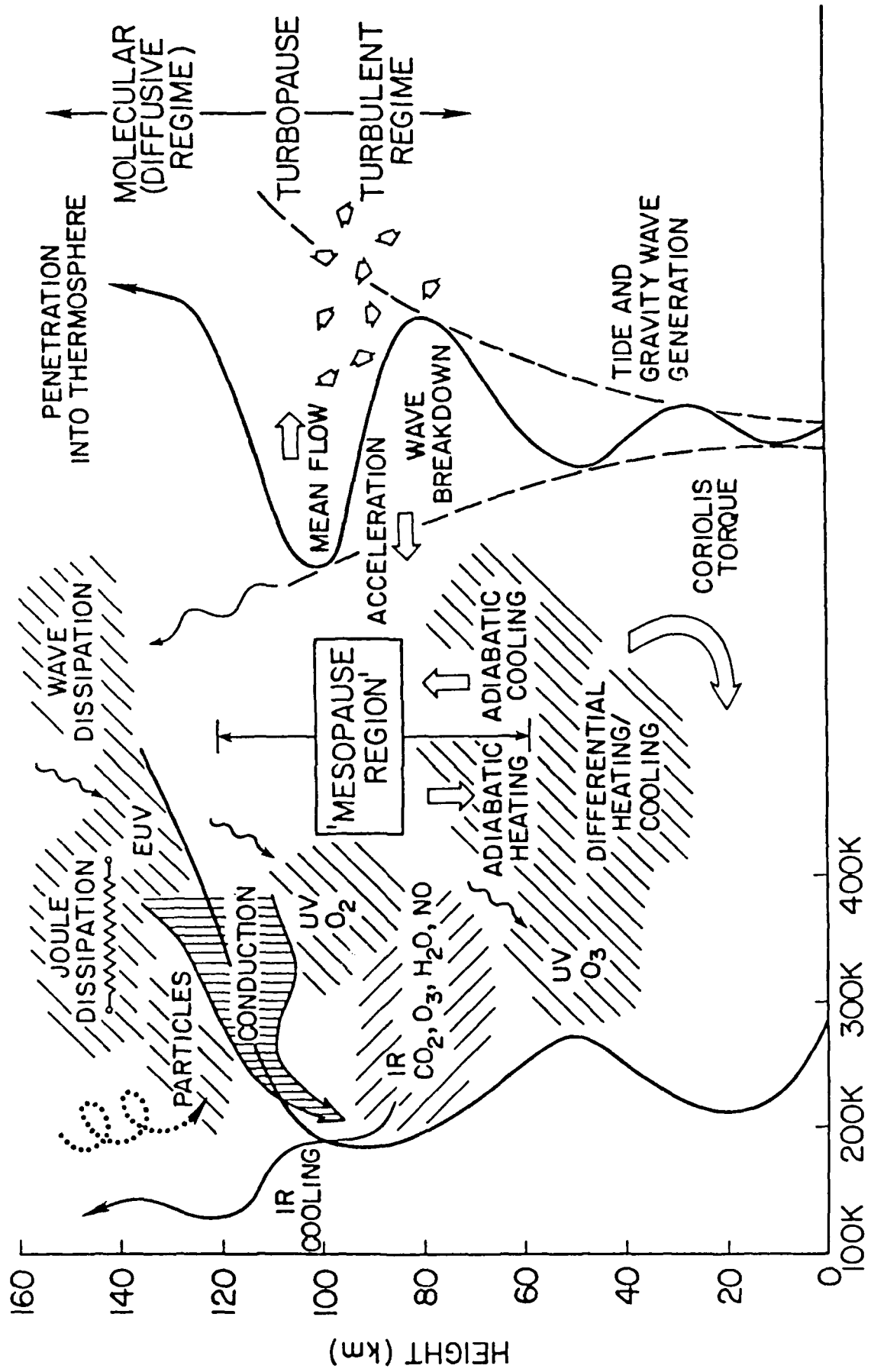


Fig. 2

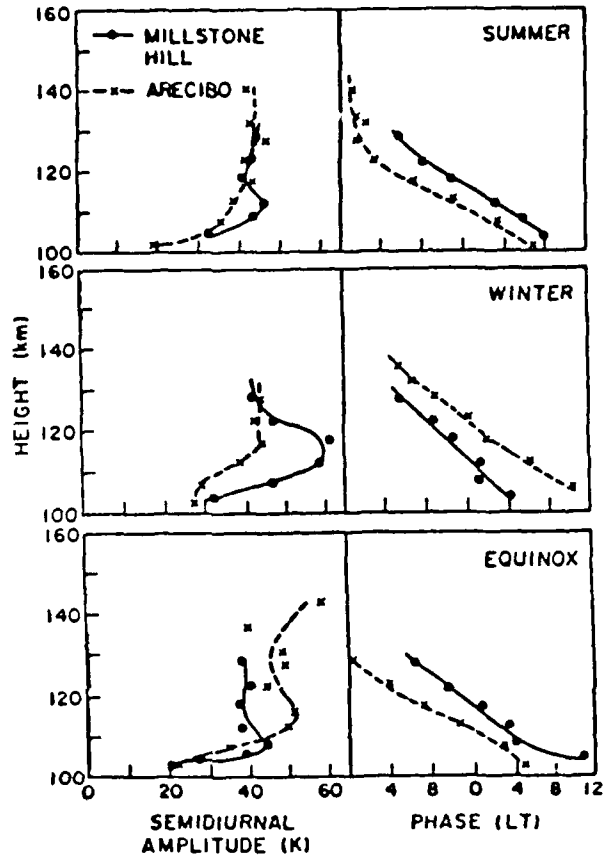


Fig 3. Seasonal averages of Semidiurnal temperatures derived from 25 simultaneous daytime experiments at Arecibo and Millstone Hill.

TIDAL LOWER BOUNDARY CONDITION (PERTURBATION GEOPOTENTIAL) FROM WIND DATA

Momentum equation from classical tidal theory:

$$\frac{\partial u}{\partial t} - fv = -\frac{1}{a \cos \theta} \frac{\partial \Phi}{\partial \lambda} \quad (1)$$

where

u = eastward velocity

v = northward velocity

θ = latitude

λ = longitude

t = time

f = coriolis parameter = $2\Omega \sin \theta$

g = acceleration due to gravity

a = radius of Earth

$\Omega = 2\pi/24 \text{ hours}^{-1}$

introducing $e^{i(\omega t + s\lambda)}$,

$$i\omega u' - fv' = -\frac{is}{a \cos \theta} \Phi' \quad (2)$$

For migrating tide $\omega = s\Omega$; therefore:

$$\Phi' = -a\Omega \cos \theta \left\{ u' + i \frac{2 \sin \theta}{s} v' \right\} \quad (3)$$

[see also Portnyagin and Kajdalov, 1986]

Fig 4

From Classical Tidal Theory:

$$\Phi' = \sum_n \phi_n \Theta_n(\theta) \quad (4)$$

$$u' = -\frac{s}{4a\Omega} \sum_n \phi_n U_n(\theta) \quad (5)$$

$$v' = -\frac{is}{4a\Omega} \sum_n \phi_n V_n(\theta) \quad (6)$$

where

$\Theta_n(\theta)$ = Hough function (orthogonal)

$U_n(\theta)$ = eastward velocity expansion function

$V_n(\theta)$ = northward velocity expansion function

The ϕ_n 's can be determined from radar wind data by least-squares fitting

(a) Φ' [Equations (3) and (4)]

(b) u' and/or v' directly [Equations (5) and/or (6)]

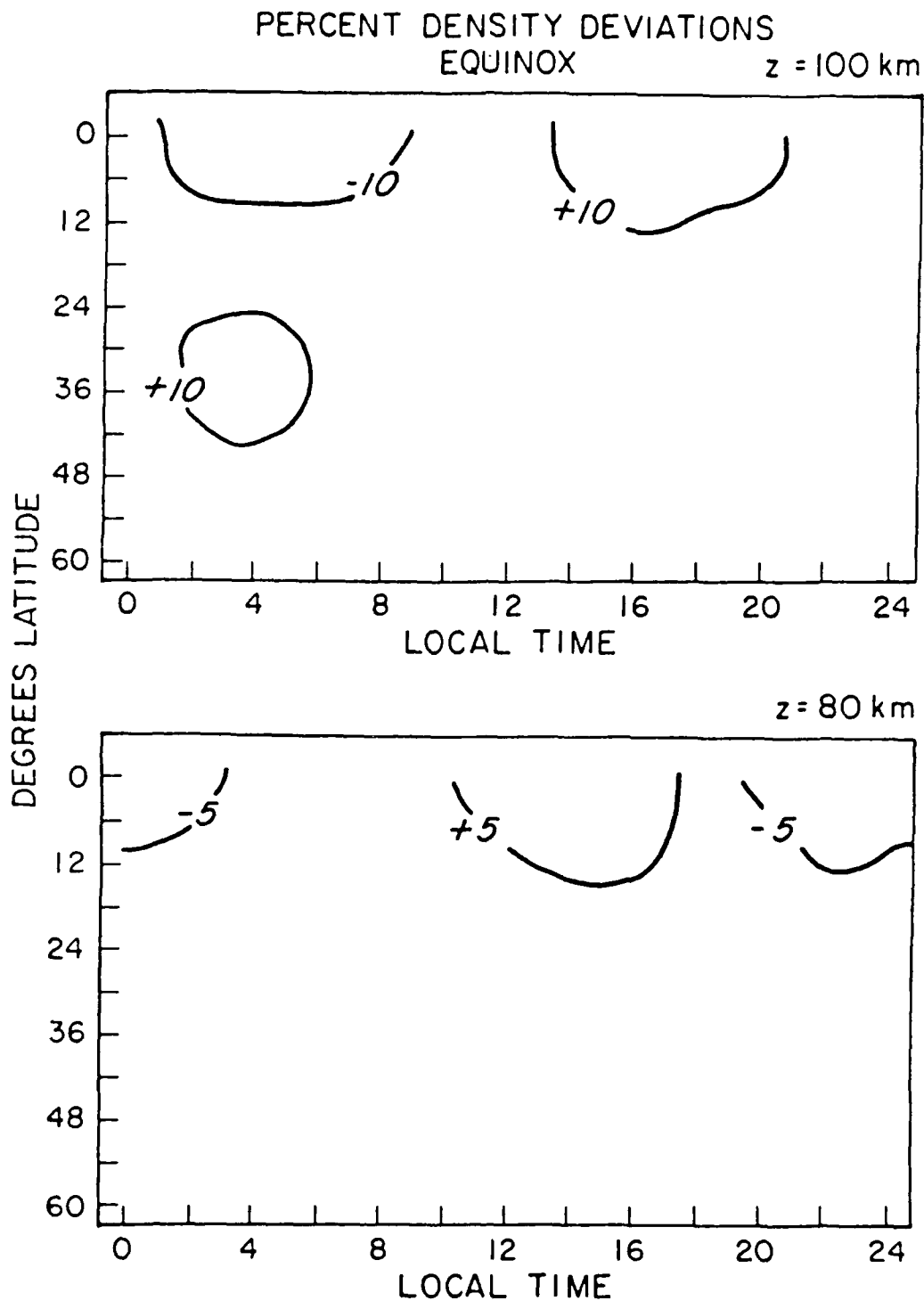


Figure 6. Estimated Percent Density derivations from the mean at equinox due to atmospheric tides.

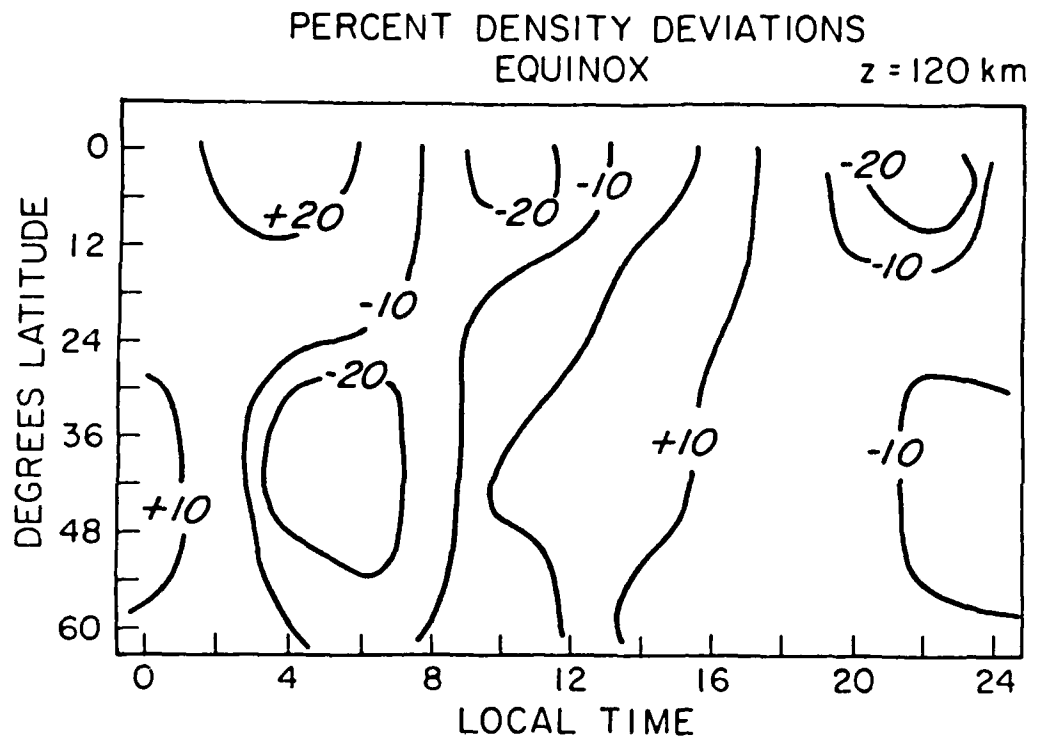


Figure 7 Estimated percent density derivations from mean at equinox due to atmospheric tides.

THE LOWER THERMOSPHERE COUPLING STUDY (LTCS)

of the
CEDAR and WITS Programs

PURPOSE AND SCOPE

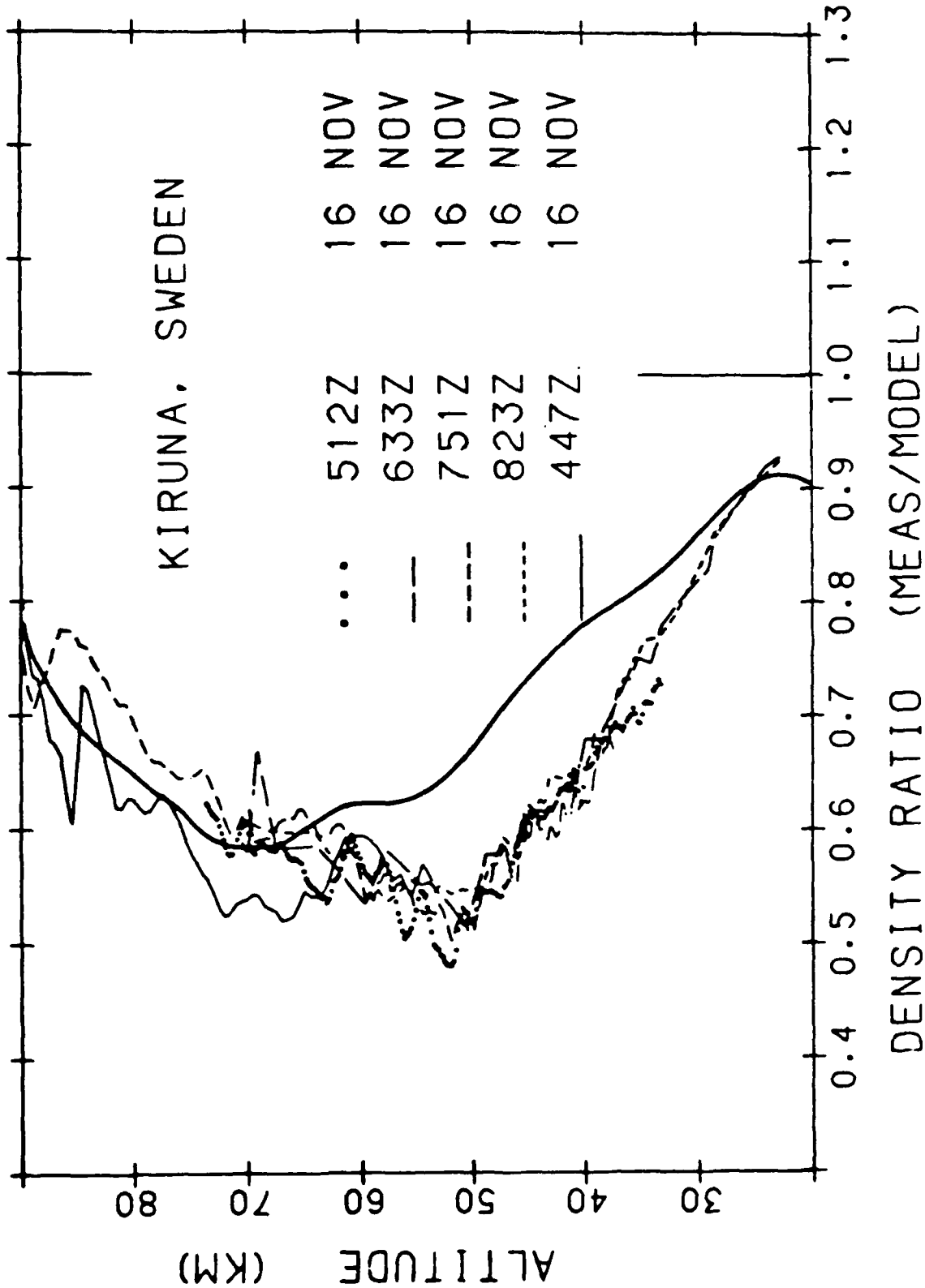
The Lower Thermosphere Coupling Study (LTCS) is a coordinated investigation of the lower thermosphere (80 - 180 km) combining observational and numerical modelling efforts with the ultimate goal of better understanding the dynamic and electrodynamic processes coupling the mesosphere, lower thermosphere, and upper thermosphere regions. Primary emphasis will be placed on neutral winds and temperatures, and electric fields and currents.

Fig. 8

ATMOSPHERIC GRAVITY WAVES

R. L. Walterscheid
The Aerospace Corporation
Los Angeles, CA

- WAVES RESULTING FROM ATMOSPHERIC PERTURBATIONS
 - GRAVITY IS RESTORING FORCE
- MESOSPHERIC GRAVITY WAVES ORIGINATE PRIMARILY IN TROPOSPHERE
 - TOPOGRAPHY, JET STREAMS, EARTHQUAKES, VOLCANOES
- THERMOSPHERIC GRAVITY WAVES ORIGINATE IN TROPOSPHERE AND AURORAL ZONE
 - OCCURRENCE ESSENTIALLY UNPREDICTABLE
- SMALL AMPLITUDE WAVES GROW ~ EXPONENTIALLY WITH ALTITUDE



RELATION BETWEEN DISTURBANCE
DENSITY AND VELOCITY

FOR $|\bar{u} - c| \lesssim 200 \text{ MS}^{-1}$

$$\left| \frac{\rho'}{\bar{\rho}} \right| \sim \frac{\bar{N}}{g} |u'| \sim \frac{|u'|}{500 \text{ MS}^{-1}}$$

\bar{N} = BRUNT-VIÄSÄLÄ FREQUENCY

g = ACCELERATION DUE TO GRAVITY

OBSERVATIONS SHOW

$$u' \approx 100 \text{ MS}^{-1}$$

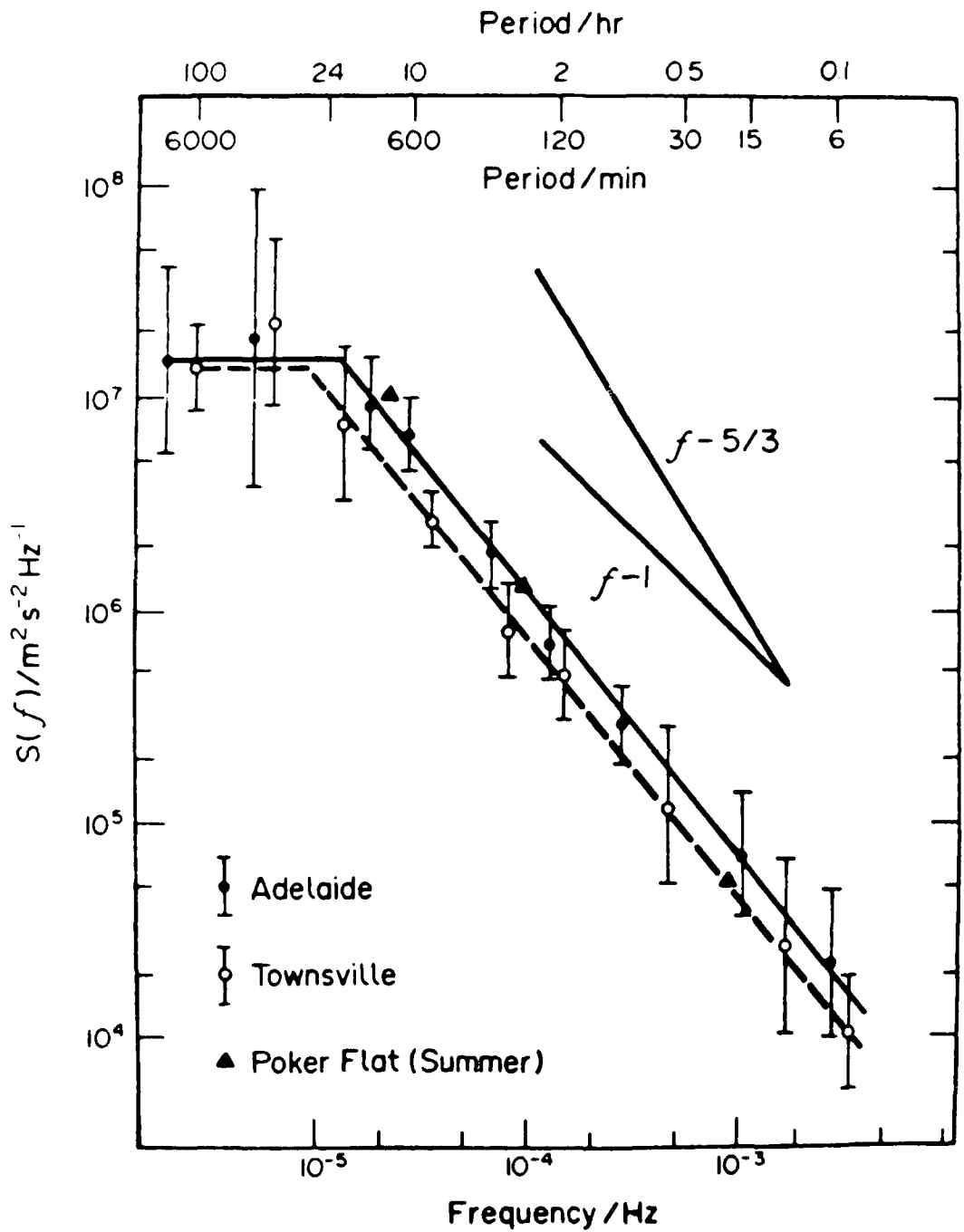
TYPICALLY $\sim 20\text{-}40 \text{ MS}^{-1}$

$$\frac{\rho}{\bar{\rho}} \approx 0.2$$

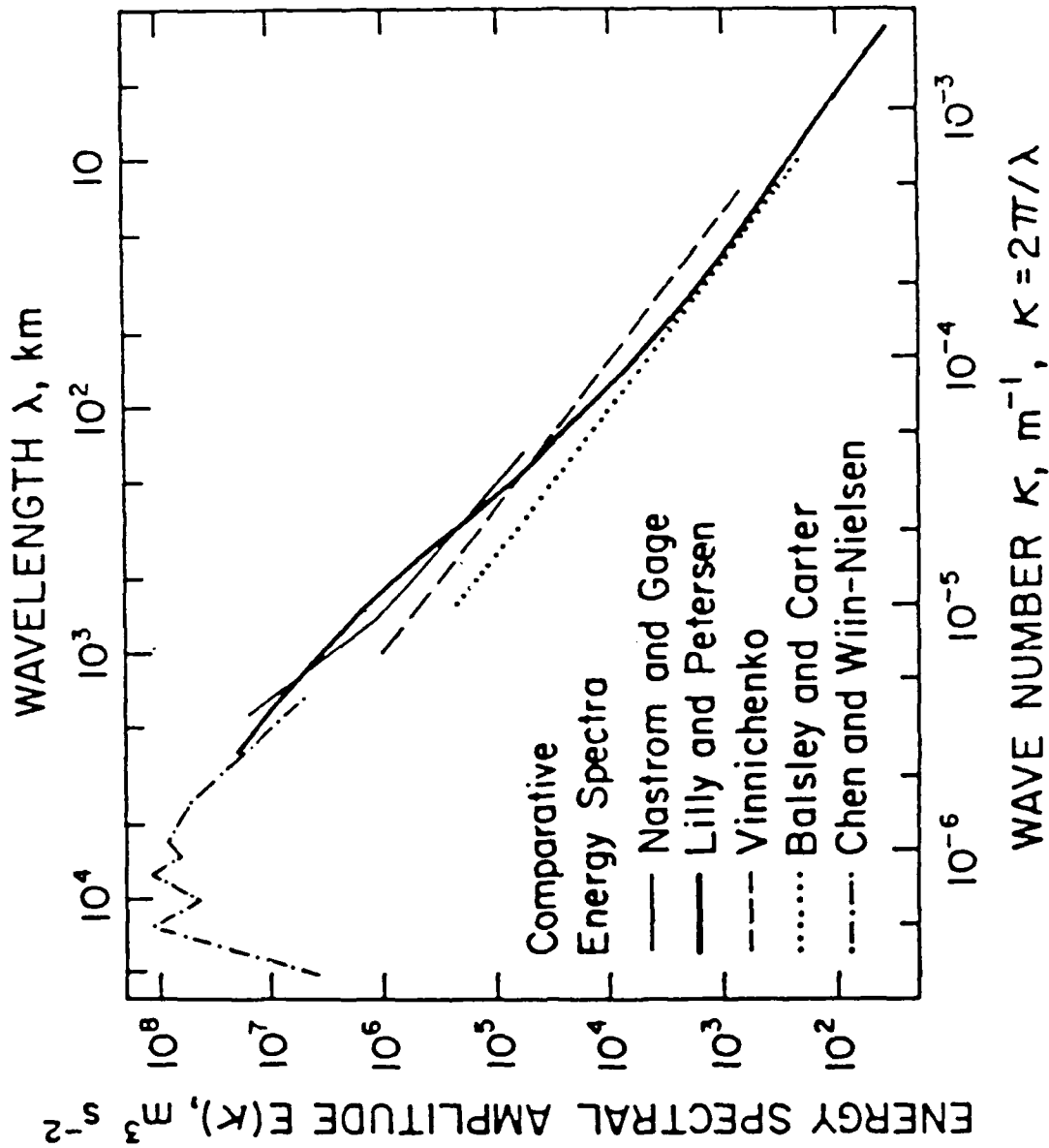


$$\frac{\rho}{\bar{\rho}} \approx 0.1$$

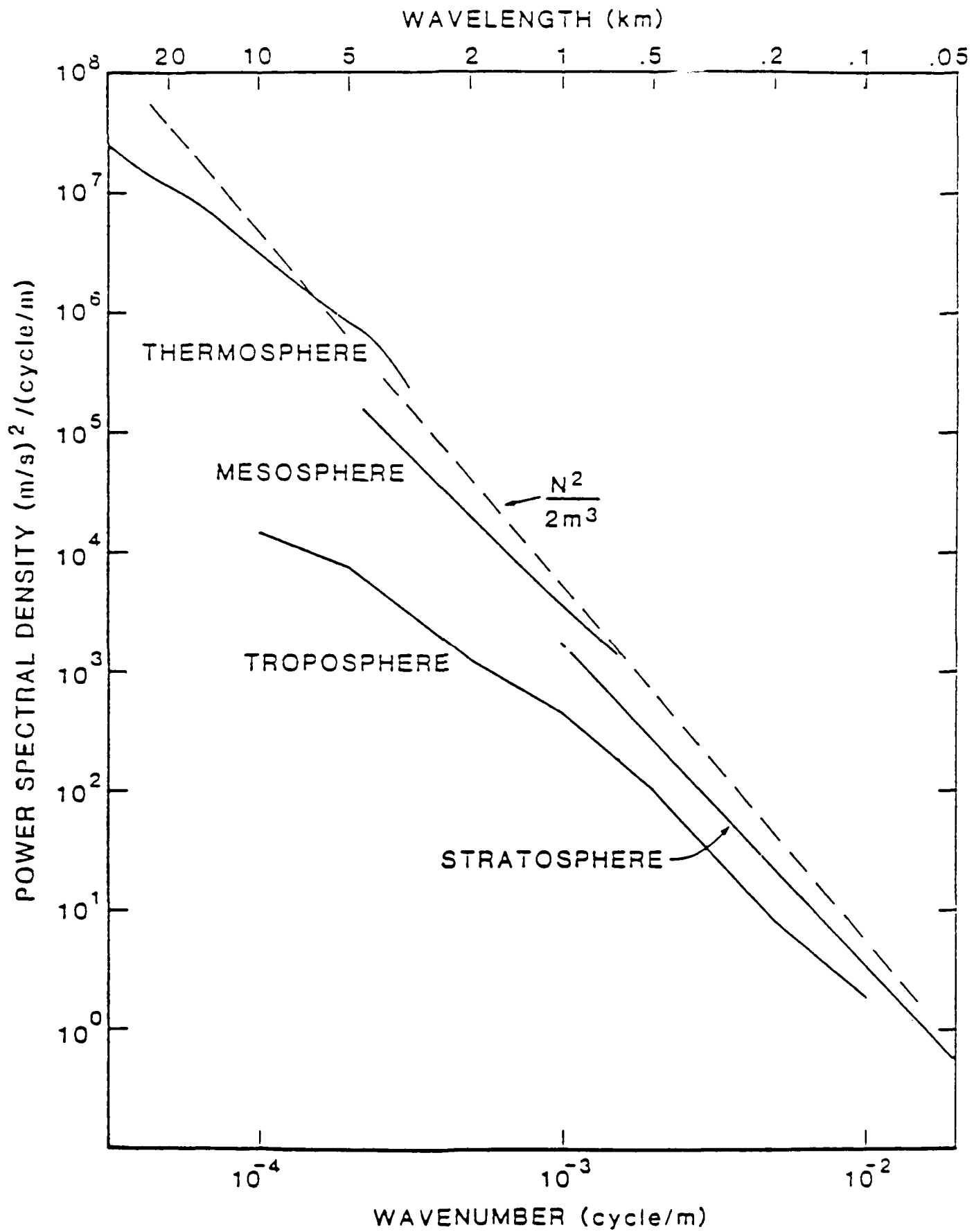
TYPICALLY



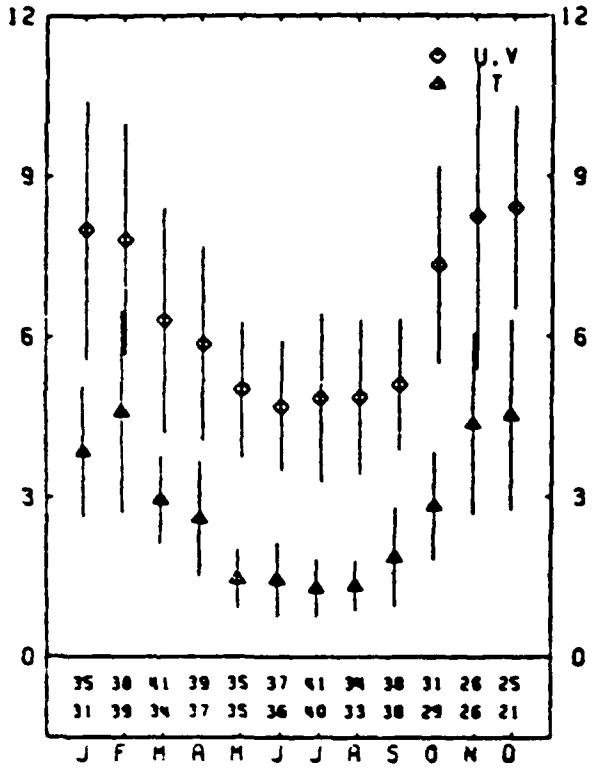
Seasonally averaged spectral densities for horizontal wind fluctuations observed at a height of 85 km at Adelaide and Townsville. The spectra are the average of the zonal and meridional spectra and the bars indicate the range of the individual spectra. ▲ Show spectral densities of wind motions observed at Poker Flat (after CARTER and BALSLEY, 1982).



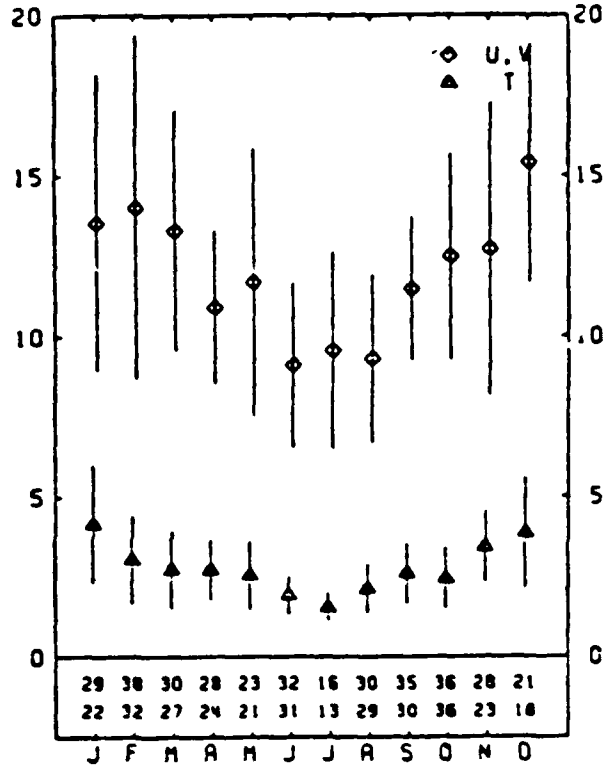
Horizontal energy spectra over the wavelength range from about 5 km to the earth's circumference. The Balsley-Carter and Vinnichenko spectra were originally produced from time records, while the Nastro-Gage and Lilly-Petersen data were obtained from jet aircraft records. Other details are given by Lilly and Petersen (1983) and Nastro and Gage (1983).



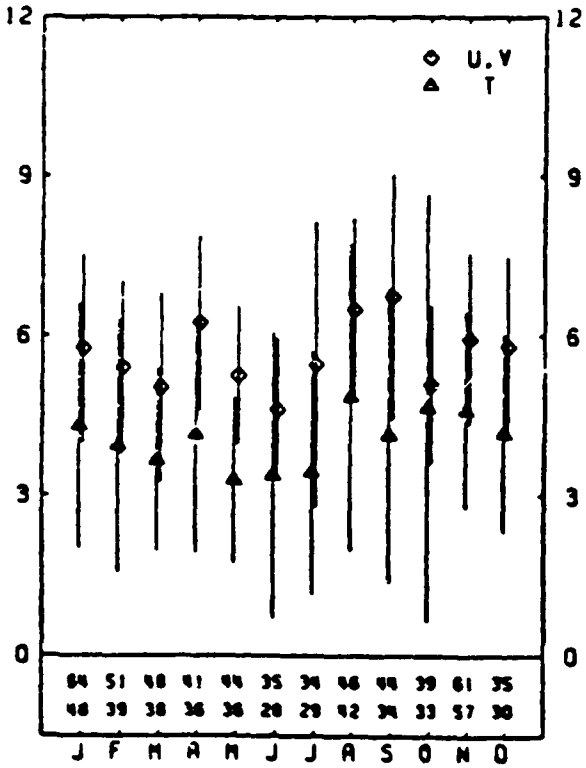
THULE (77N. 69W)



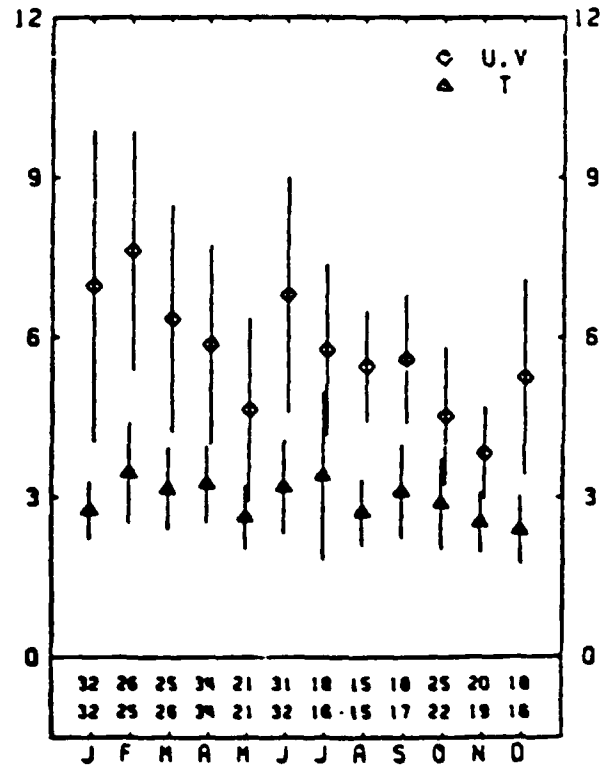
PRIMROSE LAKE (54N. 110W)



WHITE SANDS (32N. 106W)

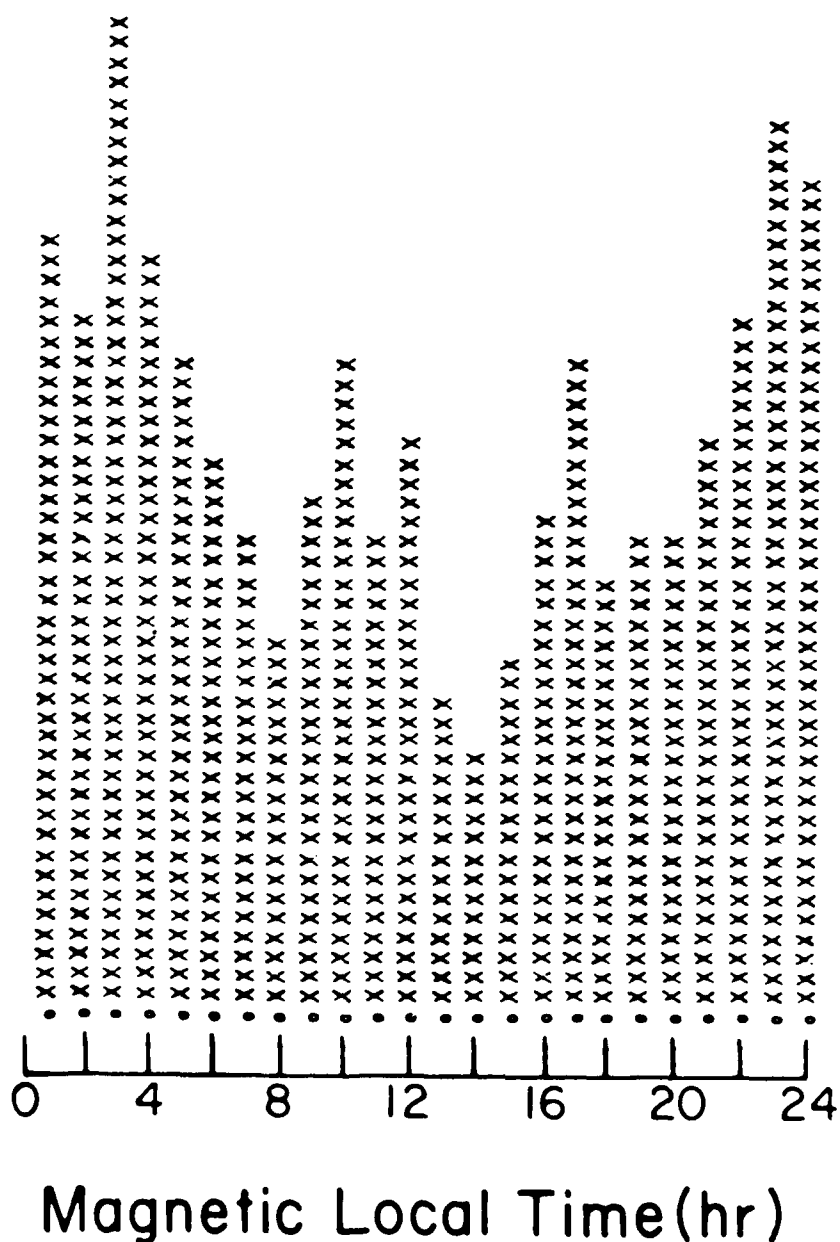


ASCENSION IS. (8S. 14W)

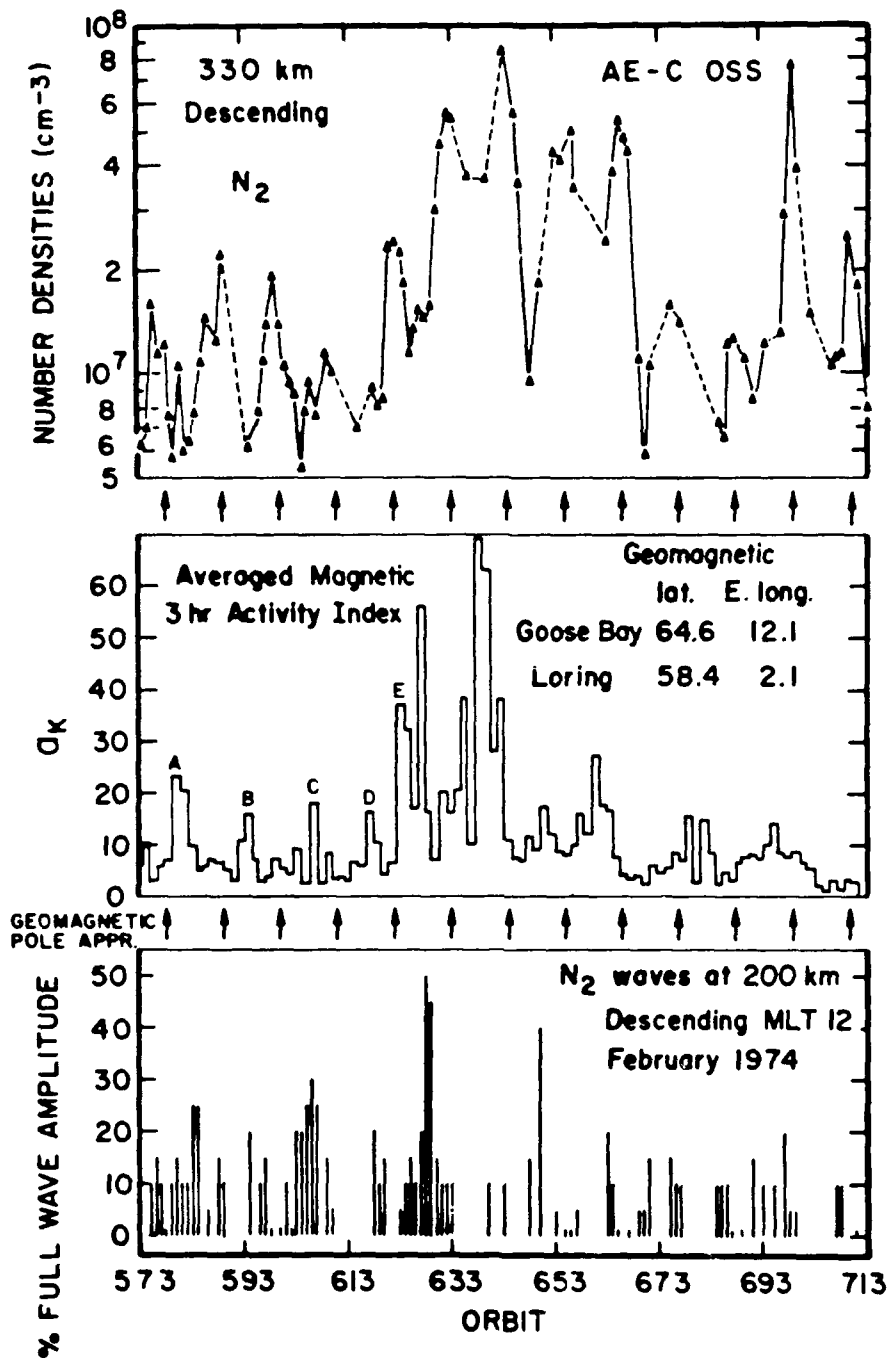


HIROTA (1984)

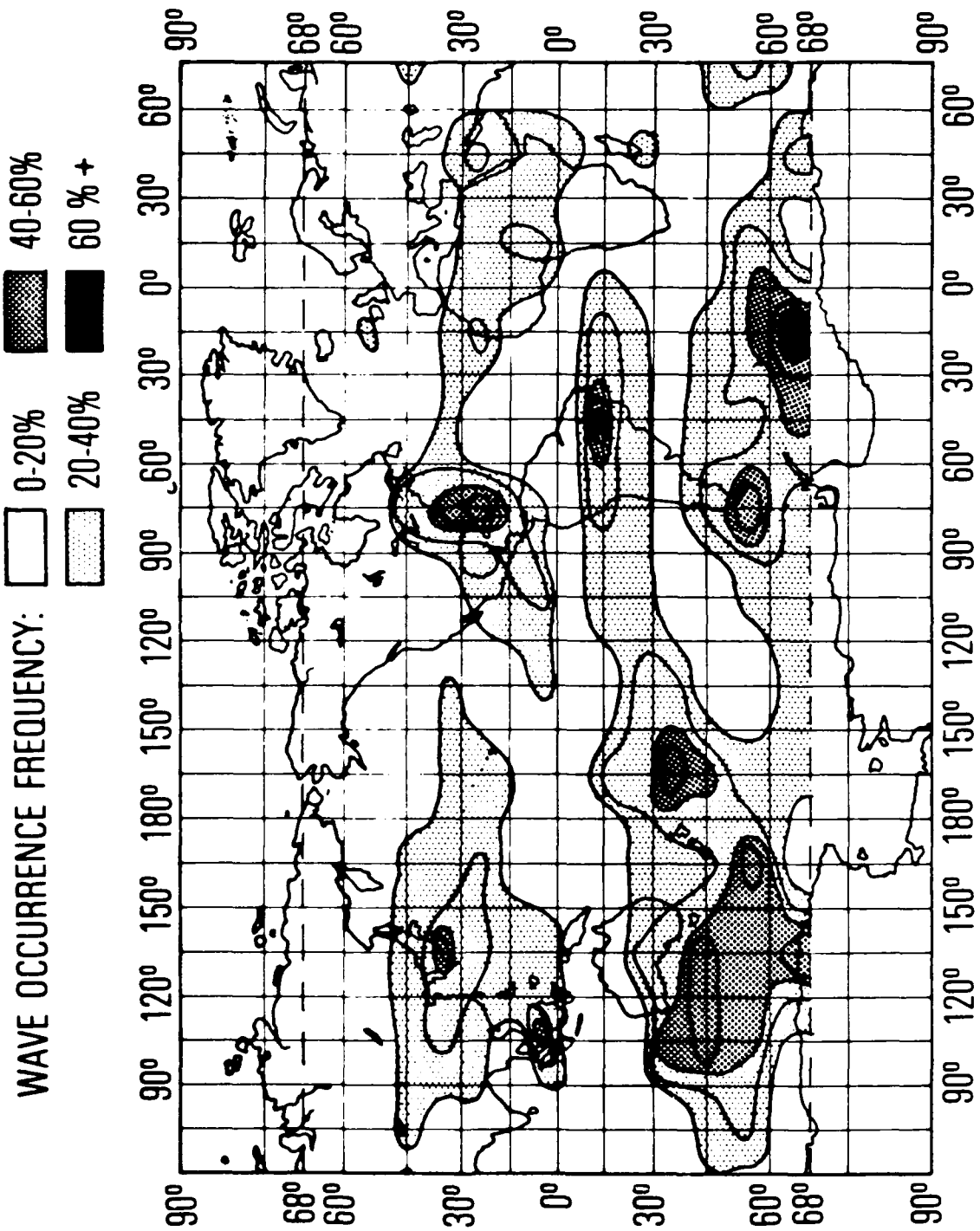
Wave Distribution 4489 Wave Samples



The wave occurrence histogram shows the distribution of waves of all amplitudes as a function of magnetic local time. The greatest number of waves are found in the midnight sector, although secondary maxima near noon indicate the possible transpolar propagation of waves assumed to be generated near midnight.



This figure shows a summary of wave occurrences during a magnetic storm in February 1974. The top and bottom panels show the N_2 number density at 330 km and wave occurrence and amplitude at 200 km, respectively. The center panel shows an averaged magnetic activity index for two high-latitude stations. The vertical arrows show the closest approach to the geomagnetic pole. The largest waves were seen near noon in regions of lower $|N_2|$ and appear to be generated near midnight, as is indicated by the increases in magnetic activity at these times.



SUMMARY

- UNPREDICTABLE (METEOROLOGICAL NOISE)
- PERIOD ~ HOURS
- HORIZONTAL WAVELENGTHS ~ 10^3 KM
- VERTICAL WAVELENGTHS ~ 10 KM
- $\rho'/\bar{\rho}$ ~ 0.1 - 0.3
- GREATEST ACTIVITY: WINTER, HIGH AND MIDDLE LATITUDES
- IMPORTANCE OF AURORAL SOURCES FOR THERMOSPHERE AS A WHOLE UNCLEAR

Tidal Effects on Thermospheric Circulation, Densities, and Temperatures

C. G. Fesen

Before discussing the influence of tides on the thermosphere, a brief review of atmospheric tides is presented. The review attempts to answer the most basic questions usually encountered in tidal research, and are listed in Figure 1. These questions include: What are tides? Why are they important? Where do they come from? The incorporation of tidal effects in thermospheric models follows, along with a brief summary of model results. Finally, suggestions are made regarding what can be done to improve the thermospheric tidal research now being done.

Tides are defined to be global scale oscillations of atmospheric quantities with periods that are integral multiples of a solar (or lunar) day. Observations which show variations with a 6 hr, 8 hr, 12 hr, or 24 hr period are exhibiting the effects of a tidal perturbation.

Figure 2 shows an example of tidal effects seen in neutral wind observations from Arecibo. The top two panels are plots of the meridional winds, and the bottom panel the vertical winds, as a function of height and local time for consecutive days. The shading indicates southward or downward winds. There is an obvious oscillation in the winds, with about a 12 hr period, or a semidiurnal tide. Higher in the atmosphere, this changes to a diurnal tide.

Similar behavior would be found in observations of the temperatures and the densities. Further, these oscillations are seen at other observatories around the globe, differing in the degree of variability, but still exhibiting time-dependent behavior.

Figure 2 therefore illustrates why tidal effects are important in thermospheric studies: tides are very evident, very strong in the upper atmosphere. In fact, in the lower thermosphere, tides dominate the thermospheric response; i.e., in analysis of wind, temperature, and density observations, the semidiurnal component typically overwhelms the mean component.

Since tides are time-dependent, they arise due to time-dependent forcings. There are three sources in the thermosphere, as listed in Figure 3. The sources due to solar heating and ion-neutral momentum coupling are relatively easy to include in numerical models of the thermosphere. The source due to the upward propagation of energy from the lower atmosphere is more difficult to parametrize; this is the only tidal source discussed in detail here.

The solar energy absorbed in the troposphere and stratosphere generates a tidal response in these atmospheric regions. Since tides are a form of internal gravity wave, they can and do propagate vertically, growing exponentially in amplitude with altitude, and carrying energy with them. Figure 4 shows a model calculation from Walterscheid, in which he calculated the semidiurnal zonal wind from the ground up to 100 km, resulting from the absorption of solar energy in the lower atmosphere. The three different curves are for three different model runs; the most accurate result is the solid curve. A wavelike behavior is evident, with amplitudes growing with height which implies that the phases increase downwards. Obviously, by the time the wave reaches the thermosphere it is quite large. This is part of the explanation for the strong semidiurnal wave seen in the lower thermosphere in the Arecibo observations in figure 2.

Thermospheric models must be able to include the effects of the tides that are generated in the lower atmosphere and subsequently penetrate into the thermosphere. Models which extend from the ground through the thermosphere are not possible at present. A simpler, do-able scheme is based on the following approach: if a model such as that shown in figure 4 is correctly formulated, it should be able to reproduce the model results at upper levels by taking the model solutions at some lower level, using them as new lower boundary conditions, and running the model from this new lower boundary. If correctly formulated, the model should reproduce the solutions from the original "full" model for those altitudes above the new lower boundary.

This is the approach used in incorporating lower atmosphere tidal effects in the NCAR TGCM. A distribution of the model variables is prescribed at the lower boundary which is wavelike. The wavelike distribution represents the waves that were generated in the lower atmosphere, and travelled up to the thermosphere. An alternate description is that the wavelike distribution is analogous to shaking the lower boundary, like shaking a rug: this will cause oscillations, which will travel upwards as described by the model equations.

The wave description at the lower boundary of the NCAR TGCM is in terms of Hough modes. The Hough modes represent part of the solution to a simplified set of tidal equations which are approximately valid near and below 100 km. The Hough modes describe the latitudinal distribution of a particular wave, and are functions of Legendre polynomials which are well known mathematically. Figure 5 shows the semidiurnal Hough modes. The modes are identified as the (2,2), (2,3), (2,4) and (2,5). The first subscript is a zonal wavenumber, denoting the number of waves that fit around a latitude circle. Two waves represent a semidiurnal tide. The second index is the meridional wavenumber, which measures the degree of waviness or structure in the meridional direction. Subtraction of these two numbers (the zonal and meridional wavenumbers) gives the number of nodes, or zero-crossings of the equator, for each of these modes. Thus, the 2,2 has no nodes and is symmetric about the equator, the 2,3 has one node at the equator, and is asymmetric, etc.

Figure 5 also lists the vertical wavelengths of these modes, which increase with meridional wavenumber. Thus, the higher order modes do not penetrate far into the thermosphere, since they are more likely to suffer interference. Consequently, the lower thermosphere exhibits more wave-like structure and variability, which gradually damps out higher in the thermosphere, until only the lowest order modes such as the 2,2 and the 2,3 are contributing to the response.

The Hough modes, then, are the functions used to describe the latitudinal structure of the model variables— pressure, temperature, winds, and density — at the lower boundary of the NCAR TGCM which is at 97 km. An oscillatory time behavior is also folded into the lower boundary description. The model solutions are checked by comparison with data for similar conditions.

Figure 6 presents a brief summary of the steps followed in producing a model run of the TGCM which includes the effects of upward propagating tides. The dashed line in the figure from step 5 to step 3 indicates that if the model winds and temperatures do not agree well with observational data, a new lower boundary condition is formulated, and the model run is repeated until suitable agreement is obtained between the results and the data.

To illustrate the importance of including upward propagating tides in theoretical models, Figure 7 presents TGCM calculations for solstice solar cycle minimum which are identical except for the inclusion of the upward propagating tides. The top (bottom) panels represent the upper (lower) thermosphere, near approximately 300 (120) km. The solid contours represent perturbation temperatures, and the arrows wind vectors, with the magnitude of the maximum wind arrows for each panel shown in the center of the figure. The left (right) panels are the results without (with) upward propagating tides.

The lower thermosphere shows very obvious differences in the two results. There is a definite semidiurnal character to the temperatures, reflecting the fact that the semidiurnal tides predominate at altitudes of 100-150 km or so. The winds obviously will change to reflect this, as will the densities. There are significant meridional flows at low latitudes, unlike the results without tides. The maximum wind speed is seen to have doubled with tides. The amplitude of the temperature variation, from maximum to minimum, is also much larger with the propagating tides.

The upper thermosphere also shows significant differences, especially near midnight. Note that the wind speeds again are stronger than they were without the tides, and that the amplitude of the temperature variation is larger, which will translate into larger amplitude density variations.

Figure 8 shows that the inclusion of tides in calculations is important and necessary to produce realistic simulation of observations. The neutral wind observations from Arecibo, shown in Figure 2, are reproduced, along with model calculations of the wind at Arecibo's location, without and with the tides. The improvement is quite obvious. The lower thermosphere oscillatory behavior is not reproduced at all without accounting for the upward propagating energy in the model.

Figure 9 shows the neutral mass densities associated with the wind and temperature results of figure 7, with the same format. Again, the lower thermosphere calculations show a tremendous difference in the densities calculated with and without upward propagating tides. The densities without tides show a diurnal variation that is not realistic. The densities calculated with tides show strong latitude and local time gradients.

The upper thermosphere shows a simpler structure, predominantly diurnal, but with stronger local time variations at most latitudes in the tides case. It is obvious that the amplitude of the density variation is obviously much greater with tides than without throughout the thermosphere.

Seasonal differences are illustrated in figure 10, which shows solstice and equinox tidal calculations. Obviously, the equinox distributions are more symmetric, since the forcing is symmetric: the sun is on the equator. The solstice results are asymmetric because the forcing is asymmetric: the sun is in the southern hemisphere. Again, the tides are seen to be very important in the lower thermosphere. There are much stronger gradients and more structure at solstice than equinox, reflecting the fact that the solstice tides have contributions from all the semidiurnal modes, both symmetric and asymmetric. The amplitude variation of the density is larger during solstice than equinox. In the upper thermosphere, the local time variation at

equinox is relatively flat during the day at most latitudes, unlike the solstice case.

So far, then, the tides have shown altitudinal, latitudinal, and seasonal dependences. Figure 11 shows the solar cycle dependence of the tides. Illustrated in the top panels are the calculated temperatures near Arecibo for solar cycle minimum and maximum as a function of altitude and time; the bottom panels show the temperatures and winds at fixed pressure levels near 120 and 300 km. It is evident that the tides remain important to higher altitudes near solar cycle minimum as compared to solar maximum, which is due to the fact that the density increases at a fixed pressure level with solar activity. This means that the atmosphere is thicker, denser, and consequently more viscous during solar cycle maximum, so that the tides coming up from the lower atmosphere are damped more rapidly than during low solar activity.

The results thus far have been mainly theoretical; figure 12 shows some comparisons between the model results and observations to illustrate how well the model reproduces the observed thermospheric response. The data in figure 12 are on the right-hand side, and were taken by the Atmosphere Explorer satellite 'E' (AE-E). The data are from solstice periods from 1976 through 1978. The satellite was in a circular orbit near 275 km at this time, and was restricted to latitudes between $\sim \pm 20^\circ$. The satellite observations of temperature and number densities during this period were averaged together to determine average temperatures, and average atomic oxygen and N_2 number densities. These averages were then decomposed into mean, diurnal, and semidiurnal components. This work was done by USAF Lt. Mark Storz, as part of his master's thesis at the University of Michigan in the summer of 1987.

Only semidiurnal results are plotted in figure 12, with the corresponding results from the TGCM shown on the left of the figure. The highs and lows show the maxima and minima of the semidiurnal temperature and density variations; the amplitudes are double either of these numbers. The solid lines running through the highs represent the phases, or times of maxima, which are read off the bottom axis.

The agreement is quite encouraging. Granted, at first glance, the model results are skewed toward the north, while the data show symmetry about the equator. But the numbers and the morphology show decent agreement for a first cut. The density amplitudes are quite similar, while the phase agreement is fair, with the model phases about 2 hours early. The temperature amplitudes are 50% too high in the model, while the phase is 4 hours early. Why, then, is the agreement claimed to be "encouraging"? This represents the first attempt to match the model output to this type of extensive data coverage. There was no tuning of the model to these conditions, beyond matching the season, solar cycle, and geomagnetic conditions. And, due to certain parametrizations in the model, the low latitude region is a difficult region to model accurately. Further, data coverage is very limited in this region. The comparison, then, seems to show that the model is on the right track, and progress can be made in understanding and alleviating the differences between the two. For example, the model run had the amplitudes of the 2,2 and 2,3 modes the same at the lower boundary. As a reminder, the 2,2 and 2,3 latitude structure is repeated at the bottom of the figure. It seems quite obvious that there is too much 2,3 in the model results; the observations show a 2,2-type behavior. This illustrates how valuable observations are to these theoretical tidal studies: the observations very much guide our modelling effort. After attempting to better match these solstice observations, equinox

observations will be modelled, followed by a similar study for geomagnetically active conditions.

Figure 13 summarizes the main results of the tidal studies presented here, which are:

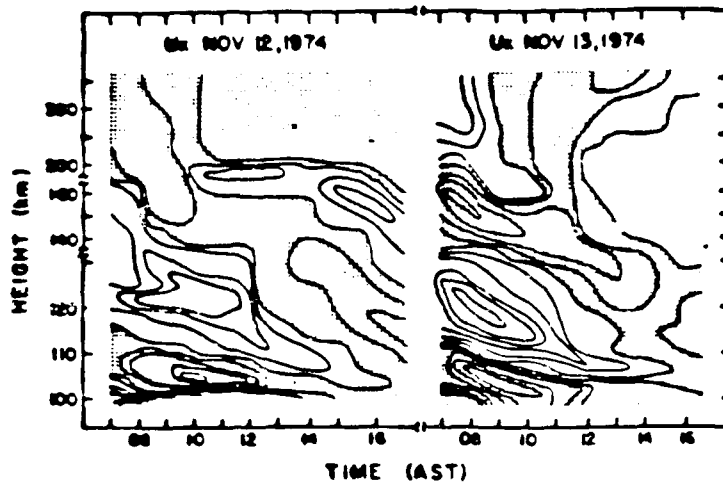
- tidal effects are an integral part of the thermospheric circulation, densities, and temperatures; this requires that
- theoretical models must account for the tides
- the tides vary with
 - season (up to and over 25% in amplitude for densities, depending on altitude)
 - solar cycle (50-100% and more in density amplitudes at high altitudes)
 - latitude (see below)
- the tides are also very variable from day to day; variations may be on the order of 30-40% in the density amplitudes, depending on altitude;
- tidal influence on the neutral densities are shown below, for three different heights. These are calculated percentage differences in the results with tides and without tides at the pole and at the equator:

Z	% ρ (pole - equator, with and without tides)
120 km	100-1000%
180 km	10-25%
300 km	10-40%

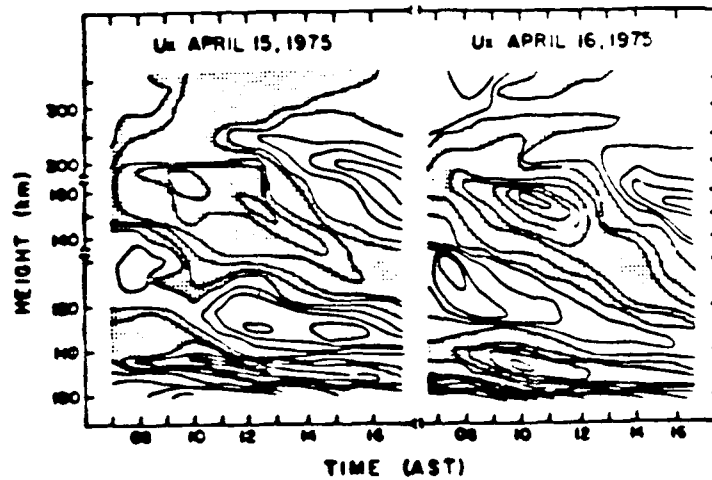
- to improve modelling and predictive capabilities, there is a great need for more observations, meaning more frequent observations, and from more sites; these should extend from the lower to the upper thermosphere, and be made at several latitudes in order to isolate the important tidal modes.
- the major obstacle to our future progress in these tidal studies is directly attributable to the lack of data: it's impossible to tell how good (or bad) the models are working without substantial amounts of data for the conditions being simulated.

Tidal Effects on Thermospheric Circulation, Temperature, and Density Structure

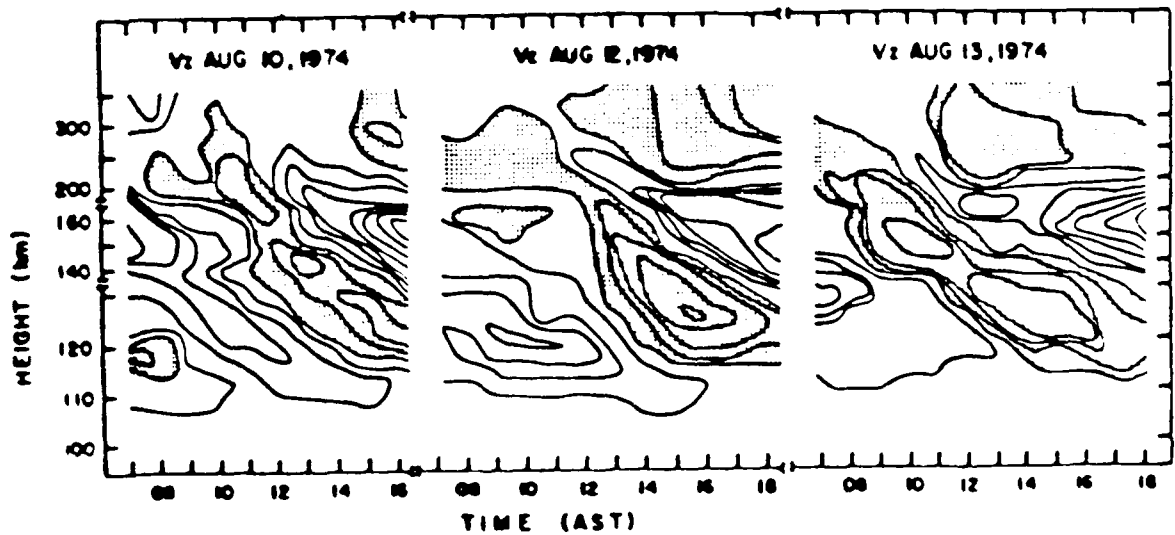
- What are tides?
- Why are they important?
- Where do they come from?
- How do we put them in models?
- What happens when we do get them in the models?
- How are we doing?
- What else needs to be done?



Southward component of the neutral wind for November 12 and 13, 1974. Contour levels are 20 m/s, and shaded contours show northward winds, i.e., negative U_z . Note changes in the altitude scale at 135 and 170 km.



Southward component of the neutral wind for April 15 and 16, 1975. Contour levels are 20 m/s, and shaded contours show northward winds, i.e., negative U_z . Note changes in the altitude scale at 135 and 170 km.



Vertical component of the ion velocity for August 10, 12, and 13, 1974. Contour levels are 10 m/s.

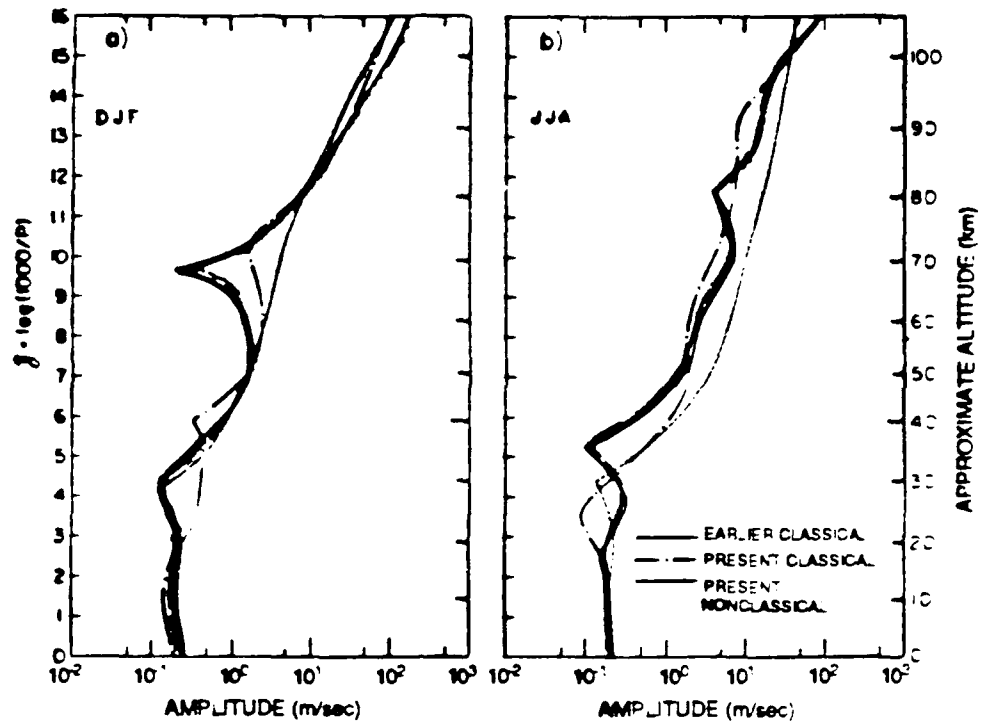
Figure 2.

Sources of Thermospheric Tides

1. In-situ absorption of solar UV and EUV energy
2. Upward propagating tides from the stratosphere and mesosphere
3. Ion-neutral momentum coupling

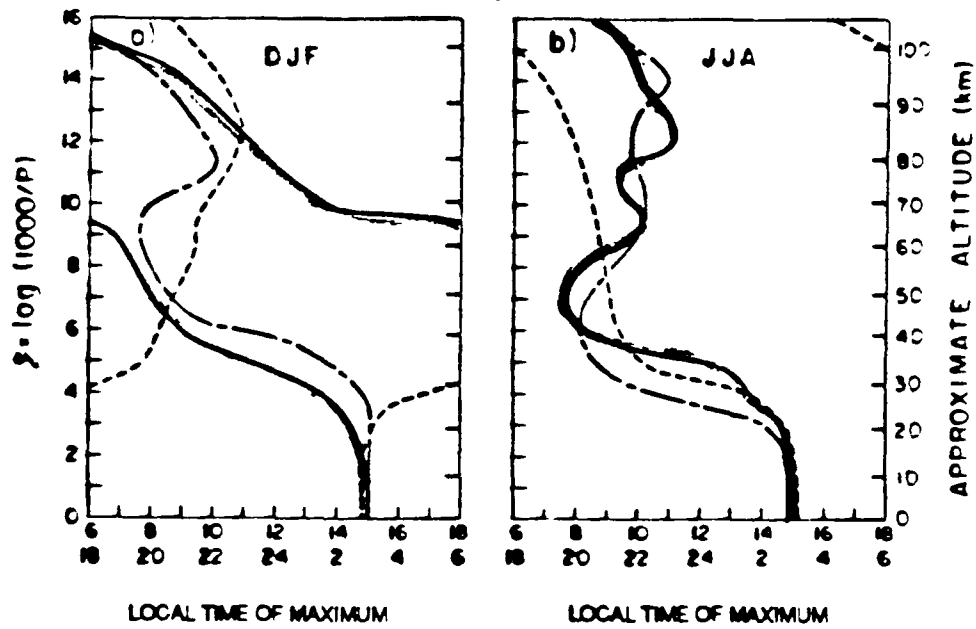
Figure 3.

SEMIDIURNAL ZONAL WIND AMPLITUDES



Amplitudes of the semidiurnal zonal wind oscillations (positive eastward) for the EC, PC and PNC models for DJF (a) and JJA (b)

PHASES



As in Fig. 7 except for the phases (local hours of maximum)

Figure 4.

SEMIDIURNAL HOUGH FUNCTIONS

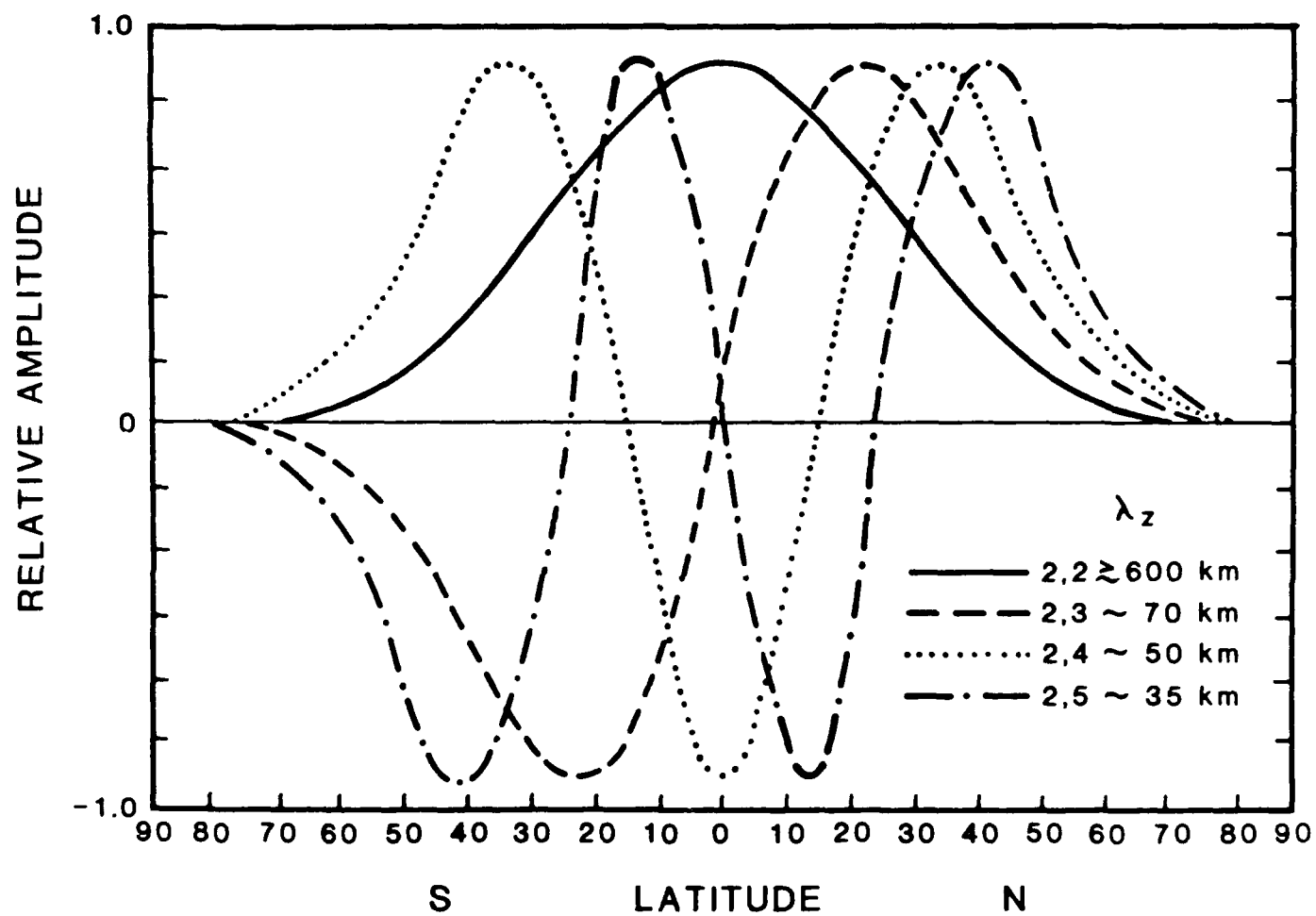


Figure 5.

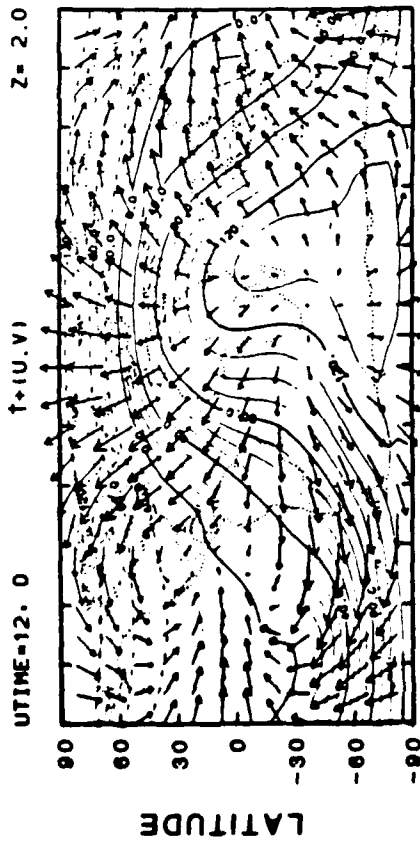
Incorporating Tides in the TGCM:

1. Specify geophysical conditions
2. Run the model to equilibrium for solar forcing only
- 3. Put in the semidiurnal tides at the lower boundary (97km)
4. Run the model to equilibrium
5. Compare T , V_{N-S} to observations:
presently, Arecibo (18°N), Saint Santin and Millstone Hill (both $\sim 45^{\circ}\text{N}$)

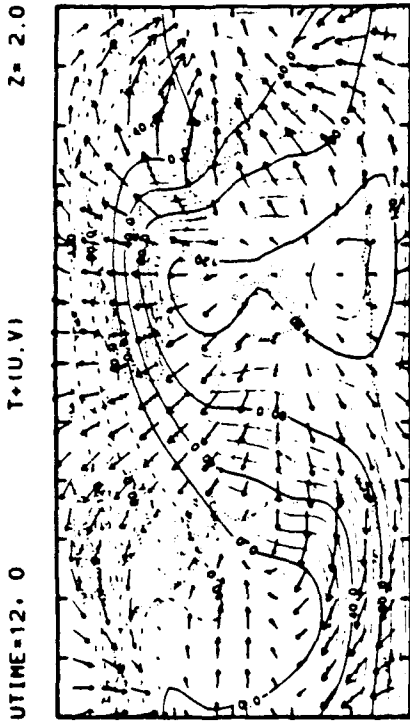
Figure 6.

SOLSTICE, SOLAR CYCLE MINIMUM

NO TIDES



TIDES



138 m/s
59

179 m/s
122

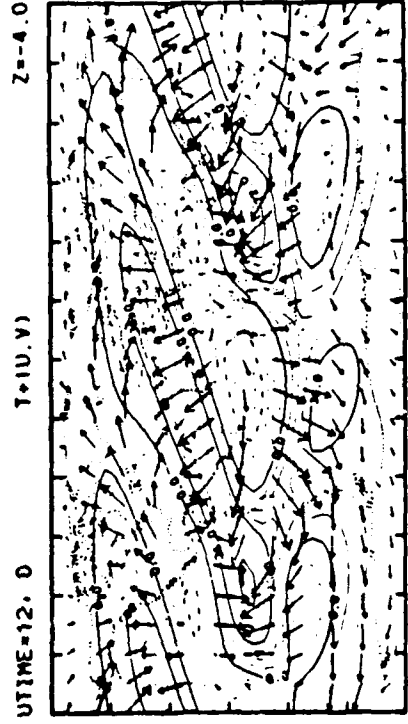
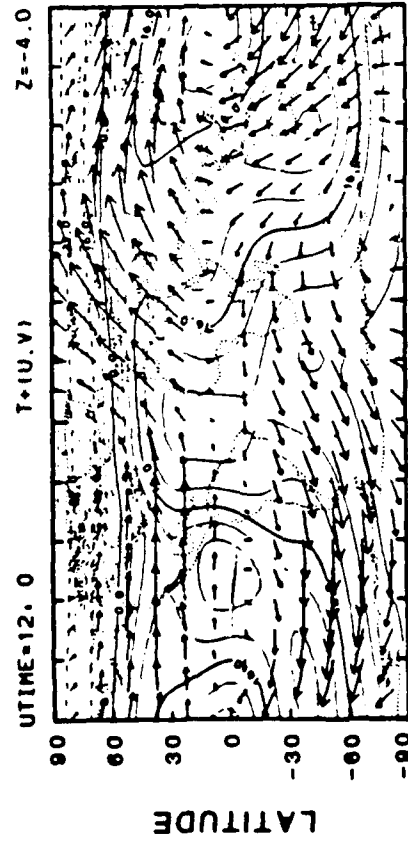
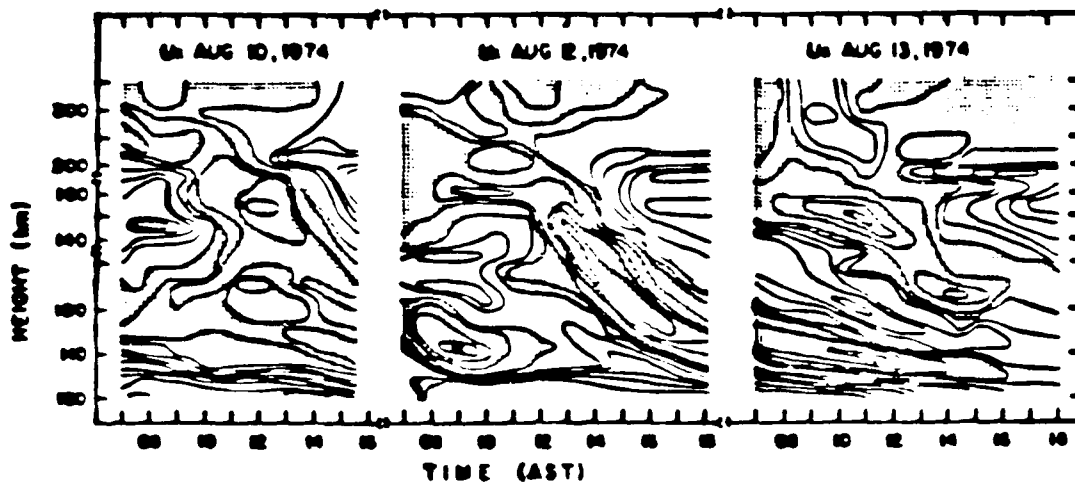
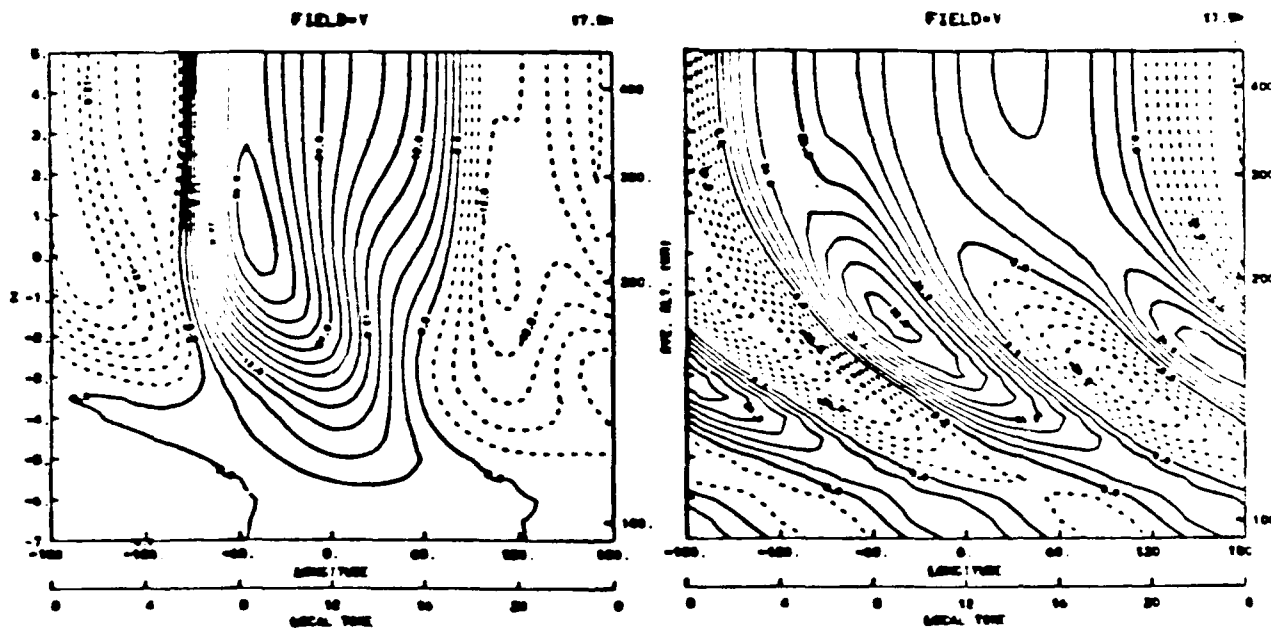


Figure 7.



Southward component of the neutral wind for August 10, 12, and 13, 1974. Contour levels are 20 m/s and shaded contours show northward winds, i.e., negative U_z . Note changes in the altitude scale at 135 and 170 km (from Harper, 1977).



Meridional winds calculated by the TGCM at 17.5°N as a function of altitude and local time. Left (right) panel shows results calculated without (with) the upward propagating tides included in the model. Positive contours are poleward.

Figure 8.

SOLSTICE, SOLAR CYCLE MINIMUM

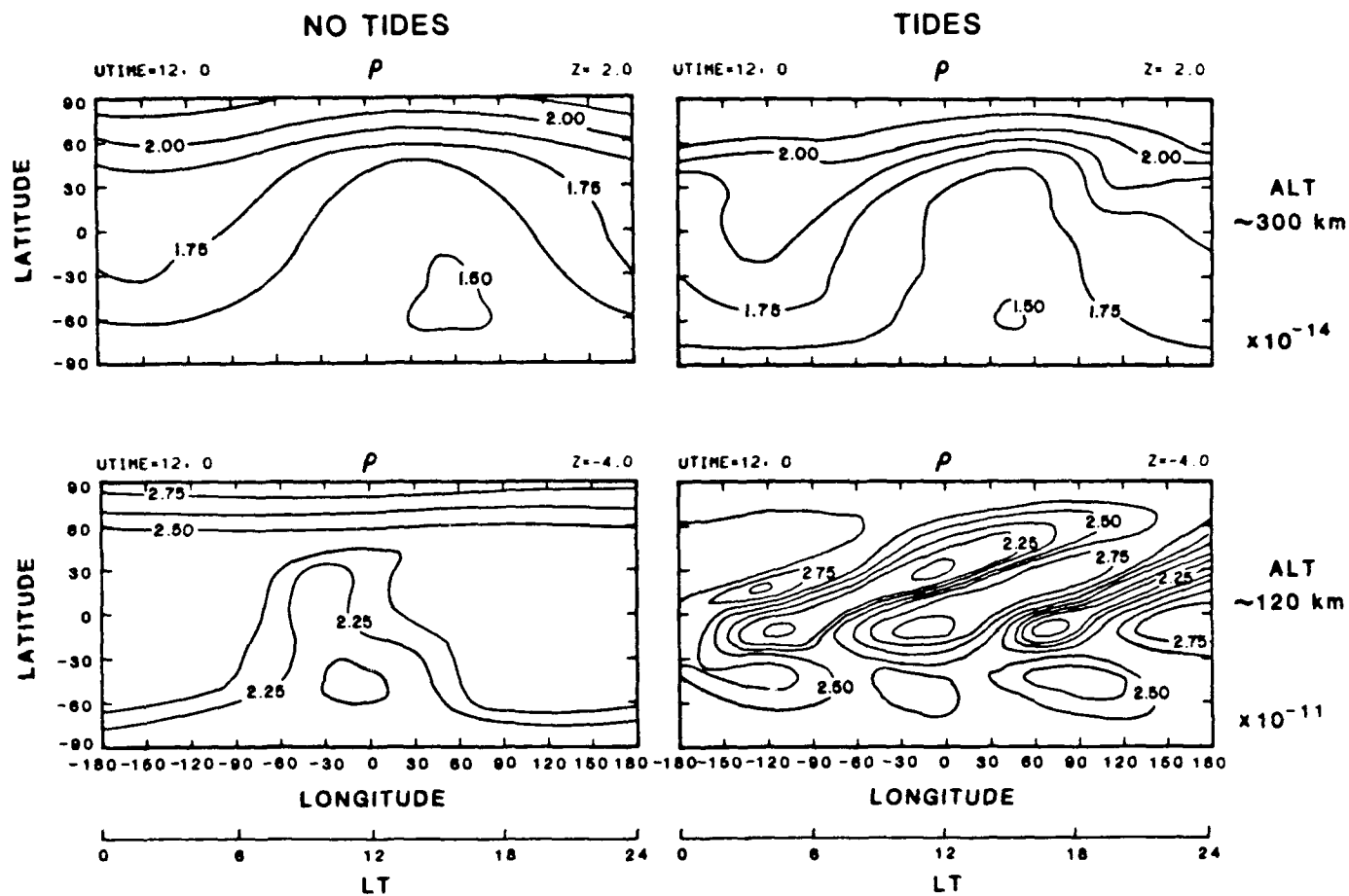


Figure 9.

TIDES, SOLAR CYCLE MINIMUM

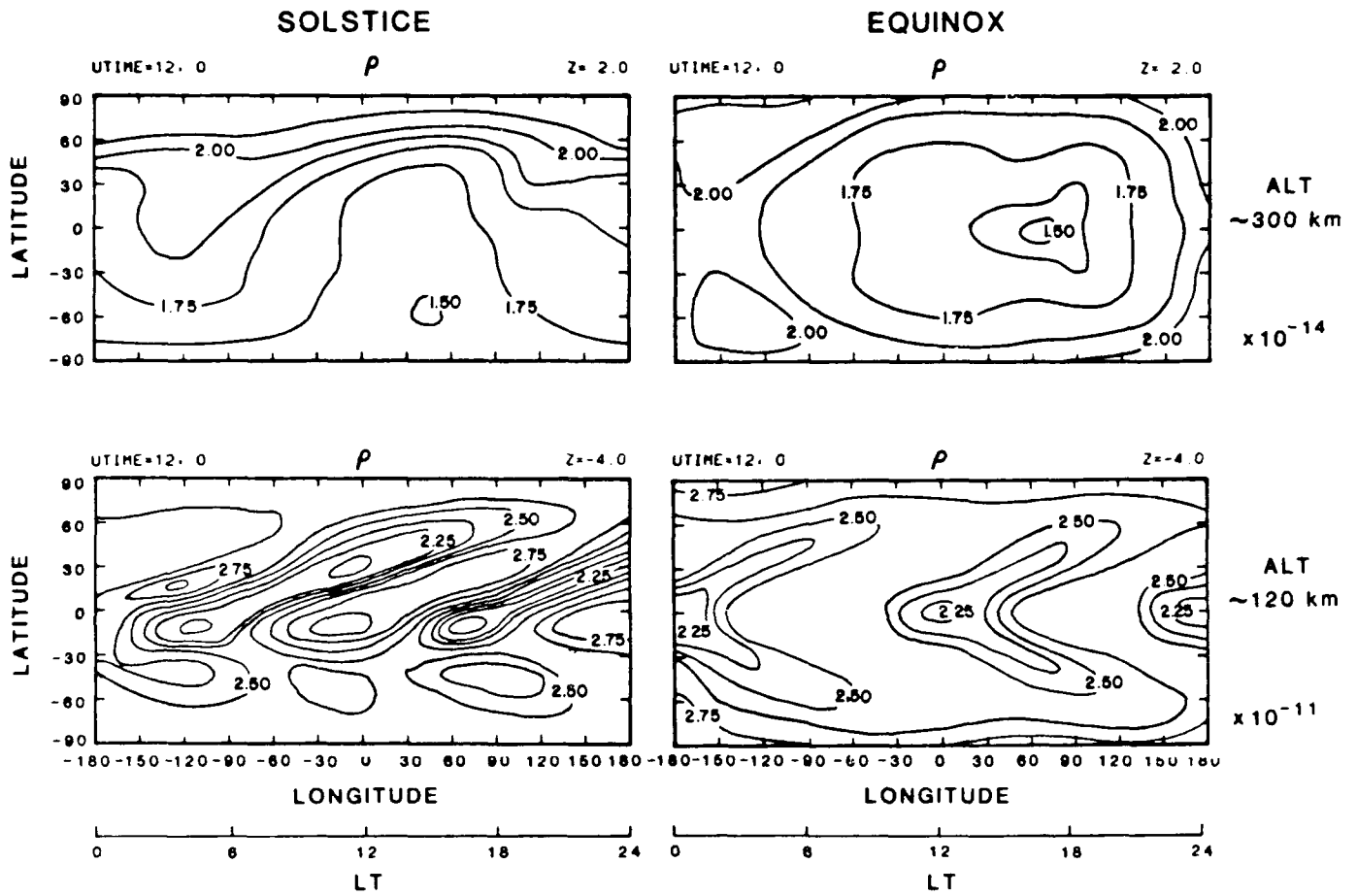
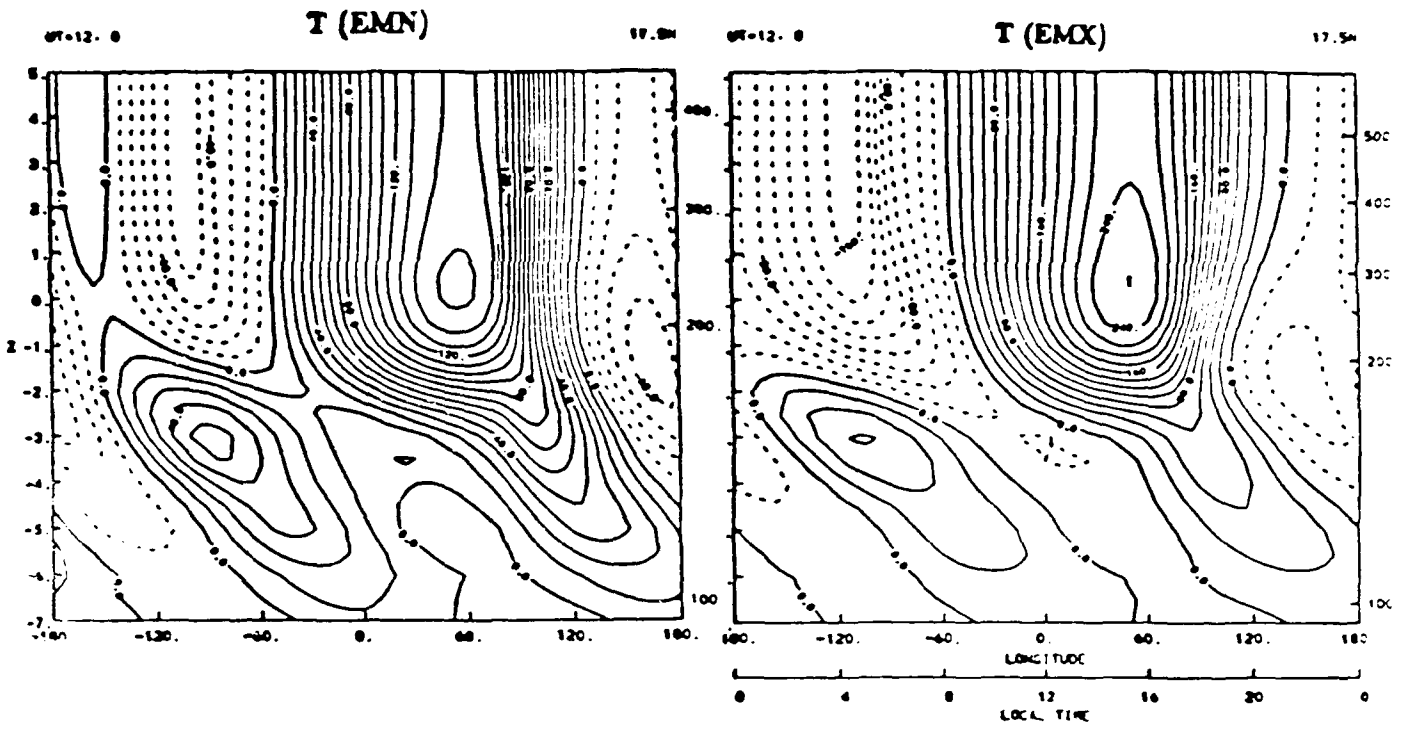


Figure 10.



TIDES

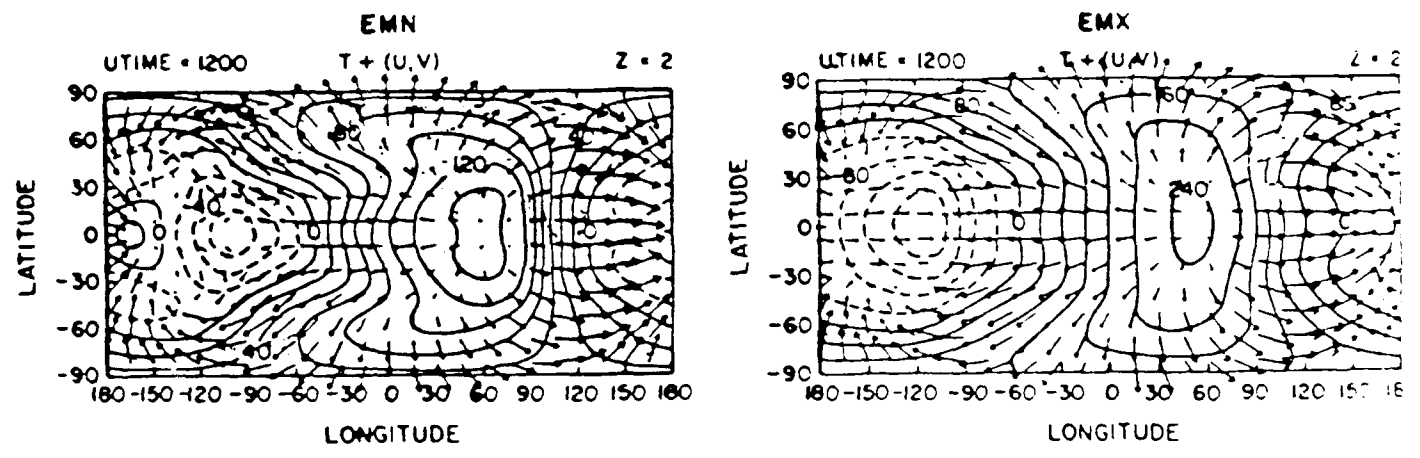


Figure 11.

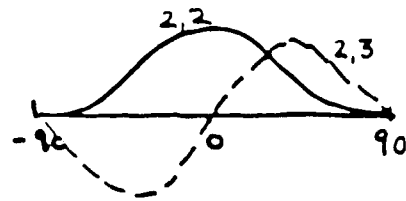
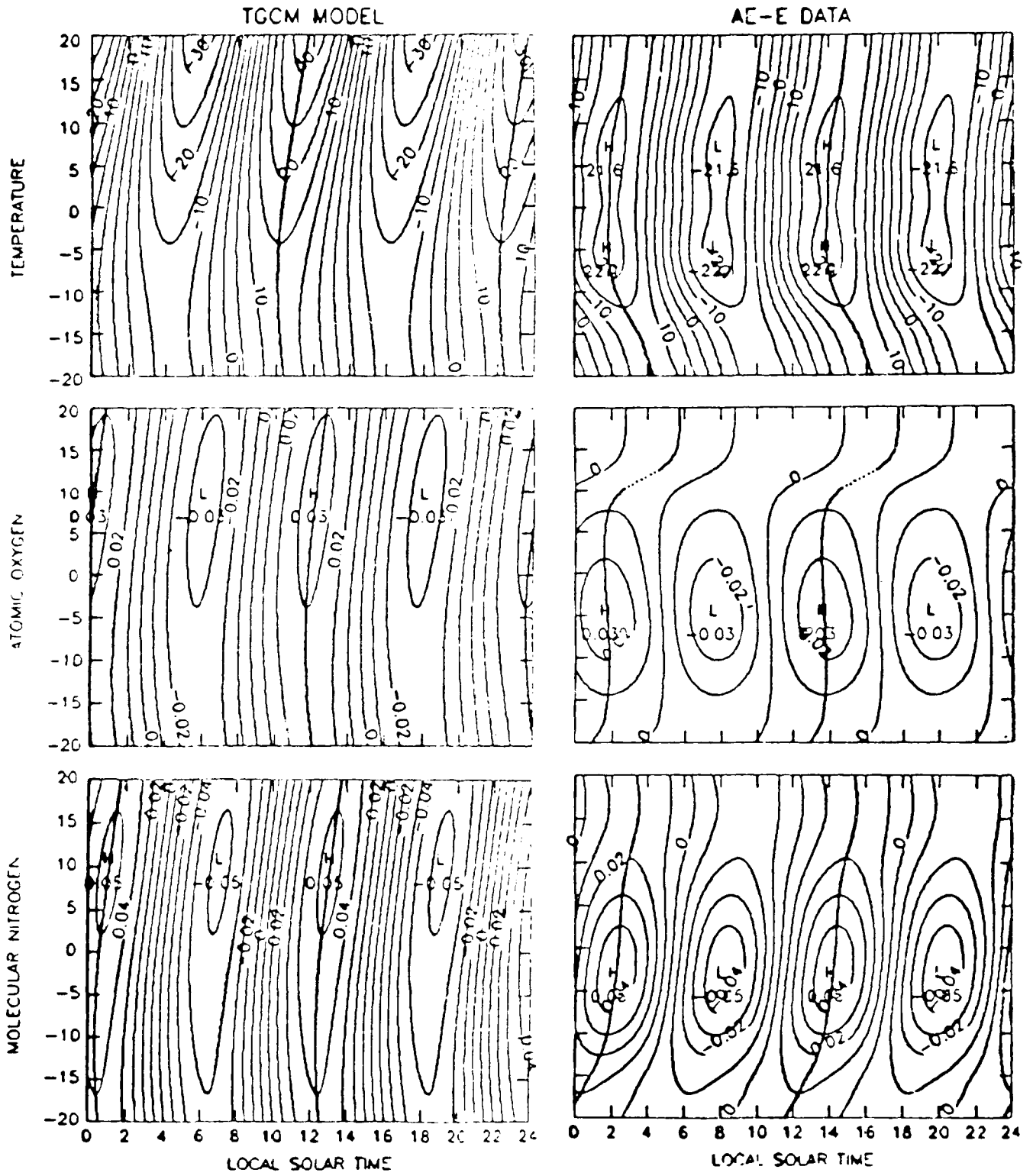


Figure 12.

Summary

- Tidal effects are an integral part of the thermospheric circulation, densities, and temperatures



Theoretical models must account for the tides

- The tides vary with
 - Season (up to and over 25% in amplitude, depending on altitude)
 - Solar Cycle (>50% at higher altitudes)
 - Latitude, Altitude
- The tides are also very variable from day to day: Variations may be on the order of 30-40% in the density amplitude
- Tidal influence on the neutral densities (fixed season, solar cycle)

<u>Z</u>	<u>% ρ (pole/equator)</u>
120km	100-1000%
180	~10-25%
300	10-40%

- To improve modelling and prediction, need observations:
at several levels, at several latitudes

Figure 13.

Thermosphere Dynamics and its influence on atmospheric density: the
Dynamics Explorer experience

T. L. Killeen,
Space Physics Research Laboratory,
University of Michigan.

Improvements in the accuracy with which atmospheric densities (100-250 km) are currently modeled may be expected to occur due to two separate, but related, efforts. The first of these is in the area of empirical or semi-empirical models. Such models are based on fits to a large body of data using analytical expressions. These expressions are typically modified through consideration of physical principles associated with the domain under consideration. For example, the assumption of diffusive equilibrium is often used for empirical modeling of thermospheric composition. This assumption provides a constraint on the analytical expressions chosen. Empirical models can be improved by increased resolution (i.e., greater number of harmonics), increased experimental coverage of the fitted parameters, and/or improvements in the analytical expressions used to convey the information. To improve accuracy of empirical models in the lower thermosphere in the next several years will require full use of the existing data set as well as efforts to provide additional systematic coverage of composition and densities in the region. New measurements are required to limit the use of extrapolations from higher altitudes.

The second effort is in the area of first-principles theoretical models, such as the thermospheric general circulation models (TGCMs). The use of realistic, time-dependent boundary conditions and inputs of energy and momentum within the framework of a TGCM can lead to reasonably accurate simulations of the thermospheric response, involving all thermospheric state variables (winds, temperatures, densities, composition, etc.). Improvements here will come about due to increased sophistication of the models, improved realism of the input parameters used and, most importantly, improved understanding of the physical, chemical, radiative and dynamical processes responsible for the modeled structure.

This talk addresses the second of the two approaches outlined above and makes the fundamental point that experience has shown that TGCMs are powerful tools that need comprehensive experimental constraints in order to be tested against reality and (incrementally) made more realistic. An analogy is drawn between anticipated future improvements in our understanding of lower thermosphere structure using TGCMs and the recent rapid progress made in modeling the dynamics, composition and thermal structure of the upper thermosphere. For the case of the upper thermosphere, data from the Dynamics Explorer-2 (DE-2) spacecraft have been used to constrain and test the NCAR TGCM and the experiment-model comparisons have led directly to improved model accuracy. DE-2 provided direct measurements of all thermospheric state variables at F-region altitudes at a formative time in the development of the NCAR-TGCM. Comparisons and critical evaluation of discrepancies between theory and experiment led to a quantitative understanding of the major upper thermospheric forcing processes and significantly more realistic predictive capability.

For future progress to be made in understanding the structure and variability of the thermosphere at lower altitudes, similar comprehensive coverage of ALL lower thermospheric state variables is needed. Such coverage will be used to test and improve the TGCM in this relatively poorly understood region. The new data are needed essentially to improve our understanding of the basic physical controlling mechanisms, without which understanding no rapid theoretical progress can be made.

Thermosphere Dynamics and its influence
on atmospheric density: the Dynamics
Explorer experience

- Our understanding of F-region thermosphere dynamics, composition, density perturbations, thermal structure and thermospheric forcing mechanisms was improved considerably due to the comprehensive coverage of essential variables by DE-2 and DE-1.
- Knowledge of magnetospheric, solar, and lower atmosphere inputs to the thermosphere - as well as all thermospheric state variables - essential.
- Iterative comparison with general circulation models, followed by detailed examination of the physics within the models, has led to a much superior predictive capability at F-region altitudes.
- Need to do the same for the lower thermosphere in order to understand and thereafter model the density perturbations. Need comprehensive experimental coverage as well as sophisticated theoretical tools.

WHAT CONTROLS COMPOSITION?

Changes in the thermospheric mass mixing ratio along a constant pressure gradient with respect to time are given by Dickinson et al., [1984] as:

$$\begin{aligned} \frac{d\Psi}{dt} = & -e^z \tau^{-1} \frac{d}{dz} \left\{ \frac{m}{m_{N_2}} \left(\frac{T_0}{T} \right)^{0.25} \alpha^{-1} L \Psi \right\} \\ & + e^z \frac{d}{dz} \left(K(z) e^{-z} \frac{d\Psi}{dz} \right) \\ & - \mathbf{V} \cdot \nabla \Psi - \omega \frac{d\Psi}{dz} + S - R \end{aligned}$$

The terms on the right hand side of this equation are from left to right:

molecular diffusion (basic restoring force):

eddy diffusion:

horizontal advection (effect of horizontal transport):

vertical advection (upwelling):

photodissociation:

recombination:

THERMOSPHERE DYNAMICS: RECENT CONTRIBUTIONS FROM DYNAMICS EXPLORER-2

T. L. KILLEEN* and R. G. ROBLE†

Instrumentation flown on the Dynamics Explorer-2 (DE-2) spacecraft enabled the dynamics of both the neutral and ionized components of the Earth's upper atmosphere to be monitored over the lifetime of the spacecraft from August 1981 to February 1983. The direct measurements of global thermospheric vector neutral winds and ion drifts were supplemented by observations of neutral and ionic constituent abundances and temperatures, precipitating particle fluxes and pitch-angle distributions, electric and magnetic fields, and global-scale auroral luminosity distributions. Analysis of this unique and comprehensive global data base has led to advances in our understanding of the manner in which the Earth's thermosphere responds dynamically to the insertion of energy and momentum from the magnetosphere. In this paper, we review the scientific progress achieved over the past five years through the efforts of members of the Dynamics Explorer science team and other interested scientists who have used the DE data base to investigate the dynamics and composition of the thermosphere.

INTRODUCTION

The Dynamics Explorer (DE) dual-spacecraft mission represents an important element of the National Aeronautics and Space Administration (NASA) program dedicated to improving our understanding of the processes that control man's near space environment. The DE mission developed out of scientific discussions in the late 1960's and early 1970's during which it became clear that a full understanding of the near-space environment would require comprehensive experimental and theoretical studies of the physical, chemical, dynamic and radiative processes that couple the Earth's magnetosphere, ionosphere, and upper atmosphere - and not just independent studies of the individual regions. A mission plan was subsequently designed, involving two companion spacecraft in co-planar orbits: a high-altitude spacecraft (DE 1) instrumented to probe the Earth's inner magnetosphere and plasmasphere and a low-altitude spacecraft (DE 2) instrumented to probe the ionosphere and neutral upper atmosphere simultaneously with the DE-1 measurements. The principal mission objective was to investigate the strong interactive processes coupling the hot, tenuous, convecting plasmas of the magnetosphere with the cooler, denser plasmas and neutral gases of the Earth's upper atmosphere, ionosphere, and plasmasphere. To pursue this task, secondary mission objectives were defined and several of these relate specifically to the investigation of the dynamical response of the upper atmosphere to the input of energy and momentum from the magnetosphere. A question of particular interest involves the processes of momentum and energy transfer between the convecting ionospheric ions (driven by high-latitude electric fields of magnetospheric origin) and the neutral gas particles in the thermosphere. An overview of the main scientific goals for the DE program has been given by Hoffman and Schmerling (1981)¹.

In this paper, we present a synopsis of the progress made during the first five years of the DE mission, with emphasis placed on the new insights obtained through use of the unique data base of thermospheric neutral

* Associate Professor of Atmospheric Science at the University of Michigan, Space Physics Research Laboratory, Ann Arbor, MI 48109. Also visiting scientist at the High Altitude Observatory, National Center for Atmospheric Research, Boulder, CO 80307.

† Senior scientist at the High Altitude Observatory, National Center for Atmospheric Research, Boulder, Colorado 80307. The National Center for Atmospheric Research is sponsored by the National Science Foundation

wind observations. Review articles touching on early DE results have been presented previously^{2,3,4}. In the next section, we briefly describe the DE-2 instrumentation that has permitted the vector neutral-wind observations and, in the subsequent sections, we describe aspects of the scientific work accomplished using the DE data base, including the very important parallel theoretical model development and the ongoing data-theory comparative studies that have been a hallmark of the program. Finally, we summarize the state of the field after the first five years of analysis of data from the Dynamics Explorer mission

INSTRUMENTATION

Two instruments on DE 2, each of which measures a single orthogonal component of the horizontal vector neutral wind, when combined, provide the horizontal neutral-wind vector. These instruments are the Fabry-Perot interferometer, FPI⁵, and the Wind and Temperature Spectrometer, WATS⁶. In this section we briefly describe the measurement technique for FPI and WATS; a more detailed discussion of these and the other DE instruments can be found in the articles published in the special issue of *Space Science Instrumentation* (Vol. 5, 1981) devoted to the DE mission objectives and instrumental details.

The Fabry-Perot Interferometer on DE 2.

The Fabry-Perot interferometer on DE 2 measures the meridional (in-orbit-plane) component of the neutral-wind vector and the thermospheric kinetic temperature as a function of altitude along and below the satellite track. A full description of the instrument has been given previously⁵. Fig. 1 illustrates schematically the measurement viewing geometry for the optical remote-sensing device. FPI measures altitude profiles of the neutral wind and the neutral kinetic temperature ahead of and below the spacecraft by remotely sensing the Doppler shift and Doppler line-broadening, respectively, for the O(¹D) thermospheric emission line profile at 630 nm. The instrument field of view is directed along and below the spacecraft velocity vector and horizon scans of the Earth's limb are performed in the orbital plane using an internal scanning mirror. The most critical component of the FPI is a plane Fabry-Perot etalon which provides the required ultra-high spectral resolution necessary to quantify the Doppler characteristics of the measured emission line profiles. The measured Doppler shift is converted into a line-of-sight neutral wind measurement by subtracting that component of the shift due to the known spacecraft velocity. The ambient kinetic temperature of the atmosphere is derived by deconvolving the calibrated instrumental broadening function from the measured signal, leading to the characterization of the Gaussian half-width of the emission line^{5,7}.

The Wind and Temperature Spectrometer

The Wind and Temperature Spectrometer, WATS, has been described in detail previously⁶. The instrument is a modified closed-source mass spectrometer, with scanning baffles providing modulation of the detected signal from which winds and temperatures can be derived. It is located on the spacecraft base-plate such that the instrument aperture faces towards the ram direction and neutral gas particles are swept into the mass spectrometer chamber by the motion of the spacecraft. The basic measurement technique is illustrated schematically in Fig. 2. Each scanning baffle is commanded to move across the instrument aperture at a precisely-determined speed during measurements of the abundances of the major thermospheric constituents, such as O and N₂. The exact baffle angle at which the incoming (ram) beam of neutral particles is intercepted maximally is a function of the cross-track wind component in the plane of the baffle motion (i.e., either in the vertical or in the zonal direction, depending on which baffle is exercised). The wind component can be simply obtained by solving the vector triangle shown in Fig. 2, where the solution obviously requires very accurate knowledge of both the speed and direction of motion of the spacecraft. The spacecraft velocity vector is considered to be known sufficiently well in the general case to provide WATS wind accuracies within ± 15 m/sec. Measurements with this precision can be made whenever the spacecraft is sufficiently low in altitude to provide statistically significant neutral particle counting rates. Typically, this factor constrains the WATS wind measurements to altitudes below about 600 km.

The neutral kinetic temperature is also obtained from an analysis of the modulation of the WATS count rate as a function of baffle location. The shape of the drop-off in count rate during the interception of the

incoming beam of neutral particles by the scanning baffle is a function of the transverse velocity distribution of the particles and, therefore, of the ambient neutral kinetic temperature. The temperature can be recovered from the measured count rate profile using a least squares fitting technique⁶.

Neutral wind vector measurements

The FPI and WATS instruments briefly described above are complementary in that they provide independent measurements of the two components of the horizontal neutral wind. A technique has been developed⁸ that merges the data from both instruments to provide a description of the horizontal vector of the neutral wind along the orbital track of DE 2. As an example of the utility of the horizontal vector wind measurement from DE 2, Fig. 3 shows wind vectors from FPI and WATS obtained during a single orbit of DE 2 where the vector winds are plotted for (a) the Southern Hemisphere polar cap and for (b) the Northern Hemisphere polar cap. The data in both hemispheres provide an indication of the characteristics of the circulation pattern, showing high-speed anti-sunward flow (~ 500 m/sec) in the central polar cap bounded by sunward flow in both the dawn and dusk sectors. This pattern of thermospheric flow is similar to the classical ionospheric convection pattern driven by magnetospheric electric fields, with two contra-rotating vortices at high-latitudes. Vector wind measurements from FPI and WATS such as these have been used in many experimental and comparative theoretical studies, reviewed in more detail below.

VECTOR WIND MEASUREMENTS AND MEAN HIGH-LATITUDE THERMOSPHERIC CIRCULATION

The availability of global-scale thermospheric neutral wind vector measurements from DE, such as those described above, has led to a number of studies over the past few years that have concentrated on providing the first large-scale morphological description of the high-latitude thermospheric circulation system. We next review the contributions made in this area through use of DE data. We note at the outset that the wind "mapping" studies are for solar maximum conditions existing during the DE-2 lifetime when the effects of the energy and momentum coupling between the magnetosphere, ionosphere and thermosphere might be expected to be at a maximum. It would be incorrect and misleading to assume that the DE measurements provide a correct description of thermospheric circulation for other parts of the solar cycle.

The Universal Time effect at high-latitudes

One of the first critical tests performed using the FPI/WATS vector wind measurement capability was to check for "ground-truth" by comparing DE-2 wind observations with simultaneously-determined and common-volume ground-based measurements of winds. This study was carried out⁹ using the coordinated measurements of R. W. Smith and colleagues from the Ulster College ground-based Fabry-Perot interferometer (UFPI) located in Svalbard, Norway for overflights and near overflights of the DE-2 spacecraft. The UFPI and DE-2 observations were found to be in satisfactory agreement for the set of simultaneous near-common-volume measurements available, indicating that the ground-based and satellite techniques were both providing realistic and consistent determinations of the thermospheric flow.

Having established the compatibility of the ground-based and spacecraft observation techniques, these authors went on to generate snapshots of the thermospheric circulation at high-latitudes by using simultaneous data from the UFPI and DE-2 for periods when the instruments were separated spatially. These snapshots illustrated the important role played by the ion-drag momentum force in establishing the twin-cell neutral thermospheric circulation pattern by demonstrating basic similarities between the measured high-latitude thermospheric neutral wind system and the classical twin-cell ionospheric convection pattern. Since the latter is controlled by magnetospheric electric fields mapping into the ionosphere along geomagnetic field lines, it was natural to expect that the component of the neutral wind system driven by ion drag or Joule heating at high-latitudes might also display some degree of geomagnetic control. To study this question, additional studies were conducted^{10,11} using averaged neutral wind data from many DE-2 orbital passes. Firstly, a statistical analysis of neutral wind data from 58 orbital passes of DE 2 over the Southern Hemisphere polar region was performed¹⁰. The data, which all came from a single LT plane, were averaged into bins of 5 degrees in latitude and two hours in UT to illustrate the basic diurnal coherence in the neutral wind pattern as seen from a polar orbit. It was also shown how the high-latitude wind field could

be described experimentally in terms of a superposition of a "background" wind field driven by solar heating with a wind field driven by high-latitude momentum and energy sources.

In a second and more comprehensive study, this approach was extended¹¹ to investigate the mean UT-dependent neutral winds in both summer and winter hemispheres, showing clearly the basic geomagnetic control of the high-latitude thermospheric wind pattern. The mean thermospheric winds were also compared with the predictions of the two thermospheric general circulation models (TGCMs), namely the University College London (UCL-TGCM)¹² and the National Center for Atmospheric Research (NCAR-TGCM)^{13,14}. The similarities and differences between the experimental observations and the theoretical model predictions indicated that the models provided reasonable predictions for the mean UT-dependent upper thermospheric winds and that they contained a reasonably valid description of the diurnally-modulated ion drag momentum force. This type of global-scale experiment-theory comparison has been very important for essentially validating the physical mechanisms incorporated within the TGCM model descriptions, for identifying physical processes missing from the theoretical formulations, and for leading to improvements in the input prescriptions and parameterizations used in the models.

The thermospheric mean circulation at high-latitude

In a later study¹⁵, all available F-region neutral wind data from seven ground-based Fabry-Perot interferometers (GBFPIs) as well as from several hundred DE-2 orbital passes taken during December 1981 were collated in order to provide the fullest possible experimental description of the mean thermospheric circulation. Since weather conditions at the ground stations limited the number of occasions when simultaneous observations were possible, the data were averaged by UT to provide 12 thermospheric "climatological maps" for every two hours of UT during a "mean day" in December 1981. Fig. 4 presents three of the experimentally-derived maps for the UT bins centered on 07:00, 09:00 and 11:00 hrs UT as well as the theoretical predictions from the NCAR-TGCM in a common format. Here, the averaged DE winds are shown as arrows and the ground-based winds are given by the meteorological symbols. It was concluded firstly, that DE measurements and data from multiple GBFPI stations could be used to provide consistent determinations of the global-scale thermospheric circulation pattern and secondly, that the mean diurnal wind pattern in the northern hemisphere high-latitude region at winter solstice could be well modeled using appropriate model inputs for the mean thermospheric forcings. This latter conclusion was important since it implied that the TGCMs could be used with confidence to study quantitatively the forcing processes responsible for the mean circulation and, furthermore, could be used to predict the mean circulation in areas where measurements are not available. The successful theoretical prediction of the mean circulation characteristics is also useful in that it provides a "baseline" or "reference" pattern for use in studies of storm-time perturbations where large departures from the mean can occur.

It was noted in this and other studies that the anti-cyclonic vortex in the thermospheric circulation pattern, associated with the dusk cell of ionospheric convection, is almost invariably stronger than the cyclonic vortex associated with the dawn ion convection cell. This large asymmetry was ascribed¹⁵ to the effects of the Coriolis force which tends to destroy cyclonic vorticity and maintain anticyclonic vorticity in both hemispheres, in accord with an earlier theoretical study¹⁶. The dominance of the dusk cell in the neutral circulation pattern is also due, at least in part, to the tendency of the dusk cell of ionospheric convection to be associated with a greater potential drop than the dawn cell¹⁷.

In an analogous investigation to the wind studies mentioned above, neutral composition data from the Neutral Atmosphere Composition Spectrometer (NACS) on DE-2 was used¹⁸ to investigate the morphology of thermospheric composition variations for N₂ and He in the polar regions during geomagnetically quiet conditions. Averaged measurements from the NACS instrument were compared with the MSIS-83 empirical model¹⁹ of neutral composition. It was found that the density for the heavier species (N₂) was enhanced in the general vicinity of the geomagnetic poles, with the enhancement more closely confined to the polar regions in winter. The lighter species (He) was depleted in the same regions, with maximum density response in the morning hours (magnetic) on average. The distribution of densities about the magnetic poles was found to be dependent on UT. These results, when combined with the morphological wind and temperature studies using DE data, show how the mean thermospheric

composition, temperature structure, and dynamics all have clear signatures that may be related to magnetospheric forcing.

Interplanetary Magnetic Field dependency of high-latitude thermospheric winds

To follow on from the morphological and mapping studies mentioned above, attempts have been made to identify additional physical processes and mechanisms that can provide order to the large DE data base of neutral wind observations. Since the neutral winds at high latitudes were found to partially mimic the twin-cell ion-convection pattern, and since previous work²⁰⁻²³ had indicated that the geometry of the ion-convection pattern is a strong function of the direction and magnitude of the Interplanetary Magnetic Field, IMF, several studies were carried out to test the sensitivity of the measured neutral wind circulation to the magnitude and orientation on the IMF.

Firstly, the dependency of the neutral circulation on the east-west (B_y) component of the IMF was investigated^{24,25}. Both single-orbit data as well as averaged data from many DE-2 orbital passes over the Northern Hemisphere polar region were used to illustrate changes in the configuration of the neutral circulation pattern in geomagnetic coordinates that were clearly ordered by the IMF B_y component. To accomplish this work measurements of the IMF from the ISEE-3 spacecraft were used to select from and order the DE neutral wind vector data. From a study of individual DE orbital passes, a "W"-shaped envelope to the anti-sunward polar cap neutral flow was reported²⁴ that resembled similar B_y -dependent signatures in ionospheric convection. In a later study²⁶, a significantly larger data set was used to characterize the B_y -dependence of the neutral circulation for both southern (summer) and northern (winter) hemispheres. Results from this study are shown in Fig. 5, where data from many hundreds of DE 2 orbital passes over six months of the mission have been separated according to the sign of B_y and averaged into bins of geomagnetic latitude and geomagnetic local time for the two hemispheres. These data were obtained during the months November 1981 to January 1982 and November 1982 to January 1983. The criteria used to separate the data sets by B_y involved the pre-existence of a definite positive or negative value for B_y as measured by ISEE-3 for 1 hour prior to the DE orbital pass. Passes occurring either during very high or very low levels of geomagnetic activity were excluded from the study and allowance was made for the propagation time to the Earth of the IMF measured at ISEE-3 altitudes. As can be seen from Fig. 5, there are significant differences in the mean thermospheric circulation patterns for B_y positive and negative. To some extent the effects are mirrored between hemispheres; that is, a B_y positive (negative) signature in the northern hemisphere resembles a B_y negative (positive) signature in the southern hemisphere. In all cases, the average circulation patterns shown illustrate the dominance of the dusk anticyclonic neutral vortex mentioned above. The spatial magnitude of this vortex, however, is greater for B_y positive conditions in the northern hemisphere and for B_y negative conditions in the southern hemisphere. A distinct rotation in the direction of the polar cap anti-sunward flow that was dependent on the sign of B_y was also noted.

A clear dependence of the neutral wind field as measured from DE 2 on the north-south (B_z) component of the IMF was also demonstrated in a separate study²⁷. For conditions of strong and steady northward (positive) B_z , neutral and ion winds were presented which showed that sunward flow of neutral gas in the center of the polar cap can be established and maintained by ion drag for positive B_z .

DE neutral wind measurements have, therefore, demonstrated clear morphological dependencies on the orientation of the IMF and these dependencies are similar in nature to those previously observed for ionospheric convection. The identification and quantification of both large and more subtle dependencies of the neutral wind circulation pattern on the orientation of the IMF has been one of the most remarkable results from the DE mission in that it clearly illustrates the strong coupling that occurs throughout the Earth's near-space environment all the way from the solar wind, through the magnetosphere and ionosphere and into the neutral atmosphere itself. Such dependencies would perhaps not have appeared intuitively obvious prior to the DE mission. Ongoing but as yet unpublished studies have shown that the thermospheric composition and density structure at high latitudes is also strongly dependent on the orientation of the IMF.

Geomagnetic dependency of mean circulation

The binning and averaging studies reviewed above tend to mask the high degree of variability that occurs in high-latitude thermosphere dynamics as a function of geomagnetic activity. This variability was first highlighted using DE observations by Spencer et al. (1982)²⁸ who presented WATS zonal and vertical wind measurements in the polar region that demonstrated the existence of strong vertical winds, having velocities of 100-150 m/sec at times, correlated with strong (many hundreds of m/sec) zonal winds. They also reported high-latitude temperature perturbations of several hundred degrees and associated these with gravity waves.

In order to quantify the geomagnetic dependency of high-latitude neutral dynamics, a statistical study using 6 months of DE-2 data was recently conducted²⁹ specifically to determine the relationship between the mean circulation pattern in the summer and winter high-latitude regions and the level of geomagnetic activity, as represented by the Kp and AE indices. Data were sorted and binned according to these geomagnetic indices and the results from this study, shown in Figs. 6 and 7, illustrate how the anti-sunward neutral winds in the central polar cap increase in speed as a function of enhanced geomagnetic activity levels. The values shown in Tables I and II are least squares fits to the specified regression relationships between the various averaged high-latitude wind features and the geomagnetic indices. This study may be considered to be a first step towards a satisfactory empirical description of the high-latitude neutral wind field, enabling experimentally-based wind values to be used for different geophysical conditions in relevant studies and providing a challenge to theoretical modelers to match quantitatively the observed dependencies.

ION-NEUTRAL COUPLING AT HIGH-LATITUDES

The various DE studies of high-latitude circulation reviewed above have indicated the important role played by the high latitude sources of momentum (ion drag) and energy (Joule heating) in the establishment of the mean thermospheric wind system. A primary conclusion is that above 60° of latitude the neutral winds in the upper thermosphere are best described in a geomagnetic coordinate system. That is, the thermosphere wind system responds primarily to magnetospheric driving functions that map into the auroral region surrounding the magnetic poles of the Earth. In order to study these processes further a large set of atmospheric, ionospheric and magnetospheric parameters must be considered. For example, the ion-drag and Joule heating driving functions are dependent on the magnitude of the ion-neutral collision frequency, as well as on the differential velocity of the ions and neutrals. Thus, in addition to the neutral winds themselves, the effects of particle precipitation, convection electric fields, ionospheric recombination, and neutral composition and temperature changes must all be taken into account to provide the framework for quantitative studies of the dynamical influence of magnetospheric processes on the upper atmosphere. The comprehensive set of instrumentation on DE 2 has enabled valuable initial studies of this type to be carried out. We next review these studies.

Data from six instruments on DE 2 were collected to investigate the detailed ionospheric and neutral atmospheric structure for a set of orbital passes over the southern hemisphere polar region³⁰. These data enabled the in-situ ion-neutral vector difference velocity and the ion-neutral collision frequency to be obtained simultaneously for the first time, leading to a determination of the instantaneous local rates of transfer of momentum and energy between the species. The simultaneously-measured ion drifts and neutral winds indicated that the spatial morphology and temporal behavior of the momentum and energy coupling between species is complex, with the neutrals responding to magnetospheric-controlled changes in ionospheric convection on time scales of many (10's to 100's) minutes, thereby filtering out much of the high-frequency structure in the ion convection. Fig. 8 illustrates this last point well, showing two examples of simultaneous zonal neutral winds and ion drifts measured along the DE-2 orbital track as the spacecraft crossed the northern hemisphere polar region. In this figure, the ion and neutral winds have been plotted with the same spatial and temporal resolution. It can be seen that the neutral wind signatures resemble those of the ion drifts, with, however, a reduction in magnitude (note the factor of 3 difference in scales for the different species) and with much less evident spatial structure. Thus, because of the long (~1 hour) ion-neutral momentum coupling time constant, the neutral thermosphere can be seen to act as an integrator, partially mimicking the ionospheric convection pattern, but displaying reduced amplitudes and generally less spatial structure.

This study of ion-neutral momentum transfer time constants was later extended³¹, providing statistical averages for solar maximum (using DE-2 measurements) and for solar minimum (using Atmosphere

Explorer-C measurements). These averaged time constants were compared with calculations using the MSIS-83¹⁹ and the Chui³² semi-empirical models for thermospheric and ionospheric densities, respectively. The comparisons showed that the models provided values for the time constants at solar maximum that were in good agreement with the measurements, but that, at solar minimum, the modeled time constants were too small, indicating that the ion-neutral momentum coupling is significantly less important than that predicted for low solar activity. The discrepancy was attributed to the overestimation of polar ion densities at solar minimum by the Chui model. This study pointed to the large dynamic range of the coupling between the magnetosphere and thermosphere which occurs as a function of time within the solar cycle, with the DE-2 mission providing information during a period when thermospheric effects of the coupling were at a maximum.

Simultaneous measurements have been presented³⁴ of global-scale auroral luminosity distributions and vector neutral winds over the northern (winter) polar cap using data from the spin-scan auroral imager, SAI³³ on DE 1 and the FPI and WATS instruments on DE 2, respectively (see Fig. 9). The purpose of this work was to illustrate the spatial relationship between large-scale morphological features of the F-region neutral wind field in the winter polar region and the location and spatial extent of the aurora. A definite correlation was found to exist between reversals and boundaries in the neutral wind field and the location of the visible auroral oval. The dusk sector reversal to sunward flow in the neutral gas was again found to be more pronounced than that occurring in the dawn sector. Ion drift and composition data were used to determine the ion drag and Coriolis forces on the neutral gas and it was concluded that the dawn-dusk asymmetry in the thermospheric neutral wind response was related to the differing effects of the Coriolis force in the dawn and dusk sectors. Examples of such simultaneous data sets indicated that the neutral wind boundaries follow the substorm-dependent expansion and contraction of the auroral oval. The superposition of vector neutral wind measurements from DE 2 and auroral imagery from DE 1 demonstrates clearly the power of the DE mission to determine parameters associated with the input of energy, momentum and charged particles to the upper atmosphere as well as its dynamical response to such inputs.

LOW-LATITUDE THERMOSPHERIC WINDS

Measurements of thermospheric winds at middle and low latitudes from DE 2 have been studied in an effort to understand better the mean circulation as well as the propagation characteristics of waves and perturbations originating at high latitudes. A major contribution of the DE 2 data has been in the area of determining experimentally the degree of atmospheric superrotation using a direct technique. Previous work in this area had suggested rather large values for the superrotation of the equatorial thermosphere based on indirect inferences from satellite drag data (e.g. Ref. 35). Such large superrotation velocities at low latitudes presented theoretical difficulties³⁶. Using WATS zonal wind observations, average profiles of the equatorial zonal wind for different levels of solar flux and for different altitude levels were obtained³⁷ and the results demonstrated an atmospheric superrotation of only a few percent in good agreement with model calculations³⁸⁻⁴⁰. Fig. 10 shows the local time dependency of the WATS zonal wind measurements at the equator in the altitude range 300-500 km. As can be seen, while there is a significant LT variation driven primarily by the diurnal variation of solar EUV and UV heat sources as well as by momentum sources associated with the diurnal tide³⁹, the average value is very near to zero. The table, shown in Fig. 10, presents the results for the mean (LT-averaged) zonal wind as a function of latitude for two altitude bins. In both cases, the latitudinally-averaged (equator - 40° latitude) zonal wind has a magnitude of less than 2 m/sec, implying that the equatorial thermosphere, on the average, simply co-rotates with the Earth.

THEORETICAL MODELING

At the time of the Dynamics Explorer launch in August 1981, two thermospheric general circulation models (the UCL-TGCM¹² and NCAR-TGCM¹³) had been developed sufficiently for use in analyzing data and for the interpretation of physical processes responsible for the observed thermospheric structure and dynamics. Both models solve the primitive equations of dynamic meteorology modified for thermospheric dynamics and include coupling between composition and dynamics.

The initial DE wind vector measurements clearly showed a high-latitude wind system that was strongly controlled by the momentum source associated with magnetosphere convection. There were strong anti-

sunward winds in the magnetic polar cap and strong sunward winds equatorward of the polar cap in the auroral zone. Both TGCMs were used to investigate the observed wind pattern and the effectiveness of the magnetospheric convection-driven ion-drag momentum source in controlling the wind system at high latitudes. The UCL-TGCM results were compared with observations for seven polar passes of the DE-2 spacecraft during November 1981⁴¹. It was found that the major features of the experimental winds, such as the mean day-to-night circulation caused by solar EUV and UV heating, augmented by magnetospheric processes at high latitude, and the sharp boundaries and flow reversals imposed on thermospheric winds by ion-drag momentum transfer from the magnetosphere, were qualitatively predicted by a version of the model that used a semi-empirical model of polar electric fields. A comparison of winds predicted by the UCL-TGCM using two different ionospheric models of electron density with measurements made by the DE-2 satellite is shown in Fig. 11. The dawn-to-dusk cuts show antisunward winds in the polar cap flanked by sunward winds in the vicinity of the auroral oval. There is good general agreement between the model predictions and observations for these polar passes.

DE-2 data from the October-November 1981 time period was compared with predictions of the NCAR-TGCM^{42,43}, and the results of the comparison indicated an effective control of the thermospheric wind system by magnetospheric convection. Roble et al. (1984)⁴³ showed that the high-latitude thermospheric temperature and neutral composition were well-ordered in geomagnetic coordinates and were able to obtain reasonable agreement between the TGCM calculations and DE-2 measurements of temperature and composition.

These TGCM results, as well as those from other theoretical and numerical⁴⁴⁻⁴⁸ studies have all shown that the neutral winds at F-region altitudes are very effectively controlled by the ion-drag momentum source associated with magnetospheric convection. The twin-cell pattern of magnetospheric convection drives a largely rotational, nondivergent, double-vortex wind system at F-region heights. The magnitude of the neutral wind is related to the strength of the forcing which, in turn, depends upon both the ion-drift speeds and the ion and neutral number densities. The TGCMs have shown that the neutral wind pattern effectively follows, but generally lags, the ion-drift pattern and has variations similar to those associated with the ion-drift pattern. In general, the TGCM simulations have indicated that, if the imposed ion-drift pattern has sharp boundaries and is relatively steady for time periods on the order of 1/2 to 1 hour, then the neutral wind pattern will develop similar features.

In a detailed recent study using the NCAR-TGCM⁴⁸, an analysis has been made of data from a number of orbits of the DE-2 spacecraft during 21-22 November 1981, which was a period of relatively steady geomagnetic forcing. This study demonstrated a reasonably good agreement between the DE-2 measurements of auroral particle precipitation and ion-drift velocity vectors and the TGCM auroral parameterizations for these parameters. Large-scale structures in the thermospheric neutral wind field were reasonably well reproduced, but the DE-2 measurements of neutral winds showed considerably more small-scale structure than the model could simulate, because of limitations imposed through use of the five degree latitude-by-longitude TGCM grid. Fig. 12 shows a comparison of the TGCM-predicted wind and temperature structure of the polar cap along with DE-2 measurements of the cross-track wind component along the satellite track for six DE-2 orbits. The results show the influence of magnetospheric forcing on the high-latitude circulation pattern, with antisunward winds in the magnetic polar cap and sunward winds on the dusk side of the auroral oval. The TGCM-predicted wind velocities, reversal boundaries, and the transition from the mid-latitude solar EUV and UV-driven wind system to that controlled by magnetospheric forcing at high latitudes are all in reasonable agreement with DE-2 measurements for this period of relatively steady geomagnetic forcing. This study represents the first time that an attempt has been made to simulate numerically the time-dependent thermospheric response to real magnetospheric and solar forcings. The encouraging results point to the need for additional future work to be conducted along these lines to investigate the perturbed thermosphere for periods when DE-2 measurements provide both the necessary information on inputs to the thermosphere as well as a detailed record of the large-scale thermospheric response to the time-dependent forcing mechanisms.

Further studies investigating the circulation, temperature, and compositional structure of the winter hemisphere polar cap have been carried out^{49,50}. The DE-2 measurements show considerable seasonal differences in all neutral atmospheric parameters. In the summer hemisphere, solar EUV and UV photoionization, photodissociation, and neutral heating generally dominate auroral inputs for all except the

most disturbed periods. In the winter hemisphere, the diminution of these solar radiative inputs, because of the relatively large solar zenith angles, makes auroral inputs more important in the maintenance of the circulation, temperature and compositional structure of the winter polar cap. Rees et al. (1985)⁴⁹ have shown that the region of the summer pole, under similar geomagnetic and solar activity conditions at a level of about 300km, and at a similar level of geomagnetic and solar activity conditions, is about 300 K warmer than that of the winter pole. The density of atomic oxygen is strongly depleted (and nitrogen enhanced) around the summer pole compared to the winter pole. They also point out that only part of the differences in temperature and compositional structure can be related to the seasonal variation of solar insolation and that both polar regions display structural variations (with latitude and UT) that are characteristic of strong magnetospheric forcing. The magnetospheric control is strong in the summer hemisphere because of the enhanced ion densities caused by solar photoionization and weaker in the winter hemisphere where this coupling is somewhat smaller.

Killeen and Roble (1984)⁴⁵ have developed a diagnostic package to examine the balance of forces within the NCAR-TGCM. Their analysis showed that at F-region altitudes the largest forces in the "steady state" are due to ion drag induced by sunward drifting ions on the dawnside and duskside of the auroral oval/polar cap boundary. At F-region altitudes, the basic balance of forces is between ion drag and pressure, whereas at E-region altitudes, Coriolis and advection forces also have significant contributions. Later, these authors extended their diagnostic package to include neutral parcel trajectories in the high-latitude E- and F-regions⁵¹. They found that trajectories analyzed for "steady state" diurnally-reproducible runs of the TGCM show the following features: 1) the magnetospheric convection throat region plays an important regulatory role for the overall flow pattern at high latitudes, 2) the trajectories of typical F-region neutral gas parcels pass through the throat region at least once and sometimes twice in a 24-hour period as a result of the convergent geometry of the ion convection pattern, 3) parcels transiting the dayside cusp region are heated rapidly in the region of soft particle precipitation and this energy is advected over the polar cap and deposited several hours "downstream" along the parcel trajectory heating the polar cap, 4) the "postmidnight" surge in the meridional neutral wind is the result of parcel acceleration in the convection throat region and subsequent deflection towards the corotation direction, and 5) E-region parcels move less rapidly than their F-region counterparts and can dwell for appreciable periods of time in the auroral oval; only a few geometrically-selected parcels escape to lower latitudes.

Finally, a spectral analysis capability to be used with the NCAR-TGCM as part of its diagnostic package has been developed⁵². This capability allows the gridded global TGCM output to be decomposed according to a series of vector spherical harmonic functions, enabling the power in the various wave modes transmitted through the TGCM grid to be intercompared quantitatively. The expansion of the wind field in vector spherical harmonics, combined with a fourier expansion in time and a polynomial expansion in altitude, has enabled the time-dependent, 3-D, diurnal neutral wind, ion drift, neutral temperature and composition fields to be reproduced using a simple and fast computer subroutine. This code, termed the VSH (vector spherical harmonic) model, is currently being used as the basis for an effort to produce a Dynamics Explorer semi-empirical model of global thermosphere dynamics. A comparison of the global output from the VSH model (currently, simply a replication of the NCAR-TGCM predictions) with neutral wind measurements made on single orbital passes of DE 2 were reported⁵². The agreement between the TGCM predictions and the experimental data was very good for both high-latitude regions, giving confidence in the TGCM itself as well as in the future use of the VSH representation to yield a realistic and useful semi-empirical model of thermosphere dynamics. Such a model will represent one of the more significant legacies of the DE mission.

CONCLUDING REMARKS

Considerable progress has been sustained over the past 5 years through use of the Dynamics Explorer data base to improve our understanding of the dynamics of the Earth's upper atmosphere. The combination of comprehensive experimental coverage of the key parameters involved in magnetosphere-ionosphere-thermosphere coupling together with improved theoretical techniques has led to important advances in both the morphological description of thermosphere dynamics and the identification and quantification of the main forcing mechanisms.

In the area of morphological studies, the DE mission has provided information on the mean circulation at F-region altitudes for both high- and low-latitudes. The high-latitude thermospheric wind pattern has been shown to have definite dependencies on UT, LT, season, IMF orientation, and geomagnetic activity level and progress has been made in quantifying these dependencies for the solar maximum conditions appropriate to the DE-2 mission lifetime. The extent to which the equatorial thermosphere co-rotates or super-rotates with the Earth has been investigated, leading to a satisfactory agreement between theory and experiment. This experimental result, indicating that very little superrotation occurs in the terrestrial thermosphere, has fundamental implications for the study of the dynamical aeronomy of other planets where superrotation is known to be an important feature. DE measurements have been used to investigate the detailed coupling between the ionosphere and the neutral thermosphere. The strong influence of energy and momentum mapping down from the magnetosphere into the ionosphere and influencing thermospheric circulation and composition has been demonstrated, and the inputs to the theoretical models improved through comparative studies. Complex feedback processes acting to modulate thermosphere-ionosphere coupling have been identified and studied. The role of ion-drag momentum forcing and the Coriolis force in establishing the thermospheric circulation has been elucidated.

Perhaps the greatest benefit of the DE-2 measurements has been to provide the evolving theoretical models of the thermosphere with rigorous and global experimental constraints. The close and interactive interaction between experimentalists and theorists working with DE data has led to great improvements in the theoretical understanding of the region, leading to a situation where a predictive capability has become a real possibility and a goal for future work. This interaction is of particular importance for the improvement of predictions of atmospheric density fluctuations from first-principal calculations. Because of the strong coupling between composition, atmospheric density perturbations and dynamics, a full and quantitative understanding of the thermospheric wind systems and their influence on other atmospheric parameters is required to constrain and test sophisticated models such as the TGCMS.

ACKNOWLEDGEMENT

This work has been supported in part by NASA grant NAG5-465 to the University of Michigan. N. W. Spencer and L. E. Wharton of Goddard Space Flight Center provided the WATS data. The authors are grateful for stimulating discussions with Drs. F. G. McCormac and P. B. Hays.

REFERENCES

1. Hoffman, R. A., and E. R. Schmerling, Dynamics Explorer Program: An Overview, *Space Science Instrum.*, 5, 345-348, 1981.
2. Mayr, H. G., I. Harris, F. Varosi, F. A. Herrero, H. Volland, N. W. Spencer, A. E. Hedin, R. E. Hartle, H. A. Taylor, Jr., L. E. Wharton, and G. R. Carignan, On the structure and dynamics of the thermosphere, *Adv. Space Res.*, 5, 283-288, 1985.
3. Killeen, T. L., Energetics and Dynamics of the Earth's thermosphere, *Rev. Geophys.*, 25, 433-454, 1987.
4. Killeen, T. L., and R. G. Roble, Measurements of the dynamics of the high-latitude thermosphere, *J. Astronaut Soc.*, in press, 1987.
5. Hays, P. B., T. L. Killeen, and B. C. Kennedy, The Fabry-Perot interferometer on Dynamics Explorer, *Space Sci. Instrum.*, 5, 395-416, 1981.
6. Spencer, N. W., L. E. Wharton, H. B. Niemann, A. E. Hedin, G. R. Carignan, and J. C. Maurer, The Dynamics Explorer wind and temperature spectrometer, *Space Sci. Instrum.*, 5, 417-428, 1981.
7. Killeen, T. L., and P. B. Hays, Doppler line profile analysis for a multi-channel Fabry-Perot interferometer, *Appl. Optics*, 23, 612-620, 1982.
8. Killeen, T. L., P. B. Hays, N. W. Spencer, and L. E. Wharton, Neutral winds in the polar thermosphere as measured from Dynamics Explorer, *Geophys. Res. Lett.*, 9, 957-960, 1982.
9. Killeen, T. L., R. W. Smith, P. B. Hays, N. W. Spencer, L. E. Wharton, and F. G. McCormac, Neutral winds in the high-latitude winter F-region: Coordinated observations from ground and space, *Geophys. Res. Lett.*, 11, 311-314, 1984.
10. Killeen, T. L., P. B. Hays, N. W. Spencer, and L. E. Wharton, Neutral winds in the polar thermosphere as measured from Dynamics Explorer, *Adv. Space Res.*, 2, 10, 133-136, Pergamon Press, Oxford, 1983.
11. Hays, P. B., T. L. Killeen, N. W. Spencer, L. E. Wharton, R. G. Roble, B. E. Emery, T. J. Fuller-Rowell, D. Rees, L. A. Frank, and J. D. Craven, Observations of the dynamics of the polar thermosphere, *J. Geophys. Res.*, 89, 5597-5612, 1984.
12. Fuller-Rowell, T. J., and D. Rees, A three-dimensional, time-dependent global model of the thermosphere, *J. Atmos. Sci.*, 37, 2545-2657, 1980.
13. Dickinson, R. E., E. C. Ridley, and R. G. Roble, A three-dimensional, time-dependent general circulation model of the thermosphere, *J. Geophys. Res.*, 86, 1499-1512, 1981.
14. Roble, R. G., R. E. Dickinson, and E. C. Ridley, Global circulation and temperature structure of the thermosphere with high-latitude plasma convection, *J. Geophys. Res.*, 87, 1599-1614, 1982.
15. Killeen, T. L., R. W. Smith, N. W. Spencer, J. W. Meriwether, D. Rees, G. Hernandez, P. B. Hays, L. L. Coggier, D. P. Sipler, M. A. Biondi and C. A. Tepley, Mean neutral circulation in the winter polar F-region, *J. Geophys. Res.*, 91, 1633-1649, 1986.
16. Fuller-Rowell, T. J., and D. Rees, Interpretation of an anticipated long-lived vortex in the lower thermosphere following simulation of an isolated substorm, *Planet. Space Sci.*, 32, 69-86, 1984.

17. Heppner, J. P., and N. C. Maynard, Empirical high latitude electric field models, *J. Geophys. Res.*, **92**, 4467-4490, 1987.
18. Hedin, A. E., G. R. Carignan, Morphology of thermospheric composition variations in the quiet polar thermosphere from Dynamics Explorer measurements, *J. Geophys. Res.*, **90**, 5269-5277, 1985.
19. Hedin, A. E., A revised thermospheric model based on mass spectrometer and incoherent scatter data: MSIS-83. *J. Geophys. Res.*, **88**, 10170-10188, 1983.
20. Heppner, J. P., Polar cap electric field distributions related to the Interplanetary Magnetic Field direction, *J. Geophys. Res.*, **77**, 4877, 1972.
21. Heelis, R. A., The effects of Interplanetary Magnetic Field orientation on dayside high-latitude ionospheric convection, *J. Geophys. Res.*, **89**, 2873-2880, 1984.
22. Reiff, P. H., and J. L. Burch, IMF By-dependent plasma flow and Birkeland currents in the dayside magnetosphere, 2, A global model for northward and southward IMF, *J. Geophys. Res.*, **90**, 1595-1609, 1985.
23. de la Beaujardière, O., V. B. Wickwar, J. D. Kelley, and J. H. King, Effect of the interplanetary magnetic field on the high-latitude nightside convection, *Geophys. Res. Lett.*, **12**, 461-464, 1985.
24. McCormac, F. G., T. L. Killeen, E. Gombosi, P. B. Hays, and N. W. Spencer, Configuration of the high-latitude neutral thermosphere circulation for IMF By negative and positive, *Geophys. Res. Lett.*, **12**, 155-158, 1985.
25. Rees, D., T. J. Fuller-Rowell, R. Gordon, J. P. Heppner, N. C. Maynard, N. W. Spencer, L. E. Wharton, P. B. Hays, and T. L. Killeen, A theoretical and empirical study of the response of the high-latitude thermosphere to the sense of the "Y" component of the interplanetary magnetic field, *Planet. Space Sci.*, **34**, 1-40, 1986.
26. Thayer, J. P., T. L. Killeen, F. G. McCormac, C. R. Tschan, J.-J. Ponthieu, and N. W. Spencer, Interplanetary Magnetic Field-dependent thermospheric neutral wind signatures for northern and southern hemispheres from Dynamics Explorer-2 data, *Ann. Geophys.*, in press, 1987.
27. Killeen, T. L., R. A. Heelis, P. B. Hays, N. W. Spencer, and W. B. Hanson, Neutral motions in the polar thermosphere for northward interplanetary magnetic field, *Geophys. Res. Lett.*, **12**, 159-162, 1985.
28. Spencer, N. W., L. E. Wharton, G. R. Carignan, and J. C. Maurer, Thermosphere zonal winds, vertical motions and temperature as measured from Dynamics Explorer, *Geophys. Res. Lett.*, **9**, 953-956, 1982.
29. McCormac, F. G., T. L. Killeen, J. P. Thayer, C. R. Tschan, G. Hernandez, and N. W. Spencer, Circulation of the polar thermosphere during geomagnetically quiet and active times as observed from DE 2, *J. Geophys. Res.*, in press, 1987.
30. Killeen, T. L., P. B. Hays, G. R. Carignan, R. A. Heelis, W. B. Hanson, N. W. Spencer, and L. H. Brace, Ion-neutral coupling in the high latitude F-region: Evaluation of ion heating terms from Dynamics Explorer 2, *J. Geophys. Res.*, **89**, 7495-7508, 1984b.
31. Ponthieu, J.-J., T. L. Killeen, K.-M. Lee, G. R. Carignan, W. R. Hoegy, and L. H. Brace, Ionosphere-thermosphere momentum coupling at solar maximum and solar minimum from DE-2 and AE-C data, *Physica Scripta*, in press, 1987.
32. Chiu, Y. T., An improved phenomenological model of ionospheric density, *J. Atmos. Terr. Phys.*, **37**, 1563-1570, 1975.

33. Killeen, T. L., J. D. Craven, L. A. Frank, J.-J. Ponthieu, N. W. Spencer, R. A. Hoelis, L. H. Brace, R. G. Roble, P. B. Hays, and G. R. Carignan, On the relationship between the dynamics of the polar thermosphere and the morphology of the aurora: Global-scale observations from Dynamics Explorers 1 and 2, *J. Geophys. Res.*, in press, 1987a.
34. Frank, L. A., J. D. Craven, K. L. Ackerson, M. R. English, R. H. Eather, and R. L. Carovillano, Global auroral imaging instrumentation for the Dynamics Explorer mission, *Space Sci. Instrum.*, 5, 369-393, 1981.
35. King-Hele, D. G., and D. M. C. Walker, Upper atmosphere zonal winds from satellite orbit analysis, *Planet. Space Sci.*, 31, 509-535, 1983.
36. Dickinson, R. E., and Rishbeth, Planetary-scale motions at F-layer heights, *Space Res.*, XIII, 413-422, 1973.
37. Wharton, L. E., N. W. Spencer, and H. G. Mayr, The Earth's thermospheric superrotation from Dynamics Explorer 2, *Geophys. Res. Lett.*, 11, 531-533, 1984.
38. Mayr, H. G., I. Harris, A. E. Hedin, N. W. Spencer, and L. E. Wharton, Thermospheric superrotation revisited, *J. Geophys. Res.*, 89, 5613-5624, 1984a.
39. Mayr, H. G., I. Harris, F. Varosi, and F. A. Herrero, Global excitation of wave phenomena in a dissipative multi-constituent medium, 1, Transfer function of the Earth's thermosphere, *J. Geophys. Res.*, 89, 10929-10959, 1984b.
40. Mayr, H. G., I. Harris, F. Varosi, and F. A. Herrero, Global excitation of wave phenomena in a dissipative multi-constituent medium, 2, Impulsive perturbations in the Earth's thermosphere, *J. Geophys. Res.*, 89, 10961-10986, 1984c.
41. Rees, D., T. J. Fuller-Rowell, R. Gordon, T. L. Killeen, P. B. Hays, L. E. Wharton, and N. W. Spencer, A comparison of wind observations of the upper thermosphere from the Dynamics Explorer satellite with the predictions of a global time-dependent model, *Planet. Space Sci.*, 31, 1299-1314, 1983.
42. Roble, R. G., R. E. Dickinson, E. C. Ridley, B. A. Emery, P. B. Hays, T. L. Killeen, and N. W. Spencer, The high latitude circulation and temperature structure of the thermosphere near solstice, *Planet. Space Sci.*, 31, 1479-1499, 1983.
43. Roble, R. G., B. A. Emery, R. E. Dickinson, E. C. Ridley, T. L. Killeen, P. B. Hays, G. R. Carignan, and N. W. Spencer, Thermospheric circulation, temperature and compositional structure of the Southern Hemisphere polar cap during October-November, 1981, *J. Geophys. Res.*, 89, 9057-9068, 1984.
44. Larsen, M. F., and L. S. Mikkelsen, The dynamic response of the high-latitude thermosphere and geostrophic adjustment, *J. Geophys. Res.*, 88, 3158-3168, 1983.
45. Killeen, T. L., and R. G. Roble, An analysis of the high latitude thermospheric wind pattern calculated by a thermospheric general circulation model, 1, Momentum forcing, *J. Geophys. Res.*, 89, 7509-7522, 1984.
46. Mayr, H. G., I. Harris, F. Varosi, and F. A. Herrero, Global excitation of wave phenomena in a dissipative multiconstituent medium, 3, Response characteristics of the Earth's thermosphere, *J. Geophys. Res.*, in press, 1987.
47. Rees, D., T. J. Fuller-Rowell, M. F. Smith, R. Gordon, T. L. Killeen, P. B. Hays, N. W. Spencer, L. E. Wharton, and N. C. Maynard, The westward thermospheric jet-stream of the evening auroral oval, *Planet Space Sci.*, 33, 425-456, 1985.

48. Roble, R. G., T. L. Killeen, G. R. Carignan, N. W. Spencer, R. A. Heelis, P. H. Reiff, J. D. Winningham and D. S. Evans, Thermospheric dynamics during 21/22 November 1981: Dynamics Explorer measurements and TGCM predictions, *J. Geophys. Res.*, in press, 1987.
49. Rees, D., R. Gordon, T. J. Fuller-Rowell, M. Smith, G. R. Carignan, T. L. Killeen, P. B. Hays, and N. W. Spencer, The composition, structure, temperature and dynamics of the upper thermosphere in the polar regions during October to December, 1981, *Planet. Space Sci.*, 33, 617-666, 1985
50. Roble, R. G., B. A. Emery, G. C. Reid, S. Solomon, R. R. Garcia, D. S. Evans, T. L. Killeen, P. B. Hays, R. A. Heelis, W. B. Hanson, J. D. Winningham, N. W. Spencer, and L. H. Brace, Joule heating in the mesosphere and lower thermosphere during the 13 July 1982 solar proton event, *J. Geophys. Res.*, 92, 6083-6090, 1987a.
51. Killeen, T. L., and R. G. Roble, An analysis of the high latitude thermospheric wind pattern calculated by a thermospheric general circulation model, 2, Neutral parcel transport *J. Geophys. Res.*, 91 11291-11307, 1986.
52. Killeen, T. L., R. G. Roble, and N. W. Spencer, A computer model of global thermospheric winds and temperatures, *Adv. Space Res.*, in press, 1987b.

TABLES

Table I.

Relationship between various characteristic features of the neutral thermospheric winds in the polar regions and Kp for the specified regression line. Taken from RTef. 29.

Table II

Same as Table I except that the relationships are for the Auroral Electrojet index AE.

FIGURE CAPTIONS

- Figure 1. Typical measurement geometry for the DE-FPI (bottom schematic). The instrument performed a limb scan of the horizon, with scan angles varying between 5° and 15° from the local horizontal (shown here as 12°). The instrument measured the Doppler shift of the $O(^1D)$ emission. A typical volume emission rate profile for this emission is shown at top right, together with a weighting function (labelled "path length") that indicates the geometrical path length through the atmosphere for the given viewing geometry shown below. The contribution function (top right) is simply given by multiplying the local volume emission rate by the path length and represents the contribution to the given line-of-sight measurement from the various altitude layers. As can be inferred from the sharpness of the contribution function, the principal contribution for any given measurements comes from the tangent point altitude along the line of sight.
- Figure 2. Schematic for the DE WATS measurement of wind and temperature (Ref. 6). The aperture of the close-source mass spectrometer is scanned systematically in the vertical and horizontal planes by the two baffles shown in Plate 3. As a baffle scans in front of the aperture, the signal counts drop with a characteristic signature as shown. The baffle location at the time of maximum signal drop-off is related to the wind component in the plane of the baffle motion and this wind can be obtained through solution of the vector triangle shown. This measurement requires precise knowledge of both the spacecraft speed and direction. The shape of the signal drop off is governed by the velocity distribution of the neutral gas particles and hence is related directly to the kinetic temperature.
- Figure 3. Horizontal neutral wind vectors at ~ 350 km altitude from merged FPI and WATS measurements. a) orbital passes over the Southern Hemisphere polar cap; b) orbital passes over the Northern Hemisphere polar cap. The winds are given by the arrows, with the arrow length plotted according to the scale at lower right.
- Figure 4. Climatological map for UT bins centered at 07:00, 09:00, and 11:00hrs UT (top to bottom). The left-hand side shows the satellite- and GBFPI-averaged measurements plotted in geographic polar coordinates (latitude and LT). The satellite-averaged winds are given by the arrows according to the wind scale at lower right. The GBFPI wind measurements are plotted as standard meteorological symbols with a barb, 100m/sec; long line, 50 m/sec; short line, 10 m/sec. The curved line is the solar terminator. The left hand side illustrates the NCAR-TGCM predictions for the midpoint of the particular UT bin. Model winds are plotted according to the same scale as the satellite winds. Figure taken from Ref. 15.
- Figure 5. Averaged thermospheric neutral wind measurements for a) north pole By positive; b) north pole By negative; c) south pole By positive; d) south pole By negative. Data collected between November 1981 and January 1982 and between November 1982 and January 1983 were averaged according to the sign of the By component of the IMF and plotted in geomagnetic polar coordinates (magnetic latitude and magnetic local time). Outer circle of each polar dial is at 40° geomagnetic latitude. The local time orientation of the polar dials and vector winds is given at top right. Figure taken from Ref.26..
- Figure 6. Averaged thermospheric neutral wind measurements for a) south pole high Kp; b) south pole low Kp; c) north pole high Kp; d) north pole low Kp. Data collected between November 1981 and January 1982 and between November 1982 and January 1983 were averaged according to the given range of Kp and plotted in geomagnetic polar coordinates (magnetic latitude and magnetic local time). Outer circle of each polar dial is at 40° geomagnetic latitude. The local time orientation of the polar dials and vector winds is given at top right. Figure taken from Ref.29..

- Figure 7. Dependence of the maximum geomagnetic polar cap anti-sunward neutral wind as a function of the geomagnetic indices Kp (top) and AE (bottom). Figures 11a) and c) are for north pole observations and 11b) and d) are for south pole observations. The expressions given represent fits to the experimental data. Wind observations over 6 months of the DE-2 mission were used to provide these relationships. Figure taken from Ref. 29.
- Figure 8. Zonal neutral wind observations from WATS for two northern hemisphere high-latitude orbital passes are compared with simultaneous zonal ion drift observations from IDM. Top panel for orbit 7210, bottom panel for orbit 7212. Data are plotted at the same temporal and spatial resolution to provide an indication of the integrating effect of the neutral atmosphere (note greater spatial structure evident in ion drift data, see text). Figure taken from Ref.27..
- Figure 9. a) Simultaneously measured neutral wind vectors from DE 2 (orbit 1813) and DE-1 auroral image (courtesy L. A. Frank and J. D. Craven, University of Iowa). The images were obtained using the SAI instrument viewing at ultraviolet wavelengths. The images are false-color coded and are oriented such that the direction towards the sun is to the top of the figure, dusk to the left. The solar terminator is evident, running roughly horizontally across each image, as is the entire auroral oval located just to the nightside of the terminator. The neutral wind vectors are denoted by the yellow arrows whose origins are positioned along the DE-2 orbital track. The wind scale is given at lower right. 9b, 9c, and 9d are for DE-2 orbits 1815, 1819, and 1823, respectively. Figure taken from Ref.33..
- Figure 10. Zonal wind average measurements from WATS at equatorial latitudes in the altitude range 300 - 500 km. Table shows the numerical results of averaging the zonal wind measurements according to latitude interval and altitude range. Figure taken from Ref.37..
- Figure 11. Comparison of neutral wind measurements from Dynamics Explorer with the predictions of the UCL-TGCM for three dawn-dusk crossings of the spacecraft over the Northern Hemisphere polar region. The neutral-wind measurements are given by the vectors plotted along the latitudinal track of the spacecraft (labelled KVEC, with orbit number) and the UCL-TGCM predictions for two model runs corresponding to different ion density input models are given by the vectors plotted to the top and bottom of the experimental measurements. Figure taken from Ref.41..
- Figure 12. Zonal neutral wind component measured by the WATS instrument along the DE-2 satellite track over the polar caps for six orbits: a) 1639, b) 1640, c) 1641, d) 1641, e) 1644, and f) 1646. All the orbits, with the exception of d) are for the Northern Hemisphere. Also shown are the TGCM-predicted neutral temperature pattern (K) and neutral wind vectors along the model $z=+2$ constant-pressure surface (~ 400 km) over the polar caps at the times of the DE-2 satellite passes. The outer circle represents a latitude of either $\pm 37.5^\circ$ latitude depending on hemisphere. Figure taken from Ref. 48.

Table I

Relationship between the neutral winds in the polar regions and K_p for the regression line

$$v \text{ (m/s)} = a + b \times K_p.$$

Direction	a	b	r (measured)	Correlation Coefficient (95% confidence Interval)
Antisunward				
Northern	261(±87)	68.7(±30)	0.97	0.80 ≤ R ≤ 0.99
Southern	269(±58)	101.6(±30)	0.94	0.54 ≤ R ≤ 0.99
Dusk Sunward				
Northern	168(±74)	45.3(±21)	0.98	0.82 ≤ R ≤ 0.99
Southern	113(±77)	30.4(±19)	0.94	0.54 ≤ R ≤ 0.99
Dawn Sunward				
Northern	68(±65)	21.0(±27)	0.91	0.14 ≤ R ≤ 0.99
Antisunward width (° latitude) [†]	24(± 4)	3.2(±1.3)	0.98	0.82 ≤ R ≤ 0.99

[†] The distance between the sunward/antisunward reversal boundaries of the neutral wind in the polar cap, expressed in degrees latitude.

Table II
Relationship between the neutral winds in the polar regions and AE for the regression line
 $v (m/s) = a + b \times AE$

Direction	a	b	r (measured)	Correlation Coefficient (95% confidence interval)
Antisunward				
Northern	261(± 71)	0.82(±0.20)	0.96	0.67 ≤ R ≤ 0.99
Southern	330(±112)	0.45(±0.37)	0.91	0.38 ≤ R ≤ 0.99
Dusk Sunward				
Northern	129(±58)	0.62(±0.20)	0.94	0.54 ≤ R ≤ 0.99
Southern	153(±78)	0.30(±0.26)	0.92	0.42 ≤ R ≤ 0.97
Dawn Sunward				
Northern	43(±47)	0.38(±0.21)	0.98	0.72 ≤ R ≤ 0.99

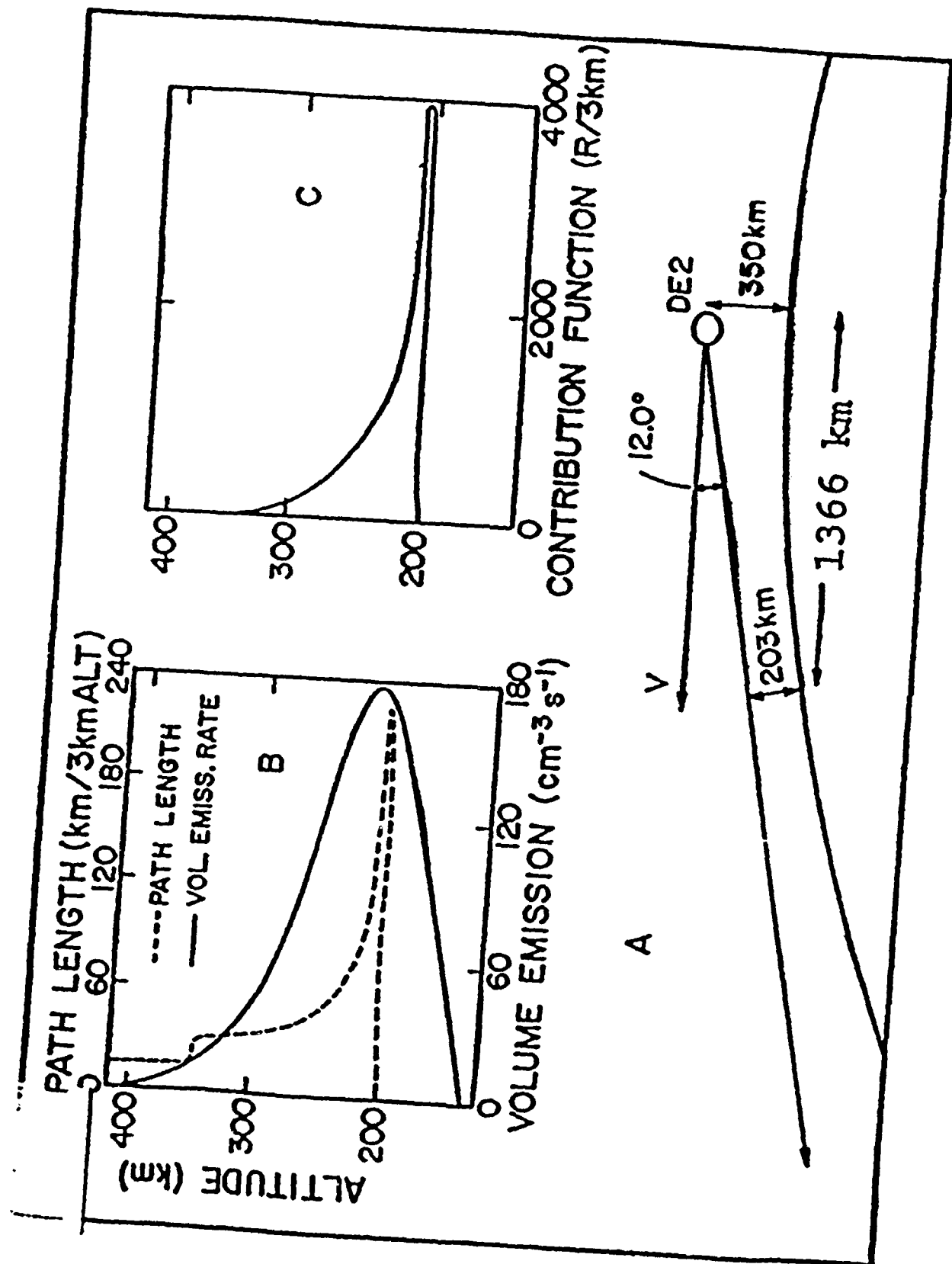


Figure 1

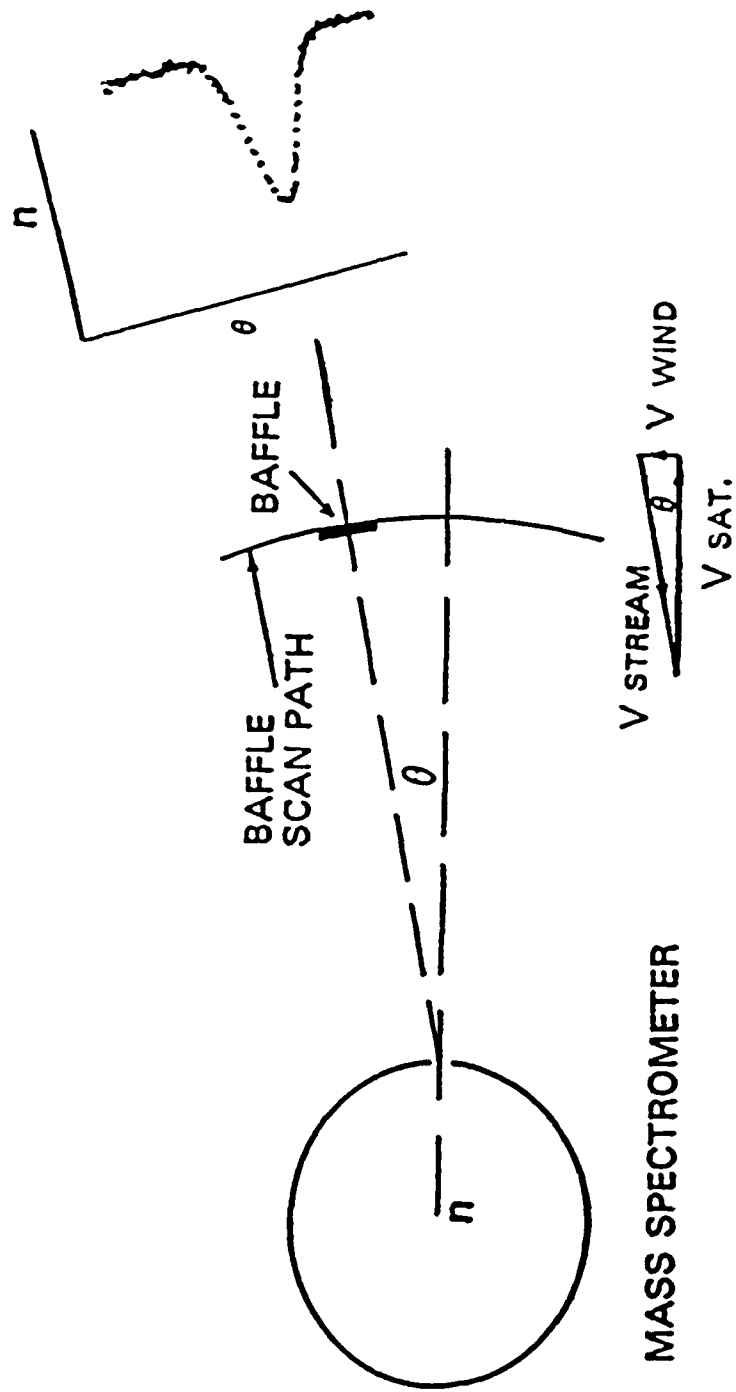


Figure 2

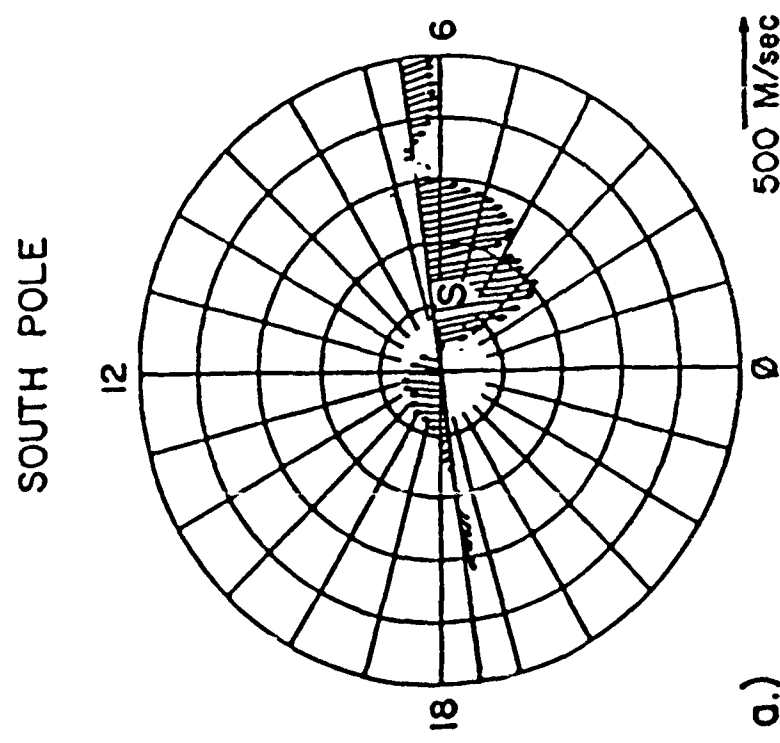
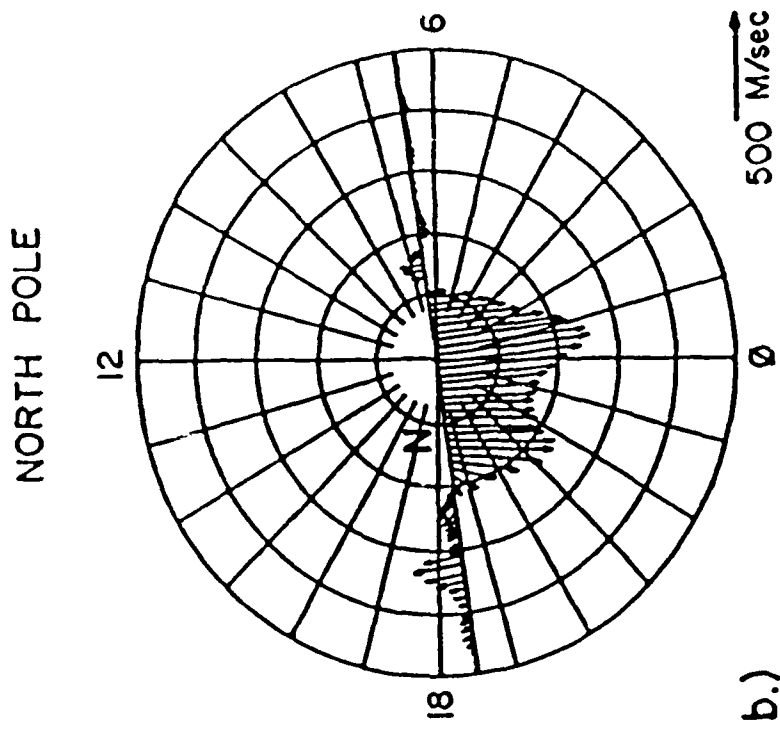


Figure 3

DE-2/GBFPI
AVERAGE NEUTRAL WINDS
DEC 1981

NCAR/TGCM
MODEL PREDICTIONS

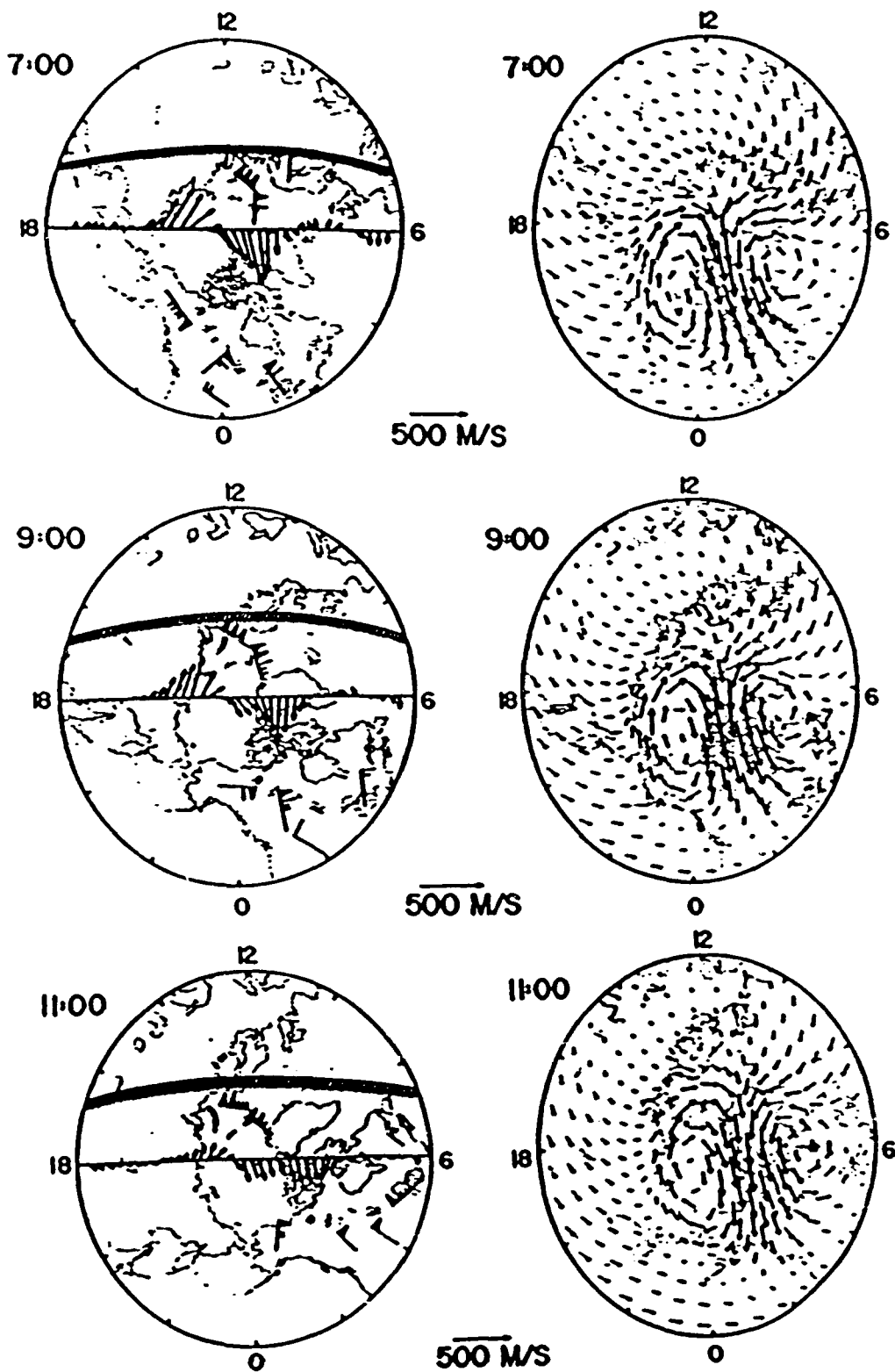


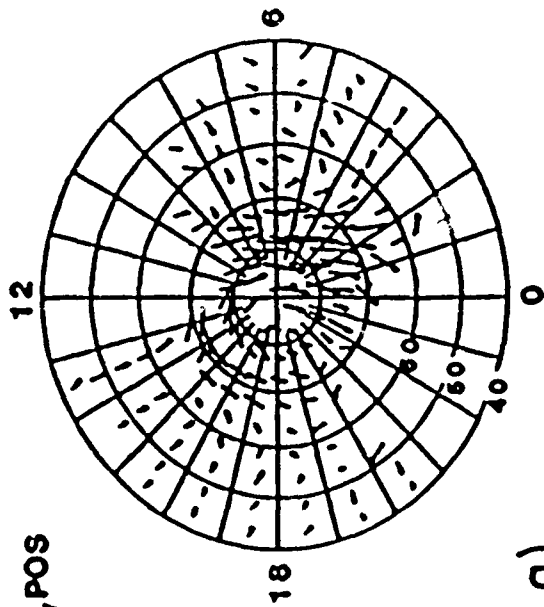
Figure 4

B_y - DEPENDENCE OF THE AVERAGE THERMOSPHERIC NEUTRAL CIRCULATION

(IN GEOMAGNETIC COORDINATES)

NORTH POLE

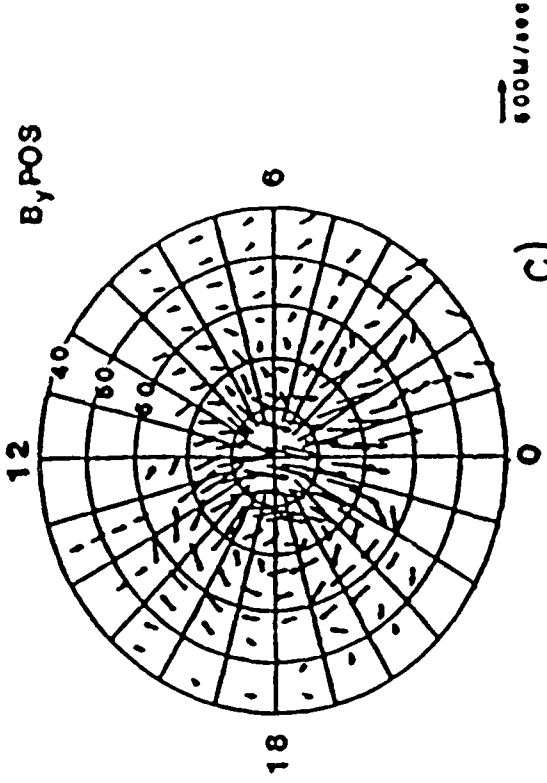
B_y POS



a)

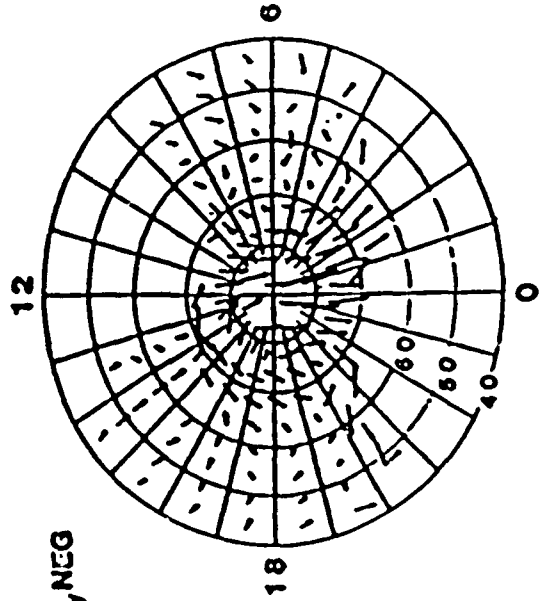
SOUTH POLE

B_y POS



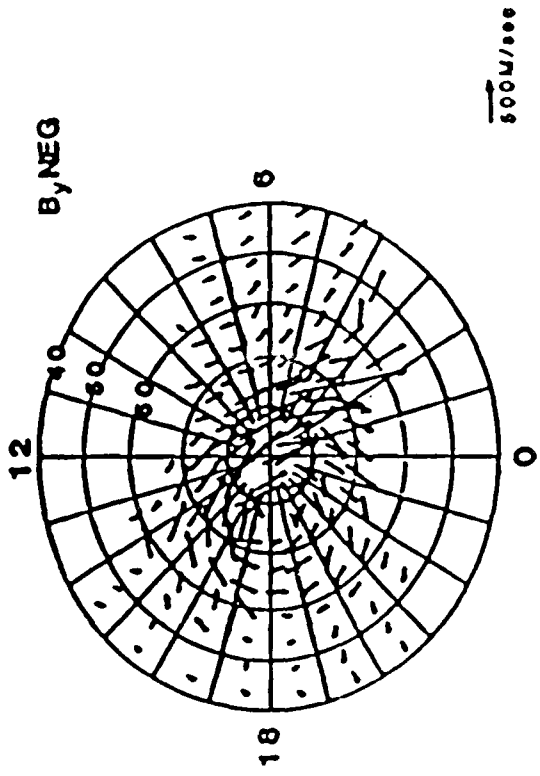
c)

B_y NEG



b)

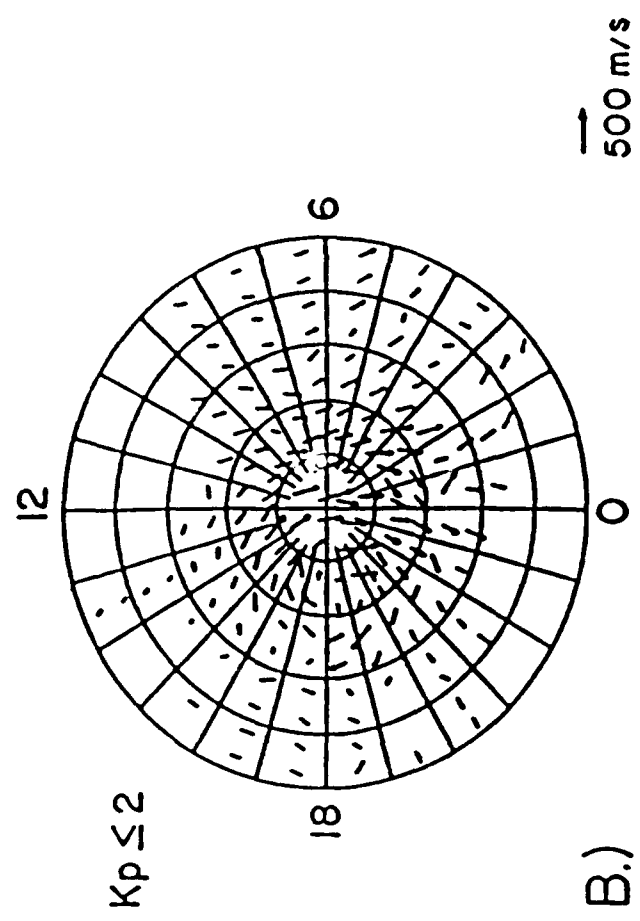
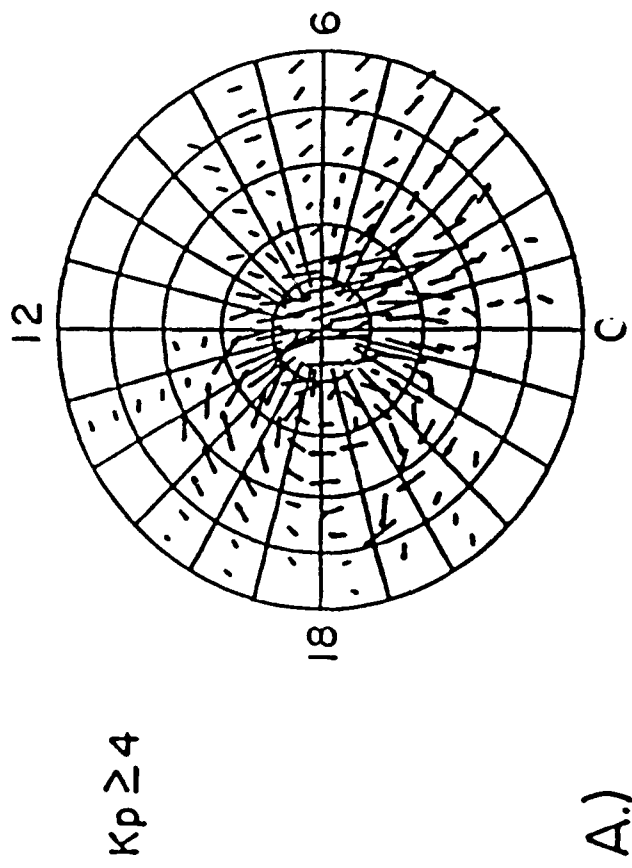
B_y NEG



d)

Figure 5

SOUTH POLE



NORTH POLE

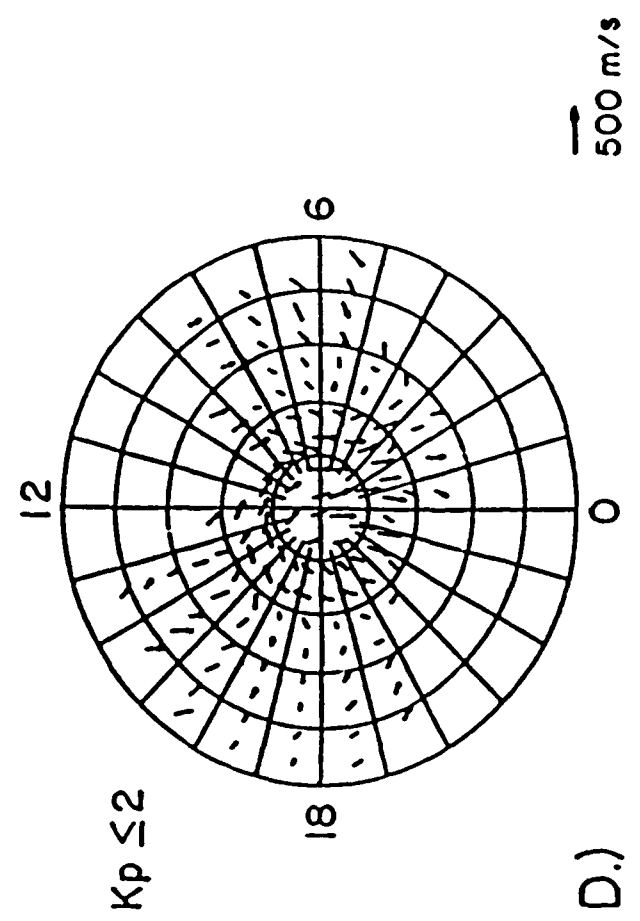
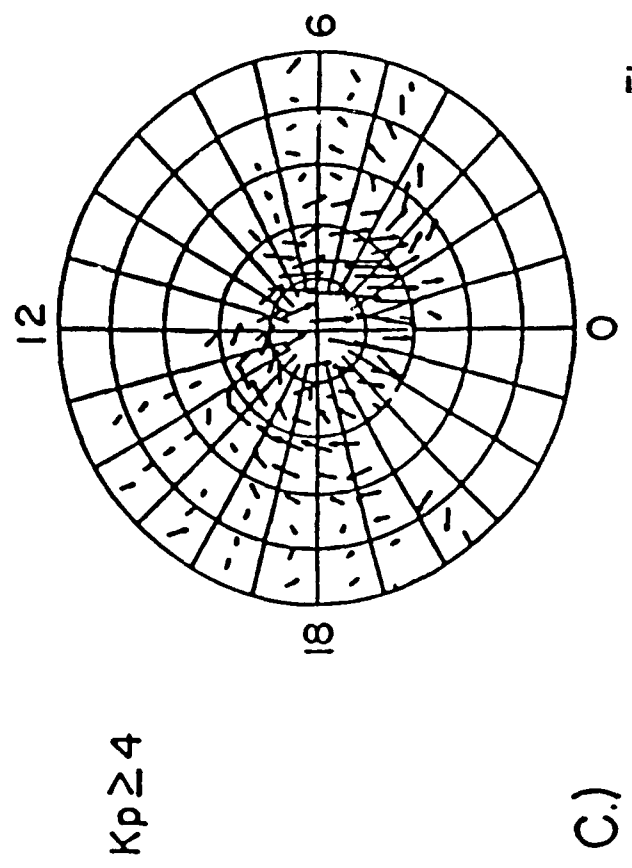


Figure 4

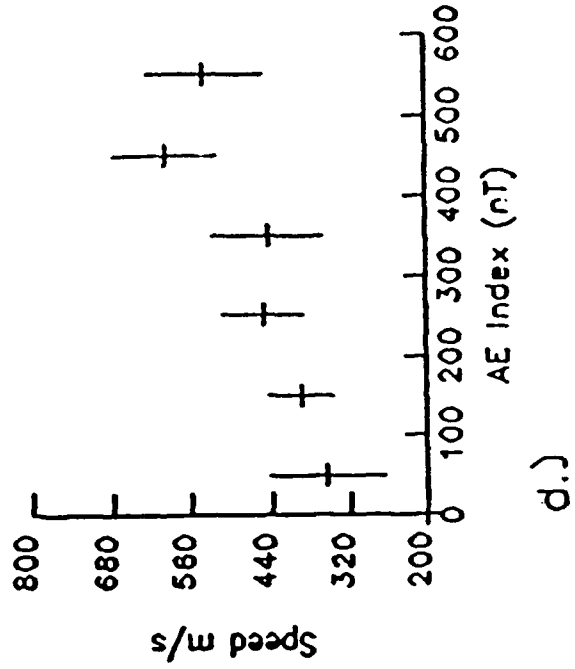
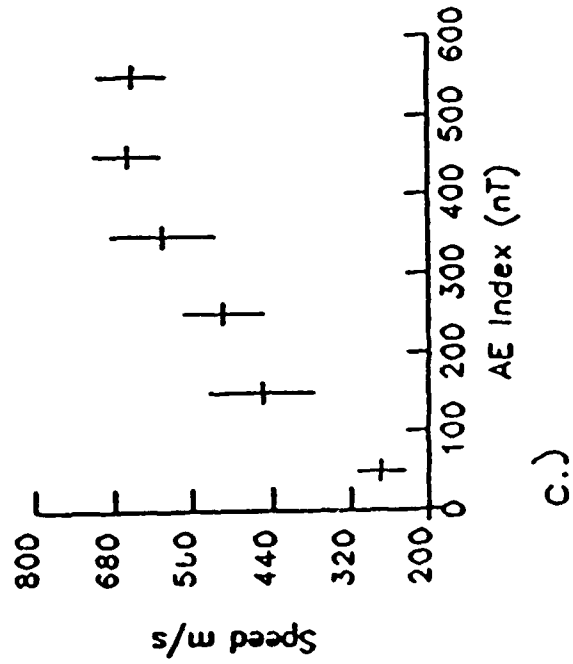
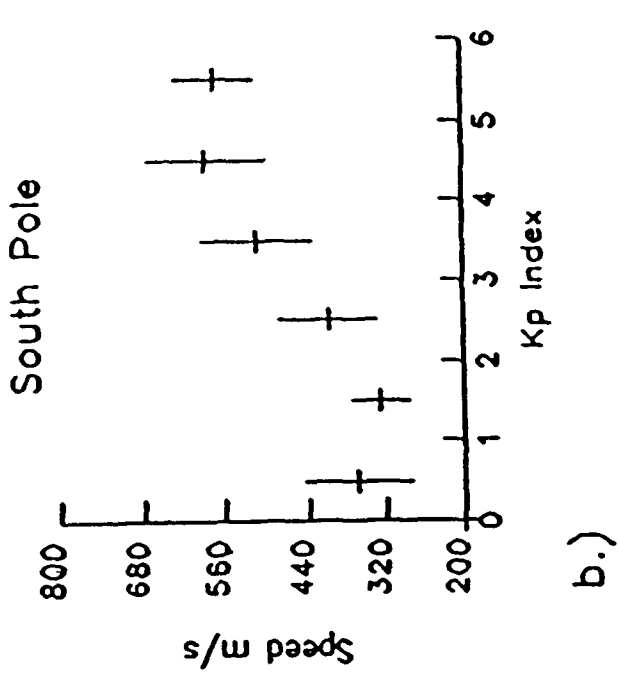
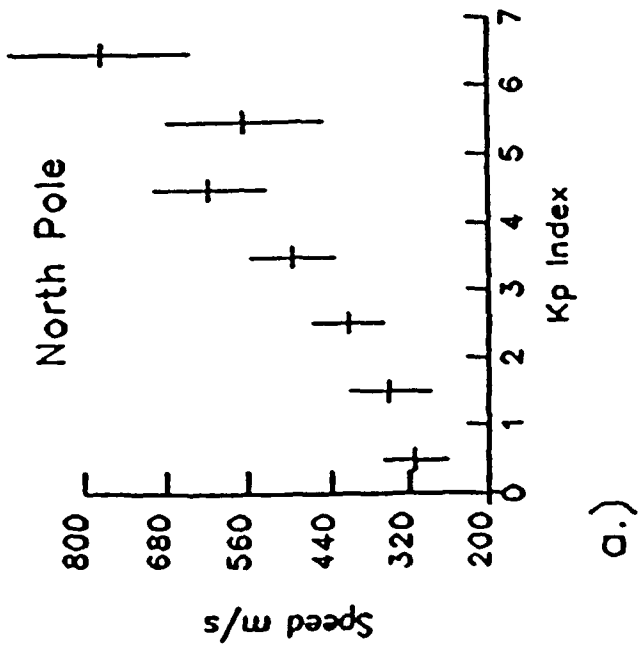


Figure 7

DE-2 WATS/IDM ZONAL NEUTRAL AND ION WINDS

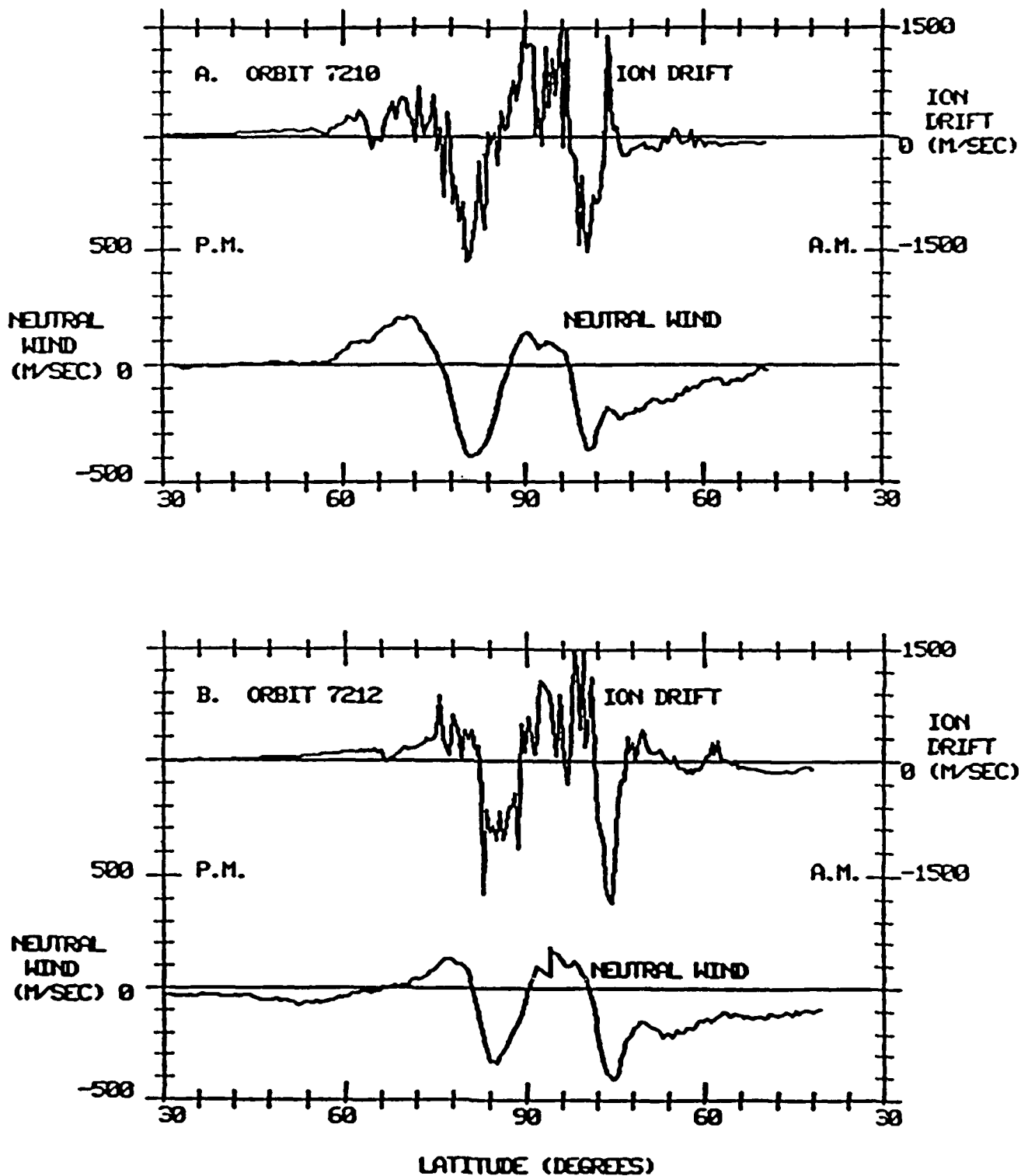
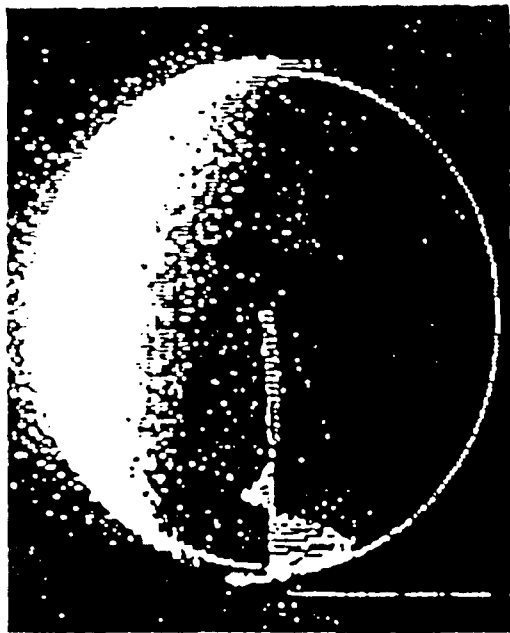


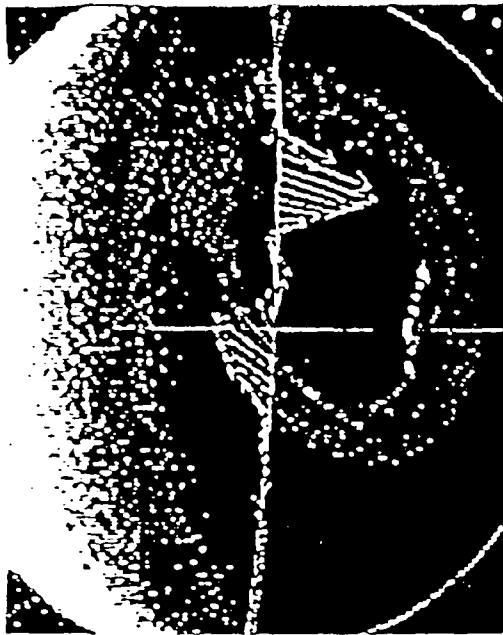
Figure 8

1813 2239 UT 3 DEC 1981



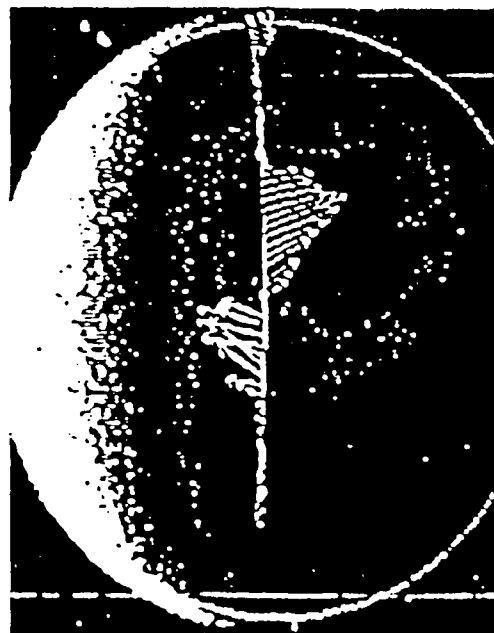
900 m/s

1815 0153 UT 4 DEC 1981



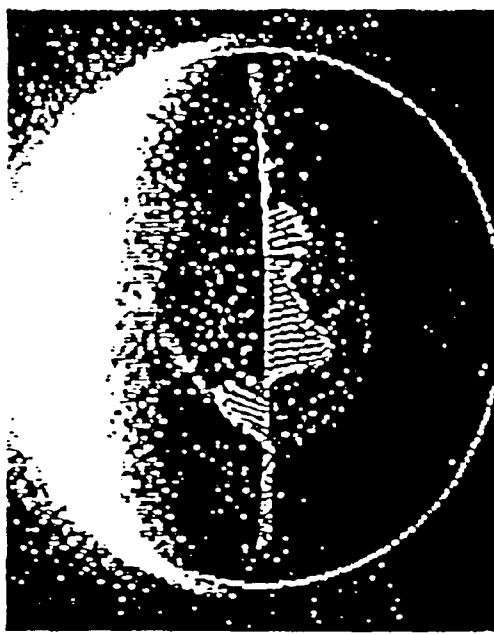
500 m/s

1819 0819 UT 4 DEC 1981



500 m/s

1823 1446 UT 4 DEC 1981



500 m/s

E

F

G

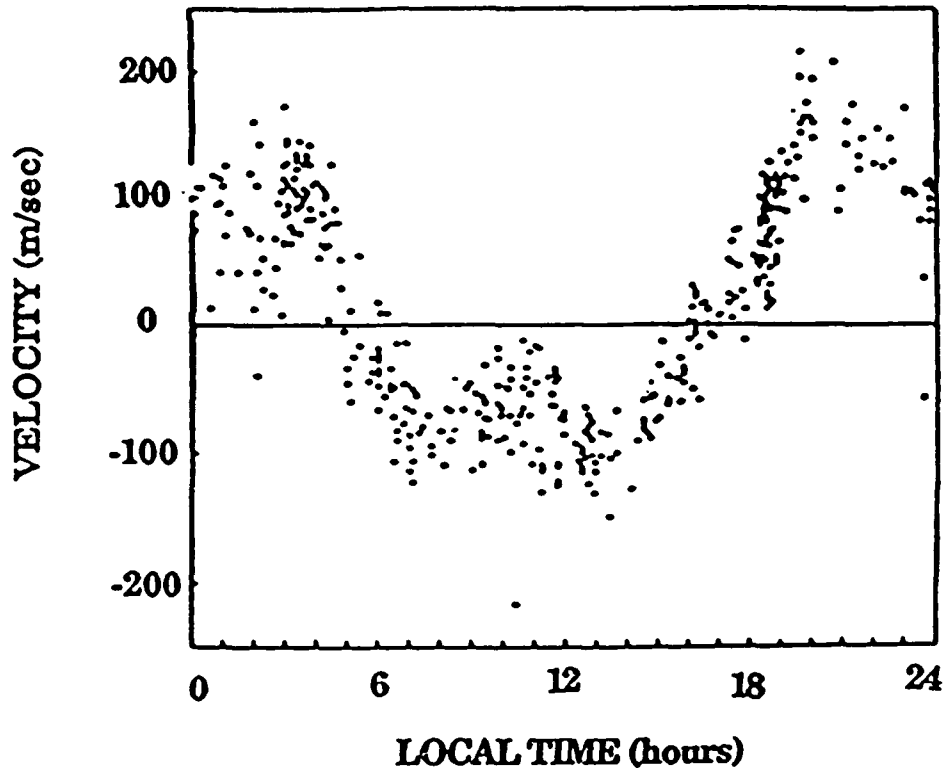
H

Figure 9

THERMOSPHERIC SUPERROTATION? DE-2 MEASUREMENTS

Wharton, Spencer and Mayr, Geophys. Res. Lett., 1984.

ZONAL WIND



Average zonal winds to the East

<u>Altitude range 200-350km</u>		<u>Altitude range 300-500km</u>	
<u>latitudes</u> <u>(deg)</u>	<u>Average wind</u> <u>(m/sec)</u>	<u>Latitudes</u> <u>(deg)</u>	<u>Average wind</u> <u>(m/sec)</u>
0-10	15.5	0-10	21.7
10-20	4.2	10-20	10.1
20-30	-7.1	20-30	-4.7
<u>30-40</u>	<u>-16.8</u>	<u>30-40</u>	<u>-20.3</u>
<u>average:</u>	<u>-1.05</u>	<u>average:</u>	<u>1.7</u>

Figure 10

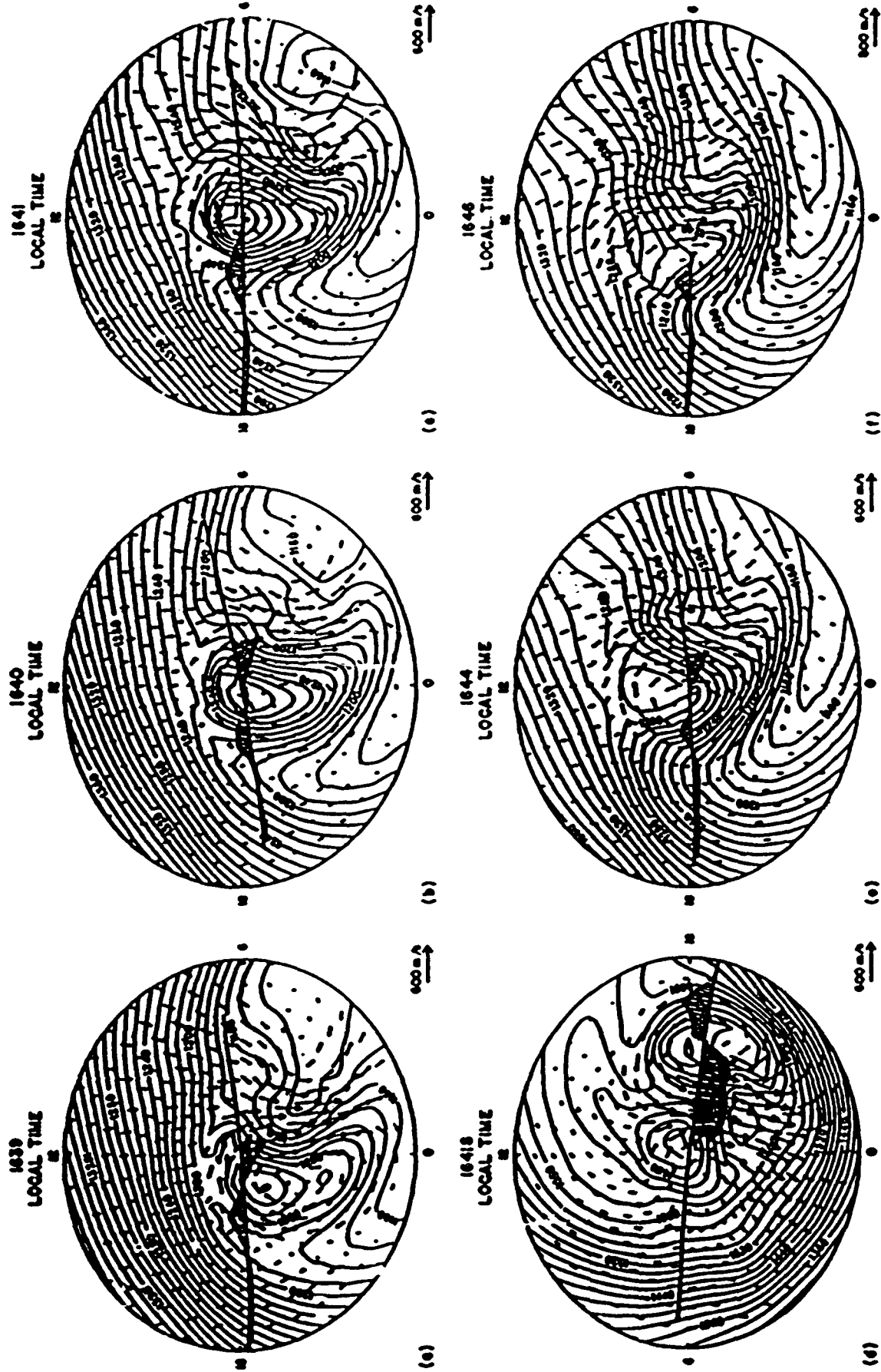


Figure 12

4. NEW DENSITY AND DRAG MEASUREMENTS

4.1
AFGL LIDAR FACILITY
Dwight P. Sipler
Air Force Geophysics Laboratory

Lidar is an acronym, Light Detection And Ranging. This is the same acronym as radar, except that light is used instead of radio waves. Other than that, the basic principles are similar, i.e. a short pulse of light is transmitted, hits a scattering object and returns to the detector. The range is determined by the delay time between transmit and receive. A very simplified description of an atmospheric sounding lidar is given by the equation

$$(1) \quad S = P_0 K n r^{-2}$$

where S is the detected signal, P_0 is the transmitted power, K is a constant containing system parameters, n is the number of scattering objects and r is the range of the objects. In a radar system the range dependence is usually written as r^{-4} , but that is for a target which is small compared to the dimensions of the transmitted beam so that the illumination of the target depends on r^{-2} and the light scattered from the target into the detector is also proportional to r^{-2} . Since we are looking at the atmosphere, the target completely fills the beam and only the light scattered into the detector gives a range dependence. The number of scattering objects is just the density of the atmosphere. The catchall parameter K includes such things as the optical system efficiency (both transmit and receive), extinction of the light by the atmosphere (mostly dust and aerosols in the lower atmosphere) and the cross section of the atmospheric molecules (basically a constant up to around 90 km).

Several different scattering processes are important to lidar measurements of atmospheric density:

Rayleigh scattering
Mie scattering
Raman scattering
Resonance scattering.

Rayleigh scattering is the scattering of light by small particles and is familiar to most people as the process which causes the blue color of the sky. Rayleigh scattering theory describes the scattering of electromagnetic radiation by particles which are small compared to the wavelength of the radiation. In the case of atmospheric sounding, the scattering particles are the atoms and molecules which make up the atmosphere. The scattering cross section is relatively small and varies as λ^{-4} .

Mie scattering theory describes the scattering of electromagnetic radiation by particles which are of the order of the wavelength of the radiation or larger. This process is important in the lower regions of the atmosphere (from the ground to about 25 km) where dusts and aerosols are significant components of the atmosphere. The wavelength dependence of this type of scattering is a complex function of particle size and wavelength but in general the scattering cross section is larger than the Rayleigh cross section and varies as λ^{-1} .

Raman scattering is similar to Rayleigh scattering except that where Rayleigh scattering is an elastic process, Raman scattering is inelastic scattering. This means that a photon, when scattering from an atom or molecule, leaves some of its energy behind in the atom or molecule. Since only discrete energy levels are available and these are different for different atmospheric components, the energy loss will be characteristic of the particle doing the scattering. The energy loss means that the wavelength of the scattered light will be longer (lower energy) than the light from the laser. Thus, by selecting a particular wavelength shift with an interference filter, measurements can be made on specific components of the atmosphere, e.g. N_2 , O_2 or H_2O . The Raman scattering cross section is very small, about 10^{-3} of the Rayleigh cross section. This limits the utility of this process to lower altitudes where the light from the laser is most intense. However, this is just where this sort of measurement is needed, since the scattering is relatively insensitive to the presence of dust and aerosols.

Resonance scattering is another process which depends on specific energy levels in a scattering atom or molecule. If the laser can be tuned to a wavelength which represents the exact energy needed to raise the target atom to an excited state from the ground state through an allowed transition then the cross section for absorption and reradiation of the light will be very large. This large cross section makes this process suitable for the measurement of minor components of the atmosphere, e.g. free atomic sodium, which occurs in a thin layer between approximately 85 and 105 km altitudes. The sodium density in this region is on the order of 10^4 cm^{-3} compared to the ambient atmospheric density of around 10^{14} cm^{-3} . However, the resonance cross section is about 11 orders of magnitude larger than the Rayleigh cross section, so measurements of sodium can be performed with moderate laser power. Other workers have used this same technique to look at calcium, potassium, lithium and iron. The technique could also be used on ions as well as neutrals.

Laboratory Lidar System

AFGL has two lidar systems for mesospheric sounding: a laboratory system for testbed applications and a mobile version for field work. The laboratory system is located at AFGL on the roof of building 1102F. The system consists of a laser transmitter, beam expander and steering optics, a telescope detector and a data acquisition system. The basic laser is a Quantel model 582 Nd:YAG laser with doubling and tripling crystals. This provides us with three wavelengths: 1064 nm (fundamental), 532 nm (doubled) and 355 nm (tripled). The 532 and 355 nm wavelengths are used for sounding and the 1064 nm is discarded since the Rayleigh scattering at this wavelength is small and we have no good detectors for 1064 nm light. The use of two wavelengths enables us to monitor the wavelength dependence of the scattering profiles and thus to identify regions in which Mie scattering from dusts and aerosols is significant. We do not currently use the data from these regions, but if the particle size distribution could be determined or accurately modelled, a determination of the particle density could be extracted from the two color returns. The laser output beam is 1 cm in diameter and has a 0.6 mrad beam divergence. This beam is expanded by a factor of 15, resulting in a 15 cm diameter beam with 0.04 mrad divergence. The expanded beam is directed vertically by an adjustable 45° mirror.

The telescope detector consists of a 36 inch Dall-Kirkham telescope coupled to a 6 channel detector with a mechanical shutter. The shutter runs at 7000 rpm and has 3 apertures, generating 350 openings per second. Timing for the lidar system is taken from the shutter to ensure synchronization. The laser is fired before the shutter opens so that the light scattered in the troposphere is blocked from the photomultipliers. Since most of the dusts and aerosols in the atmosphere are located below the tropopause and since r^{-2} is large in this region, the shutter blocks the major part of the returning light. This is done to avoid saturation and recovery effects in the photomultipliers. After passing through the shutter, the light is split into a 532 nm beam and a 355 nm beam by a dichroic beamsplitter and further split into three photomultipliers for each wavelength. These photomultipliers have different sensitivities to split the required dynamic range of the instrument into smaller ranges. A second shutter blocks the highest sensitivity photomultiplier for a time equivalent to an additional 15 km of range in order to reduce overload from the high signal levels from the lower altitudes. Since the shutter opens at 350 Hz and the laser runs at 10 Hz several shutter openings are available for background light monitoring. The background data are separated by software.

The data acquisition system is currently a LeCroy 3500M microcomputer system with an integrated camac crate. Data from the 6 photomultipliers is multiplexed and fed into two multichannel scaling modules in the camac crate. Data from the scaling modules is integrated in the computer through software. Since the read cycle time for the camac modules is 1 μsec the maximum sampling rate for the system is 2 μsec per point, one μsec for each module. Acquired data are stored on floppy disks for later analysis. We are currently installing a new 80386 based PC coupled to a camac crate which will both simplify data acquisition and enable some real-time analysis of the data.

AFGL is located under the landing pattern for Hanscom field and is close to the flyway into Logan airport. Interception of the laser beam by aircraft poses a safety hazard due to the high power in the beam. In order to avoid such problems we have installed an AN/APS 42 radar system co-aligned with the laser beam. If an aircraft is detected by the radar the laser is automatically shut down and requires manual intervention to restart the system.

In addition to the Nd:YAG laser, a Lambda Physik FL2002E-C narrow band dye laser is available for use in resonance scattering measurements. This laser has been used for measurements on the atomic sodium layer in the 85-105 km region. The ultimate bandwidth of this laser is narrower than the doppler width of the sodium D₂ line from this region, so we will be able to use it for measurements of the width of the resonance line. This will give us a measurement of the ambient temperature in this region.

A second telescope detector is included in the laboratory system for Raman scattering measurements. This telescope is a 12 inch telescope and is provided with two photomultipliers for detection of the low altitude scattering from the laser beam. One channel is used for the normal Rayleigh/Mie scattering signal and the other is used for a Raman signal. An interference filter is used which has a passband at the Raman shifted wavelength but also has a strong band rejection around the laser wavelength to avoid contamination of the weak Raman signal by the strong Rayleigh/Mie return.

Mobile Lidar System

The mobile system is similar to the laboratory system except that it is scaled down a bit to get it into a small trailer. The trailer is equipped with jacks to enable removal of the wheels for air shipment. The trailer has been shipped on a C141 to Alaska and back. The wheels are suitable for short movements of the trailer system but not for extended travel. For long overland travel the trailer is set onto a flatbed trailer.

The laser in the mobile system is a Quantel model 581C Nd:YAG laser which generates 1.7 Joule pulses instead of the 2 Joule pulses of the laboratory system. The telescope is a 30 cm telescope instead of the 96 cm telescope of the laboratory system. The telescope is mounted horizontally on an optical table and a 45° mirror is located in front of the telescope to direct the field of view. The center section of the 45° mirror is cut out and replaced with a dielectric mirror for reflection of the laser beam. This arrangement avoids any possible problem with fluorescence of the turning mirror from the laser beam since the light from the center of the turning mirror is blocked from the rest of the mirror by a metal mounting ring. Scattered light from this section is blocked by the secondary of the telescope so fluorescence in the laser turning mirror does not reach the detector. The 45° turning mirror can be rotated about the telescope axis to direct both the laser beam and the detector field of view toward a selected elevation angle from slightly below the horizon to 20° past the zenith. Small azimuth adjustments are made by moving the mirror mount about a vertical axis.

The detector is equipped with a shutter to block out the light from low altitudes. However, instead of the multiplexing system used in the laboratory system, the mobile shutter is designed to extend the dynamic range of the detector by acting as a variable aperture in the telescope. The primary of the telescope is focussed onto the shutter wheel, which has an arrow shaped aperture (see fig. 1). This shutter opening moves slowly across the image of the telescope primary and effectively opens the aperture slowly, taking the equivalent of about 20 km of range from first light to full open. Since

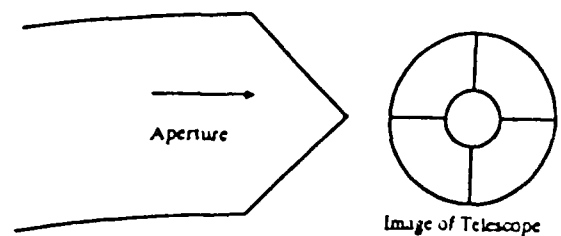


Fig. 1: Variable Shutter

the shutter is moving across the image of the primary mirror there is no time modulation of the field of view of the telescope. This avoids possible timing changes due to changes in the position of the laser return within the field of view of the telescope. The shape of the transmission function can be determined by looking at a uniform light source placed in front of the telescope. An illuminated reflector can be used but in practice, the day sky is the most uniform source available since cloud motions are averaged in time. The brightness of the sky is reduced by placing a neutral density filter at the primary focal point of the telescope. A typical transmission function is shown in fig. 2.

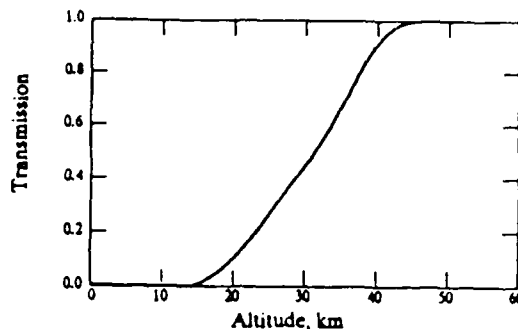


Fig. 2: Shutter Transmission Function

The brightness of the sky is reduced by placing a neutral density filter at the primary focal point of the telescope. A typical transmission function is shown in fig. 2.

A 62 cm detector telescope is also located in the trailer to extend the altitude range of the lidar system. This telescope is fixed vertically rather than being able to be directed at different elevation angles. In use, the 45° turning mirror of the laser is directed vertically and small adjustments in the mirror mount are made until the laser beam and the fixed telescope field of view overlap. This detector includes a fast-opening shutter which is phase locked to the shutter of the primary system by a servo system. Some jitter is inevitable in this system, making the opening of this system somewhat ragged. The initial data from this detector can be corrected to some extent by modelling the jitter and measuring the time-averaged response of this detector to a uniform white light (again using daylight appears to be most effective).

A Lambda Physik EMG201MSC excimer laser is being installed in the mobile lidar system for use in Rayleigh scattering at higher altitudes. The excimer will be used at 351 nm and is expected to generate 250 mJoule pulses at up to 80 Hz. This should extend our altitude measurement range by about 10 km.

The 62 cm detector is being equipped with an etalon which will be used as a very narrow band interference filter. This will cut down the continuum light passing through the filter during daylight operations. We estimate that the system will be able to measure densities up to about 55 km during daylight with this system.

System Operation

Since the shutter timing is essential to the proper operation of the system, a sensor is provided which generates a pulse at a specified time before the shutter opens. The laser firing is synchronized with this signal to ensure a constant relationship between the shutter opening and the lidar range. The pulse from the laser is detected in the laboratory system and used to trigger the data acquisition system. In the mobile system, a pulse is sent from the control electronics to the pockels cell of the laser to synchronize the laser firing with the shutter. Pulses from the photomultipliers are counted by the data acquisition system and a sequence of shots is added to generate a lidar profile. The profiles are stored on floppy disks for later analysis.

In order to minimize the contribution of ambient light from the sky, the field of view of the detector is made as small as possible consistent with the size of the laser spot in the atmosphere. In order to align the laser beam and the detector telescope, a rough alignment can be done by observing the beam through the telescope. After the rough alignment, fine adjustments are made while taking short bursts of data. This allows us to maximize the signal.

Data Analysis

The data are read from the floppy disks onto a PC. Corrections are made for the shutter transmission function in the case of the mobile system. The multiplexed photomultiplier signals are joined to make a smooth profile in the case of the laboratory system. The resulting profiles are then multiplied by r^2 . This generates a curve which is proportional to the density of the atmosphere (see eqn. 1). The constant of proportionality must be determined by some means, since the extinction in the lower atmosphere is not known. The most common method of calibration is the use of a rawinsonde profile, which is matched at the corresponding altitudes to the lidar profile. The use of Raman scattering to measure the low altitude N_2 profile is expected to give us a way to measure the density profile closer to the ground and thereby enable the matching of the profile to surface measurements.

The errors in the profiles are determined by the counting statistics of the pulses from the photomultipliers. These pulses are random and we acquire as many pulses as possible, so gaussian statistics are assumed. In order to determine the density to within 5%, we need at least 400 counts. This counting level is arrived at by (1) adding lidar shots until the desired level is attained and (2) smoothing the data over several range bins to increase the number of counts used for a determination. These procedures limit the temporal and spatial resolution of the lidar. At present, the mobile system is capable of 5% statistics at a range of 70 km with a 15 minute (9000 shot) integration time and 2.7 km (9 point) range smoothing.

Summary

AFGL has developed a lidar system for measurements of atmospheric density and temperature to high altitudes. The system has been used in a campaign of measurements at Poker Flats, Alaska. Current efforts are under way to improve the system by extending the high altitude range of the lidar and by using additional technology to provide calibration of the measurements by comparison with ground truth.

4.2 LIDAR AND ROCKET MEASUREMENTS OF ATMOSPHERIC STRUCTURE PROPERTIES

C.R. Philbrick
AFGL/LID Hanscom AFB, MA 01730

Workshop on Atmospheric Density and Aerodynamic Drag
Models for Air Force Operations
AFGL 20-22 October 1987

ABSTRACT

The results from a mobile lidar have been used to derive density and temperature profiles between 25 and 85 km over central Alaska during February-April 1986. These results allow the temporal changes of the middle atmosphere to be observed on the scales of minutes, hours, and days for the first time. This perspective has led to several new points in our understanding of atmospheric dynamics. The measurements of meteorological rockets made simultaneously with the lidar measurements have been studied together with the results from previous measurement campaigns (MAP-WINE, TRACER, EBC, ...) to explain points about the atmospheric dynamics based on the observed structure variations.

INTRODUCTION

During the period between February and April 1986 a new mobile lidar, BLINT (Ground-based Lidar Investigation-Transportable), was used to obtain data on the variations which occur in the high latitude region of the atmosphere between 20 and 85 km. The lidar measurements were undertaken to provide an improved data base on which the reentry flight characteristics of the Space Shuttle descent from a polar orbit could be based. The lidar can measure profiles with improved altitude and time resolution compared to standard rocket techniques. This is important for better understanding of the dynamical processes of the middle atmosphere. Data was obtained on 26 nights during the program. Standard meteorological balloon and rocket payloads were used to make measurements and provide a comparison study with the lidar data. More than a thousand profiles of atmospheric density were obtained with the lidar and twenty meteorological rockets were launched.

The measurement campaign has resulted in several conclusions: (1) the lidar data has provided the opportunity to observe small-scale variations and the background granularity of the atmosphere, (2) planetary waves may be associated with more than half of the total density variation in the winter middle atmosphere, (3) density and temperature variations can be used to study the source, intensity, and propagation characteristics of gravity waves in the high latitude winter atmosphere, (4) these measurements provide a major step in demonstration of the capabilities of lidar as a tool for routine meteorological and atmospheric measurements.

The properties of the mobile sounder are shown in Table 1. The mobile sounder is housed in a 32-foot trailer which is self-transportable. The trailer uses an undercarriage which can transport the trailer over the road. Adjustable jacks have been included to allow the trailer to be lowered onto a road base and leveled at an operating site. Figure 1 shows a drawing of the trailer configuration and a layout of the hardware within the facility. Figure 2 shows the arrangement of the laser, small detector and the beam steering mirror. A 30 cm telescope is collimated with the laser beam and a mirror is used to steer over a range of elevation and azimuth. A larger receiver of 60 cm diameter is used for zenith measurements.

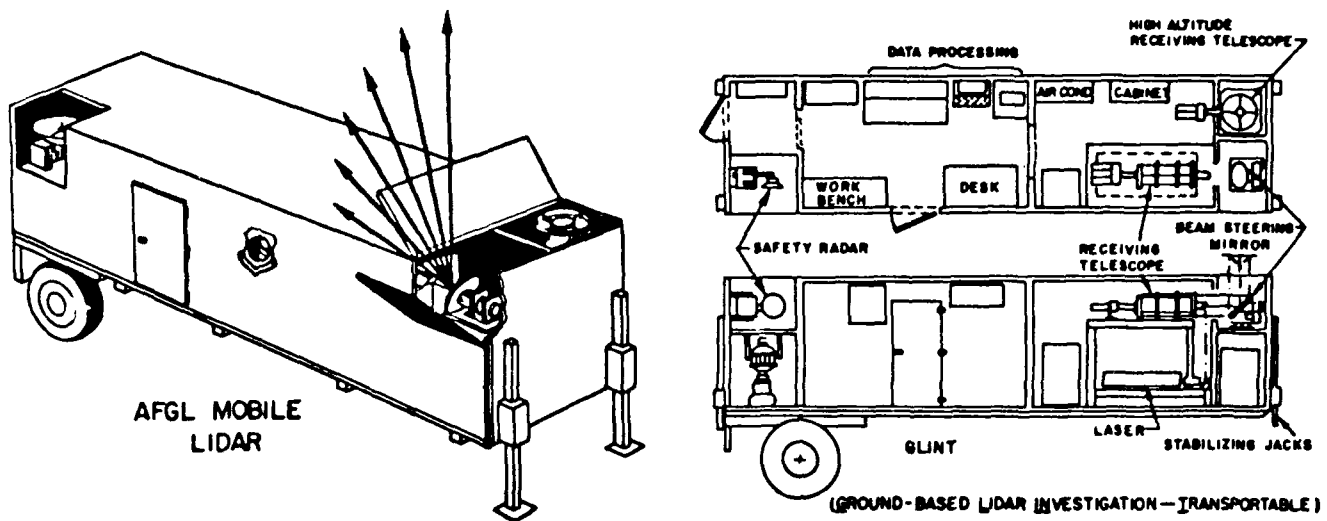


Figure 1. An artist sketch of the GLINT trailer and the primary components of the lidar. Top and side views of the lay out of the equipment in the trailer are shown.

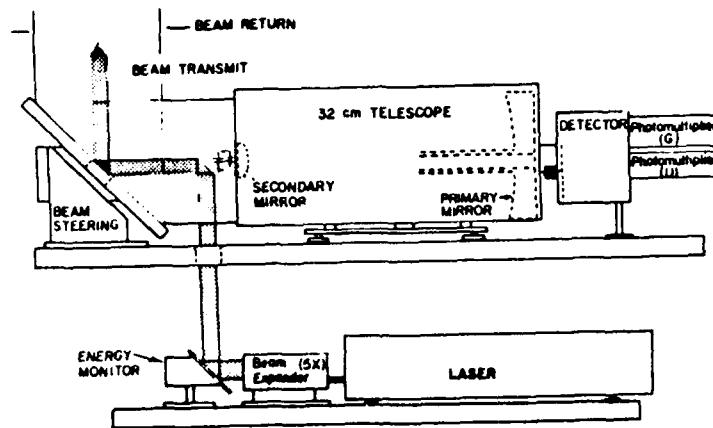


Figure 2. A side view of the optical layout of the lidar shows the principle components and the relationship of the transmit beam path and the collected signal.

Table 1. The principle components of the mobile lidar.

Transmitter - Nd:YAG laser, 10 Hz, Q-switch, 15 watt
 600 mj @ 532 nm, 250 mj @ 355 nm
 5X beam expander - divergence 0.16 mrad

Receiver - 32 cm telescope (steerable) photon counting
 with shutter closed below 15 km and variable
 aperture up to 40 km - nominal fov 1.0 mrad
 - 62 cm telescope (vertical pointed) photon
 counting with mechanical shutter below 40 km

Data System - Lecroy 3500 multi-channel scaler with 2
 microsecond range bins (300 meter resolution)
 - data stored on magnetic disk

Safety System - Electrical interlocks and radar used to
 automatically disable the laser

SUMMARY OF RESULTS

On each evening of lidar operation, a series of 3-5 profiles were obtained using the ultraviolet wave length at 355 nm and the visible wavelength at 532 nm, simultaneously. Figure 3 shows an example of the profiles measured by the green and ultraviolet detectors on the 32 cm telescope. Above 30 km, the profiles are in complete agreement and below 30 km, the signal from the green detector is significantly higher than that for the ultraviolet detector. The ultraviolet return is relatively larger for the molecular scattering and thus less sensitive to the particulate scattering. This fact is due to the $1/\lambda^4$ dependence of the molecular scattering cross section. By using the two colors, green and ultraviolet, it is possible to resolve the question of what altitude regions can be properly analyzed as pure Rayleigh scatter from which density and temperature can be directly determined.

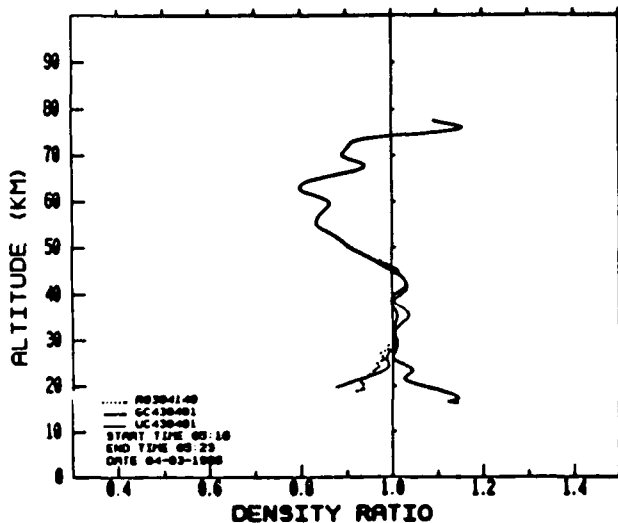


Figure 3. Comparison of the visible and ultraviolet lidar profiles.

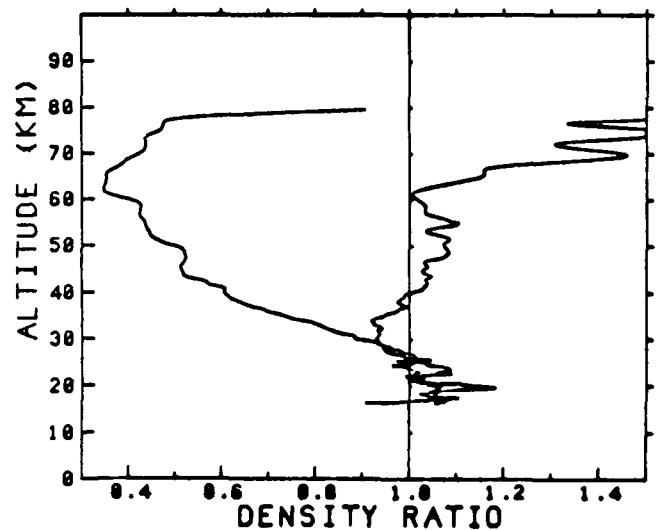


Figure 4. Comparison of the seasonal extremes measured on 14 February and 27 April.

Figure 4 shows an example of the extremes of the measured conditions. The profiles are shown as a density ratio to the US5A76 model. The profile of 14 February is typical of the lower winter density in the mesosphere and the higher density of the summer is represented by the 27 April profile. The high latitude atmosphere exhibits these large seasonal changes due to the change from complete darkness in winter to continuous sun in the summer. The solar control drives large changes in the circulation of the atmosphere in the polar region. Note that the region between 18 and 25 km exhibits intense narrow layers. This signal is due to the aerosols, polar stratospheric clouds, and volcanic dust.

The measurements conducted during this campaign represent the first serious attempt to compare lidar data and profiles from meteorological rockets. An example of the lidar profile obtained during the flight of a datasonde is shown in Figure 5. The size of the 1 σ error bar is shown on the lidar data with a spacing which indicates the length of the smoothing interval. The example exhibits rather strong wave activity, which was observed frequently in March. Cases of both excellent agreement and significant difference between the rocket and lidar results were obtained. Figure 6 shows an example of the planetary wave variations measured with the lidar during a major stratospheric warming which peaked on 20 February. The mean night profiles provide a graphic picture of the development of the stratospheric warming.

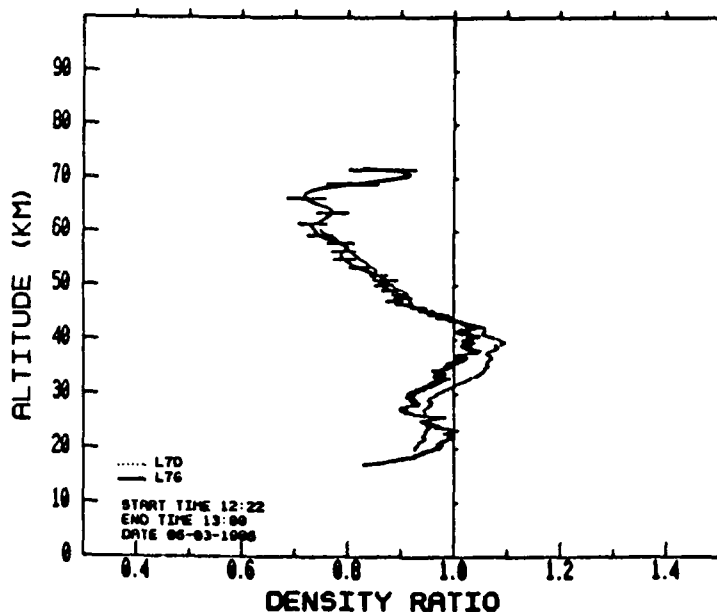


Figure 5. Comparison of the lidar profile from the 32 cm telescope detector(G) with a standard datasonde profile(D).

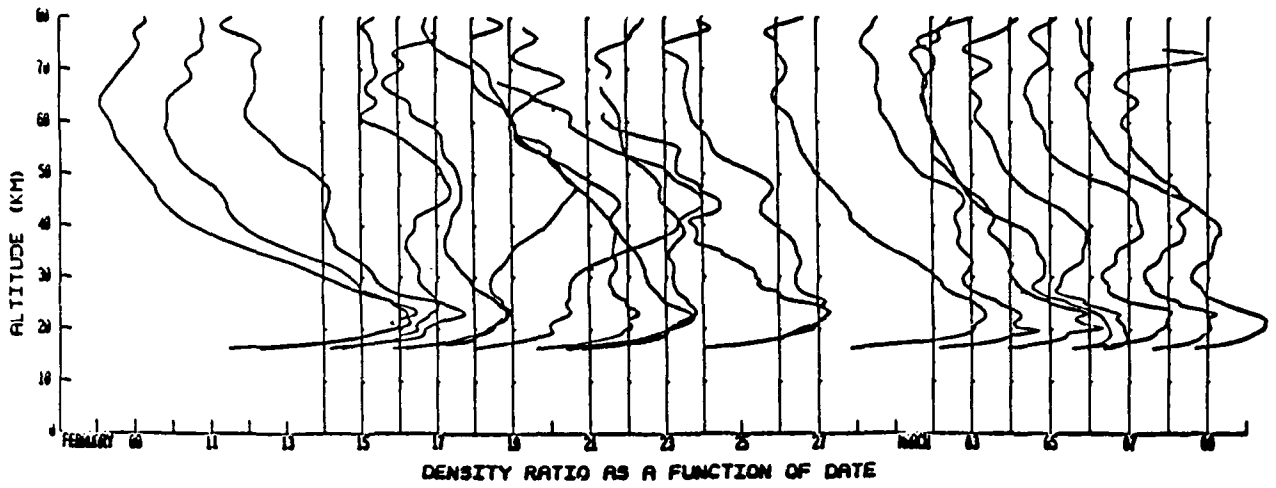


Figure 6. Sequence of mean night profiles of the density ratio to the USSA model which show the change in response to a major stratospheric warming.

GRAVITY WAVE DENSITY VARIATIONS INFERRED FROM GROUND BASED
RADAR MEASUREMENTS OF WINDS IN THE LOWER THERMOSPHERE.

Robert A. Vincent
Physics Department,
University of Adelaide,
Adelaide 5001,
Australia

1. INTRODUCTION

There are now a growing number of measurements of winds in the 80 to 100 km region of the upper atmosphere made with ground based radars operating at frequencies near 2 to 3 MHz (Vincent, 1984a). They have primarily been used to study variations of mean winds and tides in this region but recently climatologies of gravity wave motions have also started to appear (e.g. Meek et al., 1985; Vincent and Fritts, 1987). Through these and other studies it has become possible to understand better the fundamental role that gravity waves play in determining the mean circulation and thermal state of the upper atmosphere. While such radars have some advantages over other ground based systems, such as lidars, for continuous monitoring of the lower thermosphere, it is not always easy to convert the wave motions to other important wave parameters such as density. Nevertheless, as discussed below, it is possible with suitable care to develop a statistical description of the density perturbations and this is carried out for radar observations made at a mid-latitude site in Australia.

2. DATA ANALYSIS

The wind measurements were made with a spaced antenna radar at Adelaide, Australia (35°S, 138°E). Since the observations were made on an almost continuous basis over a 3 year period starting in November 1983, with a time resolution of about 10 minutes, it has been possible to study the temporal variations in wave activity over almost the full wave spectrum. Because the gravity wave spectrum covers a wide range of periods extending from a few minutes out to the inertial period, which at Adelaide is 21 hr, it is necessary to break the wave spectrum up into a number of bands. For convenience, and for ease of comparison with other studies, the data were filtered and analyzed in three spectral bands, (i) a low or quasi-inertial band covering the 8 to 24 hr period range, (ii) a medium-period band ranging from 1 to 8 hr, and (iii) a short-period band ranging from 20 min to 1 hr. In order to avoid contamination from the strong 12 and 24 hr tidal oscillations the analysis was carried out in 10 day blocks and the tidal winds calculated and

removed by harmonic analysis. The data were then processed to produce climatologies of wind and density perturbations.

3. CLIMATOLOGIES

(a) Winds

Figure 1 shows a contour plot of the mean square amplitude, $\overline{v'^2}$, due to gravity waves in the height range 80-98 km, where v'^2 is

$$\overline{v'^2} = (\overline{u'^2} + \overline{v'^2})$$

and u' and v' are the zonal and meridional perturbation velocities respectively. The wave amplitudes grow slowly, such that near 86 km the rms amplitude is about 30 ms^{-1} , a value which agrees well with a previous estimate based on a smaller amount of wind data taken in the years 1978-1981 at Adelaide (Vincent, 1984b). At 96 km the rms amplitude is about 40 ms^{-1} . Typically these values may vary by between plus or minus $15\text{-}20 \text{ ms}^{-1}$. At the lower heights, there is a pronounced semiannual variation in wave activity, with minima at the equinoxes whereas at upper levels there is a weaker semiannual variation with minima occurring near the solstices.

Comparisons of u' and v' shows that v' is larger than u' and that the covariance term, $u'v'$, is generally non-zero. These characteristics show that the wave field is anisotropic, such that a significant fraction of the wave motions have a preferred direction of orientation (Vincent and Fritts, 1987). Using the 'Stokes Parameters' approach discussed in their paper it is found at the lower frequencies, that up to 50% of the wave motions tend to lie in the NW/SE quadrants in summer and to have a preference for NS directions in winter.

(b) Density Variations

The conversion of the wind variations to other wave quantities, such as density, can in principal be easily made by using the so-called polarization relations which relate one observed quantity to another (Hines, 1960, Gossard and Hooke, 1975). The fractional density perturbations are given in terms of the wind perturbations by

$$\left[\frac{\delta\rho}{\rho_0}\right]^2 = \frac{(\omega^2 - f^2)}{(\omega^2 + f^2)} \frac{N^2}{g^2} \overline{v'^2} \quad (1)$$

Here ω is the intrinsic frequency, f is the inertial frequency, N is the Vaisala-Brunt frequency and g is the acceleration due to gravity. Unfortunately, the use of this expression is not

straightforward since intrinsic frequency (i.e. the frequency relative to the background wind) must be used, rather than the frequency observed in the ground based frame of reference.

One way to estimate ω , is to make use of the polarization relation between v' and u' , which for a wave propagating horizontally at an azimuth θ , measured clockwise from east, is

$$v' = \frac{(\tan\theta - i a)}{(1 - i a \tan\theta)} u'$$

where $a=f/\omega$. This means that gravity waves are in general elliptically polarized such that the ratio of the amplitude of the wind component along the direction of motion to the amplitude of the transverse component is ω/f . A statistical analysis based on the Stokes Parameters approach shows that rather fortuitously, most of the waves tend to be propagating horizontally at right angles to the prevailing winds, so that at this location at least, the intrinsic and ground based frequencies are very similar.

Another subtlety that must be borne in mind before (1) can be applied is that a temperature model has to be chosen before the Vaisala-Brunt frequencies can be calculated. In the present case, the recent model for the southern hemisphere given by Groves (1987) was used to calculate N .

A contour plot of the inferred rms percentage density variations are shown in Figure 2. The percentages vary from values near 5% at heights near 80 km upto values near 8-10% at heights near 100 km. This suggests that at mid-latitudes gravity waves cause the atmospheric density to fluctuate by up to at least 5-10% around its mean value in the lower thermosphere. Taking into account the natural variability of the wind fluctuations suggests that these mean fractional densities will be uncertain by about 2-3%. A further cause of uncertainty is the possibility of systematic errors in the temperature model used to derive N .

4. DISCUSSION

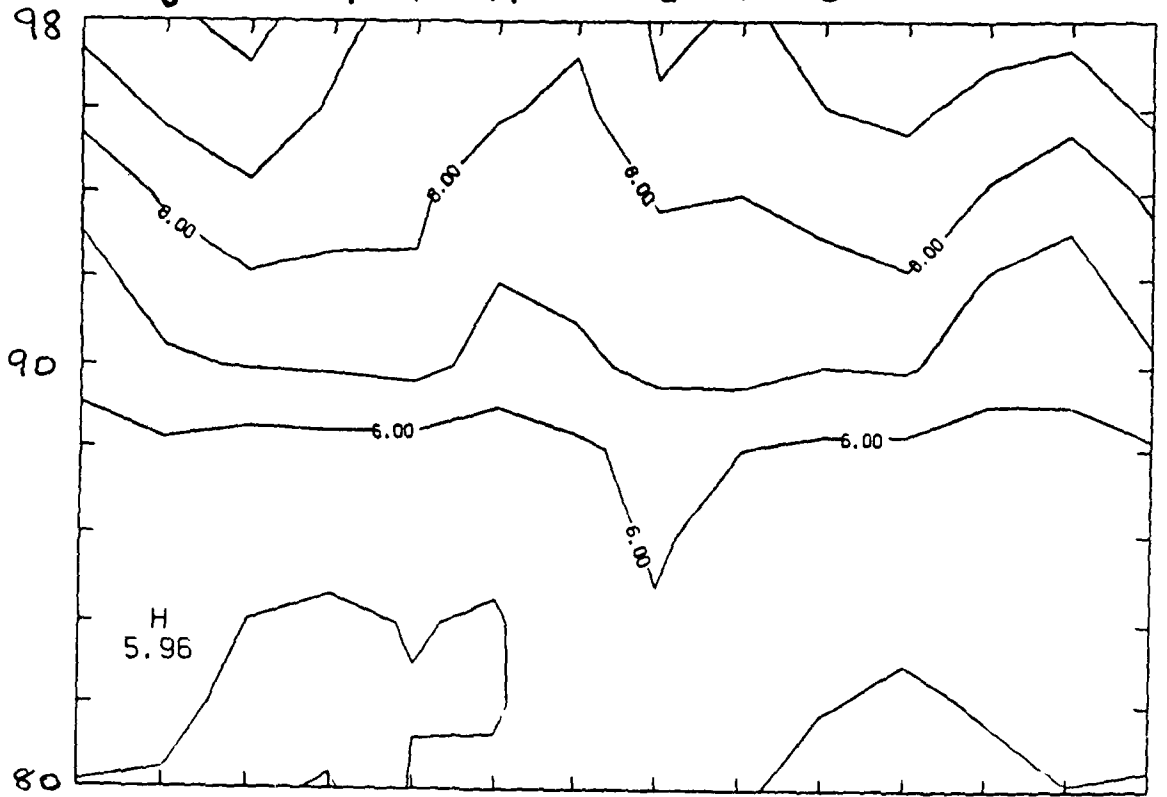
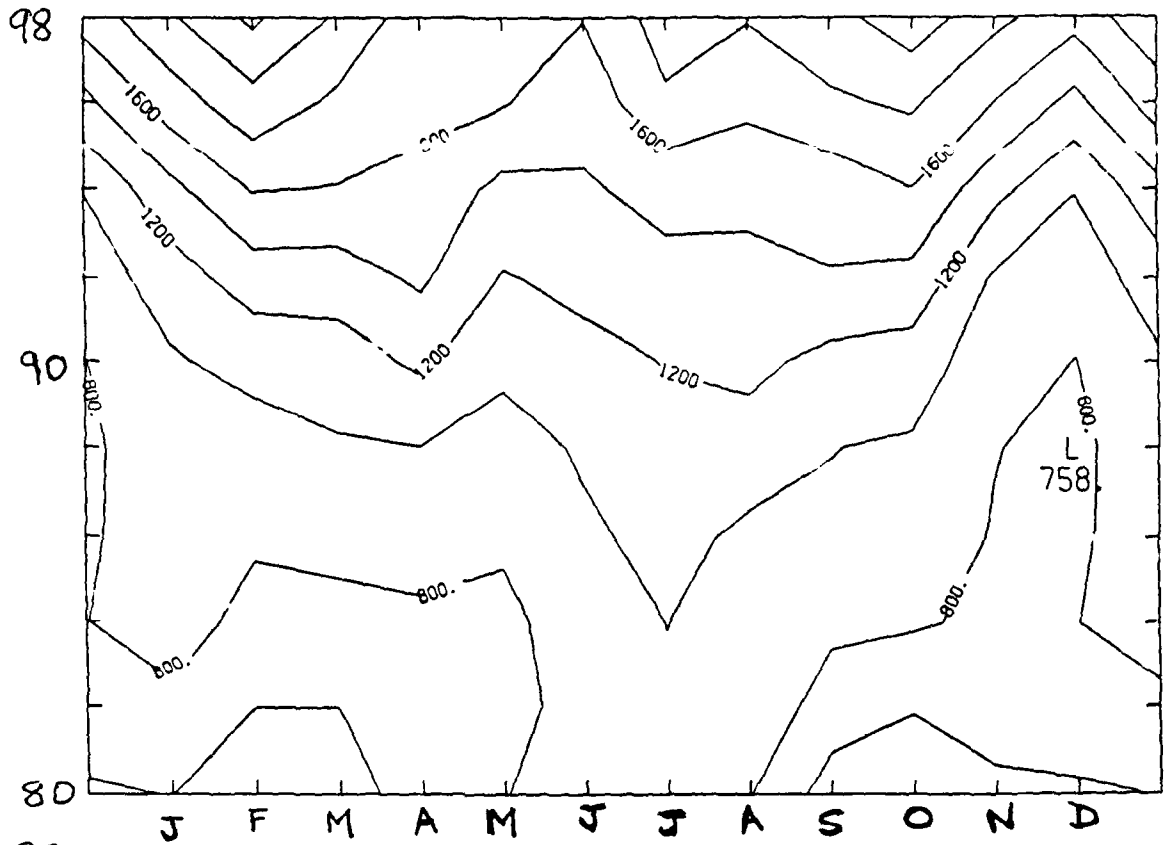
The present analysis shows some of the strengths and weaknesses of using radar wind measurements to infer wave parameters such as density. The excellent time and height resolution of the radars plus their ability to run continuously means that they can be used to derive climatologies of wave activity. However, the conversion of wind data to relative density requires information about the intrinsic frequencies of the waves, information which is not easy to obtain with a ground based system. A temperature and density model is also required to produce absolute density variations.

References

- Gossard, E. E. and Hooke, W. H.:1975, Waves in the Atmosphere. Developments in Atmospheric Sciences. Vol. II. Elsevier Scientific, 456pp.
- Groves, G. V.:1987 Modelling of atmospheric structure, 70-130 km, AFGL Surveys in Geophysics, AFGL-TR-87-0226, AD A201077.
- Hines, C. O.: 1960, Can. J. Phys., 38, 1441.
- Meek, C. E., Reid, I. M., and Manson A. H.:1985, Radio Sci., 20, 1383.
- Vincent, R. A.:1984a, J. Atmos. Terr. Phys., 46, 961.
- Vincent, R. A.:1984b, J. Atmos. Terr. Phys., 46, 119.
- Vincent, R. A. and Fritts, D. C.:1987, J. Atmos. Sci., 44, 748.

FIGURE CAPTIONS

- Fig. 1 Contours of mean square gravity wave amplitudes for the height range 80-98 km.
- Fig.2 Contours of percentage gravity wave density variations.



4.4 INCOHERENT SCATTER DENSITY

W. L. Oliver

M.I.T. Haystack Observatory

VG 1. Two primary neutral density measurements are made with the incoherent scatter radar technique: N_2 from about 80 to 120 km and O from about 200 to 500 km altitude. The N_2 density is determined directly from the measured ion-neutral collision frequency; the O density is determined through the joint consideration of ionospheric measurements and a theory of ionosphere-atmosphere interaction. Both of these measurements are limited to daytime.

VG 2. Several of the basic parameters measured by incoherent scatter radar: ion and electron temperatures, ion composition, ion-neutral collision frequency.

VG 3. The incoherent scatter spectrum, showing the effects of increasingly strong ion-neutral collisional effects. These collisional effects die out above about 120 km altitude as the neutral density decreases. Below about 90 km the spectrum is so strongly dominated by collisions that it becomes Gaussian in shape; then it becomes impossible to distinguish between temperature and collision effects and only a collision-frequency/temperature ratio is determinable. The degree of collisional effect is dependent upon the ratio of the radar operating frequency and the ion-neutral collision frequency, such that the region of such density determination will be translated several kilometers upward or downward according to the radar operating frequency.

VG 4. Example of the neutral density profile measured at Arecibo, assuming the CIRA 1972 temperature profile and ion masses as indicated. Negative ion effects contaminate the results at the lower altitudes.

VG 5. The collection of ion-neutral collision frequency results for measurements covering a full day at Arecibo. Much of the data spread results from real geophysical variability.

VG 6. Example of daytime measurement of neutral temperature and ion-neutral collision frequency throughout a day at Millstone Hill.

VG 7. Daily average neutral temperature and collision frequency profiles for three different days as measured at Millstone Hill.

VG 8. The first incoherent scatter density measurements, from 20 years ago.

VG 9. Daily averages of neutral density made at different altitudes above Saint Santin during experiments spanning 8 years.

VG 10. Mean density profiles for the 4 seasons, computed from the data in VG 9.

VG 11. Seasonal amplitudes and phases of the density, computed from the data in VG 9.

VG 12. Solar dependence of the density, computed from the data in VG 9.

VG 13. Comparison of the seasonal variation of neutral density at 100 km altitude as measured at Saint Santin with that of the Jacchia 1971 model.

VG 14. Comparison of the radar density (measured at 100 km and extrapolated to 400 km altitude using the radar-measured temperature profile) with several model densities.

VG 15. Upper atmospheric temperature profiles, illustrating the method by which the neutral temperature and density are deduced from the ionospheric temperatures. The T_n profile represents the neutral temperature computed from the T_e and T_i profiles (measured) if we choose the correct neutral density profile for use in the ion-neutral heat transfer equations. The T_n' and T_n'' profiles represent the neutral temperatures that one would compute if he were to choose a neutral density exactly twice or half, respectively, of the correct density. As we know from theory that the neutral temperature profile should be asymptotic at high altitudes, we then have a means of discerning both the neutral temperature and neutral density in the upper thermosphere by adjusting our neutral density assumption until the deduced neutral temperature profile becomes asymptotic.

VG 16. Comparison of radar-measured densities at 400 km altitude (dots) with a simultaneous satellite measurement (x), and two models, showing the excellent agreement during the middle of the day but discrepancies normally seen at other times of day.

VG 17. Seasonal variation of midday density at 400 km altitude as measured at Saint Santin compared with two models.

VG 18. The local-time/latitude behavior of exospheric temperature and neutral density at 400 km altitude as measured from Millstone Hill during the 7-day ETS campaign of 17-24 September 1984.

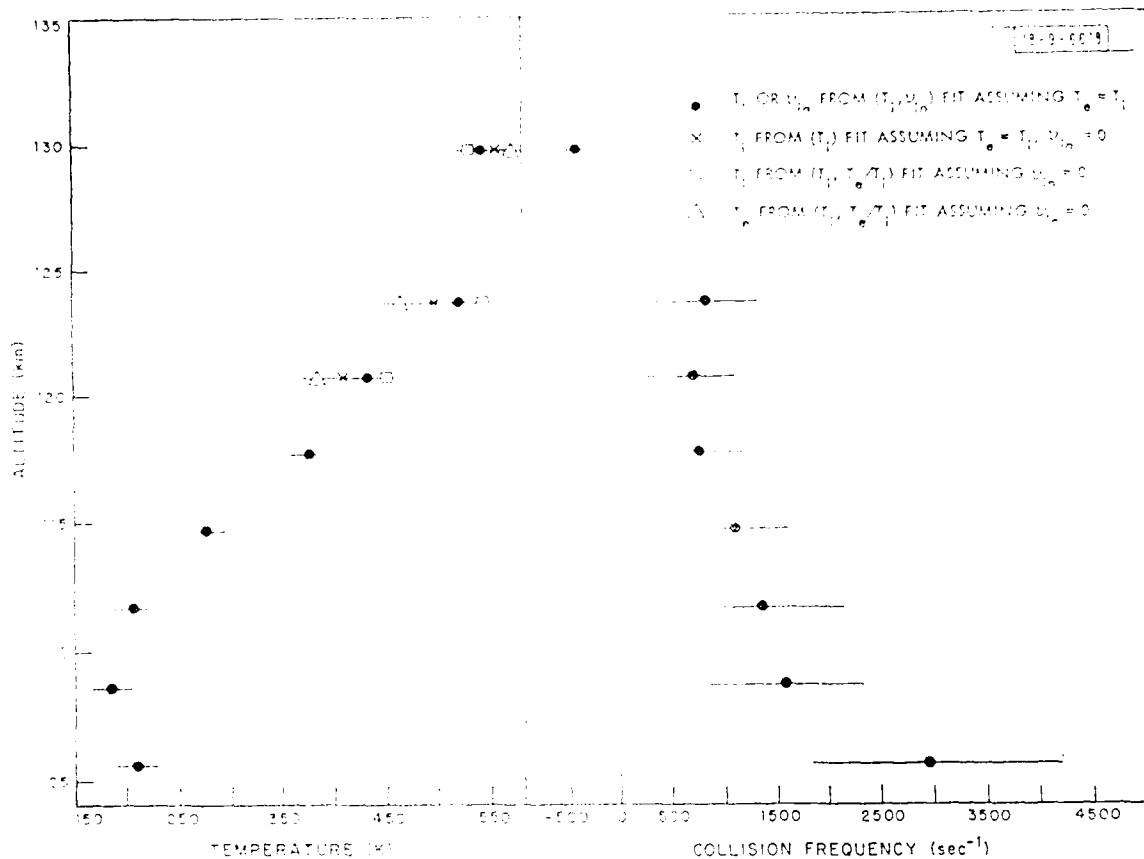
Two Primary Density Measurements

N ₂	80 - 120 km altitude	ion-neutral collision frequency
O	200 - 500 km altitude	ionosphere measurements plus theory of ionosphere/atmosphere interaction

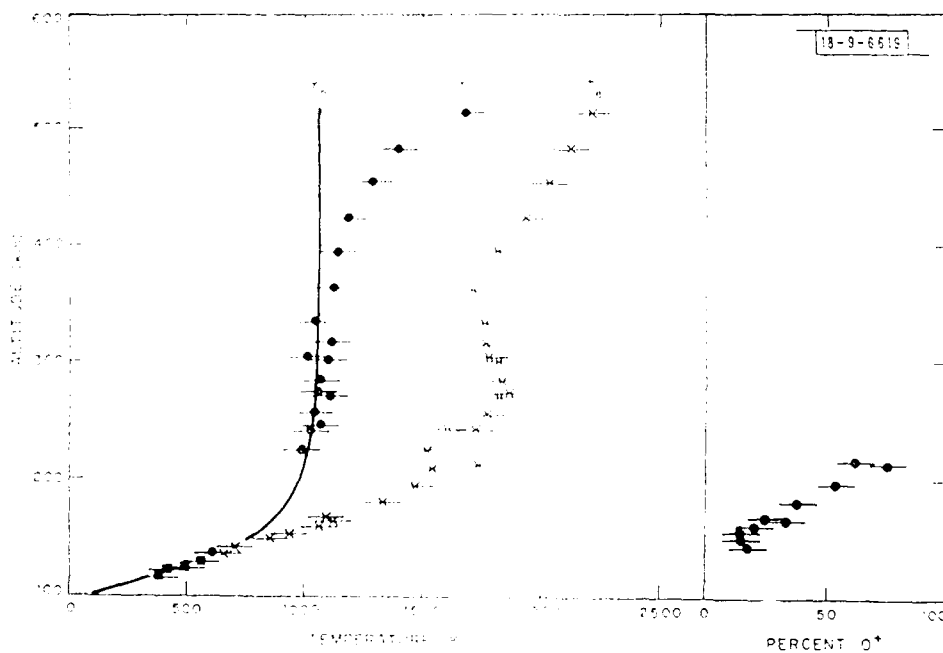
Temperature Height Profile Measurement

Extrapolates density measurements to other altitudes

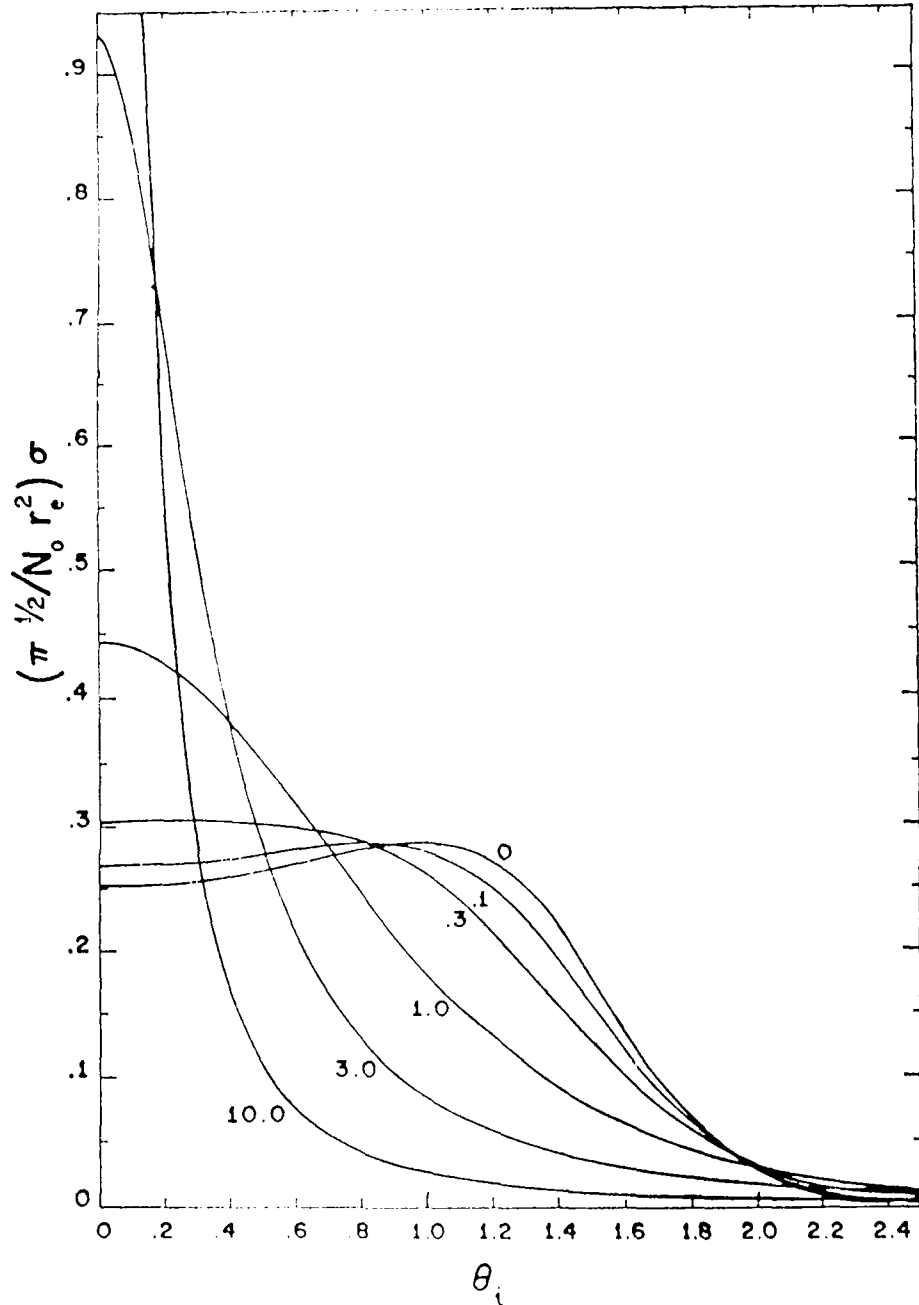
Daytime Measurements Only



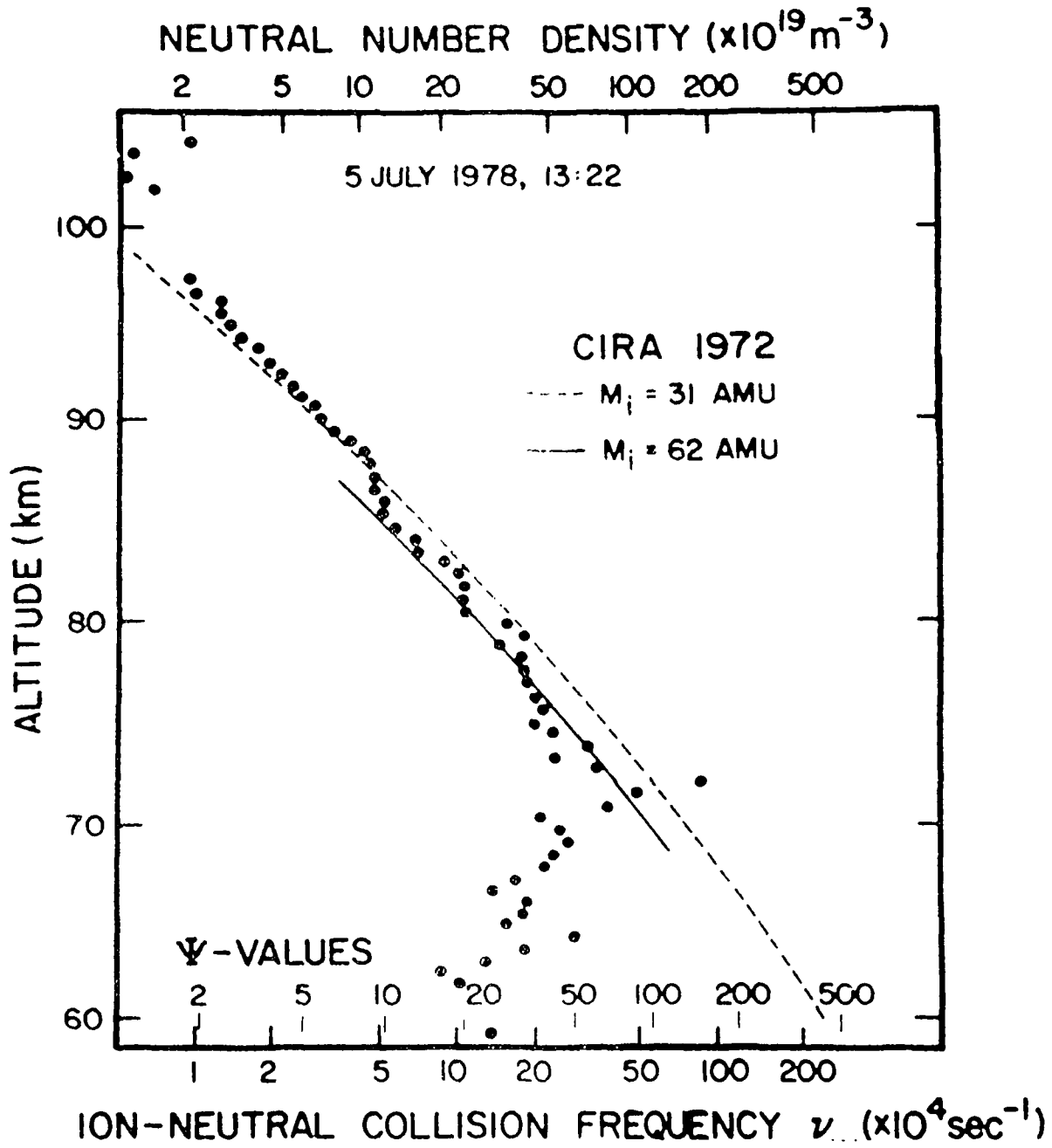
Lower F Mode results on 18 September 1974, 1735-1747 UT.

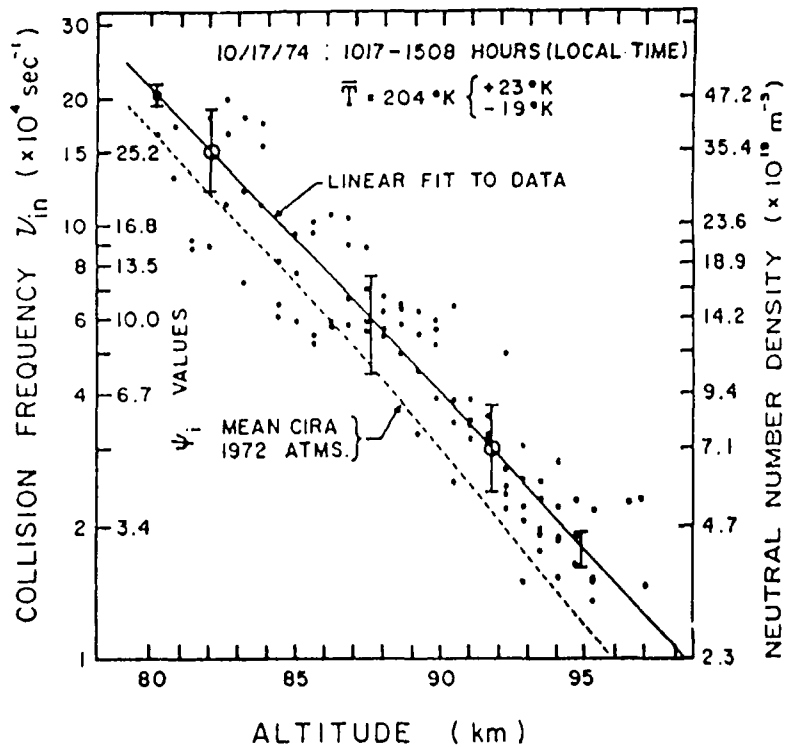


Profile analysis for data on 18 September 1974, 1731-1800 UT.
 Thermosphere results yield $T_e = 1751 \pm 17$ K, $s = 0.0262 \pm 0.0041$ km⁻¹;
 $T_{120} = 408 \pm 13$ K, and $(O^+)_{120} = 2.47 \pm 0.19 \times 10^8$ cm⁻³.



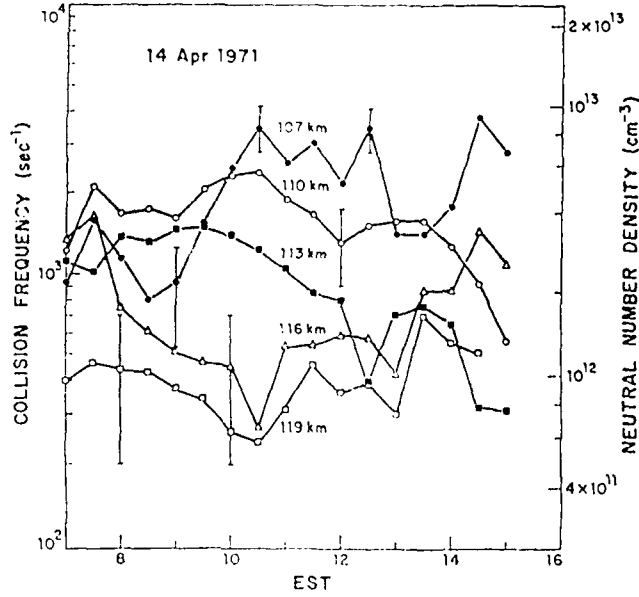
The power spectrum of the scattered signal for no magnetic field and various values (indicated on the curves) of the normalized ion collision frequency ψ_i . ψ_i is taken to be $\psi_i/10$. θ_i is the normalized Doppler shift defined by $\theta_i = (\omega/k) (m_i/2KT)^{1/2}$. The full curve is symmetric about $\theta_i = 0$.



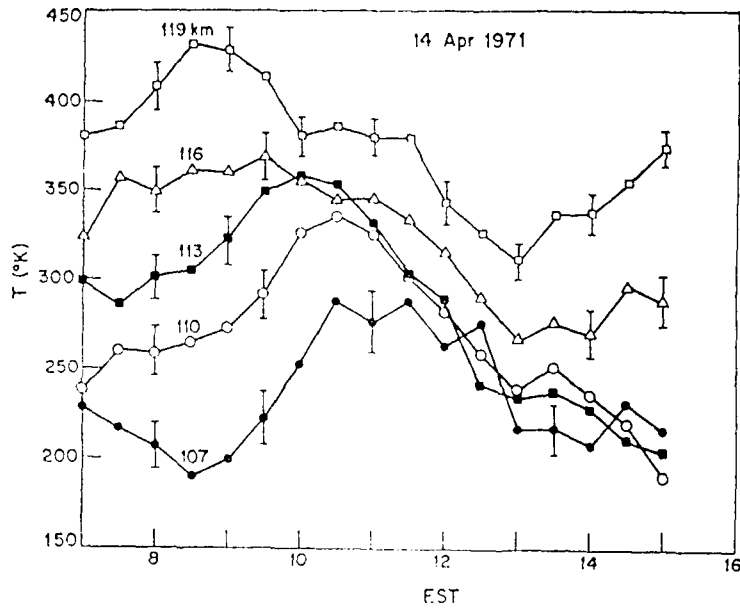


Collision frequency (ν_{in}), approximate ψ_i values, and inferred neutral number densities are plotted on the ordinate (logarithmic scale) versus altitude on the abscissa (linear scale). The solid line is the best linear approximation to the 96 data points and can be compared with the model atmosphere shown as the dashed line. The extremes of temperature in the model atmosphere over the altitude range shown is from 195°K at 80 km to 183°K at 90 km and to 193°K at 97 km with a mean of 190°K over the entire range. The observations indicate an atmosphere which is both hotter and denser than the model atmosphere.

Daily oscillations of the mid-latitude thermosphere



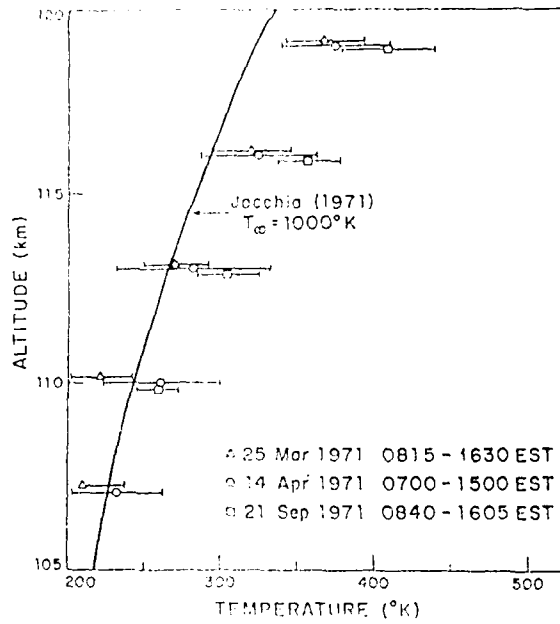
Collision frequency measurements on 14 April 1971 at Millstone Hill converted to neutral number density.



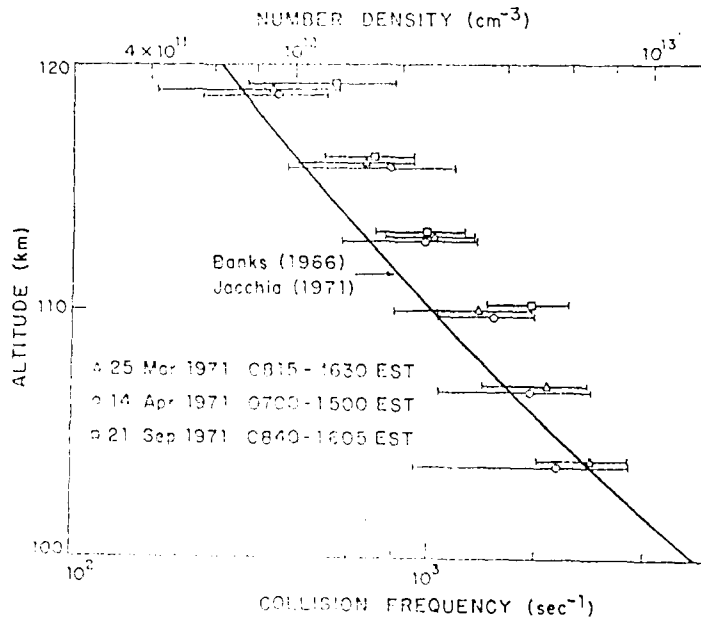
Temperature measurements at Millstone Hill on 14 April 1971.

VG 7

J. E. SALAH

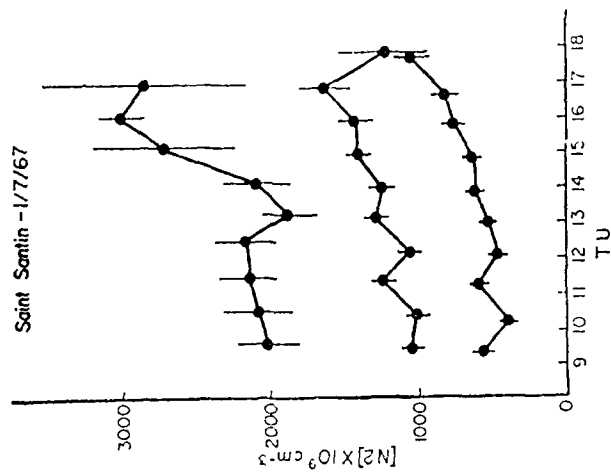


Average daytime temperature height profile in the lower thermosphere.

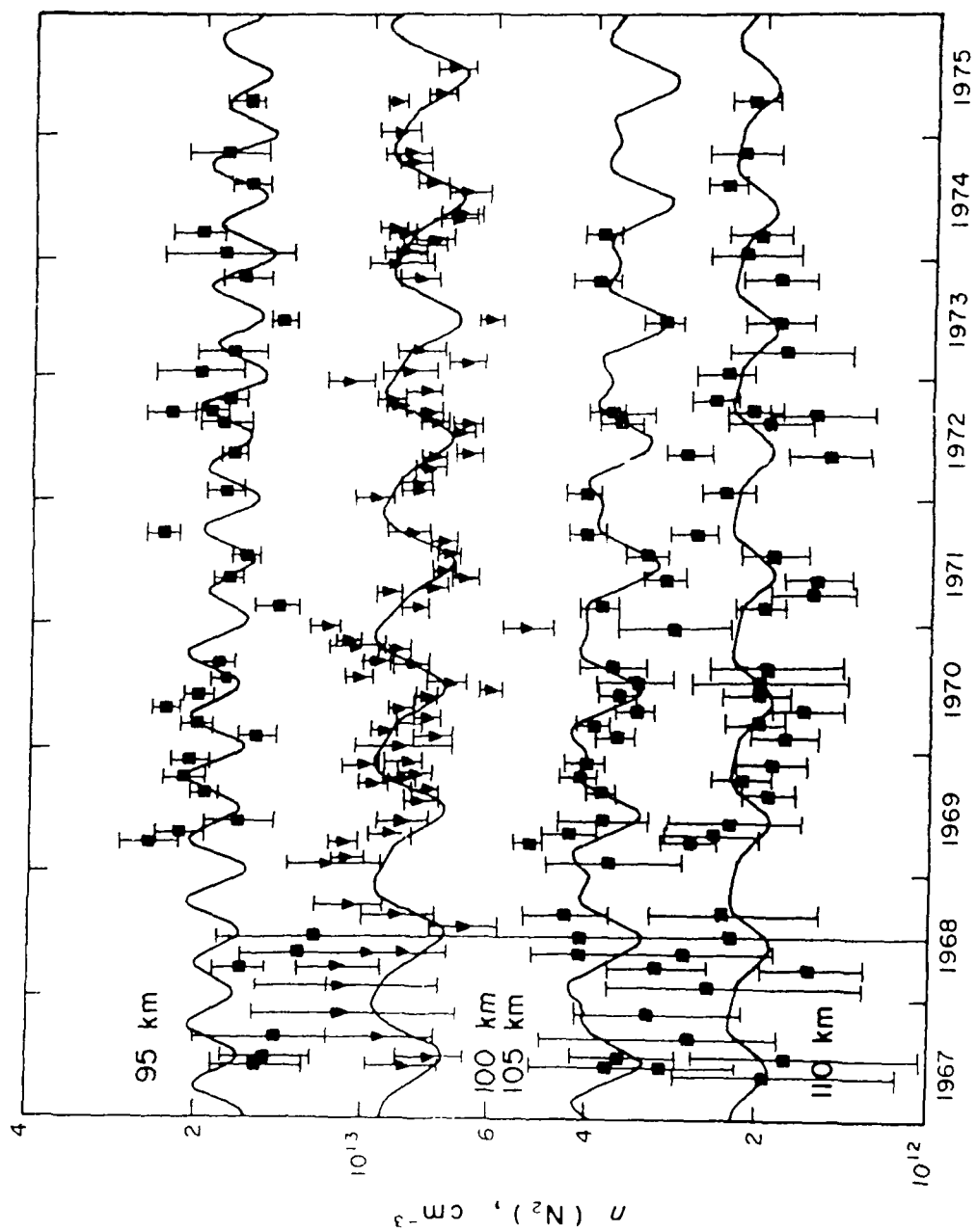


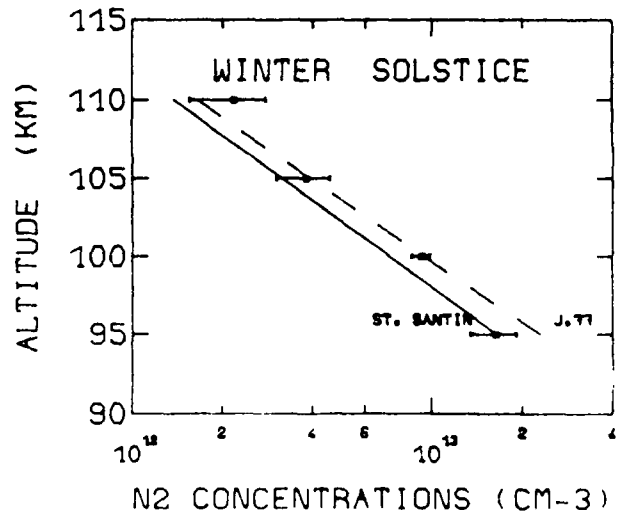
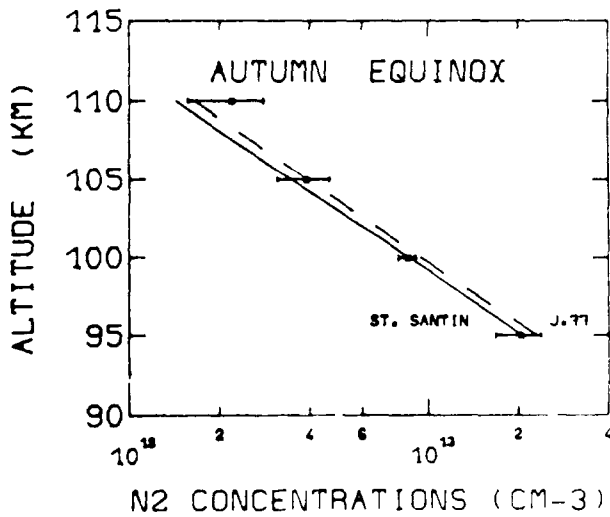
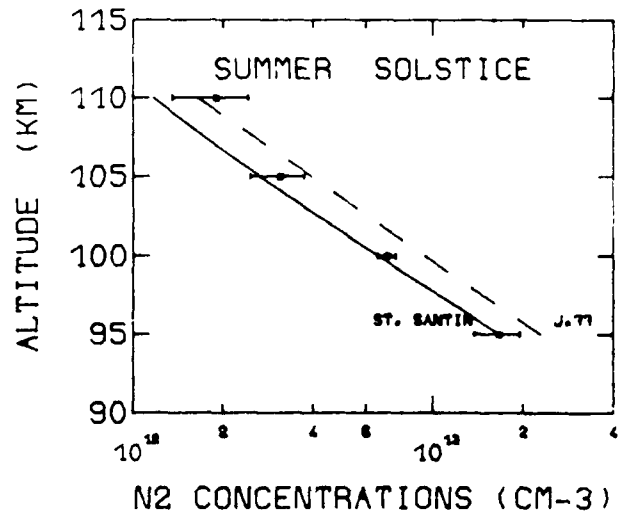
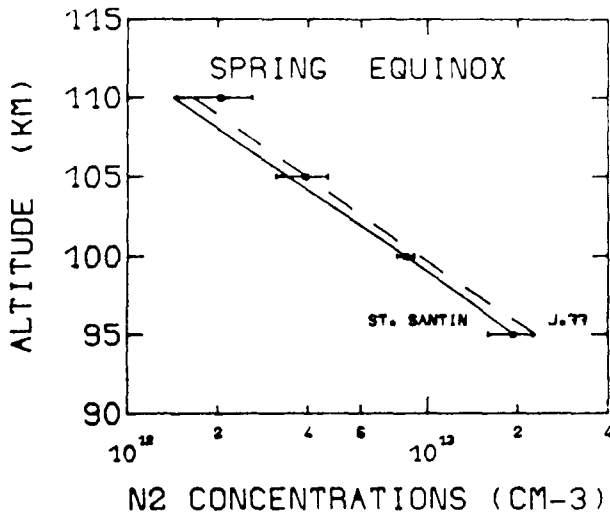
Average daytime collision frequency and neutral density height profiles.

P. WALDTEUFEL



VARIATION DIURNE DES DENSITÉS OBSERVÉES À 105, 100 ET 95 km LE 1/7/67.





The seasonal fit of observed molecular nitrogen concentrations leads to characteristic values which are shown for $\bar{F}_{10.7} = 125$ as a function of altitude. The error bars are computed from the uncertainties on the coefficients of equation (2). The full lines correspond to mixing distributions with the temperature profiles of Fig. 7 and the dashed lines represent Jacchia's (1977) values.

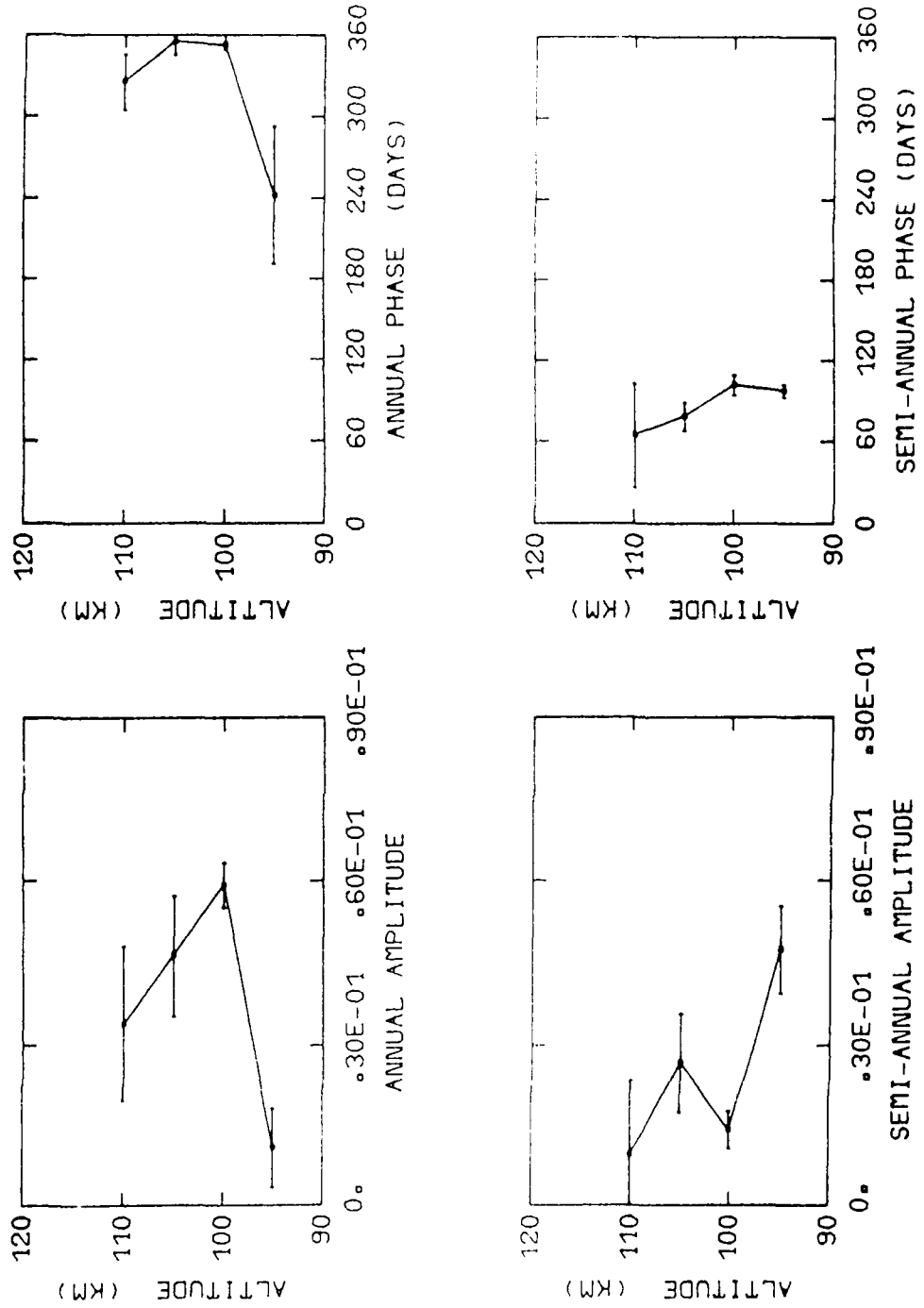


Fig. 6a.- Same as Fig. 5a for molecular nitrogen given by equation (2).

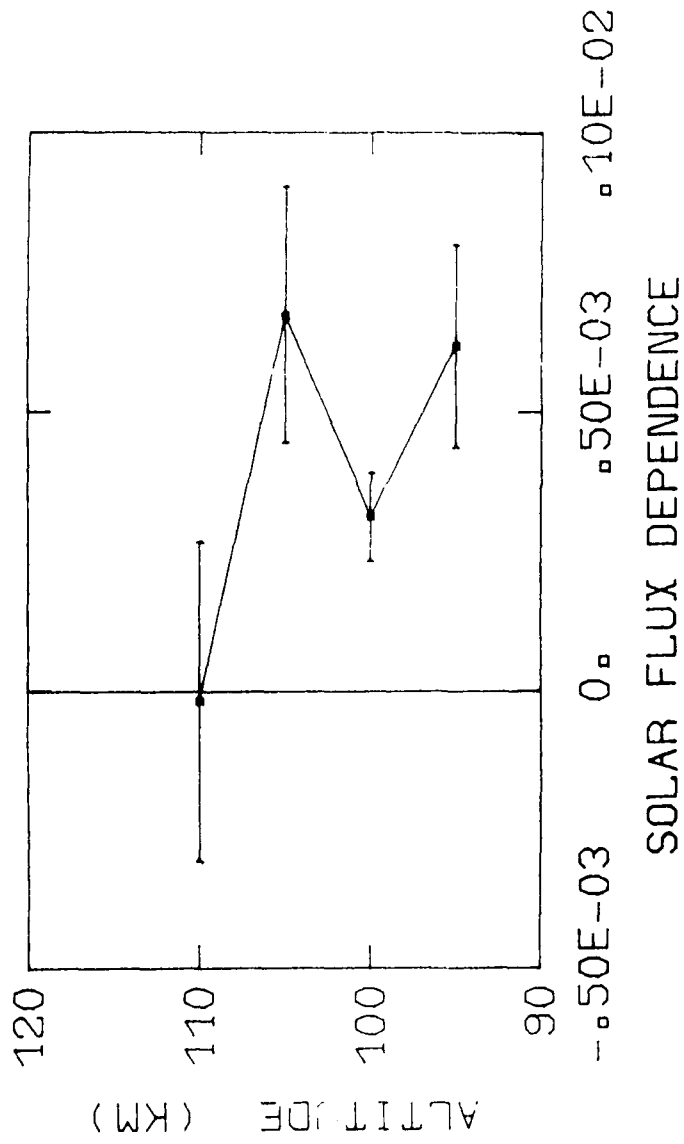
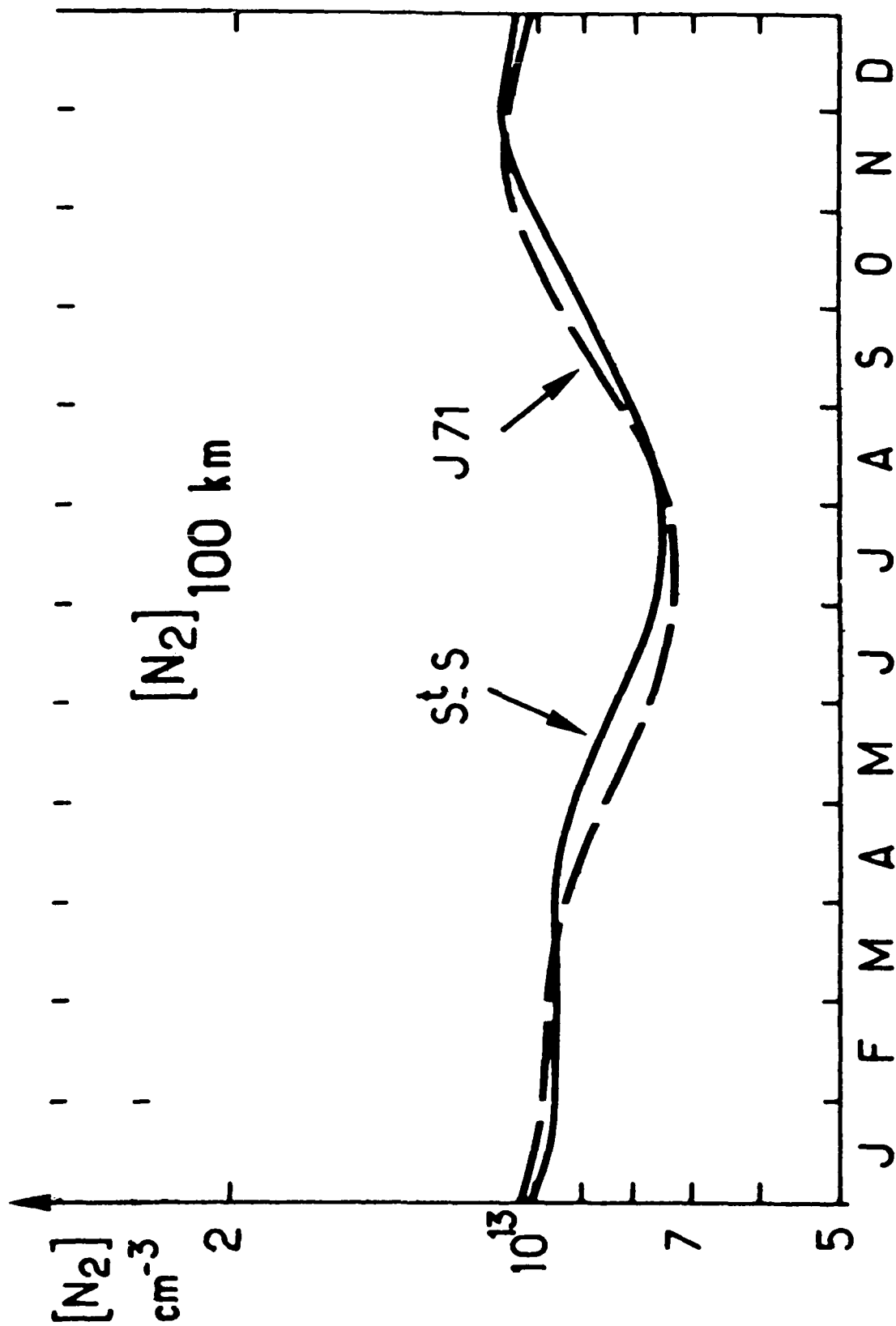
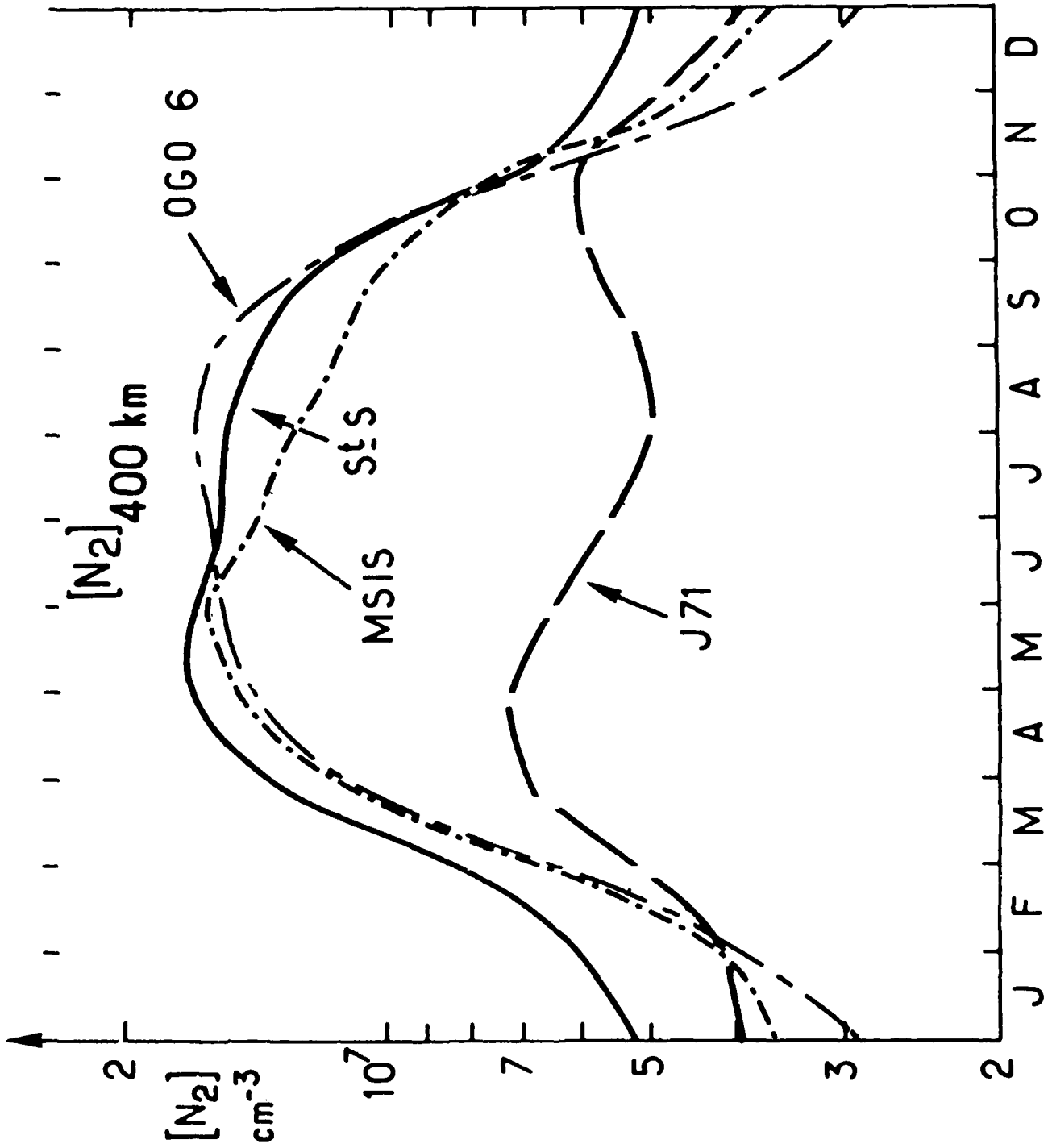
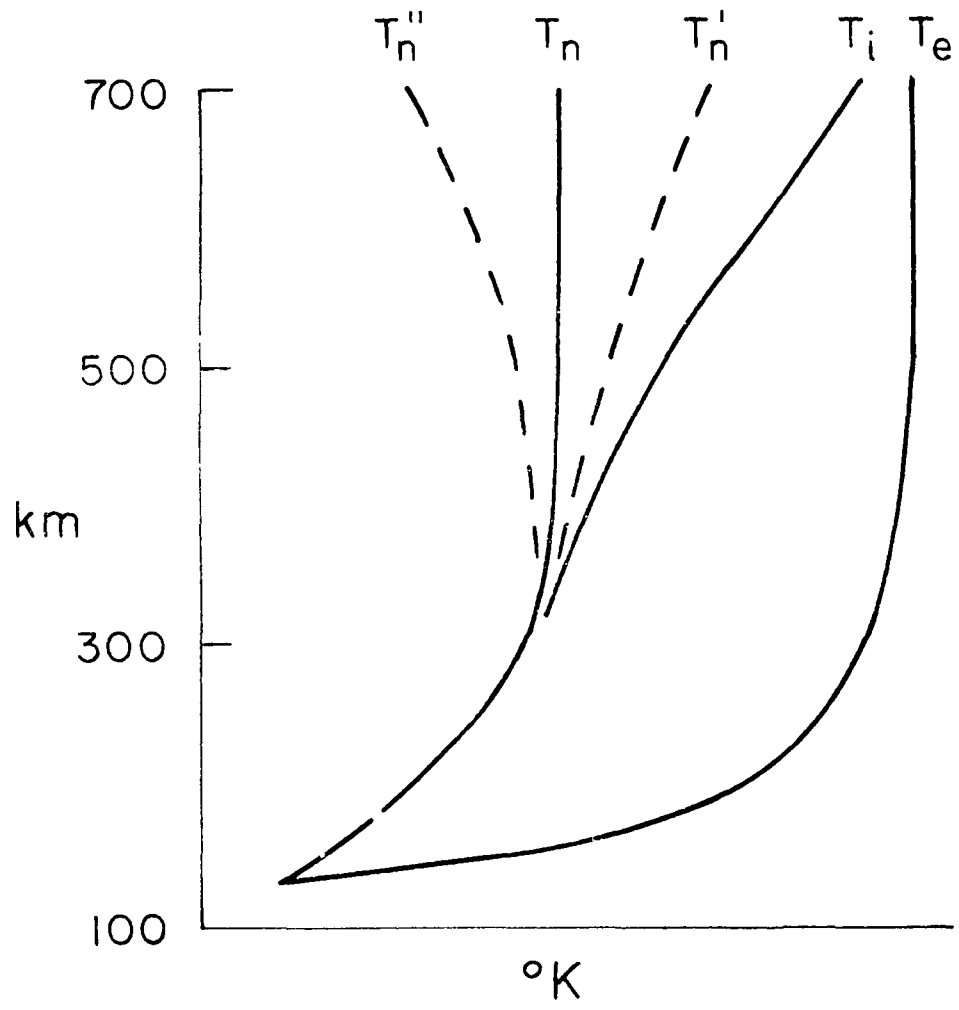
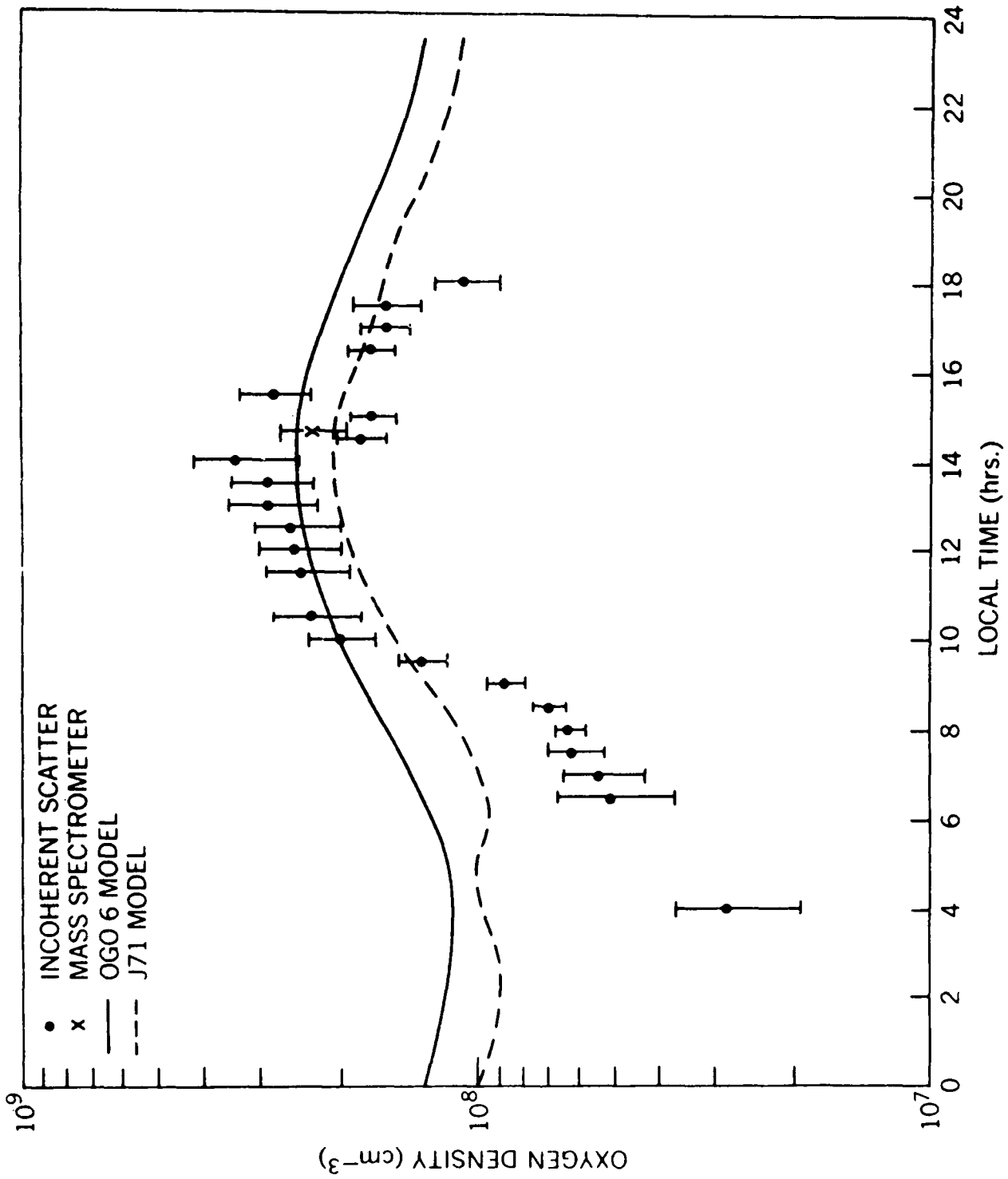


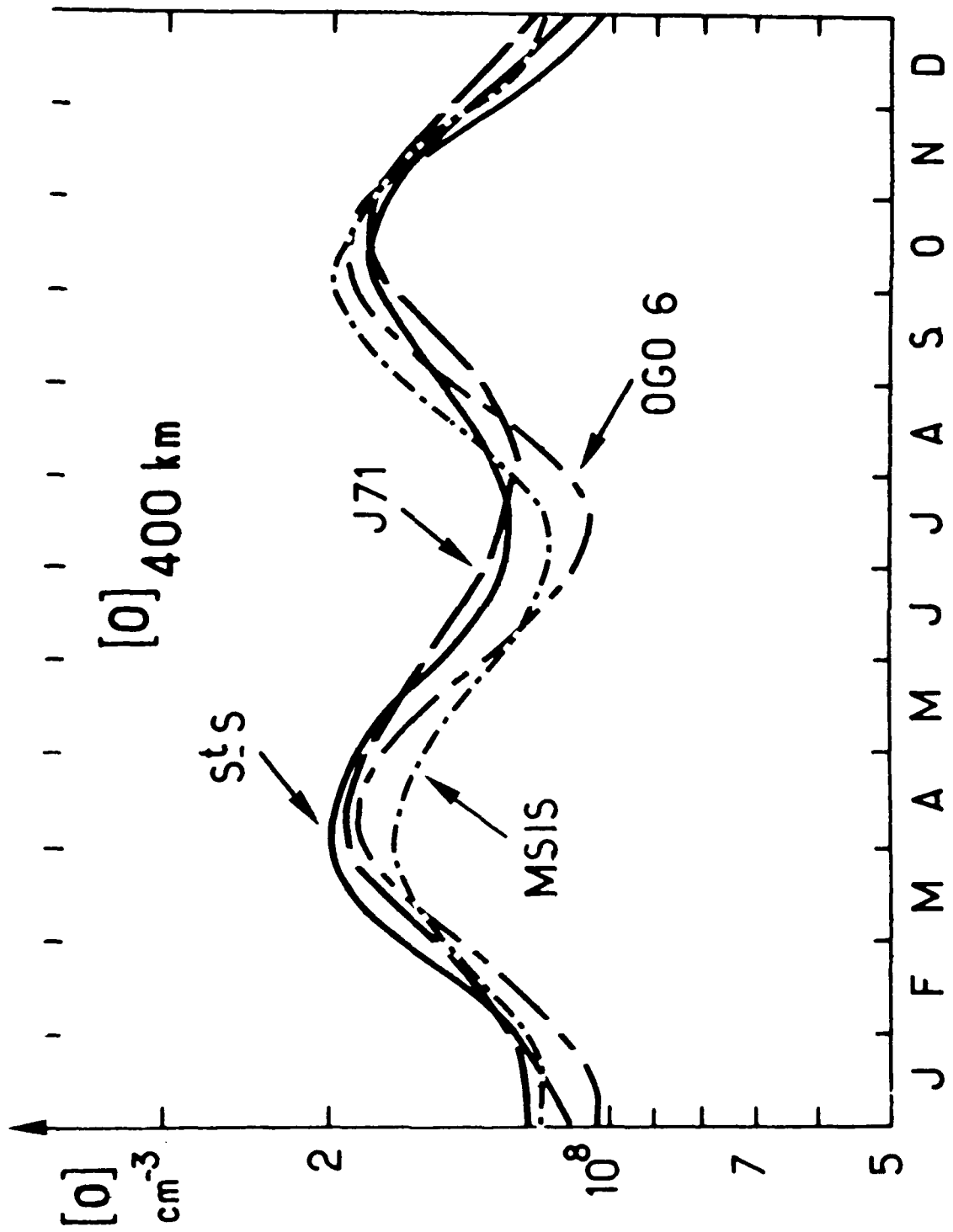
Fig. 6b: - Same as Fig. 5b for molecular nitrogen given by equation (2).





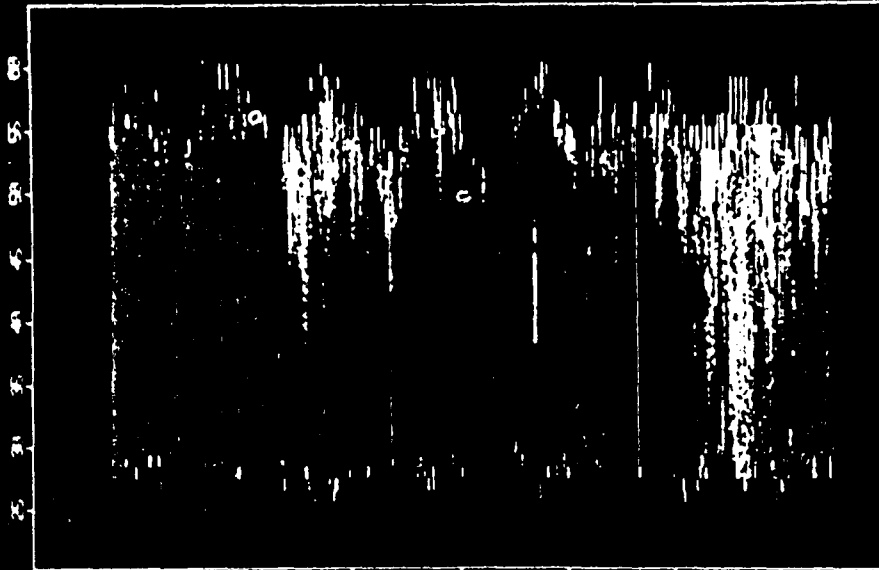






HILLSTONE HILL

17-24 SEPTEMBER 1984



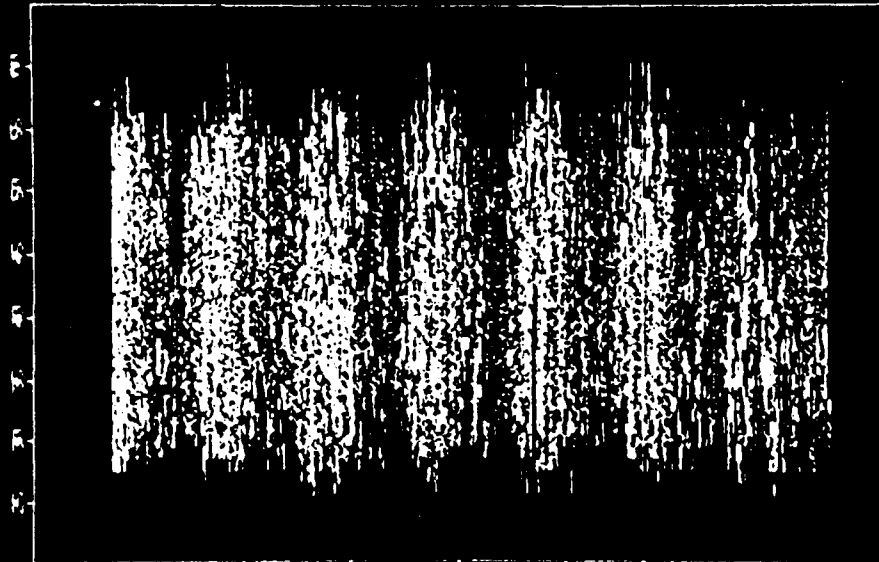
HOURS SINCE 00 UT ON 17 SEPTEMBER
EXOSPHERIC TEMPERATURE VERSUS UT AND GEOMETIC LATITUDE

HELVIN

1750
1700
1650
1600
1550
1500
1450
1400
1350
1300
1250
1200
1150
1100
1050
1000
950
900
850
800
750
700
650
600
550
500

HILLSTONE HILL

17-24 SEPTEMBER 1984



HOURS SINCE 00 UT ON 17 SEPTEMBER
ATOMIC OXYGEN DENSITY AT 400 KM VERSUS UT AND GEOMETIC LATITUDE

011-3
10-8

3.5
3.3
3.1
2.9
2.7
2.5
2.3
2.1
1.9
1.7
1.5
1.3
1.1
0.9
0.7
0.5
0.3
0.1
-0.1
-0.3
-0.5
-0.7
-0.9
-1.1
-1.3
-1.5
-1.7
-1.9
-2.1
-2.3
-2.5

**INCOHERENT SCATTER MEASUREMENTS OF
HIGH-LATITUDE LOWER-THERMOSPHERIC
DENSITY AND DYNAMICS**

by

R. M. Johnson and V. B. Wickwar

Geoscience and Engineering Center

SRI, International

333 Ravenswood Avenue

Menlo Park, CA 94025

Presented at the Atmospheric Density and Aerodynamic Drag Workshop
Air Force Geophysics Laboratory, Hanscom AFB, Massachusetts
October 20, 1987

Introduction

The incoherent-scatter technique is unique in its broad capabilities for upper-atmospheric and ionospheric research. From the electromagnetic radiation backscattered from the ionosphere, an extensive set of parameters descriptive of the physical, dynamical, and chemical state of the upper atmosphere and ionosphere can be determined. This technique allows an extended altitude region to be probed simultaneously. Depending on the observing mode, measurements over a wide range of latitudes and longitudes can be made continuously for extended intervals (up to several days) with time resolution ranging from seconds to minutes.

The return signal spectrum and auto-correlation function (ACF) obtained from the E region allow several quantities to be determined, including the electron density, the electron and ion temperatures, the ion velocity, and the ion-neutral collision frequency. Figure 1 shows an example of some of these measured quantities on a day of considerable geomagnetic activity in the auroral zone at Chatanika, Alaska (65°N). These quantities, in conjunction with atmospheric and ionospheric models, can be used to determine other parameters important at E-region heights. These include ionospheric conductivities, energy deposition by auroral particles, Joule heating, electrojet currents, and neutral wind velocity, temperature, and density.

Of particular interest here is the calculation of neutral density and winds in the lower thermosphere. Both of these calculations depend critically on the ion-neutral collision frequency, ν_{in} , which is non-negligible at these heights. The ion-neutral collision frequency can be measured directly from the changes in shape of the ACF that result from collisions between ions and neutrals. Alternatively, it can be estimated by using atmospheric and ionospheric models. Determination of the neutral winds at a given altitude additionally requires knowledge of the ion velocity at that height and the electric field vector imposed from above, both of which are measured directly by the radar.

In the next section, the calculation of ν_{in} and the total neutral number density N from incoherent scatter radar data will be discussed. The following section addresses the calculation of the neutral wind velocity \bar{u} and its dependence on ν_{in} . The importance of lower thermospheric tides and geomagnetic activity effects at high latitude is also discussed. Finally, the potential for improvements on the determination of N with this technique is discussed.

Ion-neutral collision frequency and neutral density

Determination of ν_{in} from incoherent-scatter measurements proceeds from an analysis of the scattered signal ACF. As collisions of ions with neutrals become more frequent with decreasing altitude, the characteristic two-humped form of the collisionless incoherent-scatter spectrum changes into a Lorentzian profile [Dougherty and Farley, 1963]. Over the altitude range in which this shape transition occurs, corresponding roughly to the lower thermosphere, T_i , T_e , and ν_{in} can theoretically all be calculated by a least-squares fitting procedure, although usually only two parameters can be fitted simultaneously with success [Lathuillere et al., 1983]. Below those altitudes, the ACF shape at upper-mesospheric heights is a function of the ratio of the T_i to ν_{in} ; additional assumptions are therefore required to obtain ν_{in} from the measurement [Tepley et al., 1981; Flå et al., 1985]. Additionally, the ACF broadens to the point that ν_{in} cannot be determined efficiently from a single-pulse or multipulse measurement. Instead, a pulse-to-pulse technique must be employed [Mathews, 1976; Mathews, 1978; Tepley and Mathews, 1978; Tepley et al., 1981; Kofman et al., 1984]. As a result, the method of data acquisition and analysis, as well as the requisite assumptions differ in the upper mesosphere and the lower thermosphere. Our interest here is in the lower thermosphere, where ACFs formed from single-pulse or multipulse experiments can be analyzed to obtain ν_{in} . This technique has been used by Wand and Perkins [1968], Salah [1974], Salah et al. [1975], Wand [1976], Schlegel et al. [1980], Wickwar et al. [1981], Lathuillere et al. [1983], Kofman and Lathuillere [1985],

Flå et al. [1985], Kofman et al. [1986], and Huuskonen [1986] at Arecibo, Millstone Hill, Chatanika, and EISCAT.

One difficulty encountered in determining ν_{in} from incoherent-scatter measurements arises in the theoretical specification of collision process in incoherent-scatter theory [Dougherty and Farley, 1963; Tanenbaum, 1968; Waldteufel, 1970a,b; Hagfors and Brockelman, 1971]. Depending on the treatment of collisions in the derivation of the incoherent-scatter spectrum, slight differences result in the dependence of the ACF on ν_{in} . Hagfors and Brockelman [1971] suggested that, as a result, ν_{in} obtained using the Dougherty and Farley [1963] theory would be slightly underestimated, and T_i slightly overestimated. However, in a comparison of the two theories, Salah et al. [1975] found that in the 107 to 119 km height range at Millstone Hill, the collision frequencies determined with the Dougherty and Farley model exceeded those of Hagfors and Brockelman at the lowest levels by up to 30%, attaining better agreement as altitude increased. Ganguly and Coco [1987] compared the theoretical results of Dougherty and Farley [1963] and Waldteufel [1970a,b] with one another as well as with experimental data in the collision dominated regime, and gave strong support to the formulation of Dougherty and Farley. There has been no satisfactory resolution of these problems to date, theoretically or experimentally. Except for the studies by Salah et al. [1975] and Ganguly and Coco [1987], most work in this area has proceeded from the theory of Dougherty and Farley.

Another difficulty arises in determining the relationship of ν_{in} to the neutral density. The form of this dependence is itself dependent on the dominant mode of collisional interaction between ions and neutrals. It is generally assumed at these heights and temperatures that the induced dipole interaction is the most important collisional mechanism [Banks, 1966]. However, resonant charge exchange has also been suggested as a competing process.

In the height range of interest here (90–150 km), the dominant ionic species are NO^+

and O_2^+ (of comparable concentrations), while N_2 and O_2 are the dominant neutral species. As altitude increases, the concentration of atomic oxygen ($[O]$) increases until it exceeds $[O_2]$ above 120 km, while O^+ does not become an important constituent relative to O_2^+ and NO^+ until about 150 km. Resonant charge exchange between O_2^+ and O_2 becomes important only at temperatures above ≈ 500 K, while for O^+ and O that transition temperature is ≈ 200 K [Banks, 1966]. Thus resonant charge exchange can compete with induced dipole interactions at the upper limits of the altitude range considered here, where temperatures approach the 500 K level for $O_2^+ - O_2$ collisions. However, the importance of resonant charge exchange for $O^+ - O$ collisions is reduced because both O^+ and O are minor constituents. Thus, for normal E-region conditions, where temperatures range from 200 to 400 K as altitude increases from 90 to about 125 km, and where $[O^+] \ll [NO^+]$ or $[O_2^+]$, resonant charge exchange can be neglected.

Under such conditions, the model of polarization potentials is adequate to describe the collisional process. As was shown by Lathuillere et al. [1983], the total ion-neutral collision frequency at E-region heights can be expressed as

$$\nu_{in} = \sum_{j=NO^+, O_2^+} \nu_{jn} \approx \frac{2.59 \times 10^{-11}}{30.5} (5.07\%N_2 + 4.98\%O_2 + 2.88\%O) \mathcal{N}, \quad (1)$$

where ν_{in} is the collision frequency of the j th ion with neutral species n , \mathcal{N} is the total neutral number density, and $\%n$ represents the relative proportion of the neutral species n to the neutral gases as a whole. In the derivation of this formula, a single ion with a mass intermediate between NO^+ and O_2^+ is assumed, and collisions of O^+ with the neutral constituents are neglected. This expression shows that if a model of neutral composition is available, \mathcal{N} can be determined from the ion-neutral collision frequency determined with the incoherent-scatter technique.

It is difficult to assess the variability of the neutral composition with time, since few measurements are available in the literature. The results of Offerman et al. [1981] indicate

variations in $[N_2]$ and $[O_2]$ of about 5%, while atomic oxygen has been observed to vary by factors of 4 to 5. However, over the entire height range in question, N_2 dominates over atomic oxygen ranging from a factor of 100 at 90 km to a factor of 2 at 150 km. Thus, the effect of potentially variable atomic oxygen concentration on deduction of the neutral density is reduced because the contributions from N_2 and O_2 collisions dominate the calculation over most of the altitude range.

As was mentioned briefly above, usually the data quality do not allow T_i , T_e , and ν_{in} to be simultaneously determined from the ACF. Most studies to date have therefore assumed thermal equilibrium between ions and electrons, fitting instead for $T_i = T_e$ and ν_{in} alone. While the assumption of thermal equilibrium is valid at low to mid latitudes, several physical processes which occur in the auroral zones can cause selective heating of the electrons or the ions [Lathuillere et al, 1983]. As a result, periods of high electric fields must be excluded from determination of ν_{in} when working with high-latitude measurements.

Figure 2 shows an example of ν_{in} calculated from Chatanika radar data obtained in March and November of 1978, in comparison with values calculated using the Jacchia-71 model [Lathuillere et al., 1983]. This example of good agreement between experimental ν_{in} profiles and empirical model profiles is typical of the results obtained over the upper-mesosphere and lower-thermosphere region [Wand and Perkins, 1968; Salah, 1974; Wand, 1976; Tepley and Mathews, 1978; Schlegel et al., 1980; Tepley et al., 1981; Kofman and Lathuillere, 1985; Flå et al., 1985; Kofman et al., 1986; Huuskonen et al., 1986; Ganguly and Coco, 1987]. These studies provide empirical justification for the approach of Dougherty and Farley (1963), as well as the assumption that induced-dipole interactions are of dominant importance in this height range.

E-region neutral winds

The ion velocity along the line-of-sight of the radar is obtained from the Doppler shift of the return signal spectrum. Through the use of different pulse lengths for E- and F-region measurements, altitude resolution appropriate to both of these regions can be obtained. Combination of three successive line-of-sight measurements with different pointing directions allows vector ion velocities with time resolution of the order of ten minutes or less to be obtained. The E-region ion velocity, along with the electric field, enter into the calculation of the neutral wind.

The height-dependent neutral wind velocity, $\vec{u}(z)$, is deduced from the steady state ion equation of motion appropriate to E-region heights. Perpendicular to \vec{B} , this equation reduces to

$$\vec{u}_{\perp}(z) = \vec{v}_{\perp}(z) - \left(\frac{\Omega_i}{\nu_{in}} \right) \left(\vec{E}_{\perp} + \vec{v}_{\perp}(z) \times \vec{B} \right), \quad (2)$$

where \vec{E}_{\perp} is the ionospheric electric field derived from F-region ion velocity measurements, $\vec{v}_{\perp}(z)$ is the height-dependent E-region ion velocity, and Ω_i is the ion gyrofrequency. Parallel to \vec{B} , the ion equation of motion reduces to

$$u_{\parallel}(z) = v_{\parallel}(z) - v_{ambi}(z), \quad (3)$$

where v_{ambi} is the ambipolar diffusion velocity. At E-region heights, $v_{ambi}(z)$ is usually negligible, as are vertical velocities relative to the horizontal neutral wind components.

Results from calculations of the horizontal neutral wind usually show the presence of large amplitude low-frequency motions [Rino et al., 1977; Wand, 1983a,b; Johnson et al., 1987]. The semidiurnal fluctuation is particularly important at high latitudes. Figure 3 summarizes the tidal results for summer months at Chatanika [Johnson et al, 1987]. The four different polar plots show the variation with local time of the diurnal (see panel a) and semidiurnal (panel b) tidal components obtained from a least-squares fit to the average of the data at 115 km altitude. Also shown are the resultant net tidal wind field (panel c),

and the total average flow field in which the mean flow at 115 km has been added (panel d). Wind velocities of 75 to 100 m/s are common at this altitude, and the semidiurnal component is clearly dominant.

Equation (2) shows the dependence of the neutral wind on the local ion velocity and electric field. During intervals of geomagnetic activity, enhanced electric fields drive the ions into motion and produce variations in the neutral winds as well. The study by Johnson et al. [1987] showed that neutral winds responded in a consistent and systematic fashion above ≈ 100 km at Chatanika during summer months. This response was particularly strong in the local morning sector, where zonal flow enhancements of several hundred m/s were found on occasion. Figure 4 shows the zonal geographic neutral wind at 115 km obtained for June 11, 1980 (open circles) as well as the average zonal wind for $K_p < 2$ conditions (thin line) as a function of universal time. At Chatanika, local dawn occurs at 16 UT. Throughout the local morning sector, the zonal wind was strongly enhanced over the $K_p < 2$ average values, up to ≈ 300 m/s at 20 UT.

Equation (2) also shows that the neutral wind velocity is dependent on ν_{in} . The smaller ν_{in} becomes, the more the ion velocity diverges from the neutral wind. The inverse form of this dependence causes uncertainties in ν_{in} , \vec{E} , and \vec{v} to result in proportionately larger uncertainties in $u_{\perp}(z)$ at greater heights. Figure 5 shows how uncertainty in ν_{in} can affect the resultant neutral wind obtained through Equation (2). Three different neutral density profiles were calculated, corresponding to 75%, 100%, and 125% of the MSIS-83 value. The panel at the left compares the profiles of the zonal neutral wind determined using these density profiles at a time when the second term on the right-hand side of equation (2) dominates the calculation. On the right-hand side of the figure, the zonal ion velocity dominates the calculation. Thus, depending on the relative magnitudes of the ion velocity components and the electric field, the uncertainty produced as a result of uncertainty in ν_{in} can range from negligible to the order to the neutral velocity itself (assuming a 25%

uncertainty). Obviously, in order to determine the neutral wind accurately, the ion-neutral collision frequency must be known as accurately as possible.

Potential for Improvements

At Chatanika [Schlegel et al., 1980; Lathuillere et al., 1983] and at EISCAT [Flå et al., 1985; Kofman and Lathuillere, 1985; Kofman et al., 1986; Huuskonen et al., 1986], the ion-neutral collision frequency could not be determined reliably from fits to the experimental data at altitudes above about 110 km. Above this height, the influence of collisions on the autocorrelation function (ACF) of the return signal was too small to significantly distort the shape of the ACF at the radar operating frequencies (1290 MHz and 933 MHz, respectively).

The parameter which characterizes this distortion is the normalized ion collision frequency, $\Psi_i = (\nu_{in} \lambda / 4\pi) (m_i / 2\kappa T_i)^{1/2}$, where λ is the radar operating wavelength, m_i and T_i are the ion mass and temperature, and κ is Boltzmann's constant. As Ψ_i (or ν_{in}) decreases, the ACF of the return signal gradually develops the normal oscillatory shape characteristic of the collisionless case and the damping influence of ν_{in} can eventually no longer be detected.

Figure 6 [after Dougherty and Farley, 1963] shows curves of Ψ_i corresponding to operating frequencies of 50, 430, and 1290 MHz versus altitude. The vertical line at $\Psi_i \approx 0.04$, which intersects the 1290 MHz line at 110 km, indicates the minimum value of Ψ_i from which ν_{in} could be determined reliably from the experimental ACFs at Chatanika. At lower frequencies, this same value of Ψ_i is attained at higher altitudes (≈ 120 km at 430 MHz and ≈ 140 km at 50 MHz). This indicates that with the same system sensitivity available at Chatanika, the influence of ν_{in} on the ACFs could be detected to higher altitudes at lower frequencies. Indeed, Salah [1974] and Wand and Perkins [1968] report measurements of ν_{in} up to 120 km at Millstone Hill (440 MHz) and at Arecibo (430 MHz),

respectively. With increased system sensitivity, obtained through increased transmitter power and the use of low-noise receivers these upper altitude limits could probably be raised by about half an atmospheric scale height (several km).

Whether these techniques can be used to deduce ν_{in} (and thereby neutral densities) at altitudes above 125 km, as is suggested by the 50 MHz curve on the figure, depends on the influence of other factors. As was noted by Dougherty and Farley [1963], other scattering processes may affect the measurement as the operating frequency decreases. Another factor is degradation in signal-to-noise ratio at low frequencies because of the increase in noise temperature from the sky. Finally, the interpretation of ν_{in} as a measure of neutral density needs to be reexamined at greater heights due to the increased importance of O^+ as well as resonant charge-exchange interactions and the increased importance of potentially variable atomic oxygen density. A study of these factors and their effect on the measurement and interpretation of ν_{in} is required in order to determine the potential of this technique at these greater altitudes.

Acknowledgements

This study was supported by NSF Cooperative Agreement ATM-85-16436, NSF Grant No. ATM-87-10266, and AFOSR contract F49620-87-K-0007.

References

- Banks, P., Collision frequencies and energy transfer: Ions, *Planet. Space Sci.*, 14, 1105-1122, 1966.
- Dougherty, J. P., and D. T. Farley, Jr., A theory of incoherent scattering of radio waves by a plasma 3. Scattering in a partly ionized gas, *J. Geophys. Res.*, 68, 5473-5486, 1963.
- Flå, T., S. Kirkwood, and K. Schlegel, Collision frequency measurements in the high-latitude E region with EISCAT, *Radio Sci.*, 20, 785-793, 1985.
- Ganguly, S., and D. Coco, Incoherent scattering from the collision dominated D-region. Comparison of theories with experimental data, *J. Atmos. Terr. Phys.*, 49, 549-563, 1987.
- Hagfors, T., and R. A. Brockelman, A theory of collision dominated electron density fluctuations in a plasma with applications to incoherent scattering, *Phys. Fluids*, 14, 1143-1151, 1971.
- Huuskonen, A., T. Nygrén, L. Jalonon, T. Turunen, and J. Silén, High resolution EISCAT observations of the ion-neutral collision frequency in the lower E region, *J. Atmos. Terr. Phys.*, 48, 827-836, 1986.
- Johnson, R. M., V. B. Wickwar, R. G. Roble, and J. G. Luhmann, Lower-thermospheric winds at high latitude: Chatanika radar observations, *Ann. Geophys.*, 5A, 383-404, 1987.

- Kofman, W., and C. Lathuillere, EISCAT multipulse technique and its contribution to auroral ionosphere and thermosphere description, *J. Geophys. Res.*, **90**, 3520-3524, 1985.
- Kofman, W., F. Bertin, J. Röttger, A. Cremieux, and P.J.S. Williams, The EISCAT mesospheric measurements during the CAMP campaign, *J. Atmos. Terr. Phys.*, **46**, 565-575, 1984.
- Kofman, W., C. Lathuillere, and B. Pibaret, Neutral atmosphere studies in the altitude range 90-110 km by EISCAT, *J. Atmos. Terr. Phys.*, **48**, 837-848, 1986.
- Lathuillere, C., V. B. Wickwar, and W. Kofman, Incoherent scatter measurements of ion-neutral collision frequencies and temperatures in the lower thermosphere of the auroral region, *J. Geophys. Res.*, **88**, 10137-10144, 1983.
- Mathews, J. D., Measurements of the diurnal tides in the 80- to 100-km altitude range at Arecibo, *J. Geophys. Res.*, **81**, 4671-4677, 1976.
- Mathews, J. D., The effects of negative ions on collision-dominated Thomson scattering, *J. Geophys. Res.*, **83**, 505-512, 1978.
- Offerman, D., V. Friedrich, P. Ross, and U. Von Zahn, Neutral gas composition measurements between 80 and 120 km, *Planet. Space Sci.*, **29**, 747-764, 1981.
- Salah, J. E., Daily oscillations of the mid-latitude thermosphere studied by incoherent scatter at Millstone Hill, *J. Atmos. Terr. Phys.*, **36**, 1891-1909, 1974.
- Salah, J. E., J. V. Evans, and R. H. Wand, E-region temperature measurements at Millstone Hill, *J. Atmos. Terr. Phys.*, **37**, 461-489, 1975.

- Schlegel, K., H. Kohl, and K. Rinnert, Temperatures and collision frequency in the polar E region measured with the incoherent scatter technique, *J. Geophys. Res.*, **85**, 710-714, 1980.
- Tanenbaum, B. S., Continuum theory of Thomson scattering, *Phys. Rev.*, **171**, 215-221, 1968.
- Tepley, C. A., and J. D. Mathews, Preliminary measurements of ion-neutral collision frequencies and mean temperatures in the Arecibo 80- to 100-km altitude region, *J. Geophys. Res.*, **83**, 3296-3302, 1978.
- Tepley, C. A., J. D. Mathews, and S. Ganguly, Incoherent scatter radar studies of mesospheric temperatures and collision frequencies at Arecibo, *J. Geophys. Res.*, **86**, 11330-11334, 1981.
- Waldteufel, P., A study of seasonal changes in the lower thermosphere and their complications, *Planet. Space Sci.*, **18**, 741-748, 1970a.
- Waldteufel, P., Une étude par diffusion incohérente de la haute atmosphère neutre, Ph.D. thesis, Fac. des Sci. de Paris, 1970b.
- Wand, R. H., and F. W. Perkins, Radar Thomson scatter observations of temperature and ion-neutral collision frequency in the E region, *J. Geophys. Res.*, **73**, 6370-6372, 1968.
- Wand, R. H., Semidiurnal tide in the E region from incoherent scatter measurements at Arecibo, *Radio Sci.*, **11**, 641-652, 1976.
- Wand, R. H., Seasonal variations of lower thermospheric winds from the Millstone Hill incoherent scatter radar, *J. Geophys. Res.*, **88**, 9227-9241, 1983a.

Wand, R. H., Geomagnetic activity effects on semidiurnal winds in the lower thermosphere, *J. Geophys. Res.*, **88**, 9243-9248, 1983b.

Wickwar, V. B., C. Lathuillere, W. Kofman, and G. Lejeune, Elevated electron temperatures in the auroral E layer measured with the Chatanika radar, *J. Geophys. Res.*, **86**, 4721-4730, 1981.

Figure Captions

Fig. 1 — Contour plots of E region electron density (cm^{-3} , upper left), ion temperature (K, upper right), electron temperature (K, lower left), and ion velocity (m/s, lower right) versus altitude and time on June 11, 1980. Minimum and maximum values are shown in the lower left and right corners of each panel, respectively.

Fig. 2 — Profiles of mean collision frequency for March and November, 1978 Chatanika radar measurements (solid lines with error bars) compared with Jacchia-71 model values (dashed lines) (after Lathuillere et al. [1983]).

Fig. 3 — Diurnal (a) and semidiurnal (b) wind vectors determined from a least-squares fit to the average of the summer Chatanika data at 115 km in a polar plot format. The sum of these two tidal components is shown in panel (c), and panel (d) includes the mean flow as well [Johnson et al., 1987].

Fig. 4 — Zonal neutral wind at 115 km in geomagnetic coordinates on June 11, 1980 (open circles) compared with the average for $K_p < 2$ conditions (dot-dashed curve). Local midnight at Chatanika occurs at 10 UT [Johnson et al., 1987].

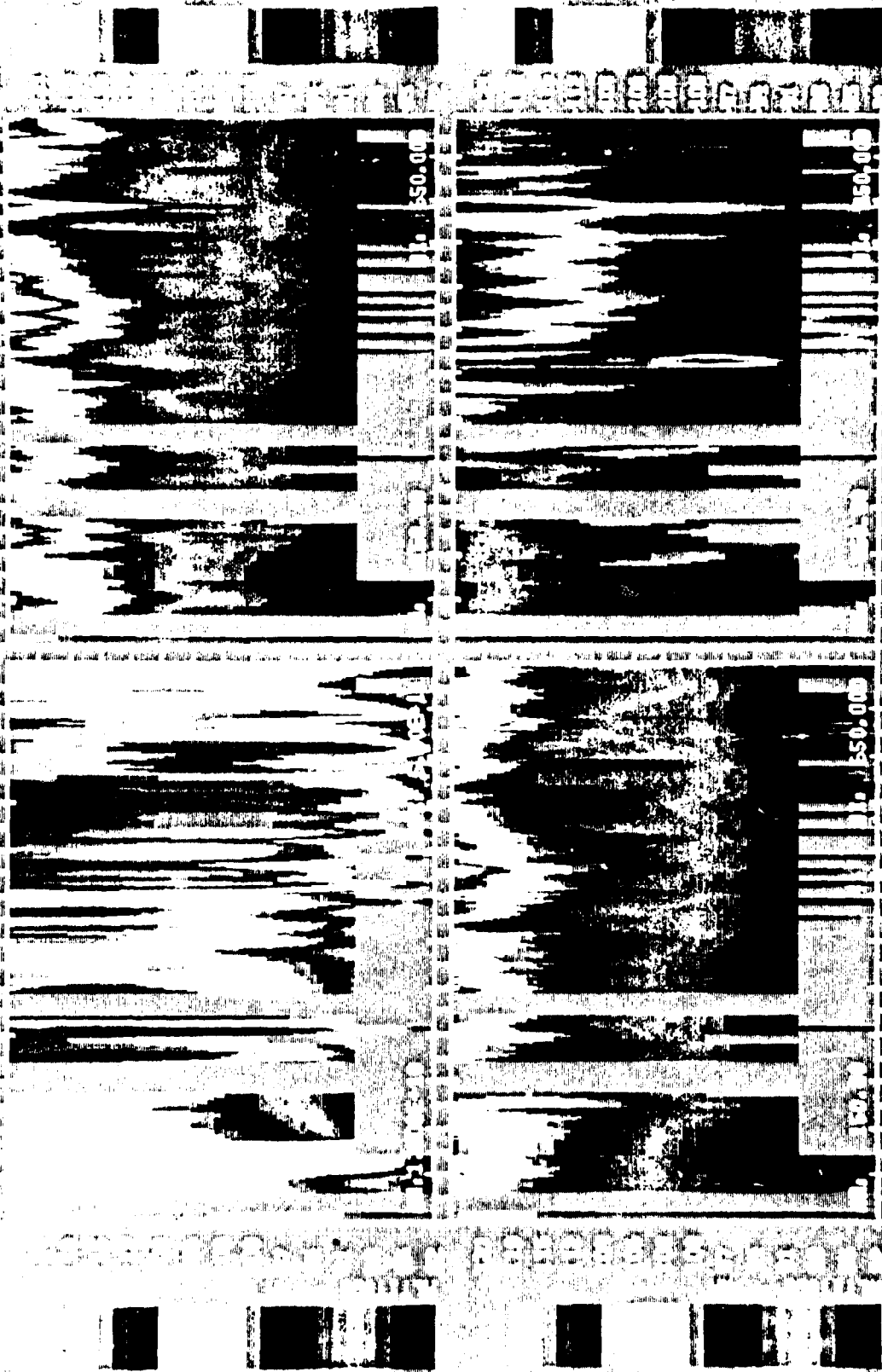
Fig. 5 — Altitude profiles of the zonal neutral wind on June 11, 1980 at two different universal times. The three curves on each panel show the neutral wind obtained using the MSIS-83 density profiles multiplied by 0.75 (dashed), 1.0 (solid), and 1.25 (dotted).

Fig. 6 — Normalized ion collision frequency, $\Psi_i = (\nu_{in} \lambda / 4\pi)(m_i / 2\kappa T_i)^{1/2}$, as a function of altitude at sunspot maximum. Curves for three different operating frequencies are shown. The vertical line indicates the minimum value of Ψ_i from which ν_{in} could be

deduced with the Chatanika radar (1290 MHz) (after Dougherty and Farley, [1963]).

CHITANKA

CHITANKA



SR167DC89

TOPIC NE. 11 BUILINGS RE. VY HIC

Fig. 1

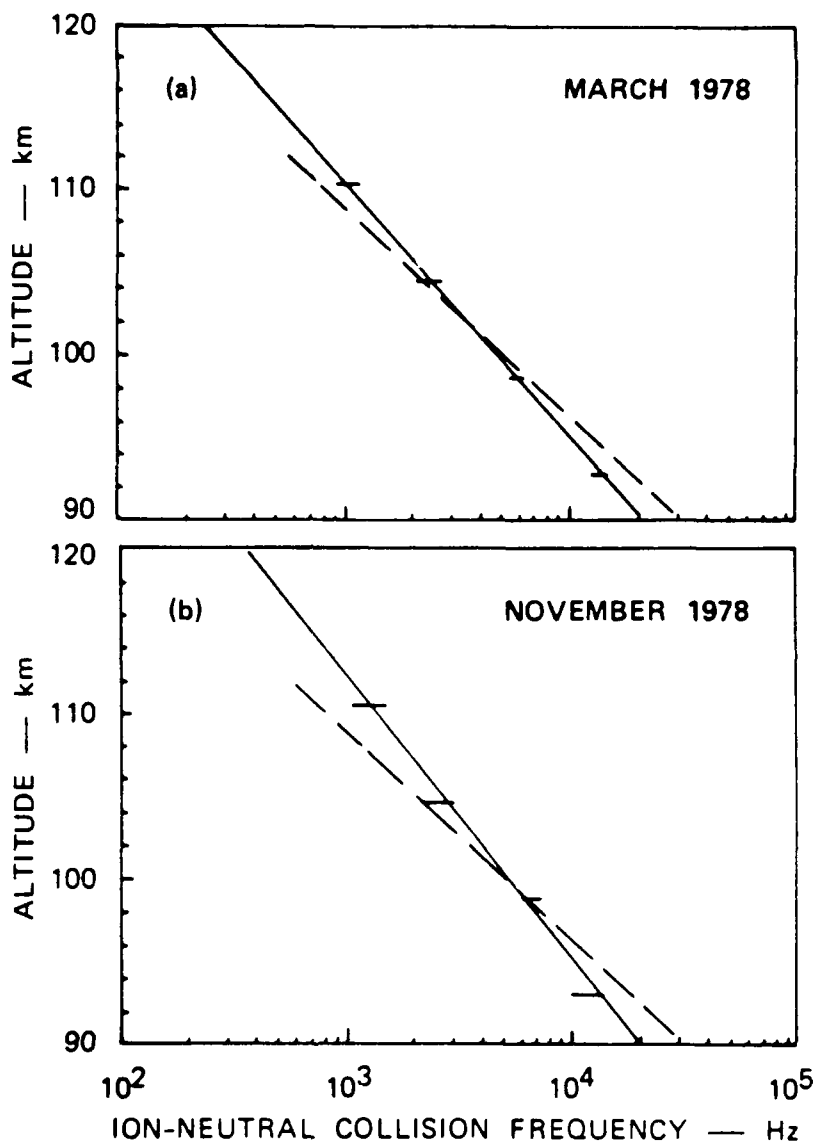


Fig. 2

Least-Square Fit
Average Neutral Winds
115 km

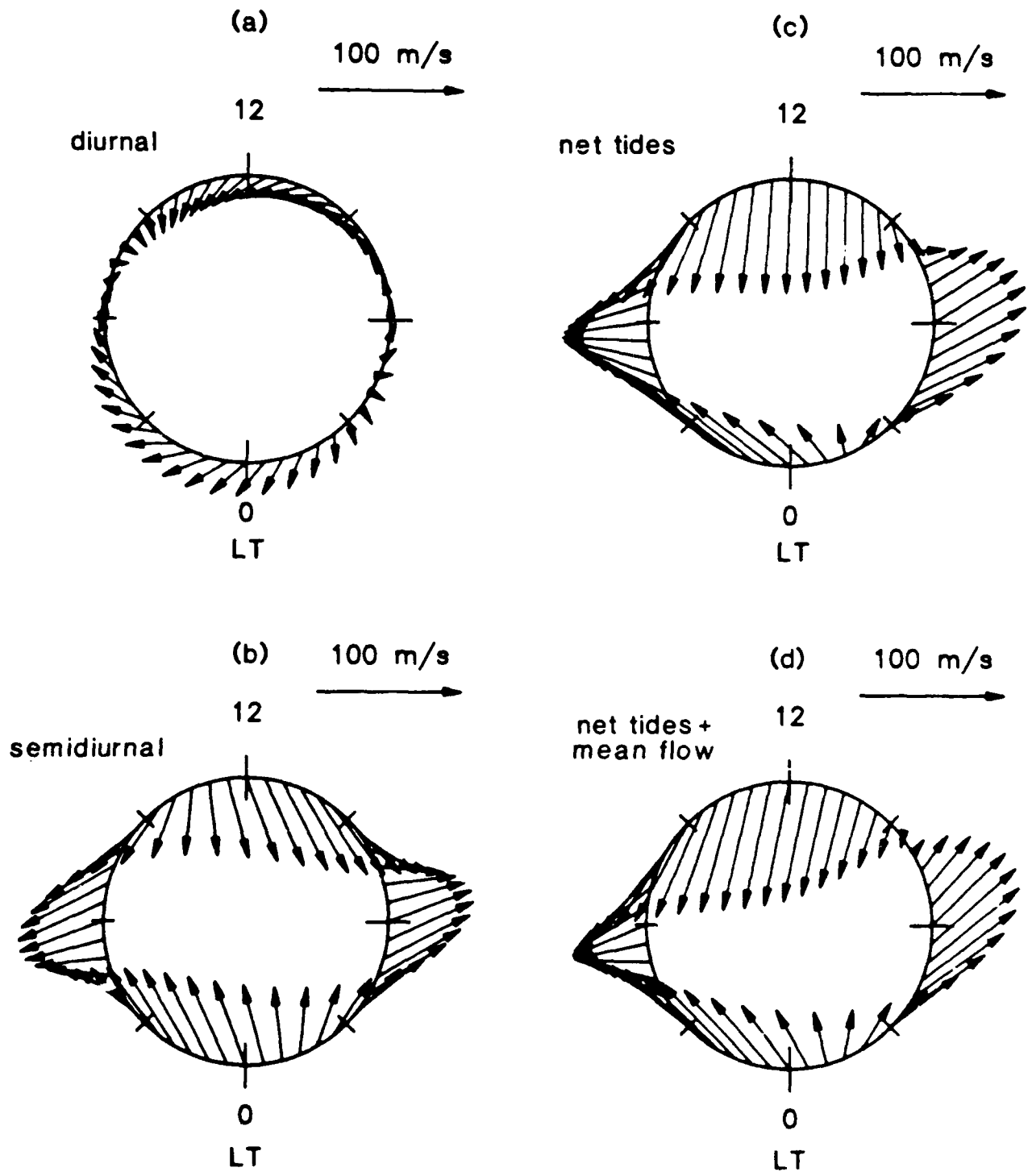


Fig. 3

Chatanika

Zonal Neutral Wind 115 km

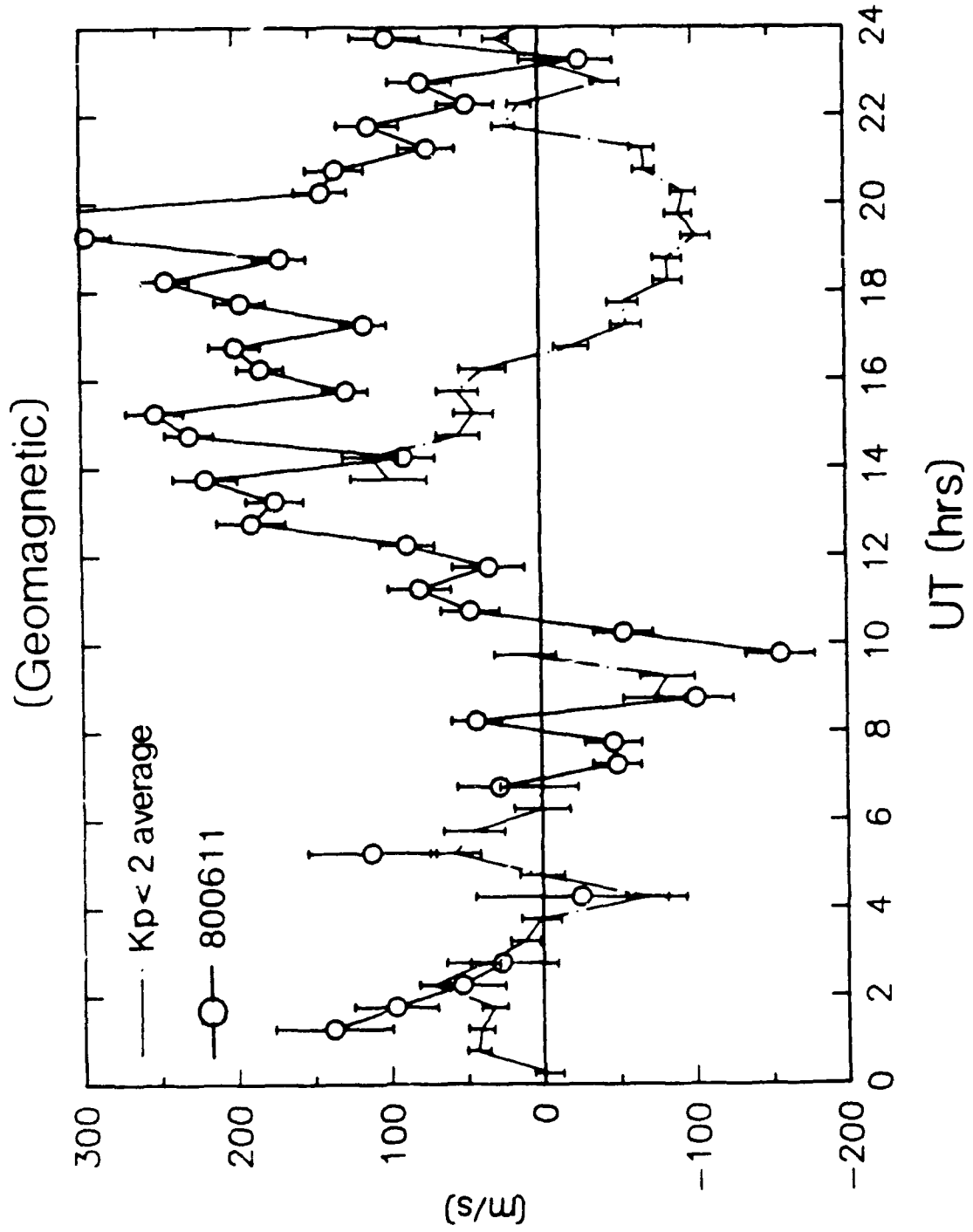


Fig. 4

ZONAL NEUTRAL WIND

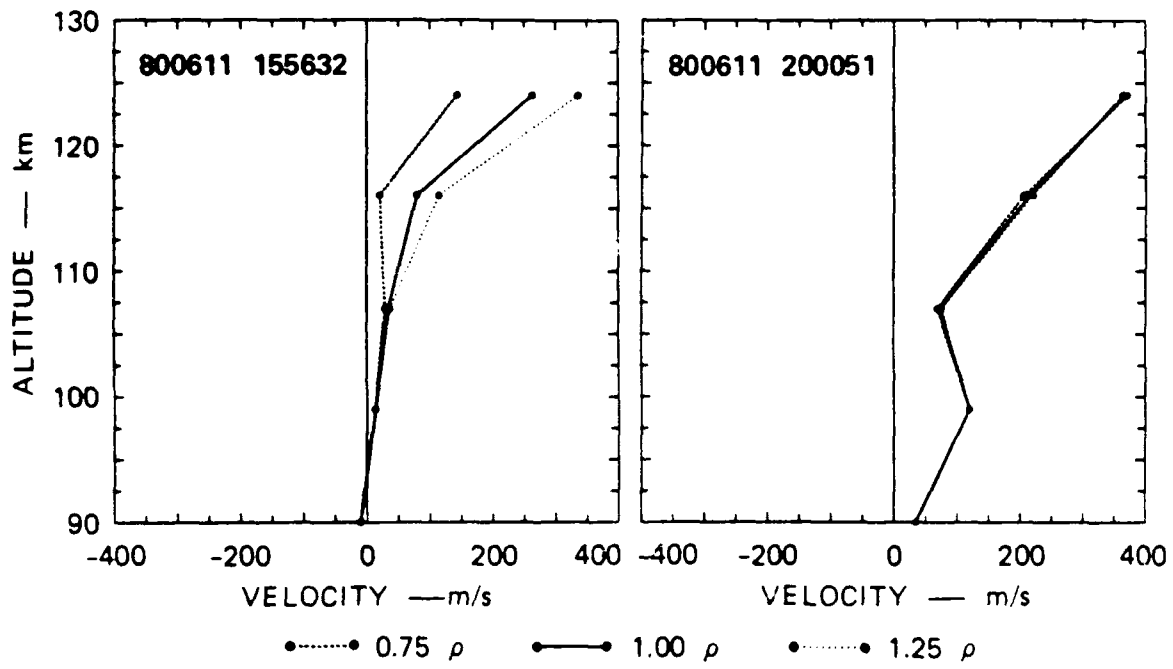


Fig.5

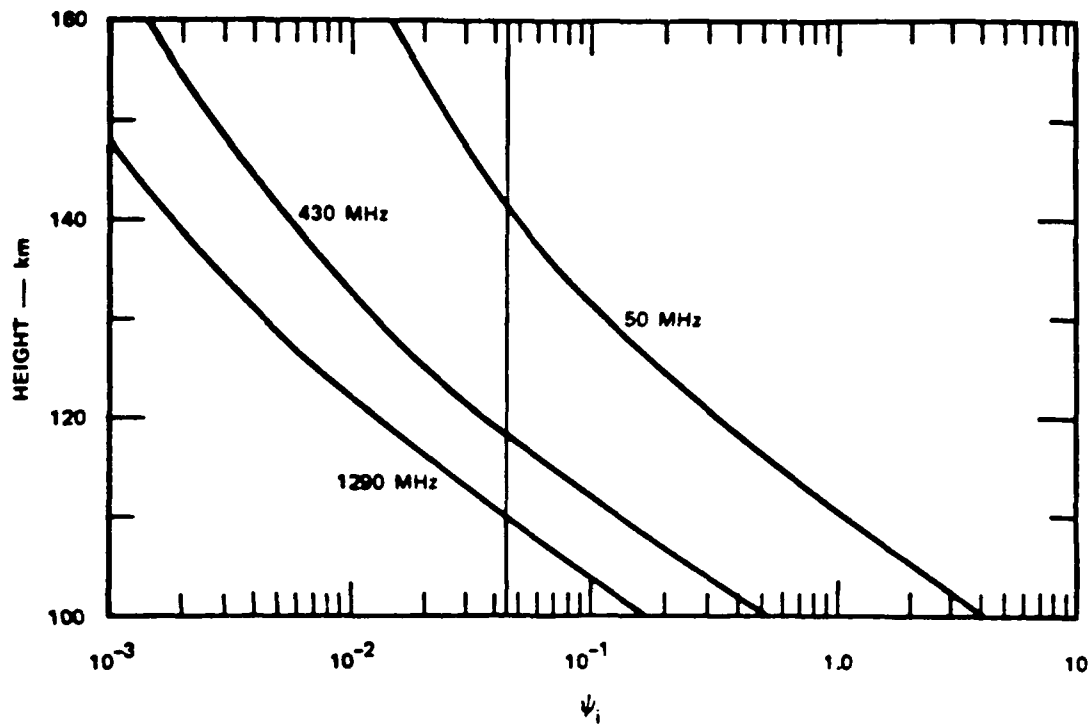


Fig. 6

Remote Measurement of Upper Atmospheric Density

P.B.Hays, V.J.Abreu, and J.H.Yee
Space Physics Research Laboratory, University of Michigan

1.0 INTRODUCTION

Orbital reentry of large maneuverable vehicles and the potential to modify orbital parameters using the aerobreaking technique have increased the need to understand in detail the variability of atmospheric density in the mesosphere and lower thermosphere. Acceleration data¹ obtained during shuttle reentry, shown in figure 1., illustrate the fact that the atmosphere exhibits variation which often exceed expectation and which raise questions regarding the safe return of heavy Shuttle payloads from polar orbit.

The variability of mass density in the mesosphere has been apparent for many years, being seen in sounding rocket data, backscatter radar profiles, and airglow optical emissions. The systematic variations that have been determined from these data sets are the obvious seasonal, latitudinal, and local time dependences that are prescribed in the major models in use today. These models, however, are based on limited data and thus, are not useful in making predictions or forecasts of the effects of planetary waves or gravity wave breaking. The wave processes will never be able to be accurately predicted, but like the weather in the troposphere we may ultimately be able to base a forecast on operational information. A primary factor holding back the improvement of these models and the development of a forecasting technique is the lack of a sufficiently large and accurate morphological data base.

This global data base must rely on a sampling technique that will provide a morphology of the atmospheric density in the critical 60 to 120 km. region, with the consistency required to quantify the higher frequency variability. The only practical method of providing global information is to use a remote sensing technique from earth orbit, given that it has the required accuracy and spatial sensitivity. Such a technique could be tested using first sub-orbital evaluation, followed by shuttle validation, and finally deployed on a satellite in earth orbit to provide the required global information.

Several possible remote sensing techniques have been proposed which have the potential to measure the atmospheric density in this important atmospheric region. These include measuring the brightness of sunlight that is rayleigh scattered by the molecular nitrogen and oxygen ², measuring the absorption of starlight during stellar occultation ³, and a new technique where the fluorescence of molecular oxygen is measured photometrically. This new method has evolved from the studies of the University of Michigan's Space Physics Research Laboratory which is providing the High Resolution Doppler Imager for the Upper Atmosphere Research Satellite ⁴. In order to evaluate the potential for a spaceborne remote measurement of density in the 60 to 120km. region it is necessary to compare the relative merits of these related techniques. Each of these methods of sensing the density has inherent advantages as well as weaknesses.

2.0 TECHNICAL DESCRIPTION AND APPROACH

The University of Michigan Space Physics Research Laboratory is in the process of evaluating several means of obtaining the density morphology in the Mesosphere and lower Thermosphere by remote sensing techniques. At this time three candidate methods have been identified, these being:

1. Resonance fluorescence of molecular oxygen
2. Absorption of starlight during stellar occultation
3. Rayleigh scattering of sunlight .

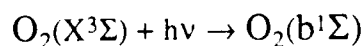
The order that these have been listed is based on the expectation of their relative usefulness in accomplishing the objective, however, the present study may on completion lead to a re-ordering of these methods, or addition to the list of potential techniques.

2.1 Resonance fluorescence of molecular oxygen

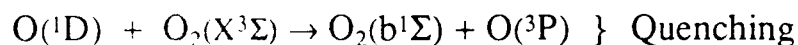
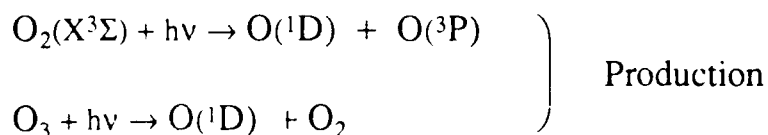
The daytime Atmospheric "A" Bands of molecular oxygen provide one of the brightest spectral emission features that are seen in the visible and near infra-red region of the spectrum of light emitted from the earth's atmosphere. Yet this band system has received very little attention since the early investigations of Wallace and Hunten ⁵, and the more recent observations obtained from the Dynamics Explorer Satellite by Skinner and Hays ⁶. This band system results from competition between processes which excite molecular oxygen to the $b^1\Sigma_g^+$ state and those that depopulate the state, where:

A) Excitation processes

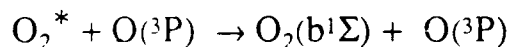
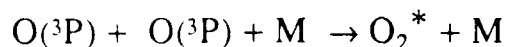
1. Resonance absorption (7650 Å)



2. Production of $\text{O}(^1\text{D})$ and quenching (Ultra-violet)

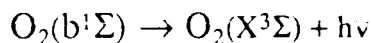


3. Chemical recombination

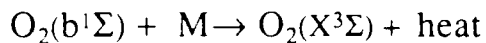


B) Loss processes

1. Radiation



2. Quenching



The various sources of production of molecular oxygen in the singlet sigma state are shown in figure 2, where resonance excitation and photodissociation of O_2 are combined. When losses are considered with these production processes in a simple photochemical equilibrium calculation, we are able to determine the contribution each makes to the volume emission rate as a function of altitude. Figure 3 shows the volume emission rate due to each of these sources of excited molecular oxygen. Note that the dominant sources of excited molecular oxygen in the 60 to 140 km. range are all directly proportional to the ground state oxygen density, and thus are directly related to the total density in that region of the atmosphere where the mixing ratio is well known. Below 60 km. the dissociation of ozone must be taken into account. We note that in this region the source of emission can be obtained from an examination of the intensity of the (1-0) Atmospheric band at 8650Å which is optically thin.

The limb brightness observed in the (0-0) "A" band at 7650Å is determined by emission in the various rotational lines of the band, attenuated through the molecular oxygen between the observer and the point of the emission. Two typical band distributions are shown in figure 4 , where the distribution of emission is seen for 200 and 1000 ° K . Since these lines are self absorbed, the column density of the absorber (here molecular oxygen) can be determined from low resolution band spectra of the light scattered, not only in the optically thin region at high altitude, but in the optically thick region below. This is achieved by an inversion process, illustrated symbolically in figure 5, where resonance absorption is indicated to be the principal source of excited molecular oxygen. Detailed spectra have been calculated as a part of the High Resolution Doppler Imager studies, conducted under the Upper Atmosphere Research Satellite program at Michigan since the late 1970's. Typical rotational line brightness for various line strengths is shown in Figure 6, where a line with strength of 20 cm⁻¹/atmos.km. has a brightness of nearly 300 kilorayleighs when viewed at a tangent ray height of 80 km. This system is extremely bright and offers one of the best possible sources of information about the density structure in the upper mesosphere and lower thermosphere.

2.2 Stellar Occultation and Absorption

Stellar occultation is used to determine the density of absorbing species in the atmosphere by a technique that is similar to classical absorption spectroscopy. The Sun, Moon, or a star are used as a source of light and the Satellite photometer as a detector, with the atmosphere between acting as the absorption cell. As the satellite moves in its orbit, the source ultimately is occulted by the Earth. During the occultation process, the intervening atmosphere absorbs progressively more of the light due to the strong photo-absorption features in the atmospheric gases. The occultation intensity data can be related to the tangential column number density of the absorbing species if the absorption cross-sections are known. This technique has been investigated in detail, with the early theoretical studies of Hays and Roble ³ describing the technique, errors were examined by Roble and Hays ⁷ , and the recent work has been reviewed by Atreya ⁸ . Figure 7 illustrates the geometry and methodology used in stellar occultation.

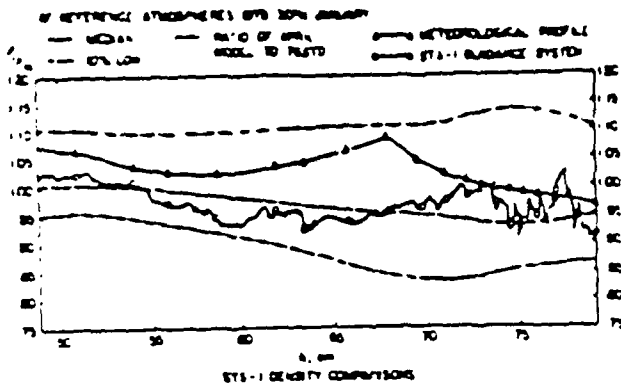
Molecular oxygen is the obvious candidate for observation, the ultra-violet absorption cross-section for this species, shown in figure 8, has features that allow the density to be observed throughout the region of interest. Typical absorption profiles are shown in figure 9 taken from reference 10 for a few selected spectral regions. We note that observations near Lyman alpha line of hydrogen allow density to be observed down to about 90 km., this is illustrated in the observations reported by Atreya ⁸ and shown in figure 10. Lower altitudes would be observable using bands in the Schumann Runge Bands near 1900 Å. This region was observed on the OAO-A2 spacecraft , but were not analyzed due to the complexity of the band system. Since that time detailed studies of these bands have been carried out

and it would be reasonable to expect that densities could be extracted in the critical 60 to 100 km. region.

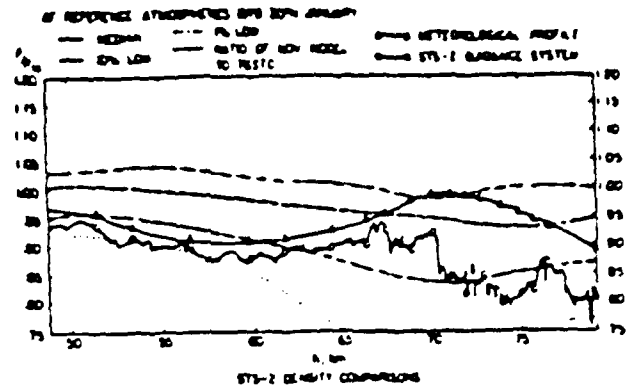
2.3 Rayleigh Scattering of Sunlight

The major gases of the atmosphere scatter light due to the processes of Rayleigh scattering in which non-resonance polarization of the molecules results in scattering of incoming light. During the daytime period the blue sky results from the preferential scattering at shorter wavelengths. Thus, like the resonance scattering technique Rayleigh scattering can be used to determine the density of the atmosphere at high altitudes. This method of observation is illustrated in figure 11 where the observation and inversion processes are indicated schematically. This technique has been used on the Solar Mesosphere Explorer Satellite to determine the density and temperature in the upper stratosphere². Questions regarding this method of measuring the density arise due to the existence of aerosols and Polar Mesospheric Clouds⁹. These particles and clouds cause scattering that is difficult to distinguish from density variations in the basic atmosphere. This problem may be resolved using a multiplicity of wavelengths.

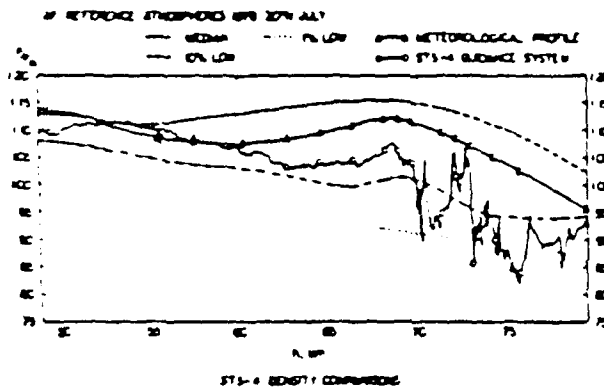
-
- ¹Champion, K.S.W., (1986), Atmospheric Structure for Low Altitude Satellite and Aerobraked Orbital Transfer Vehicles, AIAA 24th Aerospace Sciences Meeting, Reno, Nevada, Jan., paper AIAA-86-0186.
- ²Rusch, D.W., G.H. Mount, J.M. Zawodny, C.A. Barth, G.J. Rottman, R.J. Thomas, G.E. Thomas, T.W. Sanders, and G.M. Lawrence, (1983), Temperature Measurements in the Earth's Stratosphere Using a Limb Scanning Visible Light Spectrometer, Geophys. Res. Lett., **10**, 261
- ³Hays, P.B., and R.G. Roble, (1968), Stellar Spectra and Atmospheric Composition, J. Atmos. Sci., **25**, 1141
- ⁴Hays, P.B., (1982), High-resolution Optical Measurements of Atmospheric Winds from Space. 1: Lower Atmosphere Molecular Absorption, Applied Optics, **21**, 1136
- ⁵Wallace, L., and D.M. Hunten, (1968), Dayglow of the Oxygen A Band, J. Geophys. Res., **73**, 4813
- ⁶Skinner, W.R., and P.B. Hays, (1985), Brightness of the O₂ Atmospheric Bands in the Daytime Thermosphere, Planet. Space Sci., **33**, 17
- ⁷Roble, R.G., and P.B. Hays, (1972), A Technique for Recovering the Vertical Number Density Profile of Atmospheric Gases from Planetary Occultation Data, Planet. Space Sci., **20**, 1727
- ⁸Atreya, S.K., (1981) Measurement of Minor Species (H₂, Cl, O₃, NO) in the Earth's Atmosphere by the Occultation Technique, Planetary Aeronomy and Astronomy, (S.K. Atreya, and J.J. Caldwell, ed.) Pergamon Press, 127
- ⁹Thomas, G.E., and C.P. McKay, (1985), On the Mean Particle Size and Water Content of Polar Mesospheric Clouds, Planet. Space Sci., **33**, 1209



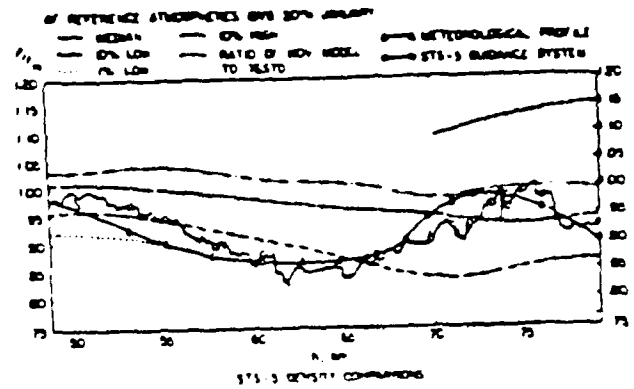
1. Ratio of density from drag on STS-1 during reentry.



2. Ratio of density from drag on STS-2 during reentry.



3. Ratio of density from drag on STS-4 during reentry.



4. Ratio of density from drag on STS-5 during reentry.

<u>Flight</u>	<u>Launch</u>	<u>Landing</u>
STS-1	April 12, 1981 0700 EST	April 14, 1981 1021 PST
STS-2	November 12, 1981 1010 EST	November 14, 1981 1323 PST
STS-4	June 27, 1982 1000 EST	July 4, 1982 0809 PST
STS-5	November 11, 1982 0719 EST	November 16, 1982 0633 PST

Figure 1

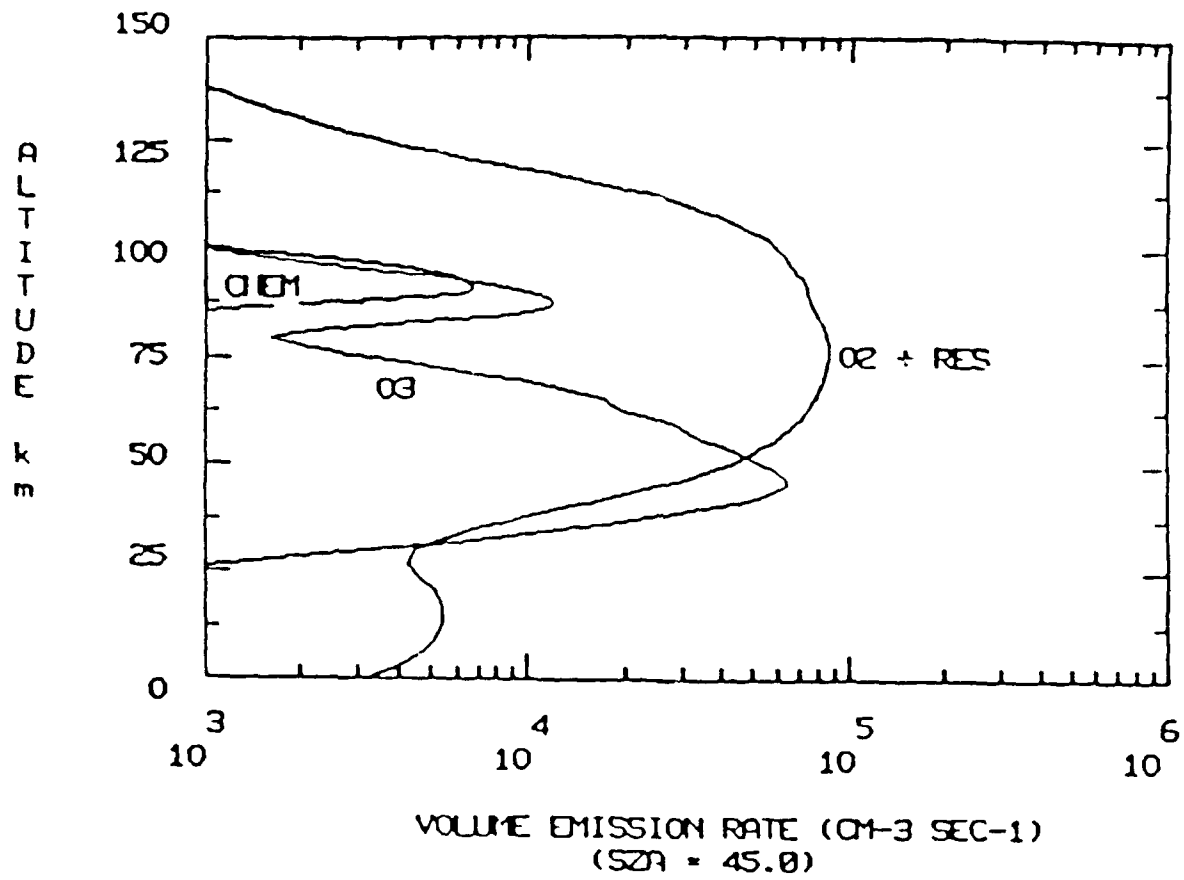


Figure 2

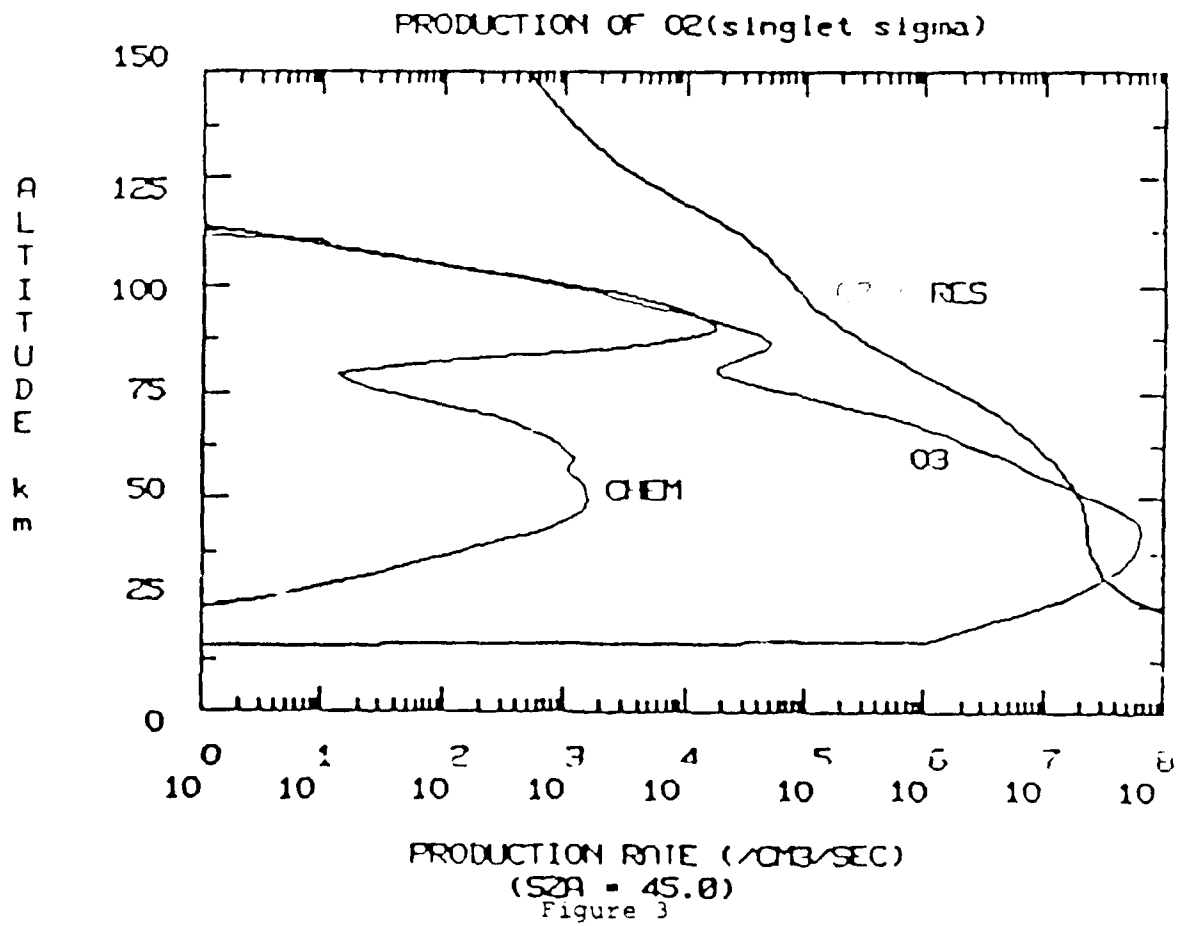


Figure 3

O₂ ATMOSPHERIC (O-O) BAND

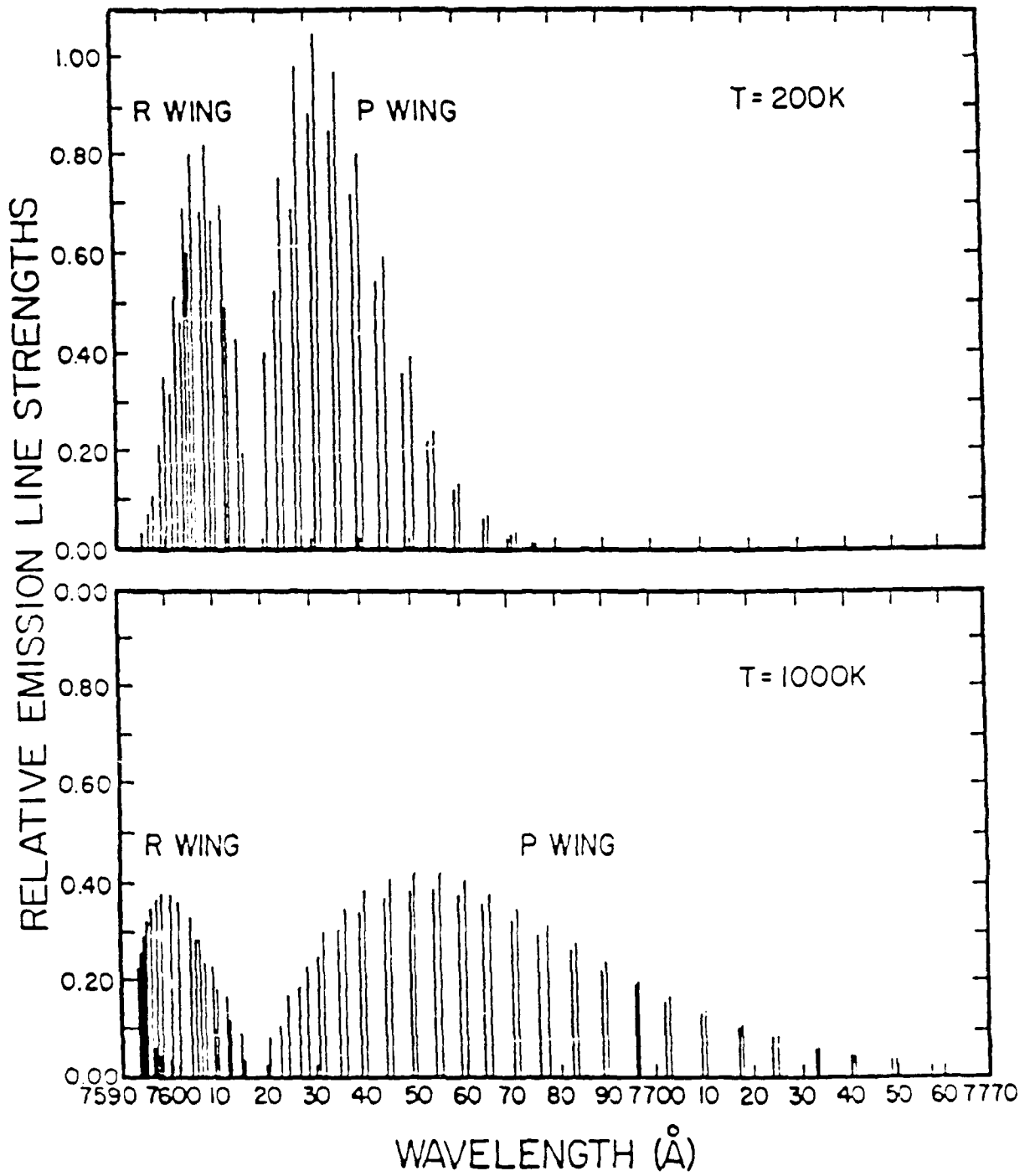


Figure 4

MOLECULAR OXYGEN RESONANCE FLUORESCENCE

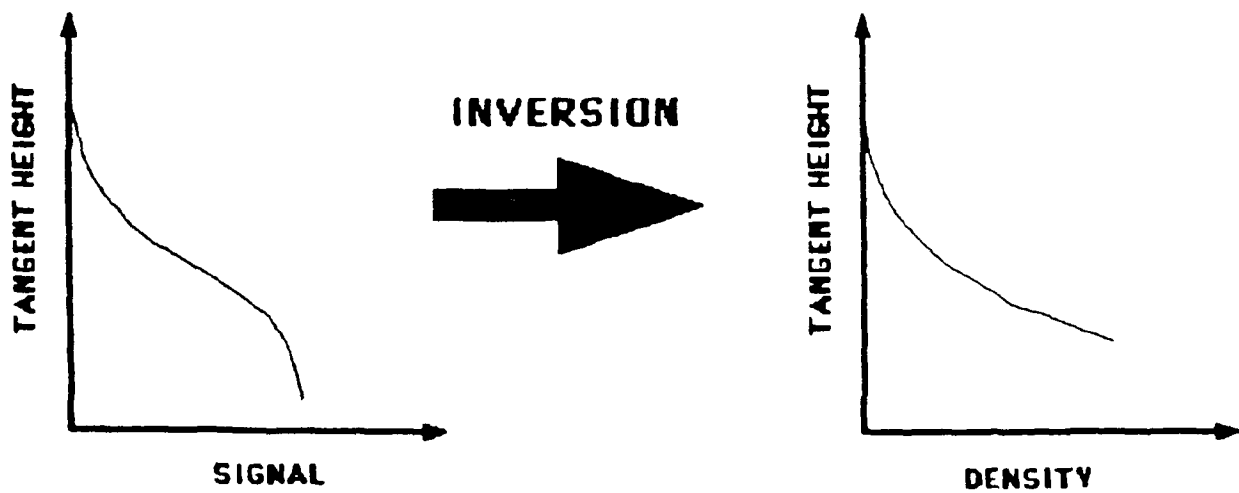
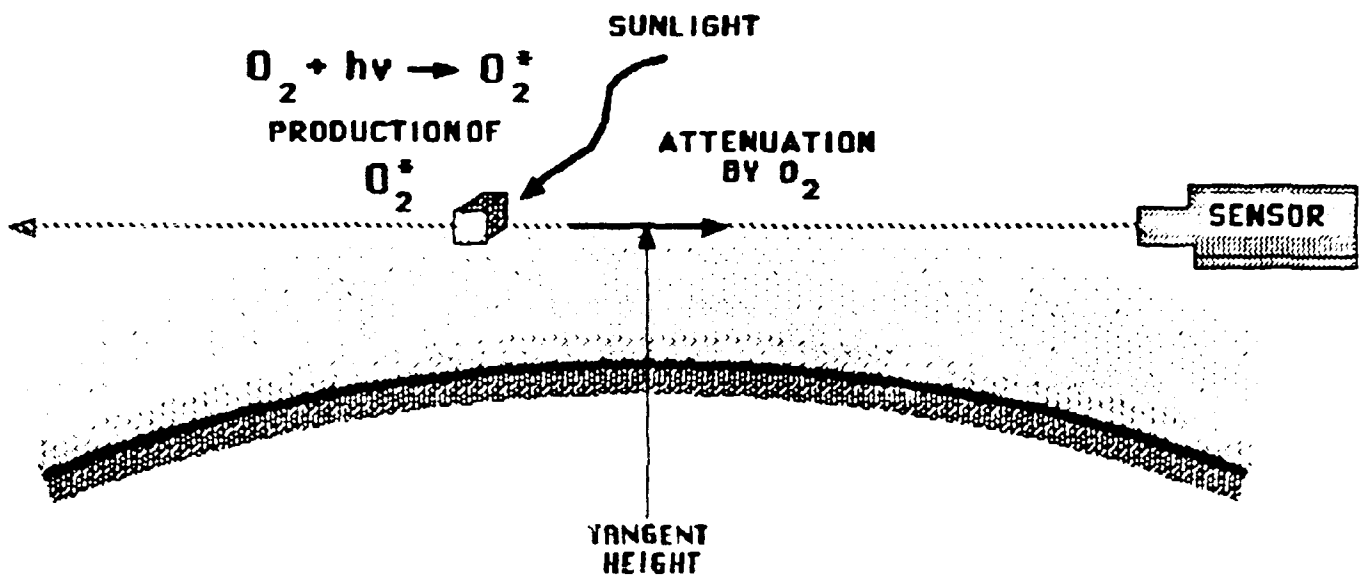


Figure 5

$O_2 (^1\Sigma)$
ATMOSPHERIC BAND LINE BRIGHTNESS

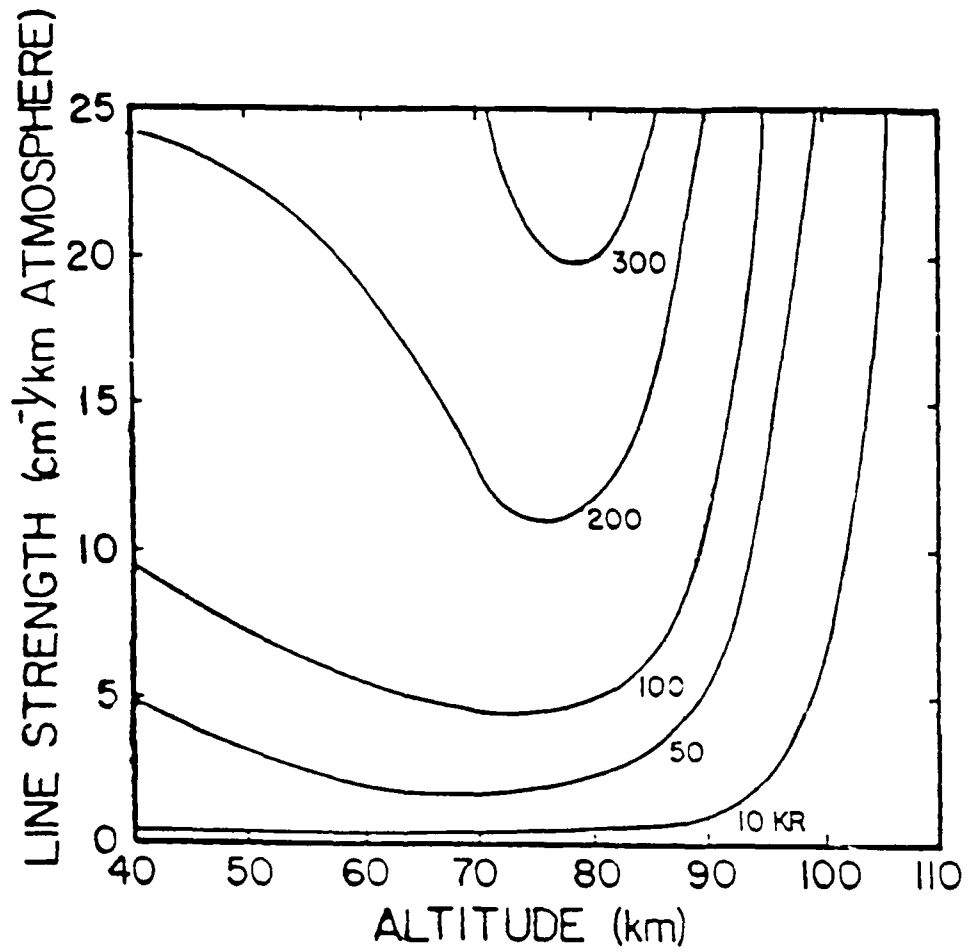


Figure 6

STELLAR OCCULTATION

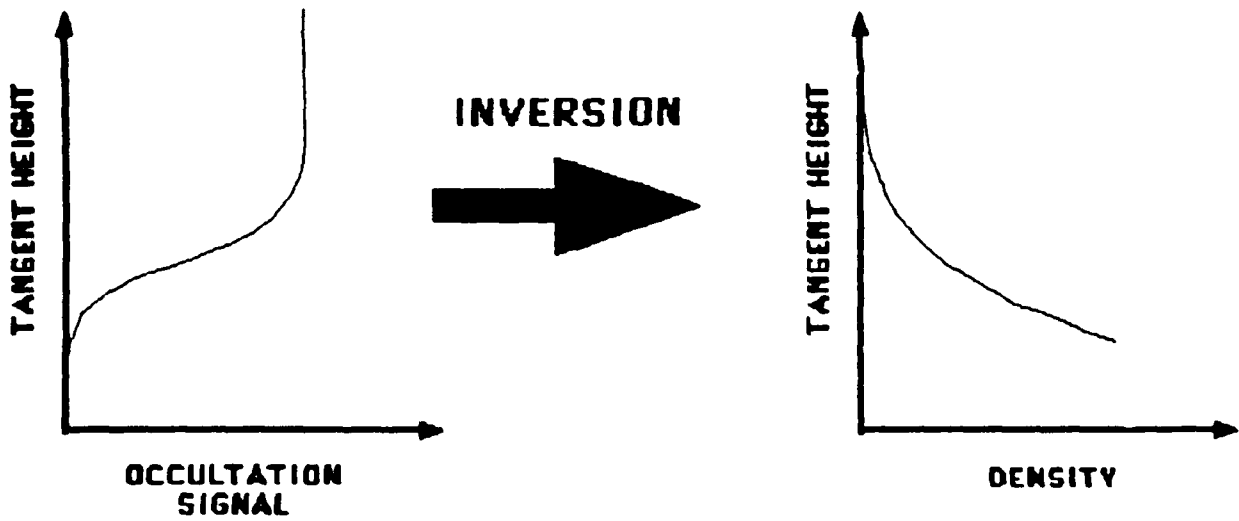
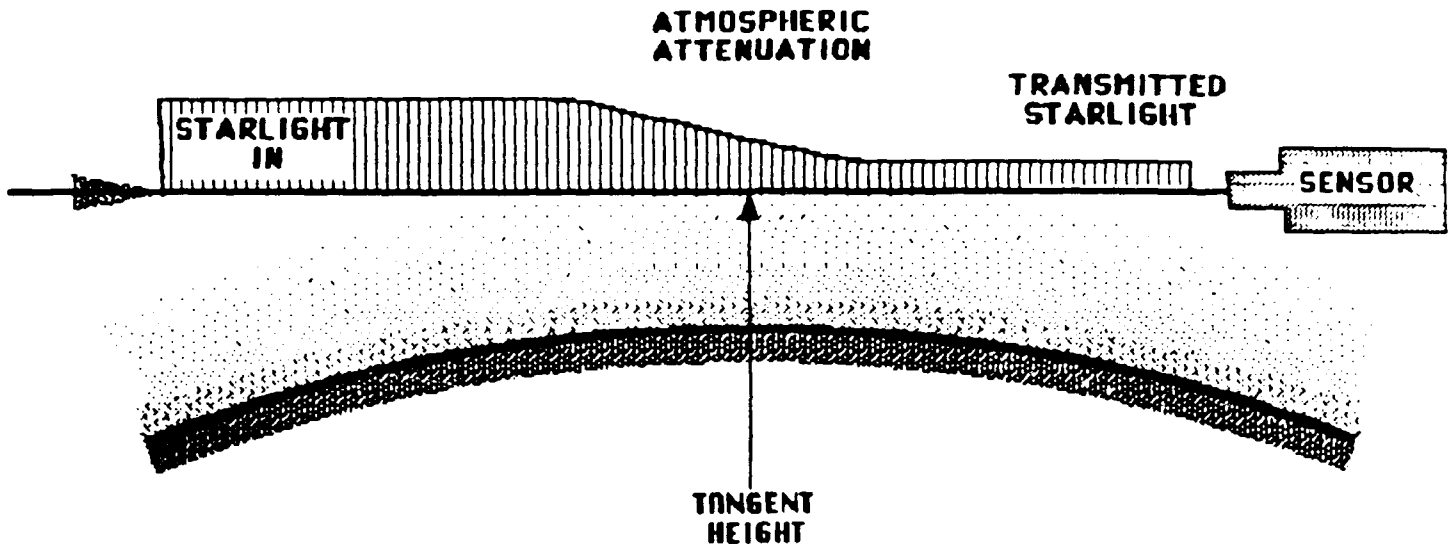
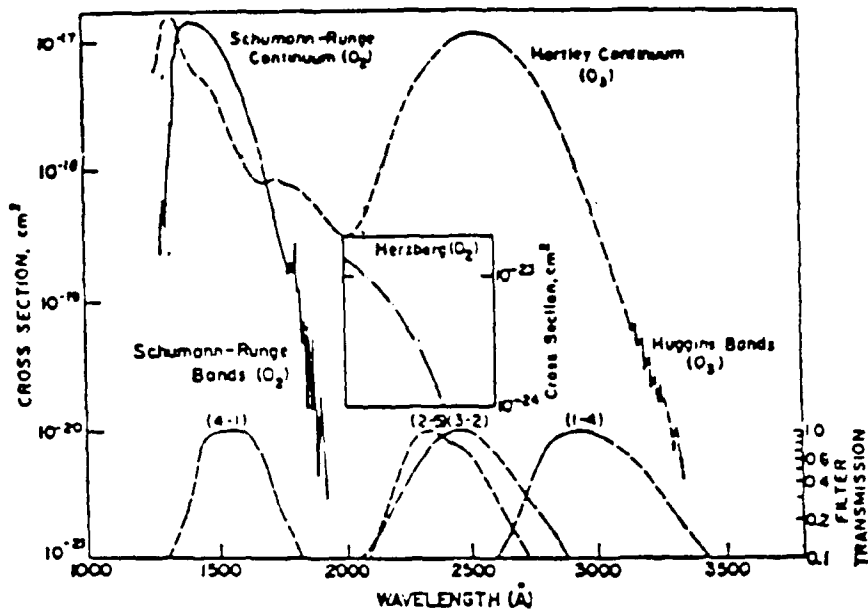


Figure 7

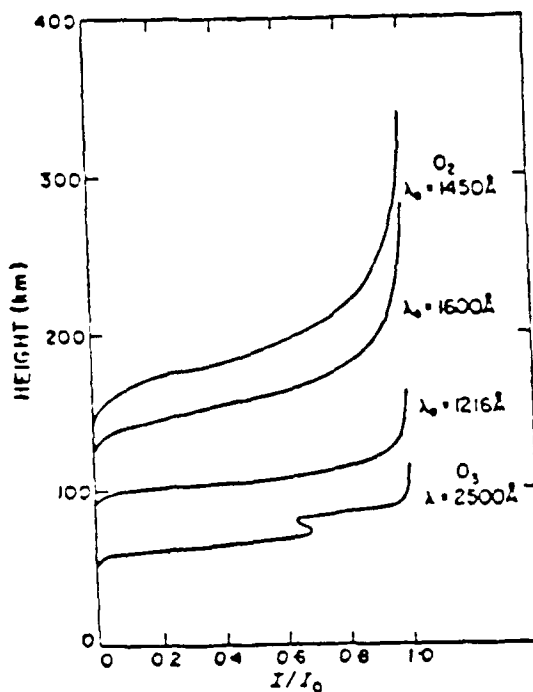
STELLAR OCCULTATION MEASUREMENTS OF MOLECULAR OXYGEN



ABSORPTION CROSS SECTIONS FOR MOLECULAR OXYGEN AND OZONE IN THE SPECTRAL REGION EXTENDING FROM 1000 TO 3500 Å. DASHED CURVES ARE THE O.A.O. STELLAR PHOTOMETER FILTER TRANSMISSION CURVES USED IN THIS STUDY.

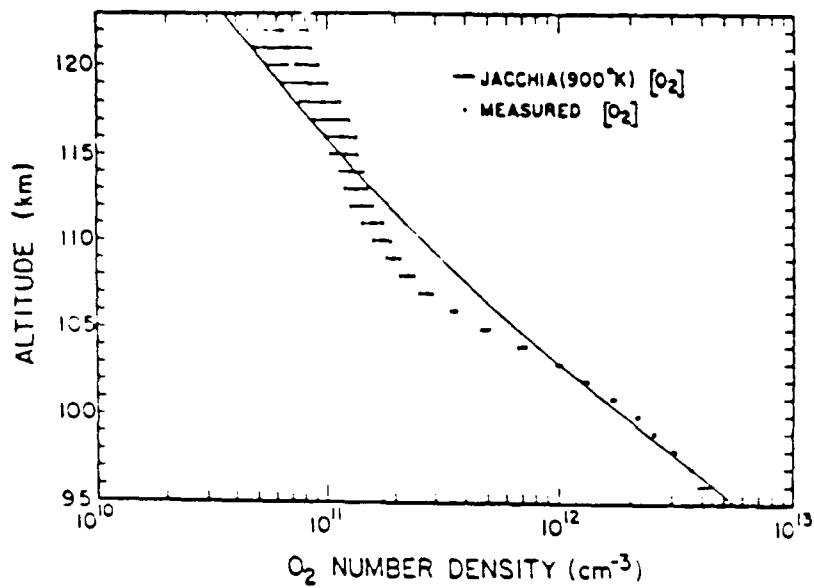
Figure 8

STELLAR OCCULTATION MEASUREMENTS OF MOLECULAR OXYGEN



THE NORMALIZED TANGENTIAL TRANSMISSION OF THE EARTH'S ATMOSPHERE AT VARIOUS WAVELENGTHS AS A FUNCTION OF HEIGHT.

Figure 9



The measured O₂ densities and associated error bars. The Jacchia [16] model (900K) O₂ density profile is shown by the solid line curve. Atreya et al [7].

Figure 10

RAYLEIGH SCATTERING

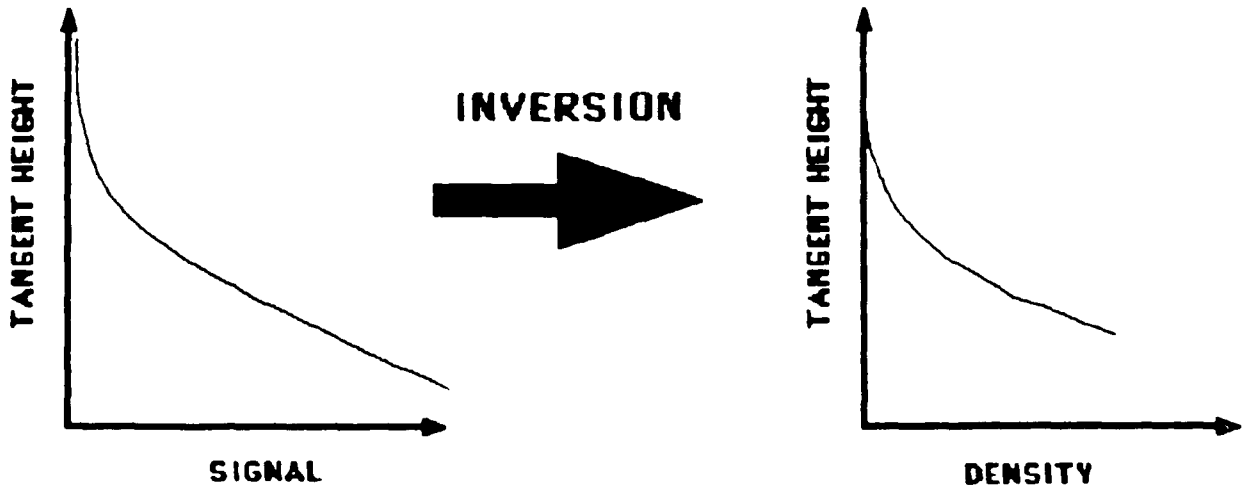
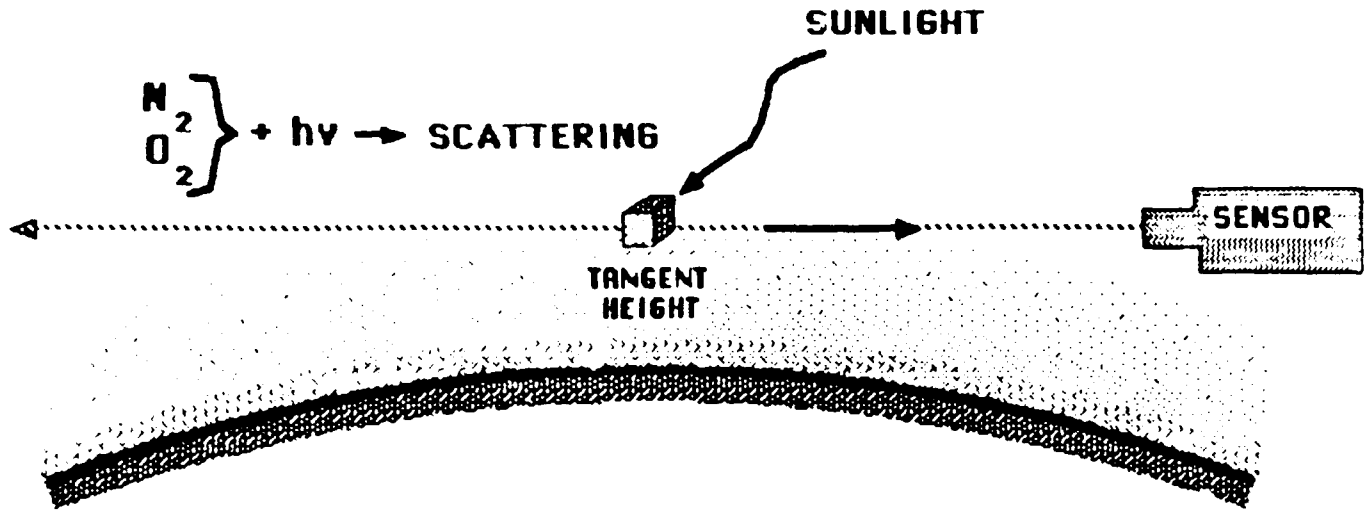


Figure 11

4.7

Determination of Atomic Oxygen
Density and Temperature of the
Thermosphere by Remote Sensing

Ramesh D. Sharma
Infrared Dynamics Branch
Air Force Geophysics Laboratory
Hanscom AFB, MA 01731

Harry B. Harlow

and

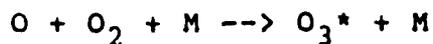
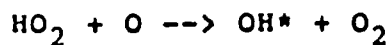
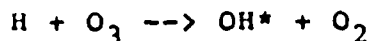
James P. Riehl
Department of Chemistry
University of Missouri-St. Louis
St. Louis, MO 63121

ABSTRACT

Measurement of emission from the earth's atmosphere in the far infrared due to transitions between fine structure levels of the ground state (3P) of atomic oxygen at $63\mu\text{m}$ ($^3P_1 \rightarrow ^3P_2$) and $147\mu\text{m}$ ($^3P_0 \rightarrow ^3P_1$) is proposed. These magnetic-dipole allowed transitions with long radiative lifetimes (~ 3.2 hrs for the $63\mu\text{m}$ transition and ~ 16.3 hrs for the $147\mu\text{m}$ transition) are assumed to be in equilibrium with the local translational temperature. A one-dimensional onion-peel inversion of the limb emissions at $63\mu\text{m}$ and $147\mu\text{m}$ from a model atmosphere is shown to yield reasonable results for both the temperature and atomic oxygen density in the 90-250 km altitude range.

I. INTRODUCTION

Atomic oxygen is an important constituent of earth's atmosphere above 90 km and the most abundant constituent above about 200 km [U.S. Standard Atmosphere, 1976]. It has long been known to play an important role in the heat balance and chemistry of the upper atmosphere. Bates [1951] suggested that the fine structure transition $O(^3P_1) \rightarrow O(^3P_2)$ at $63\mu\text{m}$ plays an important part in cooling the upper thermosphere. The $5.3\mu\text{m}$ emission from vibrationally excited nitric oxide, which in the quiescent atmosphere is produced solely [Caledonia and Kennealy (1982)] by collisions of nitric oxide in the ground state with atomic oxygen, was shown by Kockarts [1980], Gordiets et al. [1982], Stair et al. [1985] and Zachor et al. [1985] to be the dominant cooling mechanism in the lower thermosphere. Around 100 km, $15\mu\text{m}$ emission from the bending mode of CO_2 , which again is excited primarily by the collisions of oxygen atoms with ground state carbon dioxide [Sharma et al. (1981)], plays a dominant role in cooling the atmosphere [Dickinson (1984)]. At still lower altitudes [Sharma (1985)], atomic oxygen plays an important role in the emission for the hydroxyl airglow layer and chemiluminescence from O_3 via the reactions



We thus see that atomic oxygen, directly or indirectly, plays a vital role in the heat balance of the upper atmosphere.

Offermann, et al. [1981] have reviewed the methods used, all in situ, for the measurement of atomic oxygen densities in the upper atmosphere. Sharp [1985] has commented on results of these measurements: "The data show a variation in the concentrations by over a factor of 10 at 120 km, a factor of 40 for the peak at about 95 km and much larger factors below this. Peak concentrations range from $6 \times 10^{10} \text{ cm}^{-3}$ to $2 \times 10^{12} \text{ cm}^{-3}$. Within any one technique there are factors of 5 variations over altitude. Some of this variation can be due to time of day, season and dynamics. However, the principal source of the variation is probably the differing measurement techniques."

While several methods for measuring the density of atomic oxygen in the thermosphere have been undertaken and critically reviewed, we have not come across corresponding experiments or critical reviews for the measurement of thermospheric temperature. Zachor et al. (1985) tried obtaining temperature as a function of altitude from the envelope of the limb emission observed from vibration-rotation transitions of nitric oxide at $5.3 \mu\text{m}$ observed in the 110-150 km tangent height range. The results obtained were not satisfactory. This may be due, in large part, to the rather weak dependence of the vibration-rotation band envelope on temperature. Although the problem may perhaps be remedied by measuring emission from carefully selected lines of the vibration-rotation band, it has not been tried thus far. In

addition, the nitric oxide emission decreases rapidly [Stair et al. (1985)] above 150 km due to decreasing density, and, therefore, above this tangent height other methods for determining the temperature have to be developed.

In this work we describe a method of measuring the oxygen atom density and temperature by remote sensing. The method consists of simultaneous measurement of intensity in the $63 \mu\text{m}$ $^3\text{P}_1 \rightarrow ^3\text{P}_2$ transition and the $147 \mu\text{m}$ $^3\text{P}_0 \rightarrow ^3\text{P}_1$ transition (Figure 1) between the ground state fine structure levels. We assume that these fine structure levels are in thermodynamic equilibrium with the local translational temperature (LTE), and that the atmosphere is one-dimensional. Radiance in the $63 \mu\text{m}$ and $147 \mu\text{m}$ lines is calculated using a model atmosphere and a modified form of the radiation transport code of Sharma et al. [1983]. An onion-peel inversion is then carried out to show that it is possible to recover the density and temperature. Although the present inversion was performed on the "data" which had no noise, work in progress adds noise to the radiance "data" before carrying out the inversion. The principal aim of this work is to show that it is possible to develop reliable procedures for the recovery of oxygen atom density and temperatures as a function of altitude from the limb radiance data.

The assumption that the fine structure levels are in thermodynamic equilibrium with the translational temperatures (LTE) needs some elaboration. Grossmann and Offermann [1978] concluded from their measurements at $63 \mu\text{m}$ that this assumption is not a

valid one and that the population of the 3P_1 level is less than that given by the LTE model. Iwagami and Ogawa [1980] argue that the Grossmann-Offermann results are consistent with LTE formulation if radiative transfer is properly treated. Our computation of the 63 μm radiance using the model atmosphere kindly supplied by Dr. D. Offerman agrees with Grossmann-Offermann results. Grossman et al (1985) have re-examined the situation and have suggested that if a value of the Einstein Coefficient $A_{12}=4.5 \times 10^{-5} \text{ s}^{-1}$ for the 63 μm transition is used (nearly one-half the calculated value), the computed radiances are in reasonable agreement for one (1981) of the two sets of rocket experiments. We are not quite sure of uncertainties involved in the model atmosphere. For example, an increase of about 25% in atomic oxygen density would bring the results obtained from this model atmosphere in agreement with the emission observed by the 1981 rocket experiment. There are serious reasons not to either alter the value of the radiative lifetime of the 3P_1 excited state or to discard the LTE hypothesis. In an elaborate study, Fischer and Saha [1983] have calculated the radiative lifetime of the 63 μm transition to be 3.192 hrs (11,491 seconds) (Fig. 1). Allison and Burke [1969] estimate the cross-section for transition between the fine structure levels during collisions between two oxygen atoms to be between 0.01 and 1 times the gas kinetic cross-section. At an altitude of 250 km such collisions occur about once every second or about 11,000 collisions per radiative lifetime, enough to populate the 3P_1 state in accordance with LTE.

Lin et al. (1987) have conducted a balloon experiment which measures $63\mu\text{m}$ emission at elevation angles of $+30^\circ$ and $+1^\circ$. From this experiment these authors assuming LTE and using calculated value of Einstein Coefficient A_{12} , have derived peak atomic oxygen density of $3.6 (\pm 1.9) \times 10^{11} \text{ cm}^{-3}$ at an altitude of about 110 km. We would like to reiterate that we are not foreclosing the possibility that either the LTE hypothesis or the values of the Einstein Coefficients may have to be modified in light of further observations. However, the best evidence available at this time favors these hypotheses.

It has been pointed out earlier that the method proposed here is a passive remote sensing technique. The advantages of the method are best exploited by a space-shuttle or a satellite experiment which, in principle, can yield not only diurnal, seasonal, latitudinal and variations due to geomagnetic disturbances but also time constants for reaching new steady states. There is no reason why the method outlined here should not be used to study other planets. For example, in both Venus and Mars, the atomic oxygen is believed to be an important constituent of the atmosphere above 100 km [Chamberlain (1978)]; the method outlined here may be used to obtain quantitative results.

II. THEORY AND METHODOLOGY

A derivation of the radiative transfer equation has been given by Sharma et al. [1983], Sharma and Zachor [1983] and Zachor and Sharma [1985]. We present here a brief summary of the

formalism. In one-dimensional models of the atmosphere, the atmospheric parameters, e.g., temperature, density, etc., depend only on the altitude z . To calculate the emission and transmission of radiation we divide the line-of-sight (LOS) into segments of thickness (Δz) such that the atmospheric parameters over each segment may be assumed to be constant.

We express the radiance in terms of n_ν , the number of photons (of frequency ν cm^{-1}) per wavenumber per unit area per steradian which are observed at a point z along the line-of-sight per unit time. The change in n_ν in a path length ds is described by

$$dn_\nu/ds = \{-n_\nu(h\nu_0/c)[n_l B(l \rightarrow u) - n_u B(u \rightarrow l)] + A_{u1} n_u / 4\pi\} f(\nu - \nu_0) \quad (1)$$

where h and c are Planck's constant and the speed of light; n_l and n_u are the number densities of the lower and upper radiating states; $B(l \rightarrow u)$ and $B(u \rightarrow l)$ are Einstein coefficients for absorption and induced emission; A_{u1} is the Einstein coefficient for spontaneous emission, and f is a normalized lineshape function such that

$$\int f(\nu - \nu_0) d\nu = 1 \quad (2)$$

The Einstein coefficients are related by

$$g_l B(l \rightarrow u) = g_u B(u \rightarrow l) \quad (3)$$

and

$$A_{u1} = 8\pi h\nu_0^3 B(u \rightarrow 1) \quad (4)$$

where g_l and g_u are the statistical weights of the lower and upper radiating states. Through use of Eqs. (3) and (4), Eq. (1) can be cast in the form

$$dn_\nu/ds = (h\nu_0/c)B(1 \rightarrow u)n_1[-n_\nu(1-\gamma) + 2c\nu_0^2\gamma]f(\nu-\nu_0) \quad (5)$$

where γ is defined as

$$\gamma = g_l n_u / g_u n_l \quad (6)$$

The factor $(1-\gamma)$ corrects the simple absorption term (which is proportional to $n_l n_\nu$) for stimulated emission. The second term in brackets corresponds to spontaneous emission.

We now define the optical depth, τ_ν , by

$$d\tau_\nu/ds = (h\nu_0/c)B(1 \rightarrow u)f(\nu-\nu_0)n_l(1-\gamma) \quad (7)$$

Substituting Eq. (7) in Eq. (5) we get the result

$$dn_\nu/d\tau_\nu = [-n_\nu + 2c\nu_0^2\gamma/(1-\gamma)] \quad (8)$$

This equation has a very simple physical meaning. The rate of change of the number of photons with absorption depth decreases

as the numbers of photons incident on the segment and increases with the source function. Under conditions of LTE the source term is seen equal to the black-body function when we recall that γ (Eq. 5) under these conditions equals

$$\gamma = \exp[-(E_u - E_l)/kT] = \exp[-C_2 \nu_0/T] \quad (9)$$

where E_u and E_l are the energy levels of the upper and lower states; k is the Boltzmann constant; C_2 [$= 1.4388$ (K/cm^{-1})] is the second radiation constant, and T is the temperature.

This equation can easily be integrated across a segment of constant temperature and density. The solution is

$$n_\nu(z_{i+1}) = n_\nu(z_i) \exp(-\Delta\tau_{\nu i}) + 2c\nu_0^2 [1 - \exp(-\Delta\tau_{\nu i})] \gamma_i / (1 - \gamma_i) \quad (10)$$

where the segment-dependence of γ has been made explicit with the subscript i . In Eq. (10), the first term represents the absorption within the i th segment of radiance incident upon it at z_i , and the second term represents the contribution from the i th segment alone; $\Delta\tau_\nu$ the change in optical depth across a segment can be written as

$$\Delta\tau_\nu = (A_{ul} g_u / 8\pi c \nu_0^2 g_l) n_l (1 - \gamma) f(\nu - \nu_0) \Delta s \quad (11)$$

where Δs is the length of the segment.

In this study the Einstein coefficients for ground-state atomic oxygen along with assumed density, temperature, and pressure atmospheric profiles were input data for a modified form of the NLTE computer code developed at the Air Force Geophysics Laboratory (Sharma et al. [1983], Wintersteiner and Sharma [1985]). The modifications were accomplished such that the program calculates the radiance for the $O^3P_2 \leftarrow O^3P_1$ transition at $63\mu\text{m}$ and the $O^3P_1 \leftarrow O^3P_0$ transition at $147\mu\text{m}$ in the earthlimb (or Zenith) geometry for any range of tangent heights (or altitudes) within the range of the assumed atmospheric profile.

The atmospheric density and temperature profiles used in this study are plotted in Figure 2. This density profile was selected by comparison with previous estimates of O-atom densities, and represents a reasonable guess at the true density. Two additional density profiles corresponding to atmospheres two times and five times as rich in atomic oxygen as that given in Figure 2 were also studied in order to test the accuracy and reliability of the numerical inversion technique.

The integrated line radiances calculated from Eq. 2 are plotted versus tangent height in Figure 3 for both transitions appropriate for the atmospheric profile given in Figure 2. In these calculations it was assumed that the energy levels were in local thermodynamic equilibria. A voigt lineshape with a collisional line width equal to 0.1 cm^{-1} per amagat was assumed in all of the work reported here. A weak $T^{-1/2}$ dependence of collisional linewidth upon temperature [Penner (1959)] was ignored.

For the purpose of this initial study, as was pointed out earlier, it is assumed that this data corresponds to "exact" total integrated radiance data for the two transitions. In the next section, we describe a numerical procedure to "invert" this data for the purpose of recovering the assumed density and temperature profiles. Consideration of errors due to finite signal to noise and other experimental factors will be presented and discussed in a later paper.

III. Numerical Inversion of the Integrated Radiance

In order to start the inversion procedure, it was assumed that, at the highest tangent heights considered, the transitions are optically "thin". That is, no significant self-absorption takes place. In this case, the integrated radiance for the transition $i \leftarrow j$, N_{ij} , depends only on the excited state (O^3P_j) density profile, which is directly related to the ground state density through the temperature under the assumed conditions of thermodynamic equilibrium. Formally, we may write

$$N_{ij}(H_T) = (1/2\pi) \int \epsilon_{ij}(z)W(z, H_T)dz, \quad (12)$$

where H_T is one tangent altitude and $\epsilon_{ij}(z)$ is the total volume emission rate at altitude z .

$$\epsilon_{ij}(z) = n^*(z)A_{ij} \quad (13)$$

In Eq. (12), $W(z, H_T)$ is a geometrical weighting factor that

converts distance dl along limb line-of-sight to altitude dz , $Wdz = dl$,

$$W(z, H_T) = (R+z)[(R+z)^2 - (R+H_T)^2]^{-1/2} \quad (14)$$

where R denotes the radius of the earth.

The high altitude density profile is obtained by first assuming that the density decreases exponentially

$$n_j^*(z) = n_j^*(H_T)\exp(-\beta z) \quad (15)$$

Using Eqs. (13) and (15) in Eq. (12) we obtain the result

$$N_{ij}(H_T) = (1/2\pi)n_j^*(H_T)A_{ij} \int \exp(-\beta z)W(z, H_T)dz \quad (16)$$

The integral in Eq. (16) can be evaluated analytically with the result

$$N_{ij}(H_T) = A_{ij}n_j^*(H_T)\exp[\beta(R+H_T)](R+H_T)K_1[\beta(R+H_T)] \quad (17)$$

K_1 is the modified Bessel function. The two unknowns in this equation [n_j^* and β] can be evaluated by considering the integrated radiance at the two highest tangent heights for which radiance data is available. An approximate excited state density profile for the highest altitude regions can then be constructed from Eq. (15). We have made the additional assumption that the

temperature in this region varies in a linear fashion, and can be approximated from known temperature profiles. These approximations appear to be reasonable, and, in fact, as long as the highest measurement is far removed from the atmospheric region of interest these "starting" values have little effect on the results at lower tangent heights.

Inversion of the radiance through the lower tangent heights is accomplished by solving for the minimum in the function

$$L(T, n, H_T) = \frac{[N_{21}(H_T) - N_{21}^P(H_T)]^2}{N_{21}(H_T)^2} + \frac{[N_{10}(H_T) - N_{10}^P(H_T)]^2}{N_{10}(H_T)^2} \quad (18)$$

$N_{ij}^P(H_T)$ denotes the predicted radiance at tangent height, H_T . The two terms in this equation have been separately normalized in order for them to be weighted equally. In the work described here, we have also multiplied this function by a "penalty" function in order to avoid mathematical diversions involving large temperature changes. Such diversions in temperature are not uncommon in problems of this type in which the variables T and n are somewhat correlated. The resultant function is given below

$$f(T, n, H_T) = \bar{\xi}(T, n, H_T) \exp(0.01|\Delta T|) \quad (19)$$

where $\Delta T = T - T_p$. T_p denotes the temperature of the previous slab, and the bar denotes that this function has been normalized. If some constraint is not placed upon the temperature variable, then relatively large oscillations in temperature may occur in

certain regions of function space. These temporary oscillations around the true solution are due to a very flat function in which relatively large changes in temperature can be offset by opposing all changes in density.

The inversion technique that we have chosen to use in this initial study is a so-called "onion-peel" method. In this approach, one determines the best value for the density and temperature for the atmospheric slab of thickness 1 km at the current tangent height. Following the generation of a high atmosphere profile, as described above, we begin the solution of eq. (19), by choosing as our initial guess, the oxygen atom density and temperature of the previous slab. The limb radiance at the current tangent height depends, of course, on the density and temperature of all slabs of higher altitude. This requires the inversion to be performed with high accuracy at each tangent height, so that the cumulative errors do not result in making inversion at lower tangent heights impossible.

In order to minimize the number of computations, for each tangent height all of the frequency independent parts of the radiative transfer equation are calculated only once. Even with this effort, because the path length through each slab changes for each tangent height, the calculated total radiance for the two transitions is computationally expensive, especially for low tangent heights where the number of slabs is large. It is important, therefore, to select a numerical procedure that will lead to rapid convergence. A common approach to rapid solutions of

problems of this complexity is to use so-called conjugate methods in which the good attributes of more than one method are combined. For this reason, we have chosen to solve for the minimum in Eq. (19) through a combined "steepest descent" and Newton-Raphson numerical procedure. Efficiency of the solution of Eq. (19) is improved due to the insensitivity of the steepest descent method to the initial guess, and the rapid (quadratic) convergence of the Newton-Raphson method. This numerical technique is commonly referred to as a "modified Newton method" [Bazarra (1979)].

Formally, we write the solution vector for the (k+1)th slab, $x_{k+1} = (n_{k+1}, T_{k+1})$ as follows

$$x_{k+1} = x_k - [H + \lambda \text{diag}(H)]^{-1} \nabla J|_x \quad (20)$$

where λ is a parameter selected to make the matrix in brackets negative definite, and H is the Hessian matrix of second derivatives.

$$(H)_{ij} = [\partial^2 J / \partial \alpha_i \partial \alpha_j] \quad (\alpha_i = n; \alpha_j = T) \quad (21)$$

Additional savings in computation is achieved by approximating the Hessian matrix of second derivatives (which is required in the Newton-Raphson procedure) by the vector product of the gradient (∇J) and its transpose. If the matrix in eq. (20) is not invertible, then the eigenvalue and eigenvectors of the Jacobian matrix of derivatives are evaluated. This process essentially

transforms the dependent set (n, T) into an approximately independent set of pseudovariables which are derived from the eigenvectors. The eigenvalues of the Jacobian are used for scaling purposes. This numerical method is a variation of the method developed by Marquardt [1970]. In the work described here, this combined method is found to converge for initial guesses far from the true value, while it converges at least supralinearly for convex regions "close" to the true solution [Harlow and Riehl (to be published)].

One cycle of the numerical procedure described above yields a next guess for the solution vector x_k . For each new estimate of T_k and n_k , boundary conditions are checked, and, if exceeded, the result is reflected back into a preset allowed region. The process is repeated until $\xi(T, n, H_T) \leq 1 \times 10^{-6}$.

IV. Results and Conclusions

The results from the inversion procedure described above are plotted in Figures 4, 5, and 6 for the three different atmospheric profiles. The solid lines in these figures are the assumed temperature and density profiles. In Figure 4, it can be seen that the inversion was started at a tangent height of 200 km, i.e. below the highest altitude used in the calculation of the radiances (230 km), in order to simulate the kind of data that would be available from an actual experimental measurement. In Figures 5 and 6, the numerical inversion was begun at the highest

value of the assumed atmospheric profile. [In these cases the profile was extended out to 300 km.] As can be seen in these figures, the errors associated with the assumptions for the high altitude regions are not large, and are significantly reduced after a small number of inversion steps.

As is evident from the results in Figures 4-6, the inversion is quite successful for both temperature and density until the very "optically thick" regions of the atmosphere are reached. Below about 90 km (95 km for the high density atmospheres) self-absorption is so strong that the integrated radiances for the two transitions are almost constant. This can be seen, for example, in the plots of radiance versus tangent height in Figure 3. Continuation of the inversion through these regions leads to large oscillations in both temperature and density.

All three results show one or more small discontinuities in the inversion results especially in the recovered temperature values. In Figure 4, for example, these occur at approximately 120 and 130 km. These discontinuities, which are not unusual for nonlinear optimization problems of this complexity, are due to the fact that multiple solution pathways exist at these particular tangent heights. These oscillations are significantly reduced through use of the "penalty" function as described above.

Extensions of the work reported here are underway. In particular, more advanced numerical techniques are under study, and procedures to invert radiance data in which noise and finite

spectral resolution have been added are under development. It is felt that measurements of emission at $63\mu\text{m}$ and $147\mu\text{m}$ have enormous potential in remote sensing of atomic oxygen and temperature.

ACKNOWLEDGMENTS

Research sponsored by the Air Force Office of Scientific Research/AFSC, under Contract F49620-85-c-0013. The United States Government is authorized to reproduce and distribute reprints for governmental purposes notwithstanding any copyright notation hereon. The authors are grateful to Dr. Don Ball and Dr. Frank Wodarczyk for generous support of this work. Dr. R.E. Murphy kindly provided the stimulus and environment for this work.

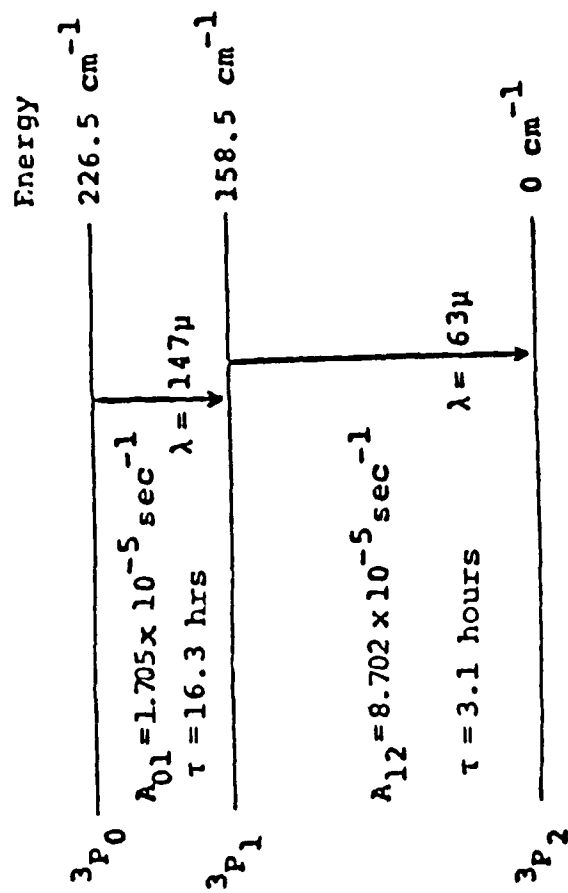
REFERENCES

- Allison, D. C. S., and P. G. Burke, Inelastic collisions of slow atoms, J. Phys., 2, 941, 1969.
- Bates, D. R., The temperature of the upper atmosphere, Proc. Phys. Soc., 64b, 805, 1951.
- Bazaraa, M. S., and C. M. Shetty, Nonlinear Programming, John Wiley and Sons, New York, 1979.
- Caledonia, G. and J. Kennealy, NO infrared radiation in the upper atmosphere, Planet. Space Sci., 30, 1043, 1982.
- Chamberlain, Joseph W., "Theory of Planetary Atmospheres", Academic Press, New York, N.Y. (1987).
- Dickinson, R. E., Infrared radiative cooling in the mesosphere and lower thermosphere, J. Atmos. Terr. Phys., 46, 995-1008 (1984).
- Fischer, C. F., and H. P. Saha, Multiconfigurational Hartree-Fock results with Breit-Pauli corrections for forbidden transitions in the $2p^4$ configuration, Phys. Rev. A, 28, 3169, 1983.
- Gordiets, B.F., Yu. N. Kulikov, M. N. Markov, and M. Ya. Marov, Numerical modeling of the thermospheric heat budget, J. Geophys. Res., 87, 4504, 1982.
- Grossmann, K. U., P. Barthol, W. Frings, R. Henning, and I. Offermann, Eine analyse von messungen der infrarotemissionen atmosphärischer spurengase, Berische Universität --- Gemathochschule Wuppertal, 1985.
- Grossman, K. U., and D. Offerman, Atomic oxygen emission at $63 \mu\text{m}$ as a cooling mechanism in the thermosphere and ionosphere, Nature, 276, 594, 1978.
- Iwagami, N. and T. Ogawa, Thermospheric $63 \mu\text{m}$ emission of atomic oxygen in local thermodynamic equilibrium, Nature, 298, 594, 1982.
- Kockarts, G., Nitric oxide cooling in the terrestrial atmosphere, Geophys. Res. Lett., 7, 137, 1980.
- Liu, F. J., K. V. Chance, and W. A. Traub, Atomic oxygen in the lower thermosphere, J. Geophys. Res., 92, 4325, 1987.
- Marquardt, D. W., Generalized inverses, ridge regression, biased linear estimation, and nonlinear estimation, Technometrics, 12, 591, 1970.

- Offerman, D., V. Friedrich, P. Ross, and U. Von Zahn, Neutral gas composition measurements, Planet. Space Sci., 29, 747, 1981.
- Penner, S. S., "Quantitative Molecular Spectroscopy and Gas Emissivities", Addison-Wesley, Reading, Massachusetts 1959.
- Sharma, R. D., Infrared Airglow, "Handbook of Geophysics and the Space Environment" (Chapter 13), NTIS No. ADA167000 Air Force Geophysics Laboratory, Air Force Systems Command, U. S. Air Force, 1985.
- Sharma, R. D., and R. M. Nadile, Carbon dioxide (v_2) radiance results using a new non-equilibrium model, Paper presented at the 19th Aeroscience Meeting, Am. Institute of Aeronautics and Astronautics, St. Louis, MO, Jan. 12-15, 1981.
- Sharma, R. D., R. D. Siani, M. K. Bullit, P. P. Wintersteiner, A Computer Code to Calculate Emission and Transmission of Infrared Radiation Through Non-Equilibrium Atmospheres, AFGL-TR-83-0168, NTIS No. ADA137162, Air Force Geophys. Lab., Hanscom AFB, Mass. 1983.
- Sharma, R. D., and A. S. Zachor, Tests of an inversion algorithm for spectrally resolved limb emission, Appl. Opt., 22, 2665, 1983.
- Sharp, W. E., Upper limits to [O] in the lower thermosphere from airglow, Planet. Space Sci., 33, 571, 1985.
- Stair, A. T., Jr., R. D. Sharma, R. M. Nadile, D. J. Baker, W. F. Greider, Observation of limb radiance with cryogenic Spectral Infrared Rocket Experiment, J. Geophys. Res., 90, 9763, 1985.
- U.S. Standard Atmosphere, 1976, National Oceanic and Atmospheric Administration, National Aeronautics and Space Administration, United States Air Force, Washington, D.C. (October 1976).
- Wintersteiner, P. P. and R. D. Sharma, "Update of an Efficient Computer Code (NLTE) to calculate Emission and Transmission of Radiation Through Non-Equilibrium Atmospheres", AFGL-TR-85-0240, NTIS No. ADA172556, Air Force Geophysics Laboratory, Hanscom Air Force Base, Jan. 1985.
- Zachor, A. S., R. D. Sharma, R. M. Nadile, and A. T. Stair, Jr., Inversion of a spectrally resolved limb radiance profile for the NO fundamental band, J. Geophys. Res., 90, 9776, 1985.

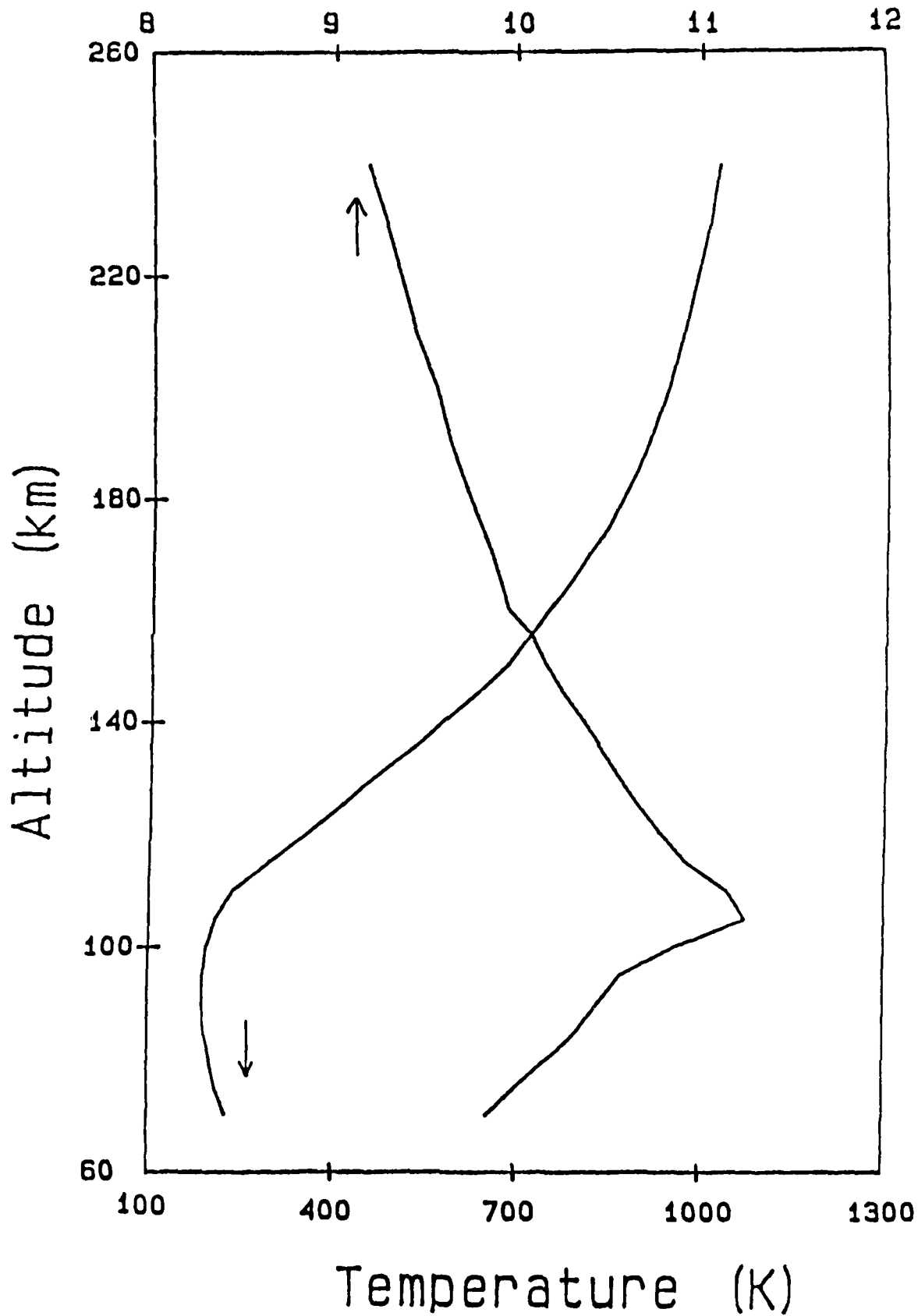
Figure Captions

1. Schematic energy level diagram for the ground state (3P) of atomic oxygen.
2. Assumed atmospheric temperature and density profile for atomic oxygen.
3. Calculated radiance (watts/cm² ster.) versus tangent height (km) for the 63 μm and 147 μm transition of atomic oxygen using the atmospheric profile given in Figure 2.
4. Oxygen atom density and temperature results obtained from numerical inversion for the atmospheric profile given in Figure 2. The solid lines are the assumed density and temperature profiles.
5. Oxygen atom density and temperature results obtained from numerical inversion for an atmospheric profile in which the atomic oxygen density is two times that given in Figure 2. The solid lines are the assumed density and temperature profiles.
6. Oxygen atom density and temperature results obtained from numerical inversion for an atmospheric profile in which the atomic oxygen density is five times that given in Figure 2. The solid lines are the assumed density and temperature profiles.

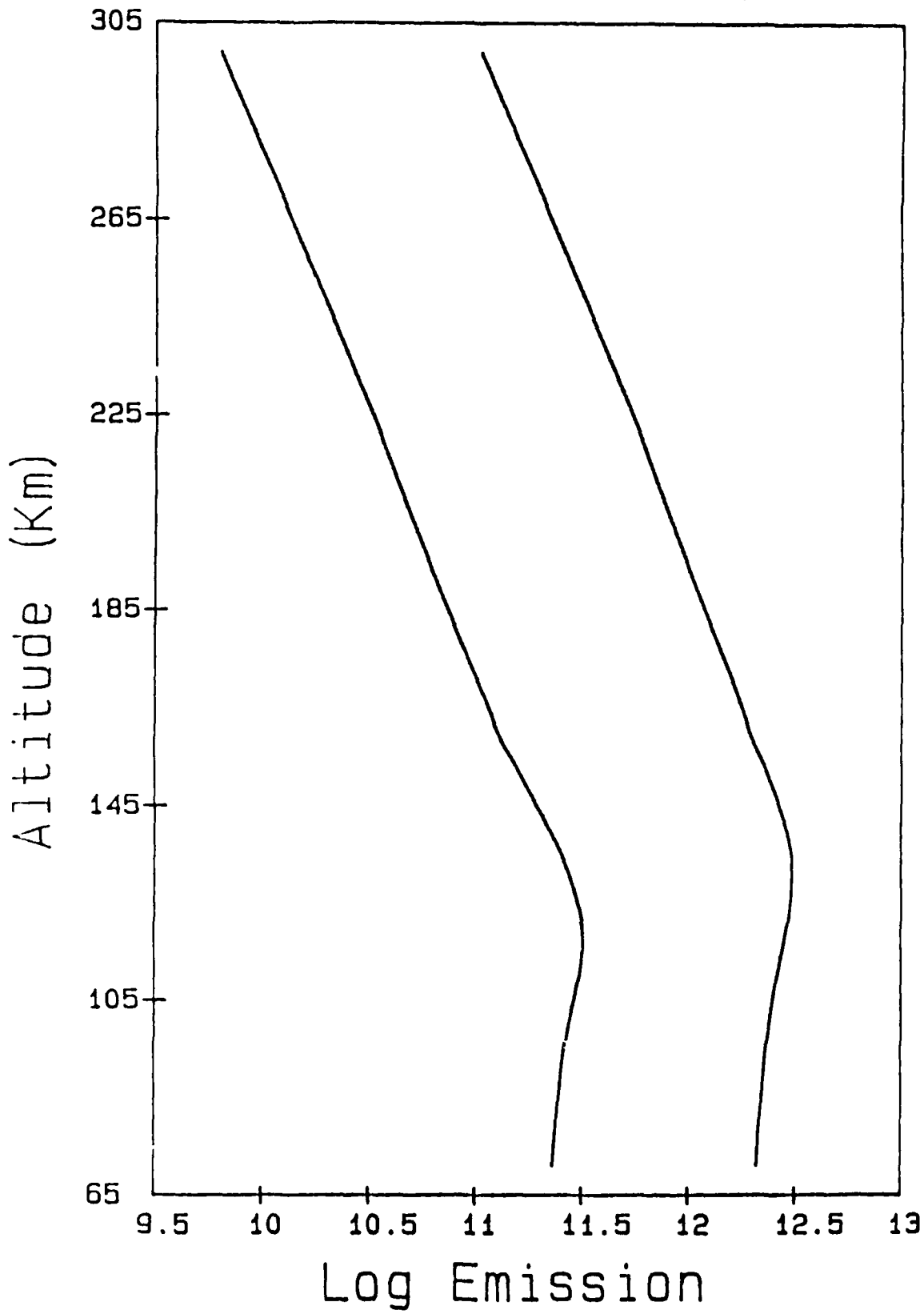


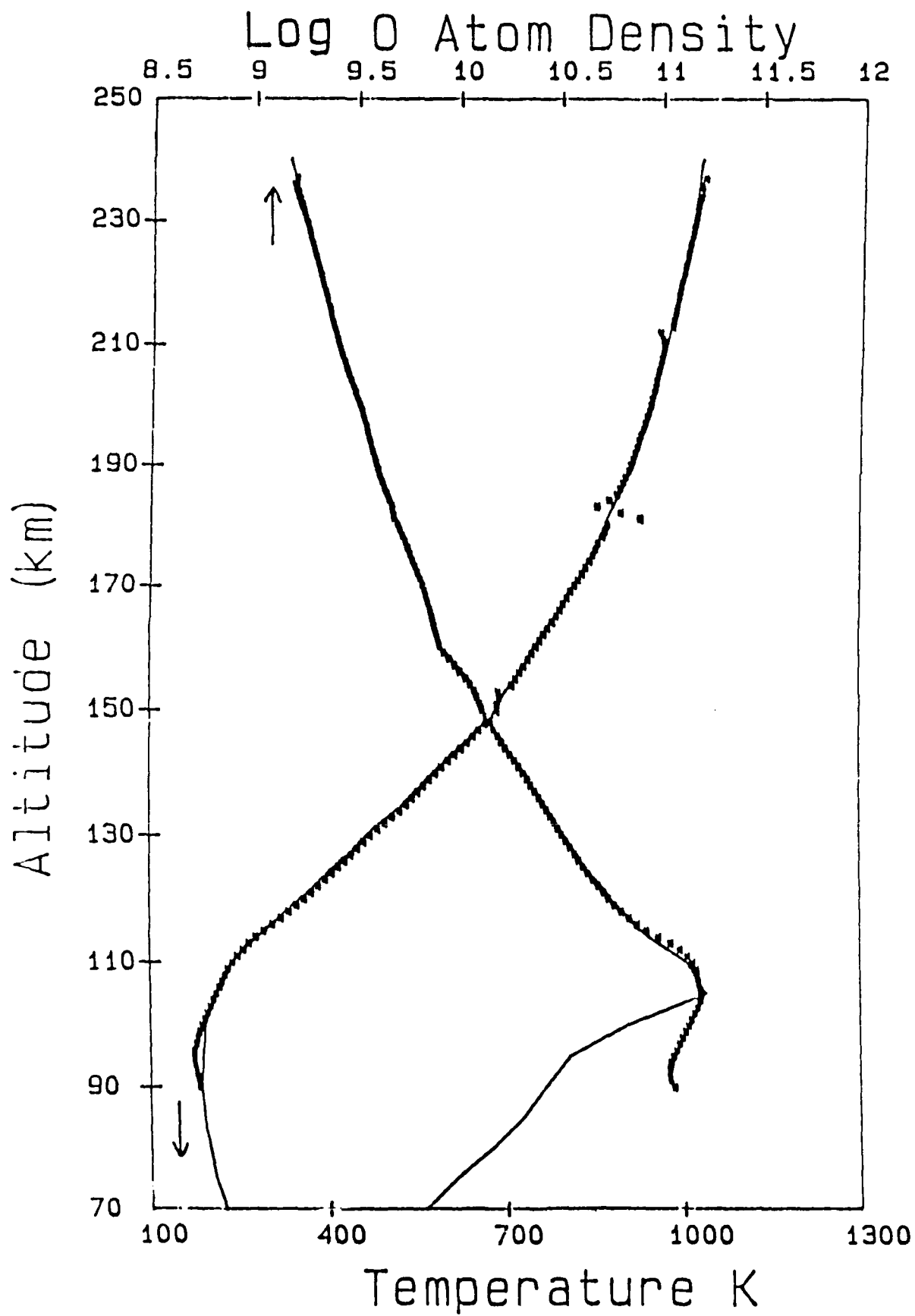
Einstein Coefficients (A's) from Fischer, C.F. and H.P. Saha, Phys. Rev. A
28, 3169 (1983)

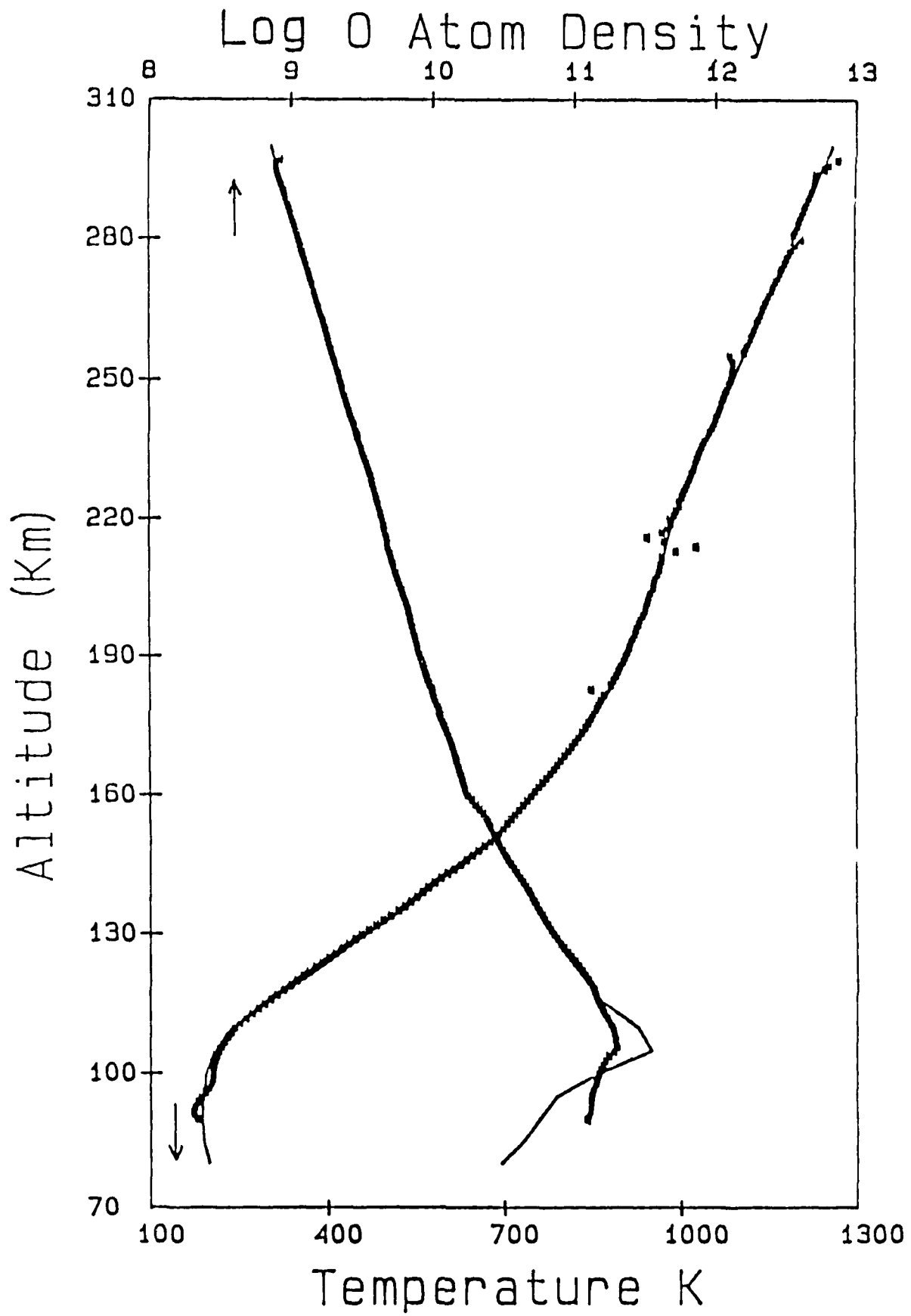
Log O Atom Density



O Atom Emission







ATMOSPHERIC DENSITY MEASUREMENTS
WITH THE REMOTE ATMOSPHERIC AND
IONOSPHERIC DETECTION SYSTEM (RAIDS)

Robert P. McCoy
Code 4142.1
Naval Research Laboratory
Washington, DC, 20375-5000
(202) 767-6109

INTRODUCTION

The scientific objectives of the Remote Atmospheric and Ionospheric Detection System (RAIDS) include the measurement of the dayside and nightside F-region electron density profile, neutral composition and temperature, energetic electron flux distribution and several minor species abundances. The dayside electron density profile will be determined from measurement of the multiply scattered O^+ dayglow emission in the extreme ultraviolet (EUV) primarily at 834 Å. The nightside electron density and temperature will be determined from analysis of O^+ and recombination in the far ultraviolet (FUV) 1300-1700 Å spectral region and at 7774 Å and from O_2^+ recombination at 6300 Å. The neutral composition will be determined from N_2 and emissions and O_2 absorption in the 1300-1700 Å band, and neutral O atom recombination in the 2500-3200 Å O_2 Herzberg I bands. Energetic electron information will be obtained from the N_2 airglow in the Lyman-Birge-Hopfield (LBH) bands (1300-1700 Å) and the N_2 second positive and first negative systems in the near ultraviolet. Density distributions of several minor species such as H, He, N, NO, Mg, Mg^+ , and Na will be obtained from measurements of their emission lines and bands. The sodium measurements will also provide verification of the satellite attitude. A more detailed description of the RAIDS remote sensing techniques is given below.

The RAIDS experiment will be flown on a NOAA TIROS satellite which occupies a sun-synchronous polar orbit at 830 km at a local time of 0730. RAIDS is currently selected to fly on the TIROS J satellite which is scheduled for launch in September 1991 although there is some possibility that RAIDS will fly on an earlier TIROS scheduled to launch 15 months sooner. The actual launch date depends on the health of one or more of the operational satellites

in the orbiting TIROS constellation.

The RAIDS instrument complement includes seven limb-scanning and one limb imaging sensors viewing in the orbital plane of the satellite. The limb-scanning sensors are mounted to a mechanical scan mechanism which scans the instrument fields-of-view through tangent altitudes 75-750 km. The limb-imager continuously views altitudes 75-300 km tangent altitude. The scan platform takes about 97 seconds to complete a limb scan in which time the satellite has moved about 5 degrees in latitude.

REMOTE SENSING OF NEUTRAL TEMPERATURE:

Neutral atmospheric temperatures will primarily be determined with the RAIDS experiment by measurement of topside scale heights of emission profiles of a number of airglow emitters including N_2 , O, and NO. The primary candidates for these temperature measurements are those optically thin emissions produced by photoelectron impact excitation. At the higher altitudes the photoelectron flux is essentially independent of altitude so the scale heights depend on the density of the emitting species. Similarly, scale heights of optically thin emission produced by resonant or fluorescent scattering of sunlight depend only on the density of the emitting species as long as the chemical lifetimes are long.

Additional techniques for temperature sensing with RAIDS will include measurements of the rotational line intensity distribution in molecular bands such as the O_2 Atmospheric bands. Even with limited spectral resolution it will be possible to sample the intensity distribution over several parts of the band. The results will be compared to synthetic spectra to provide the temperature. This technique will be most useful during the daytime at low altitudes.

ATOMIC OXYGEN DENSITY

DAYSIDE:

The most promising technique so far for obtaining the O density involves measurement of the ratio of emission lines at 1304 Å and 1641 Å. Meier and Conway (Geophys. Res. Lett., 12, 601, 1985) have shown that this ratio is a linear function of the O density and should provide the O density above 120 km. Additional techniques for O determination involve modelling of photoelectron impact excitation of O emissions (eg. 1356 Å) and O^+ emissions (eg. 617 Å).

Atomic oxygen densities can be inferred indirectly by examination of the effects of quenching of airglow emissions. For

example, the upper excited state of N_2 Vergard-Kaplan (VK) bands are susceptible to quenching and observations of these emissions could yield the O density in the 120-200 km altitude region.

The delta bands of nitric oxide are produced by the two-body association of N and O atoms. If the NO delta bands can be reliably observed on the dayside above the rayleigh scattering background these emissions would yield the O density down to 100 km or lower.

NIGHTSIDE:

The principal techniques for measuring O at night using the RAIDS observatory will involve the measurements of nightglow emissions produced by the release of chemical energy associated with O atom recombination. The primary candidates are the O_2 Herzberg I bands ($O + O + M \rightarrow O_2 + M$), the NO delta bands ($N + O \rightarrow NO$), and the NO_2 continuum ($NO + O \rightarrow NO_2$). All three band systems have been observed in the terrestrial nightglow. Since these emissions mechanisms involve chemical reactions, some modelling will be required to extract the O density. Ultimately, the success of these methods will depend on the quality of the signal obtained from these nightglow emissions.

MOLECULAR NITROGEN DENSITY

Photoelectron impact excitation of N_2 produces observable airglow emissions in a number of band systems including the Birge-Hopfield (BH), LBH, VK, Second Positive, and First Negative. Observations of these emissions, when combined with a photoelectron flux model as discussed above, can be used to infer the N_2 density on the dayside. Emissions from N^+ at 1085 Å and N at 1493 Å are produced by solar photodissociation and ionization of N_2 and observations of these line emissions can be used to infer the N_2 density.

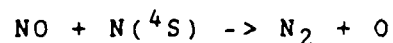
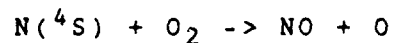
MOLECULAR OXYGEN DENSITY

DAYSIDE:

The RAIDS experiment will employ a number of techniques to determine the O_2 density on the dayside. The near infrared spectrometer (NIR) on RAIDS will measure the O_2 Atmospheric bands which are produced by solar scattering by O_2 . Since the O_2 Schumann-Runge bands are strong absorbers in the FUV, comparisons of measured N_2 LBH band intensity ratios to synthetic spectra will yield the O_2 density above 120 km. Similarly, the Schumann-Runge bands will attenuate starlight and the spectra of stars passing through the RAIDS instrument line of sight may provide a means for

O₂ density measurement.

On the dayside, the NO gamma bands are produced by resonant-fluorescent scattering of sunlight. Above 140 km, the NO molecule is in chemical equilibrium between source and loss reactions given by:



resulting in an equilibrium NO density given by:

$$[NO] = k(T) [O_2] ,$$

where $k(T)$ is the temperature dependent ratio of source and sink reaction rates. If the temperature is known, measurements of the NO gamma bands above 140 km can be used to infer the O₂ density.

NIGHTSIDE:

As mentioned in the introduction, O⁺ ions undergo charge exchange with O₂ molecules forming O₂⁺ ions which can then recombine with electrons and dissociate producing atomic oxygen airglow (principally at 6300 Å). The 6300 Å emission rate is proportional to the product of the electron and O₂ density and can be used to infer the O₂ density at night. Absorption of starlight in the Schumann-Runge bands will also provide a means for O₂ remote sensing at night.

CONCLUSION

The eight optical instruments that make up the RAIDS orbiting observatory will provide a valuable database of airglow emission profiles which will be used to test techniques for remote sensing of the neutral atmosphere and ionosphere. All of the airglow emissions mentioned above have been observed before by a number of investigators and all of the remote sensing techniques discussed here have been attempted before - at least tentatively. RAIDS will provide a unique opportunity to test and intercompare these techniques with a global dataset of airglow observations.

4.9 THE ATMOSPHERIC DENSITY SPECIFICATION (ADS) SATELLITE

Frank A. Marcos

John O. Ballenthin

Air Force Geophysics Laboratory

David C. Kayser

Aerospace Corporation

and

Timothy L. Killeen

University of Michigan

1. INTRODUCTION

The statistical accuracy of empirical models has remained at about 15% (one sigma) during the past 15 years. Model improvements will require parameterizations of upper atmosphere dynamics and appropriate representations of actual physical energy inputs (to replace present "proxy" indicators). There is no alternative to a satellite experiment to gather the inputs critical for understanding the dynamic processes that affect the variability of the neutral atmosphere. The proposed ADS satellite mission will generate a coordinated and comprehensive global data set of lower thermospheric state variables needed to improve the performance of operational density models.

2. OBJECTIVE

The purpose of this proposed low altitude satellite experiment is to obtain coordinated measurements of aerodynamic drag, density, neutral composition, winds and temperature to:

a) develop new, more accurate operational satellite drag models by measuring atmospheric dynamic processes and relating them to high latitude energy inputs

b) meet AF requirements for 10% absolute density specification by advancing state-of-the-art sensing techniques to measure neutral density within 5%.

3. INSTRUMENTATION

The instrumentation consists of the AFGL Satellite Electrostatic Triaxial Accelerometer (SETA) and Quadrupole Ion/Neutral Mass Spectrometer (QINMS), the University of Michigan Fabry-Perot Interferometer (FPI) and the Aerospace Corporation Composition and Density Sensor (CADS). This coordinated payload provides the inputs critical for understanding the dynamic processes that affect the variability of the neutral atmosphere. A brief description of each experiment is given below:

a) Satellite Electrostatic Triaxial Accelerometer (SETA)

This instrument measures satellite orbital accelerations at micro-g levels. It is an outgrowth of the single axis accelerometer systems flown by AFGL on the three Atmosphere Explorer satellites and on six Air Force satellites. The triaxial version has been successfully flown on Air Force satellites in 1979, 1982 and 1983, and on the S85-1 spacecraft in 1984. The accelerometer sensing element consists of an electrostatically suspended proof mass. Input accelerations cause this proof mass to be displaced slightly from its null or zero-acceleration position. Movement of the order of a millionth of a centimeter causes electrostatic forces equal and opposite to the applied acceleration to re-center the proof mass along three orthogonal axes. The output is a digital pulse rate directly proportional to the input acceleration. High accuracy atmospheric density and neutral winds are obtained from the along-track and cross-track accelerations respectively.

b) Quadrupole Ion-Neutral Mass Spectrometer (QINMS)

A major feature of this experiment is its capability to obtain the first satellite high accuracy total mass density measurements. The objective is to measure the density to within five percent. The QINMS sensor is closely related to the instrument successfully employed on STS-4 for ion and neutral spacecraft contamination studies and to three other instruments awaiting space shuttle flights. It consists of a self-contained vacuum system containing a switchable electron impact ion source, a total density sampling grid, a retarding potential analyzer, a quadrupole mass selection filter, a high sensitivity ion detector/electron multiplier combination, and a wide dynamic range logarithmic electrometer amplifier. After launch, a commandable cap opening mechanism exposes the instrument to the ambient atmosphere to initiate the data collection process.

This versatile package is capable of providing measurements of neutral density, neutral composition, ion density, and ion composition at a very fast sample rate (80 meter spatial resolution composition measurements and 8 meter spatial resolution density measurements). Gases with molecular weights between 1 and 64 atomic mass units can be measured over an altitude range of 140 km to more than 500 km. Neutral measurements are made possible by

electron impact ionization of the incident neutral gas and subsequent analyses of the resulting ions. An accommodation sphere surrounding the ion source is used to thermalize the energetic incoming gas molecules to a known temperature and molecular state and thereby allow highly accurate measurements of neutral mass density. A movable flag within the accommodation sphere allows unperturbed measurements of the reactive ambient gasses. The instrument is highly programmable; it permits measurement of peaks associated with an ambient gas (e.g. O, O₂, N₂) at a 100 times per second rate. A programmable and commandable ROM allows tailoring the sampling program to retarding potential analyzer scan, ion mode mass scan, or neutral mode mass scan while simultaneously sampling total ion density or neutral pressure.

c) Composition and Density Sensor (CADS)

The CADS design incorporates flight-proven concepts to measure in-situ densities of neutral thermospheric reactive species such as, atomic oxygen and nitrogen, nonreactive gases such as He, N₂ and Ar, the neutral gas temperature and the neutral wind component along the satellite velocity vector. Composition of the major species can be measured from perigee to above 400 km. This measurement is accomplished through the electron-impact ionization of the incoming neutral gas followed by mass filtering and ion detection. Temperature and wind are derived from a special technique involving a retarding potential analysis of ion energy.

The CADS sensor consists of a quadrupole mass filter, electron-impact ionization ion source with two independent electron guns, a low sensitivity electrometer ion detector, and a high sensitivity spiraltron ion detector--all enclosed in a vacuum housing. Once on orbit a cutter mechanism opens the sensor to the ambient atmosphere. Several measurement sequences can be invoked through the command system. Among these are: scan from 3 to 48 AMU, dwell on N₂ for composition and energy analysis, visit a selected set of important masses. The chosen sequence is repeated every few seconds, thereby providing high along-the-track resolution.

d) Fabry-Perot Interferometer (FPI)

The FPI is a remote sensing instrument designed to measure the meridional neutral wind and the temperature of the upper atmosphere. Optical measurements of thermospheric emission features provide winds to 5 m/sec from Doppler line shifts and temperature to 10 K from the line broadening. The measurements are made with an extremely stable, high-resolution Fabry-Perot etalon. A wavelength analysis is performed on the detected light by spatially scanning the interference fringe plane with a multi-channel array detector. A commandable horizon scan mirror permits viewing the earth's atmosphere at various tangent heights, providing a cross-sectional view of the thermodynamic and dynamic state of the thermosphere in 16 steps, over a 200 km vertical region.

The etalon is the central component of the instrument. It performs the high resolution spectral analysis by multiple path interference of the transmitted light. This etalon consists of two fused silica substrates upon each of which is deposited a semi-reflecting dielectric multi-layer. These mirrors are flat to 1/100

wavelength. Other major components of the FPI are the main scanning telescope and baffle, filter wheel, atomic emission line calibration source, etalon objective telescope lenses, and the image plane detector that converts the intensity of light falling on the image plane into a set of discrete electron pulses.

A more detailed description of this experiment is given in this section's paper "Fabry-Perot Interferometer for ADS" by Timothy L. Killeen.

4. ORBITAL REQUIREMENTS

A low altitude, high inclination mission is required to make progress in modeling the atmospheric region below 250 km. A perigee as low as 140 km is desired with a relatively low apogee (preferably about 500 km) to permit data collection over a wide latitude region on each pass. Nominal lifetime desired is fifteen months and the minimum is seven months. The low orbit, long lifetime requirements are mutually exclusive without an on-board propulsion system. It is recognized that tradeoffs in perigee and apogee may be necessary. A three-axis stabilized satellite is preferable to maximize duration and accuracy of the sensor measurements.

5. SUMMARY

The ADS satellite experiment complement consists of the following flight-proven sensors: a) Satellite Electrostatic Triaxial Accelerometer (SETA) to measure in-situ drag, density and cross-track winds, b) Quadrupole Ion/Neutral Mass Spectrometer (QINMS) to measure in-situ absolute density within 5% and neutral and ion composition, c) Composition and Density Sensor (CADS) to measure in-situ along-track winds and neutral composition and d) Fabry-Perot Interferometer (FPI) to remotely measure along-track winds and neutral temperature. A low perigee is necessary to provide data in the altitude regions of interest while the high inclination permits global coverage. This well-designed and focused mission to determine thermospheric state variables with high absolute accuracy and appropriate geophysical coverage is critically needed to significantly improve our density specification capability.

ACCELEROMETER MEASUREMENTS OF DENSITY AND WINDS FOR ADS

FRANK A. MARCOS
AIR FORCE GEOPHYSICS LABORATORY

AND

ANDREW J. MAZZELLA, JR.

RDP, INC.

1. INTRODUCTION

The Satellite Electrostatic Accelerometer (SETA) experiment is designed to measure density and winds on the low-perigee altitude ADS satellite. This instrument has been flown successfully on Air Force satellites in 1979, 1982, 1983 and 1984. It has provided our only extensive lower thermosphere neutral density data base during Solar Cycle 21. The ADS mission extends these measurements into the present solar cycle.

2. EXPERIMENT DESCRIPTION

The accelerometer consists of a proof mass in the shape of a flanged hollow cylinder, a temperature monitor and supporting power and signal conditioning electronics. A complete description of the instrument operating principles is given by Marcos and Swift (1982). The one gram proof mass is constrained in all three axes by means of electrostatic forces generated by electrodes (Fig 1). The proof mass cylinder is 0.025 cm thick and its flange is 0.0375 cm thick. The spacer has a thickness of 0.056 cm. The gap between the flange and each Z-axis carrier is 0.089 cm. Between the X- and Y- axes carrier electrodes and the inside of the proof mass cylinder the gap is 0.033 cm. The proof mass is suspended electrostatically along its X and Y (radial) axes by the eight electrodes on the cylindrical carrier extending through the proof mass. In the Z (longitudinal) axis its position is controlled by the three annular electrodes on each side of the proof mass housing. The relative motion between the proof mass and these electrodes is sensed in three orthogonal directions, and restoring forces are generated in three separate feedback constraint loops to keep the proof mass centered. Figs 2 and 3 show the force rebalance loops for the cross-track and along-track axes respectively. Each restoring voltage is proportional to the input acceleration in the corresponding direction. Typical accelerations for atmospheric drag data are at the micro-g level.

3. DATA ANALYSIS

The analysis method for extracting atmospheric density from the acceleration measurements has been described by Marcos and Swift (1982). Fig. 4 shows a sample of 3-axis raw acceleration data obtained for one orbit. The acceleration data, in units of micro-g's, are plotted vs universal time. Numerical filtering techniques are used to remove high-frequency acceleration components which are due to vehicle dynamics. Fig. 5 shows the result of applying a filter passing only frequencies less than 0.01 Hz to the data of Fig 4. An example of the detailed density structure obtained from measurements on these low altitude satellites is given in Fig. 6. These data were obtained during one orbit on 14 July 82, a period of very enhanced geomagnetic activity. Coverage is from 34 degrees north latitude on the nightside (local time of 2200 hr), up to 83 degrees north latitude and down to 57 degrees south latitude on the dayside (local time 0930 hrs). This coverage is typical of the density data obtained on each orbit.

To illustrate the derivation of winds, wind measurements during an active geomagnetic period, when Kp was 7-, are described (Marcos and Forbes, 1985). Fig. 7 shows raw acceleration data from the X axis plotted against universal time, geographic and geomagnetic latitude, local time and altitude. Atmospheric rotation velocity is included in the data. The result of applying the numerical filtering is shown in Fig 8. Neutral horizontal winds derived from these data are shown in Fig 9. Unsmoothed data are shown as a light line. To account for very low frequency small-amplitude oscillations in the raw data, the heavy line was added by Marcos and Forbes. These results demonstrated that information concerning the general positions and magnitudes of the nighttime and morning cells characteristic of the polar thermosphere wind system can be derived from the SETA data.

4. EXPERIMENT OBJECTIVES

Specific goals of the SETA experiment on ADS are to measure atmospheric density from perigee to about 300 km and to measure cross-track winds from perigee to about 200 km. The density data will be used as follows:

- a. To extend the density measurements made by this instrument during the previous solar cycle into solar cycle 22.
- b. To provide a cross-check on the new absolute density mass spectrometer measurements. Due to its extensive flight history, the errors in extracting density from the accelerometer are well understood. Comparison with the mass spectrometer density values can provide confidence in this new technique. Also, the orbit-to-orbit variations will be accurate to within a few percent, except where in-track winds are significant (greater than about 200 meters per second).
- c. To provide a cross-check on the total mass densities derived from summing up mass spectrometer individual constituent densities obtained in the neutral composition

mode. This technique is less accurate than densities obtained in the absolute density mode.

d. To attempt to derive the spacecraft drag coefficient as a function of altitude and composition. With measured drag acceleration, absolute density and winds, and knowing the area-to-mass ratio, the only unknown in the drag equation is the drag coefficient. This approach assumes that the absolute density accuracies are independently determined. Thus ADS provides a unique opportunity to determine this important spacecraft parameter.

5. SUMMARY

The SETA experiment can measure atmospheric neutral density and winds. For the 1979 flight, drag accelerations (proportional to density) were sensed to apogee, about 280 km. Winds were determined to a height of about 200 km. The altitude limits of useful ADS data will depend on the satellite's area-to-mass ratio, vehicle dynamic "noise", perigee altitude and level of solar activity.

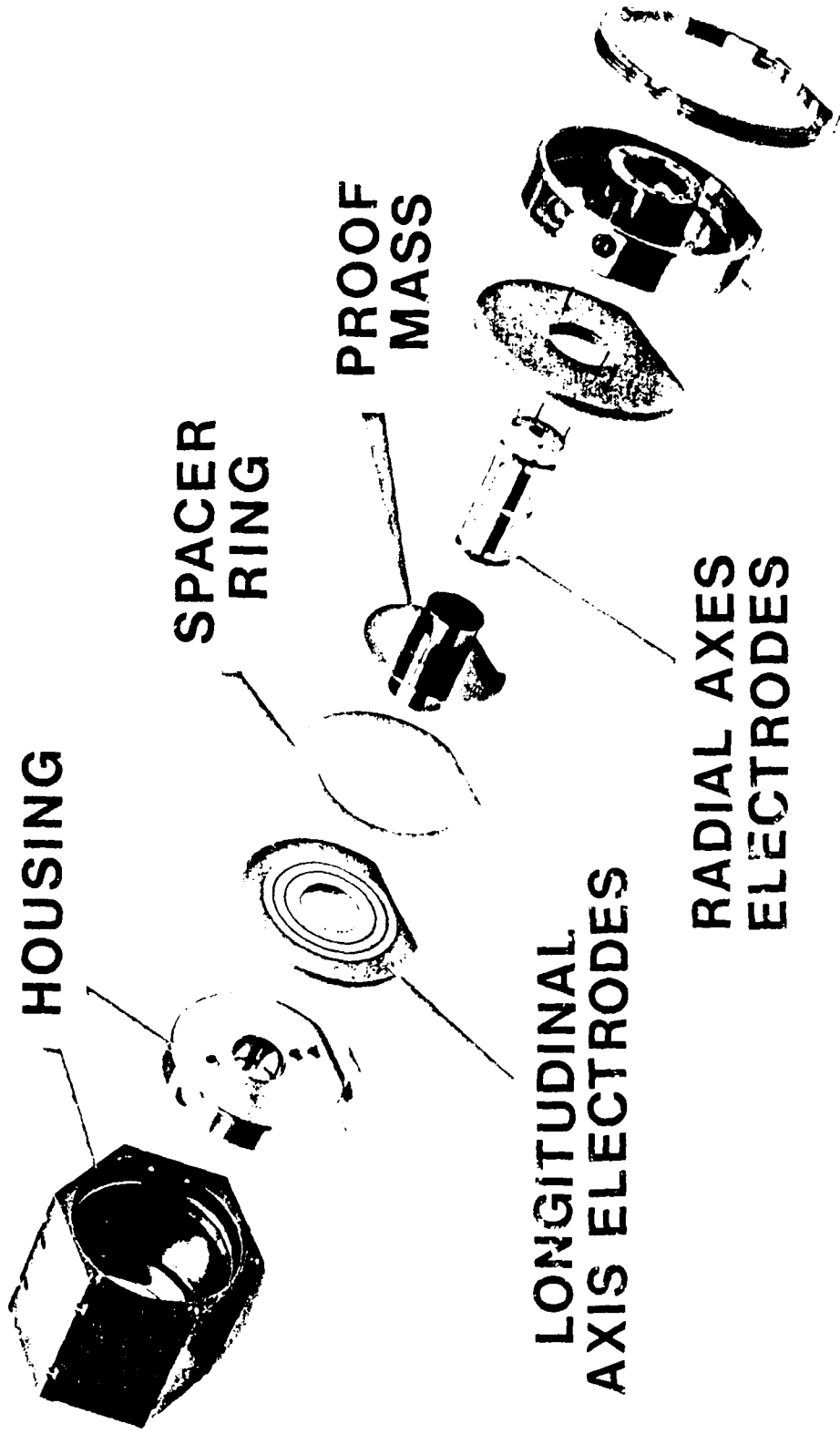
REFERENCES

Marcos, F. A. and E. R. Swift (1982) "Application of the satellite triaxial accelerometer experiment to atmospheric density and wind studies", AFGL-TR-82-0091, AD A120852.

Marcos F. A. and J. M. Forbes (1985) "Thermospheric winds from the satellite electrostatic triaxial accelerometer system, J. Geophys. Res., 90, 6543-6552.

Figure 1. Instrument Mechanical Assembly

THREE AXIS ACCELEROMETER MECHANICAL ASSEMBLY



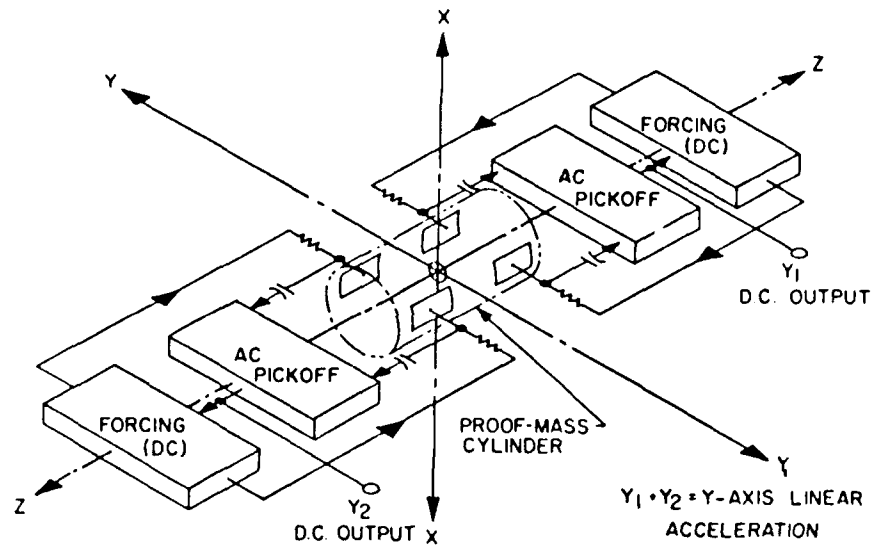


Figure 2. Block Diagram of Y- (or X-) Axis Force Rebalance Loop

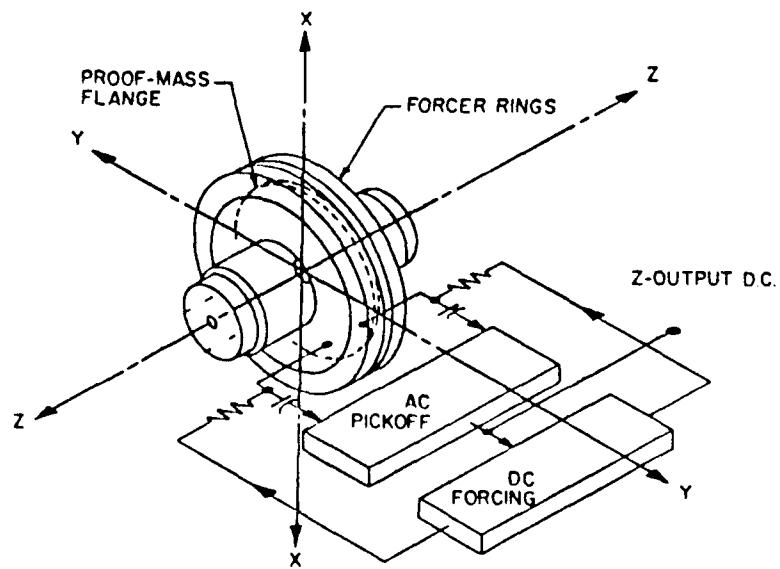


Figure 3. Block Diagram of Z-Axis Force Rebalance Loop

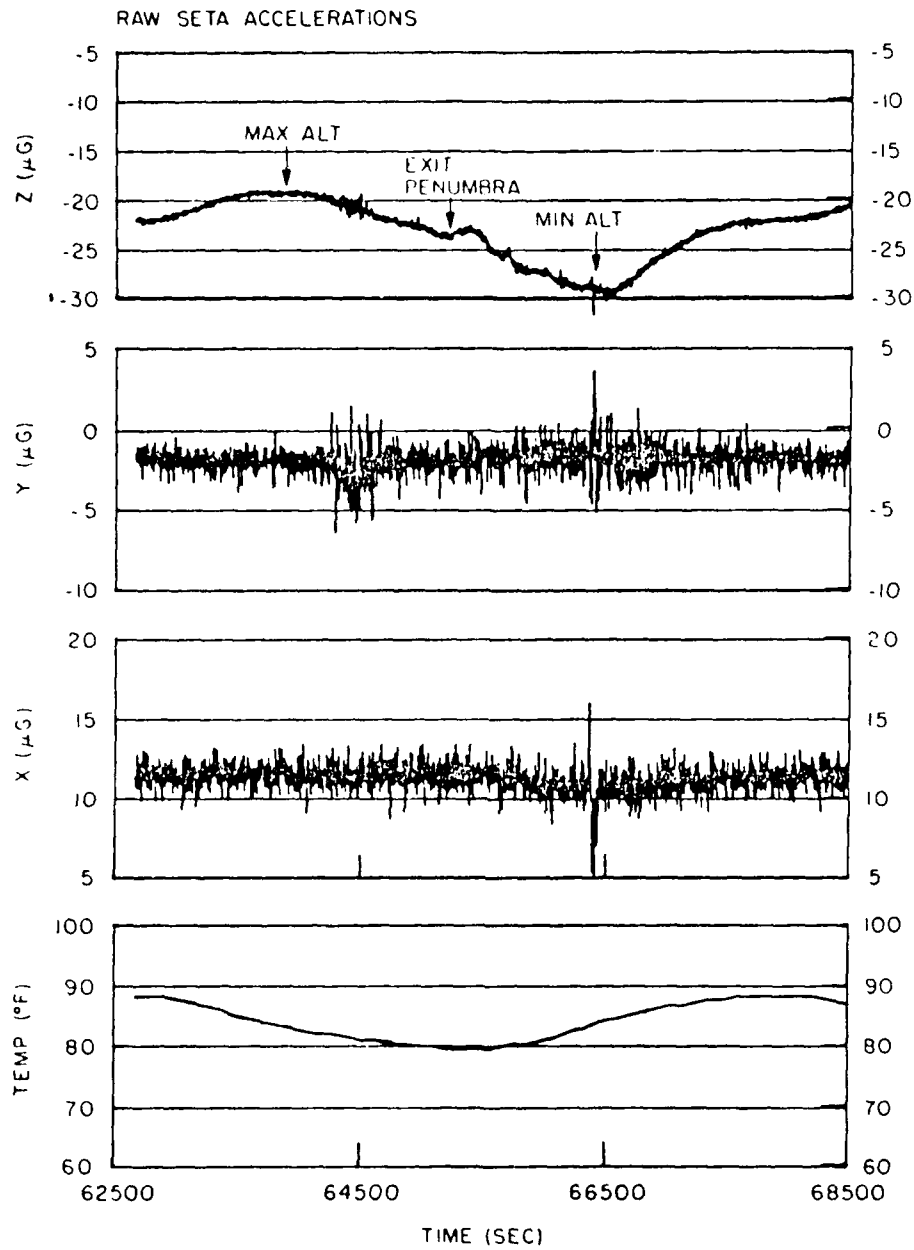


Figure 4. Raw Data for Test Flight

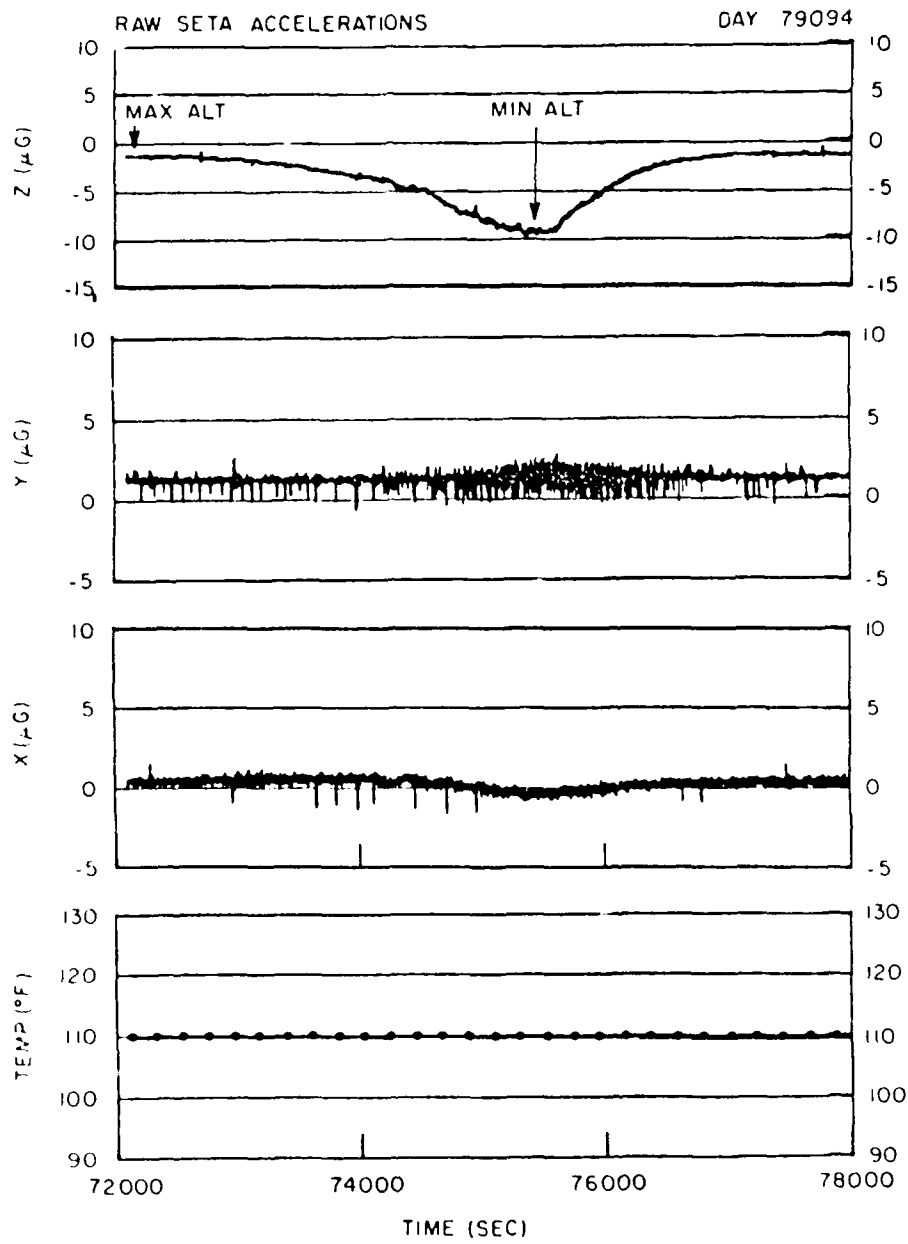


Figure 5. Raw Data for One Orbit, Day 79094

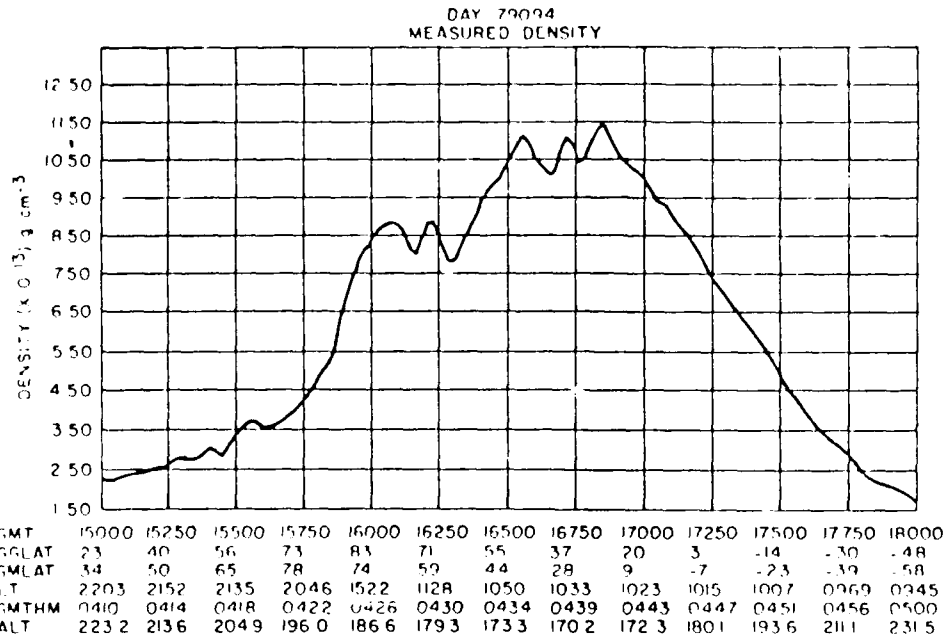


Figure 6. Atmospheric Density as a Function of Altitude, Latitude, and Local Time

X-AXIS RAW ACCELEROMETER DATA
DAY 79089

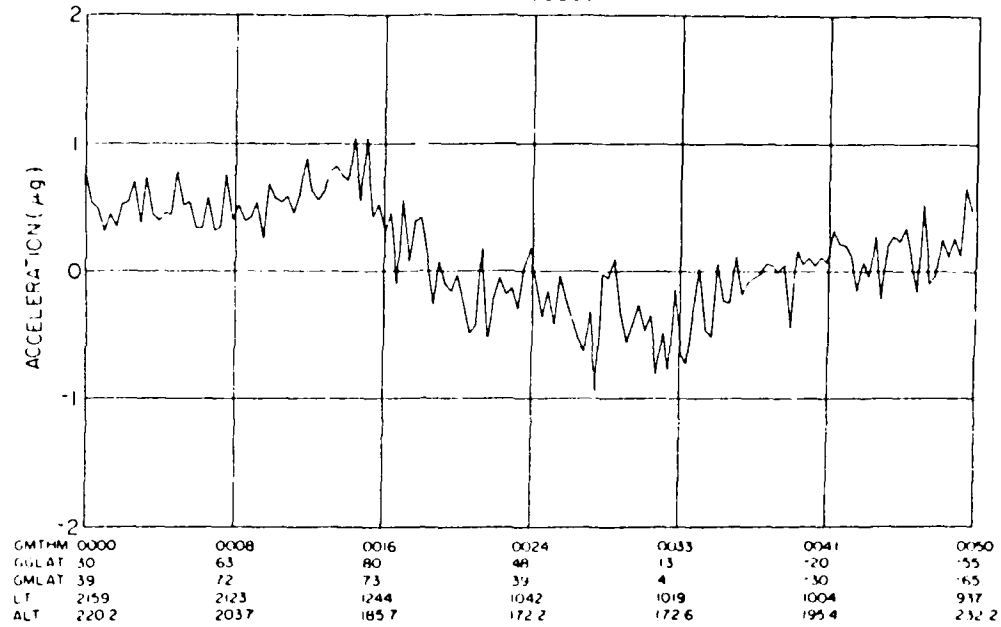


Fig. 7 Cross-axis acceleration data during a period of high geomagnetic activity ($K_p = 5$) showing raw data, plotted versus universal time (GMTHM), geographic latitude (GGLAT), geomagnetic latitude (GMLAT), local time (LT), and altitude in kilometers (ALT).

X-AXIS FILTER ACCELEROMETER DATA
DAY 79089

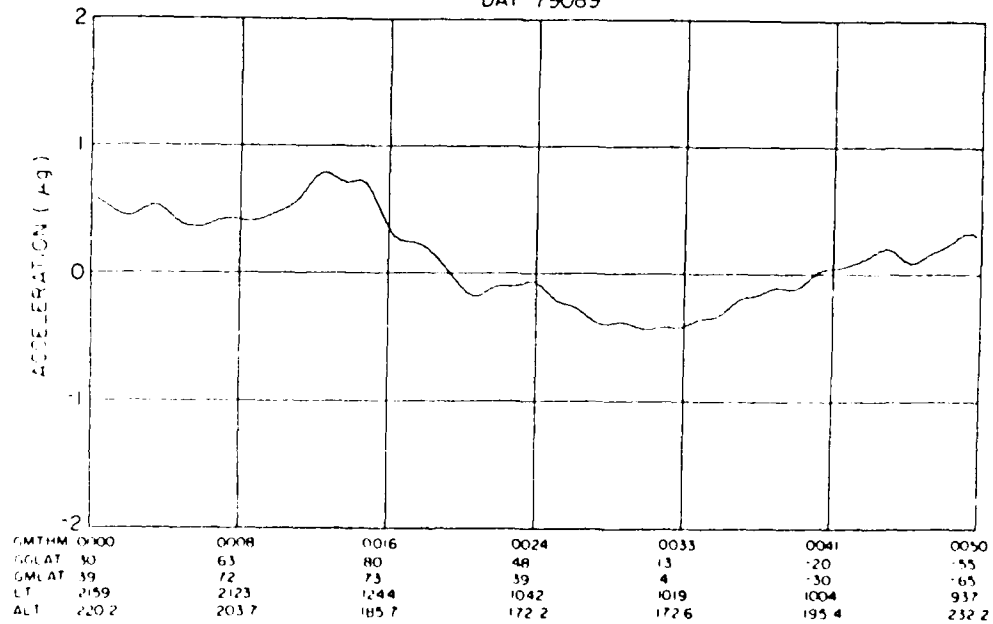


Fig. 8. Same as Figure 7 but showing filtered data.

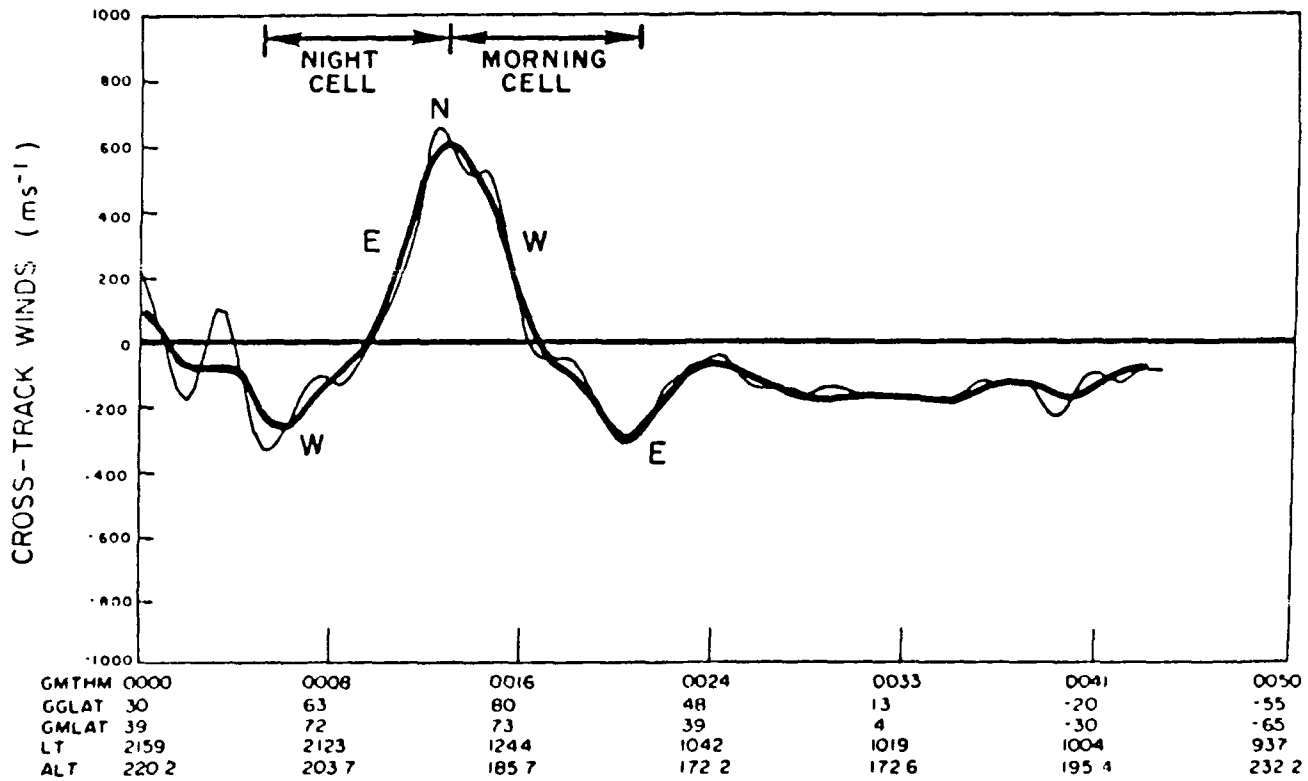


Fig. 9. Cross-axis winds corresponding to the data in Figure 8 plotted versus universal time, geographical latitude, geomagnetic latitude, local time, and altitude. Unsmoothed (light line) and smoothed (heavy line) data are shown.

4.11

Atmospheric Density and Aerodynamic
Drag Models for Air Force Operations

ADS Mass Spectrometer
Absolute Density

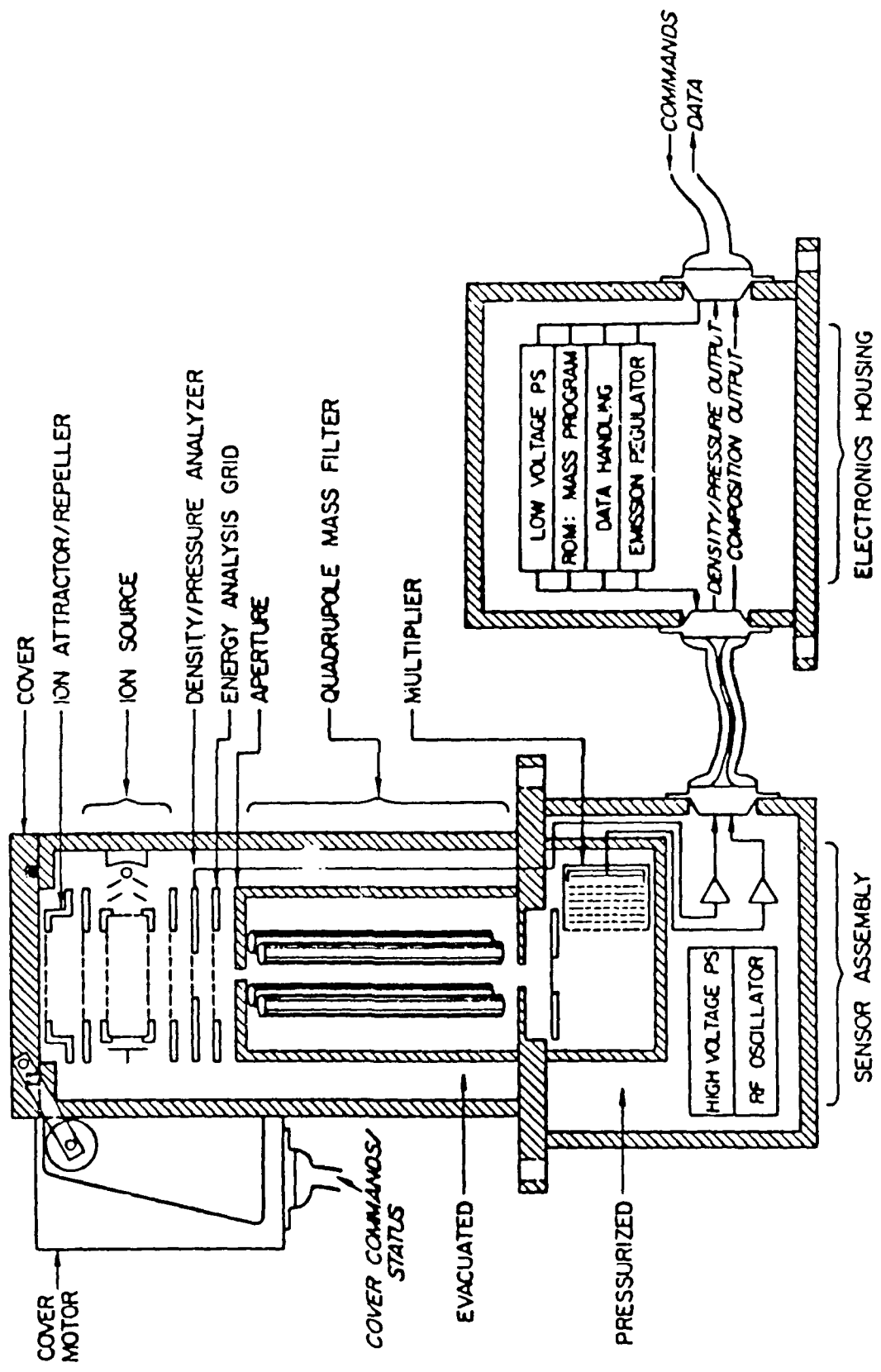
John O. Ballenthin
AFGL/LID
[617] 377-3755

Outline

Review some error sources of mass spectrometers.

Show how improvements in technique and calibration facilities can substantially reduce these errors.

Present a schematic of the ADS Absolute Density Mass Spectrometer and its expected accuracy.



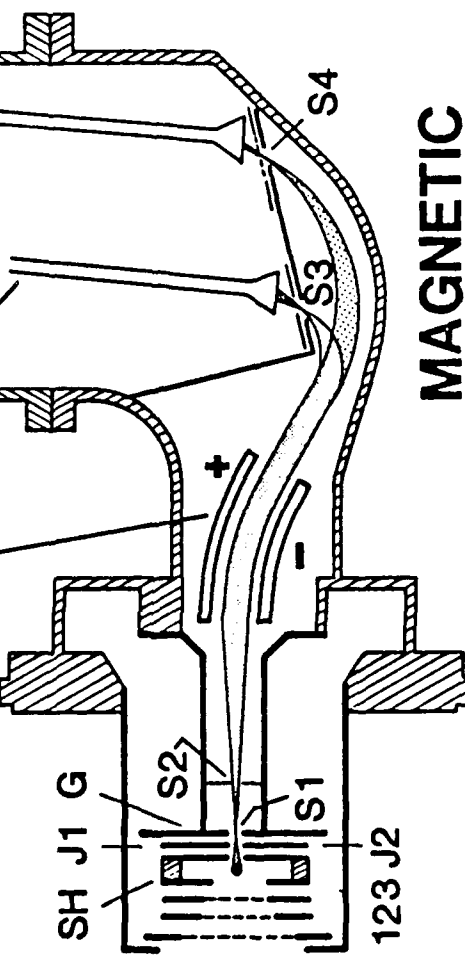
QUADRUPOLE ION-NEUTRAL MASS SPECTROMETER

ELECTRON MULTIPLIERS

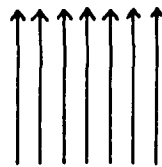
LOW MASS HIGH MASS

ELECTRIC ANALYZER

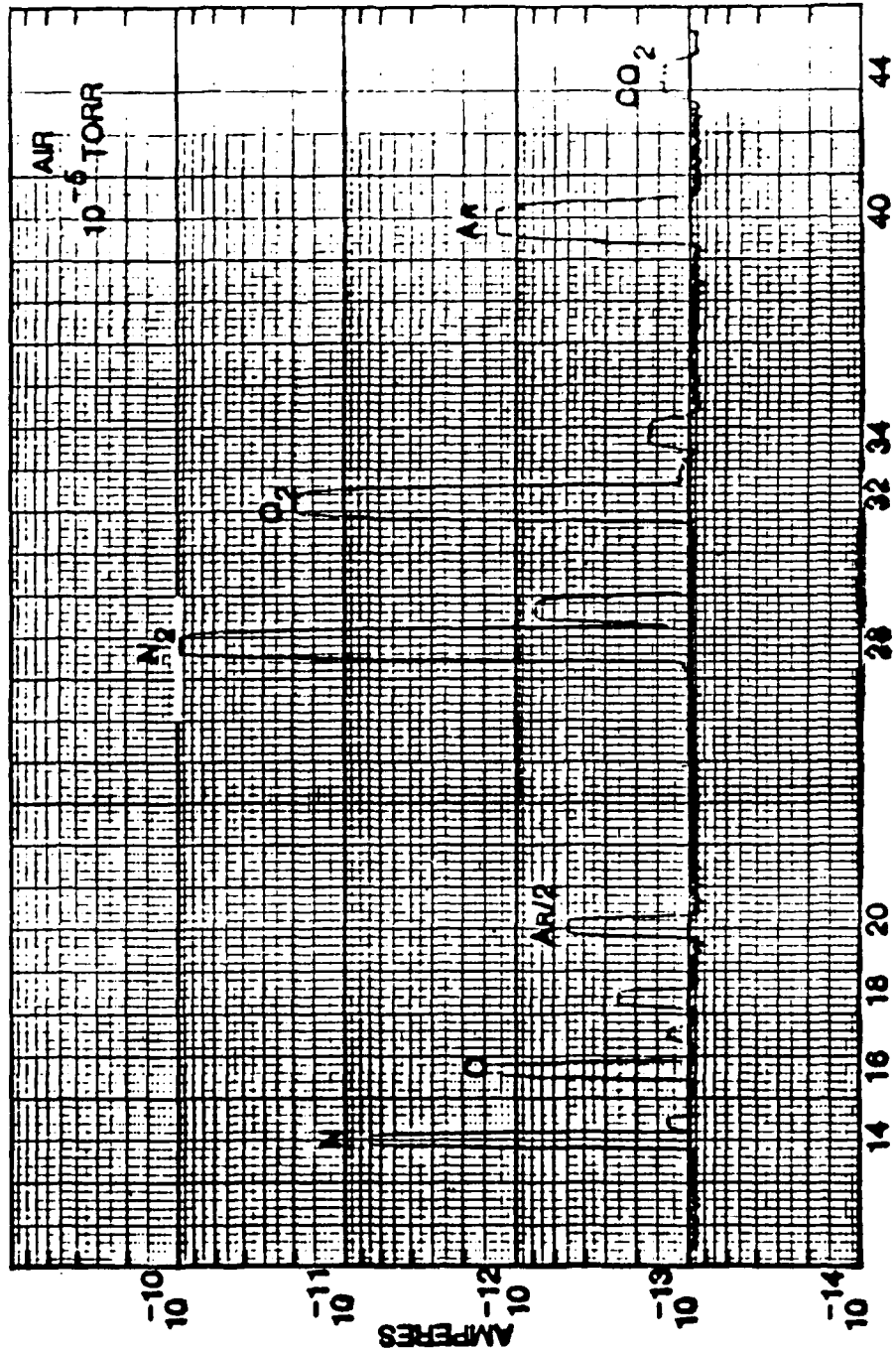
MAGNETIC ANALYZER

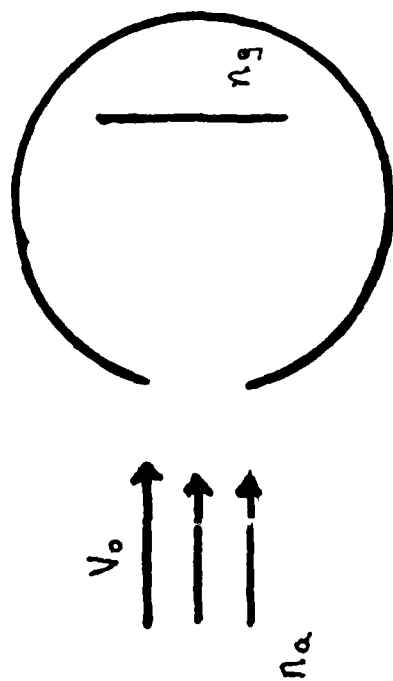


MOLECULAR BEAM



5 cm





Closed Source

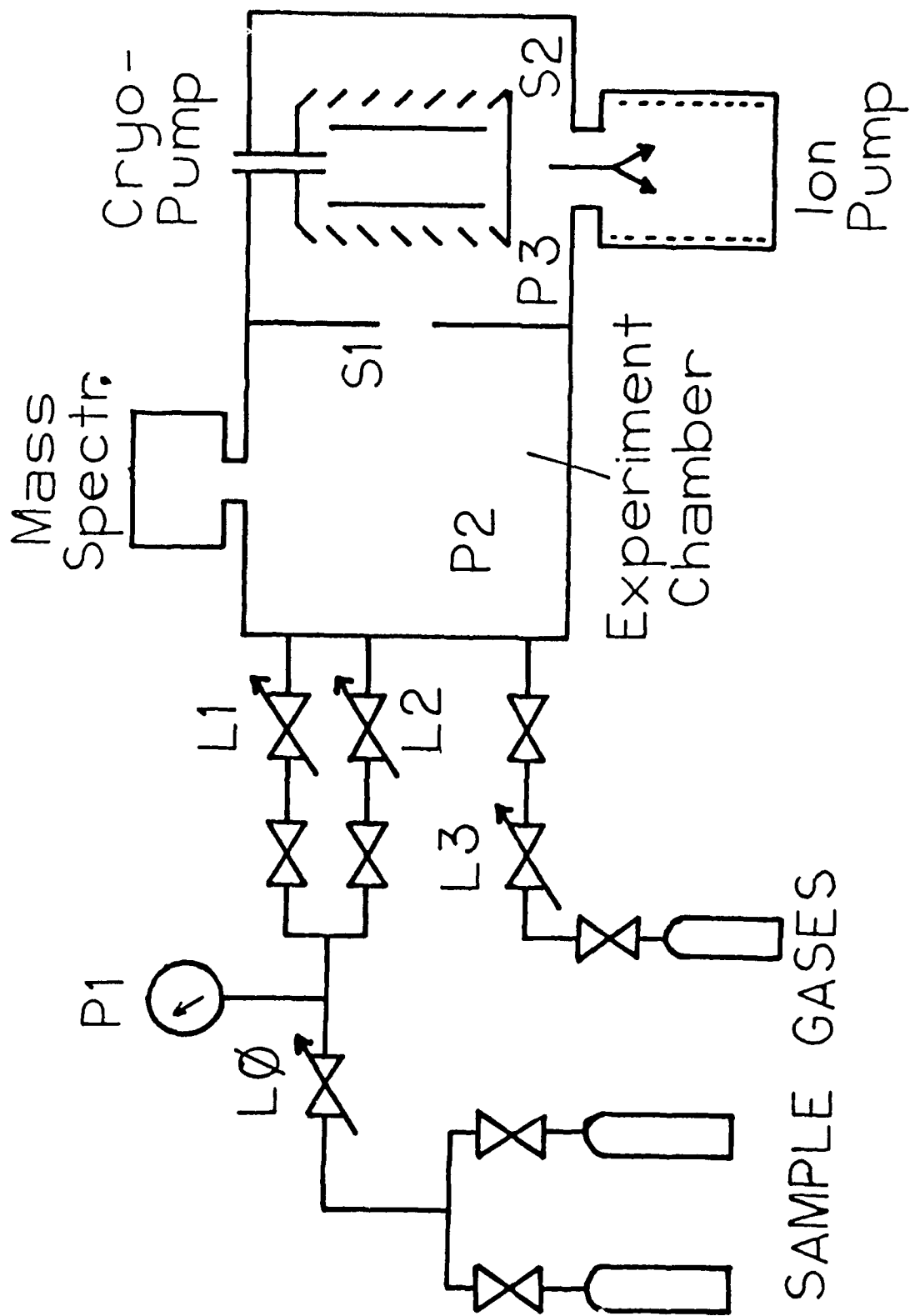
$$n_g = (T_a/T_g)^{3/2} F(s) n_a$$

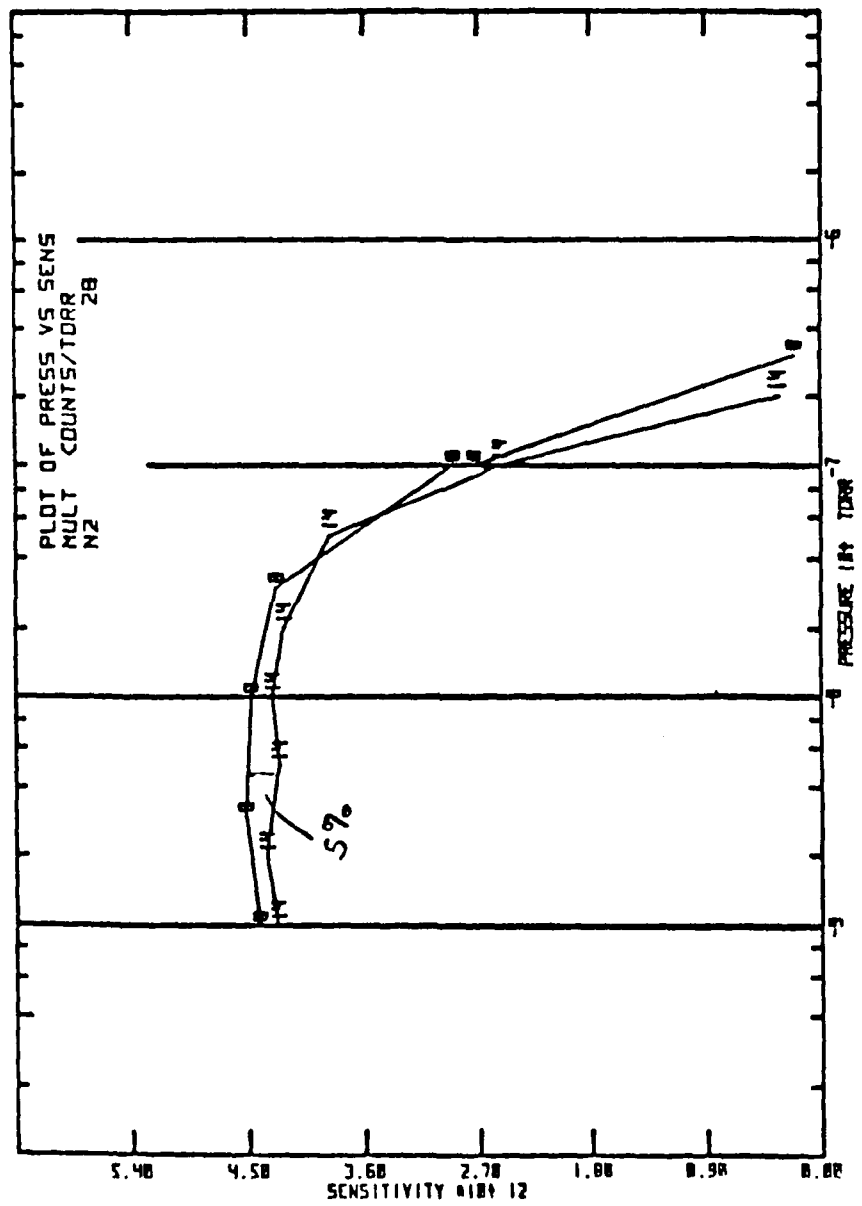
$$F(s) = \pi^{3/2} \cdot s \cdot [1 + \operatorname{erf}(s) + \exp(-s^2)]$$

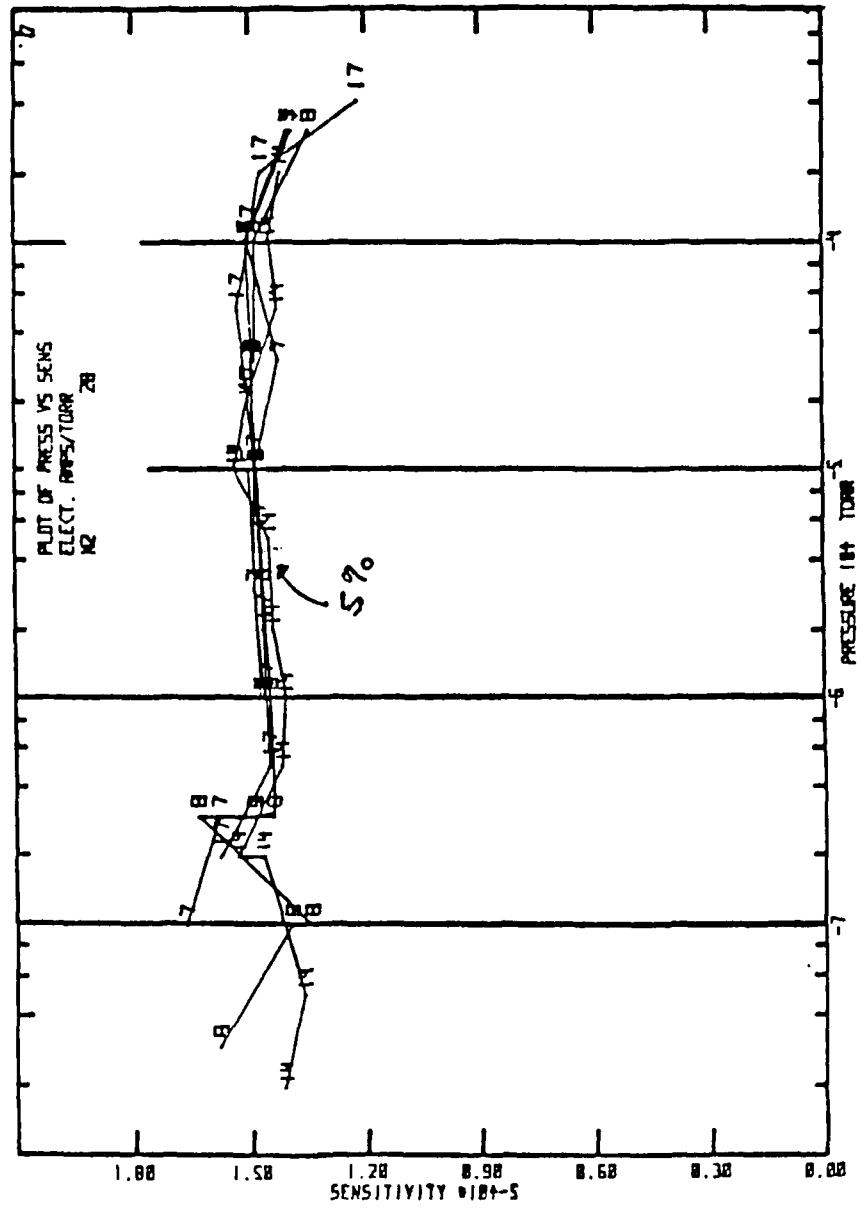
$$s = V_r/V_0 \quad V_0 = [8RT_a/\pi M]^{1/2}$$

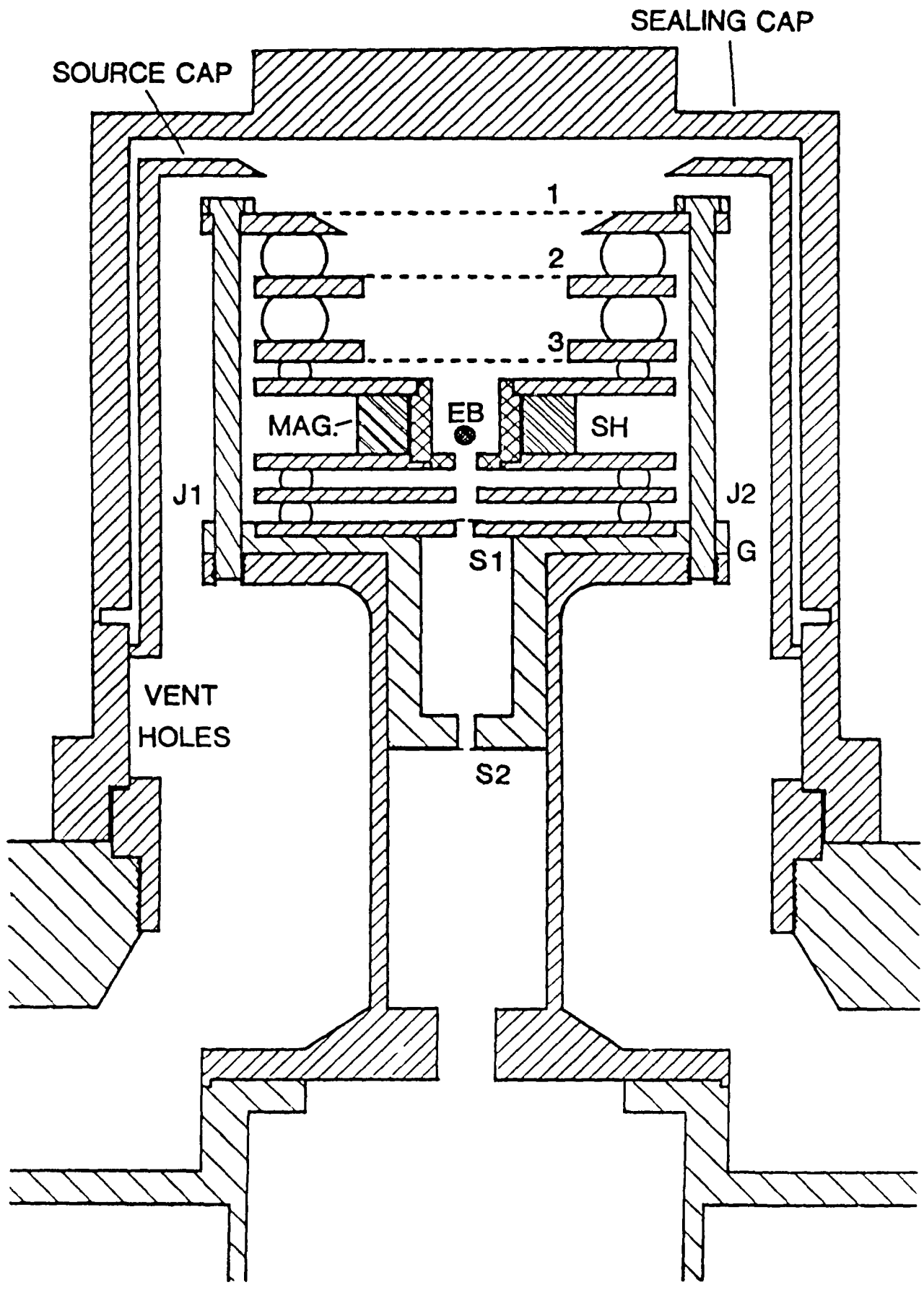
V_r = ambient rms velocity R = gas constant

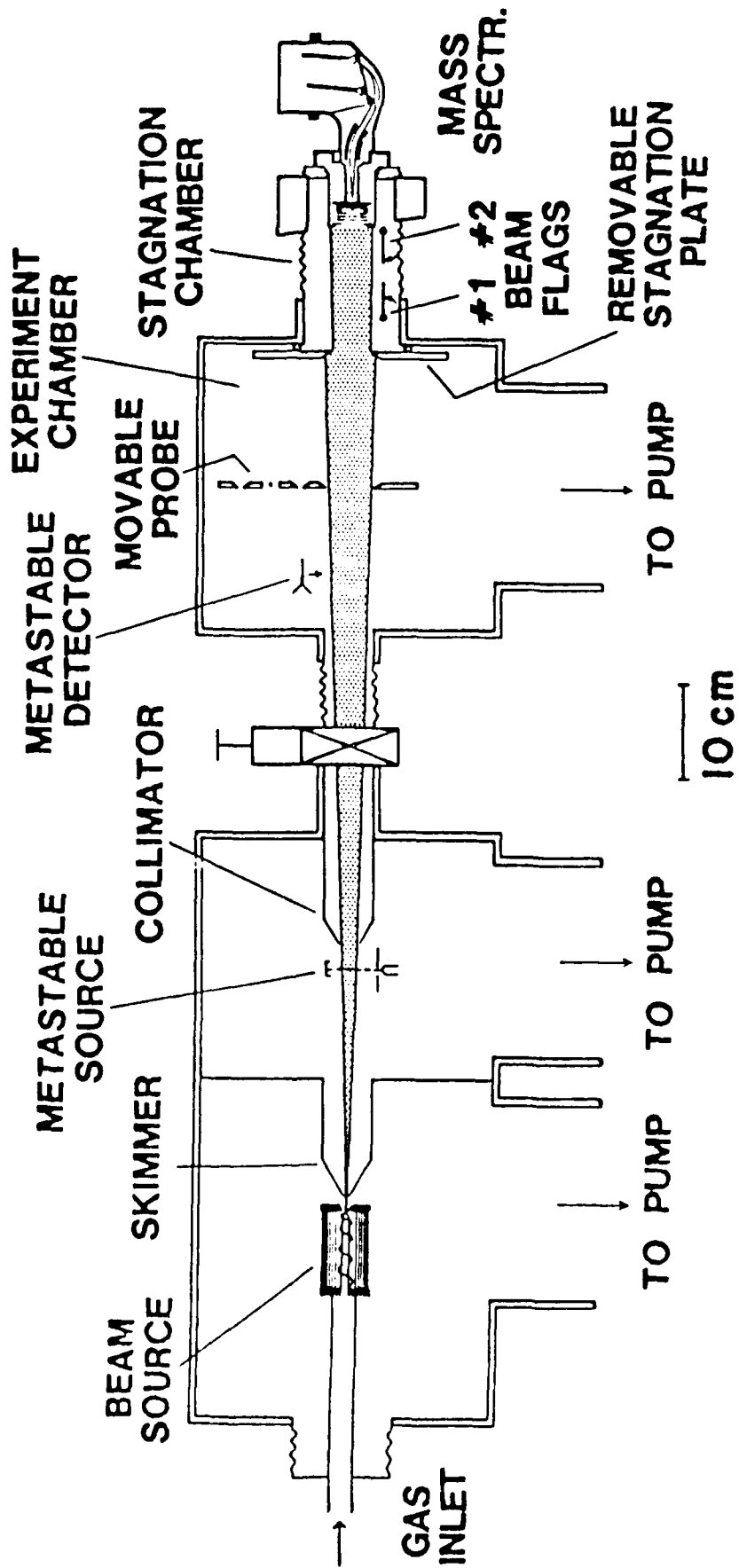
M = atomic mass of measured species











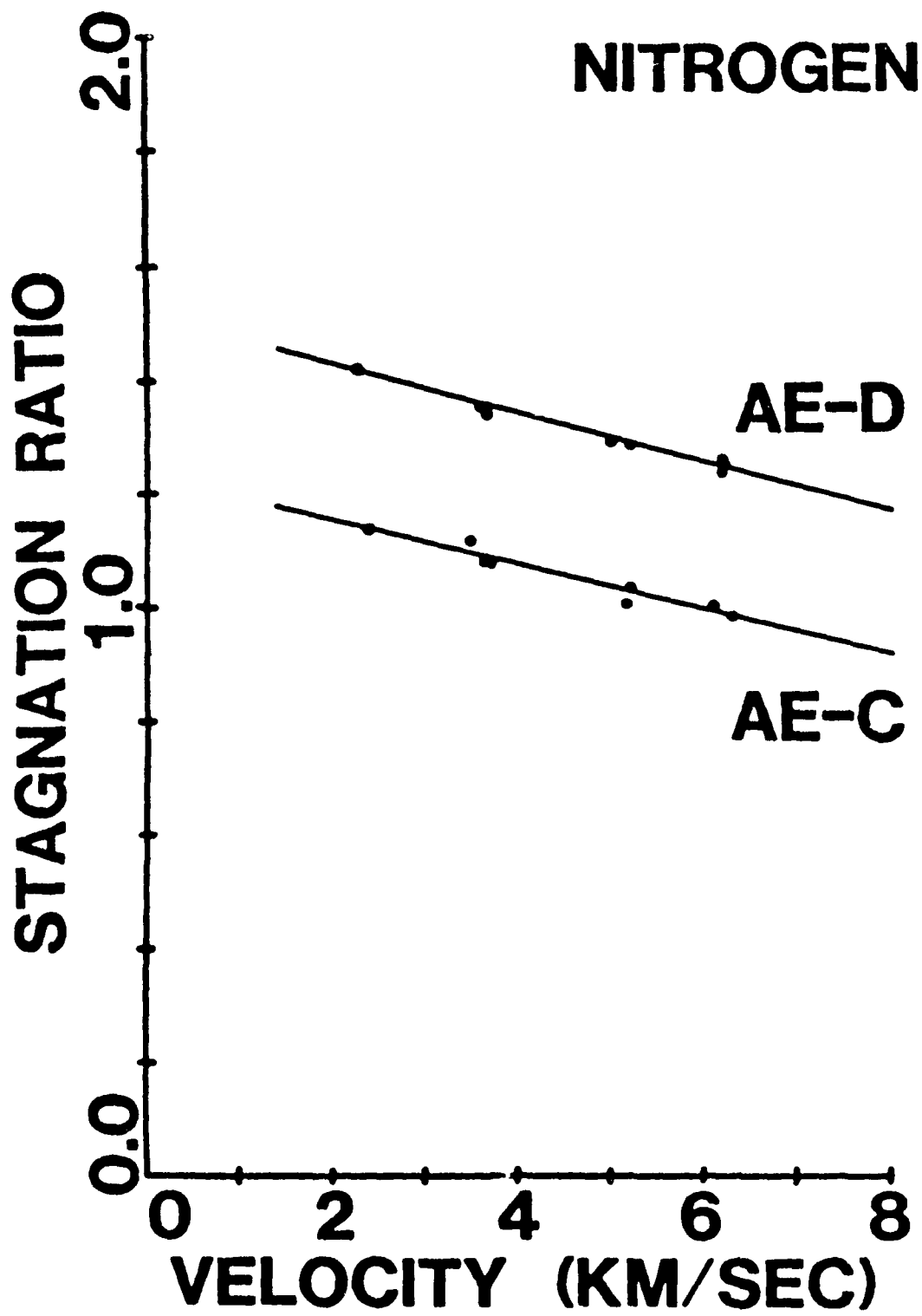
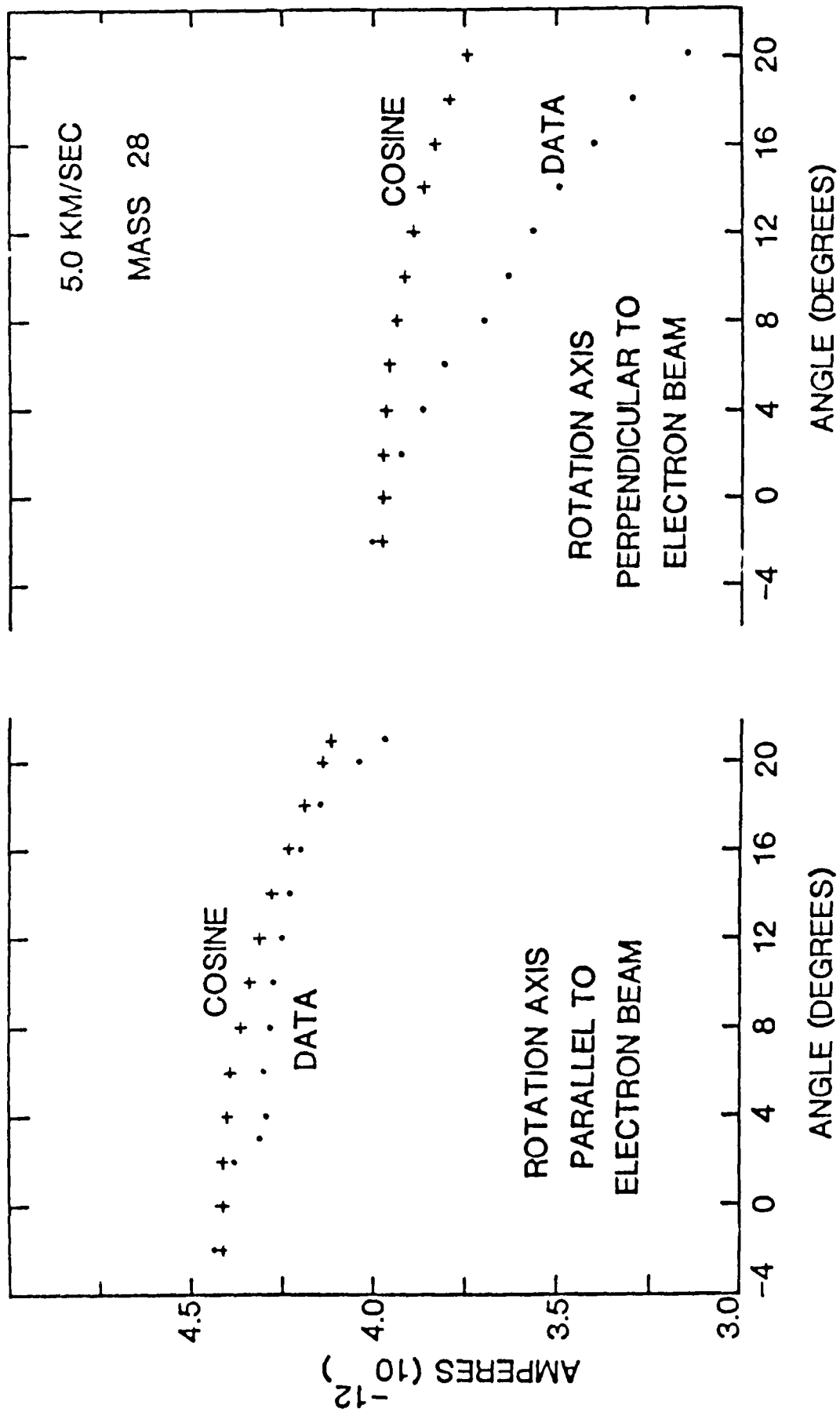
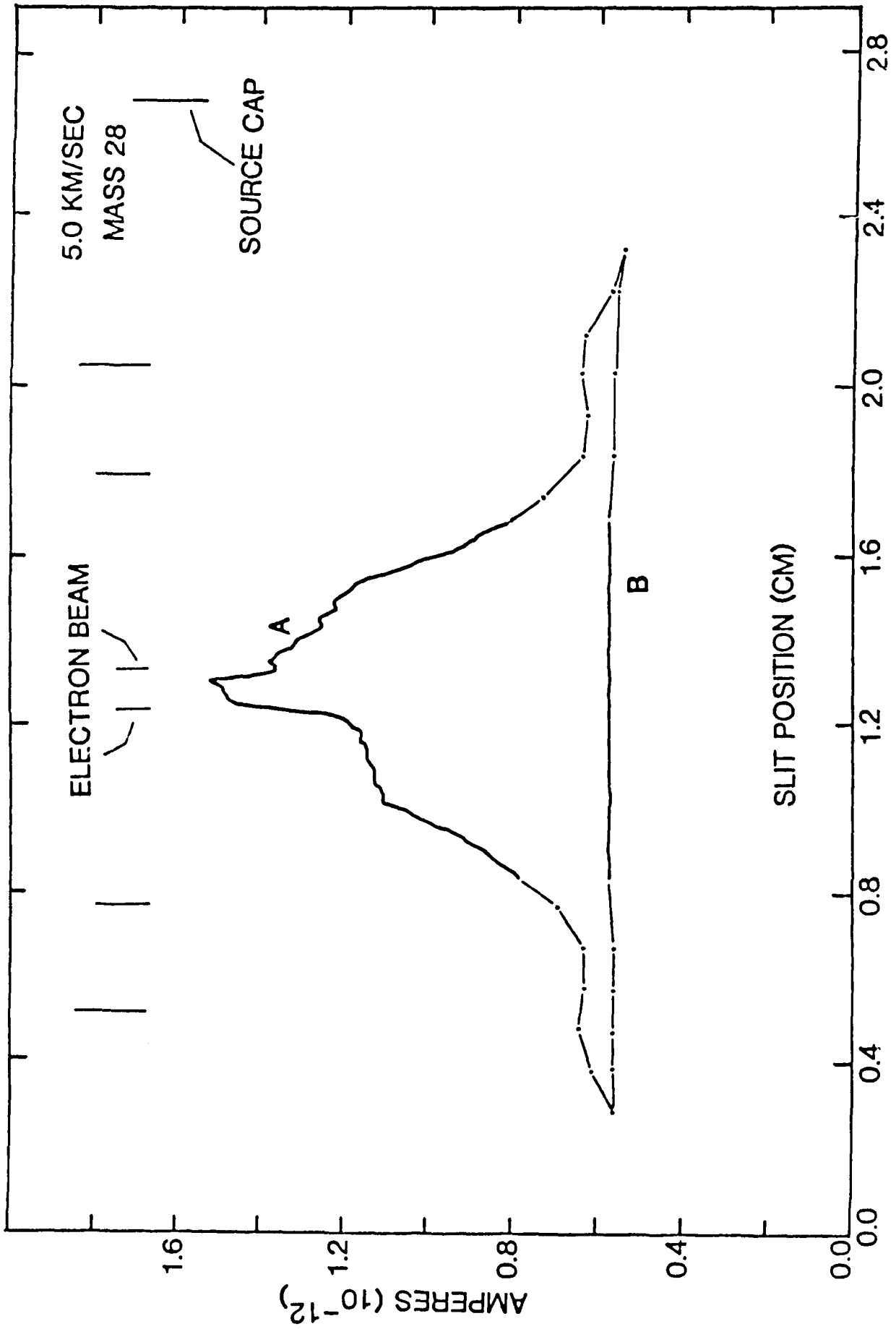


Figure 21. Stagnation ratio plotted versus velocity.

Table 5. The stagnation ratio measured for various spectrometers.

MASS SPECTROMETER	VELOCITY (KM/SEC)	STAGNATION RATIO
AE-C	6.0	1.0
AE-D	6.0	1.25
Viking	4.4	1.15
Pioneer-Venus	5.5	0.93
Sounding Rocket	1.4	0.65





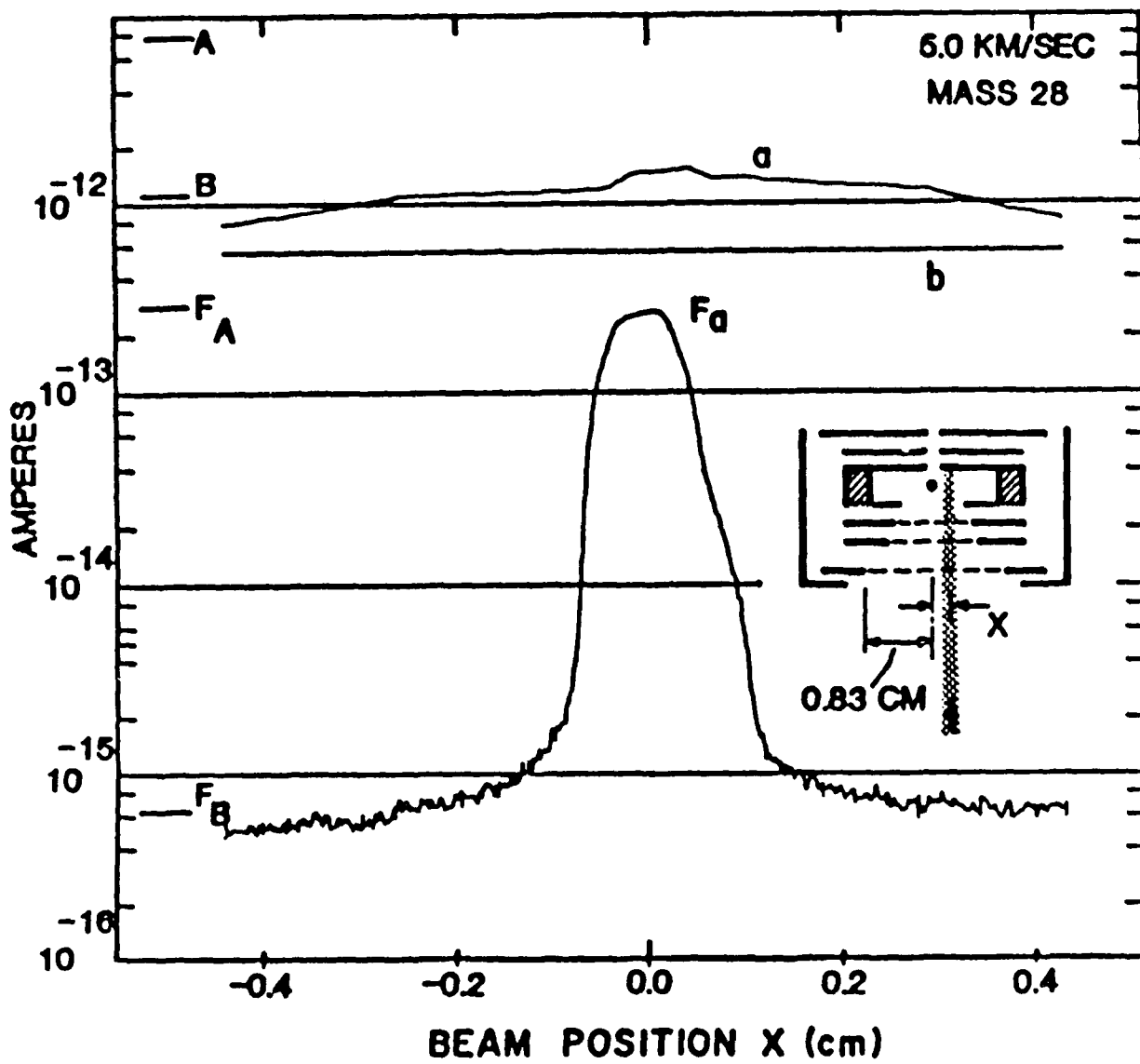
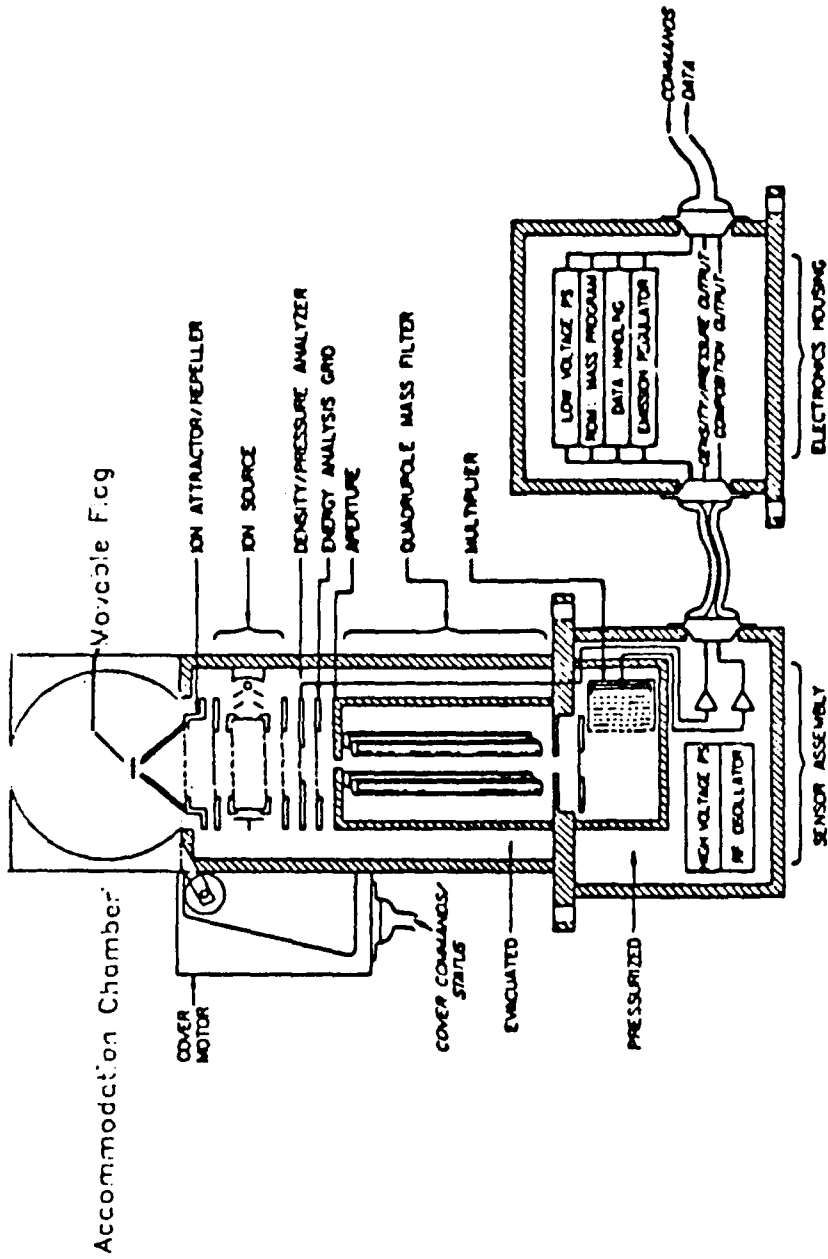


Figure 29. The flythrough mode response when scanned by a thin sheet beam.

Some Error Sources in Mass Spectrometric Measurements

Error Source	Mitigation	Magnitude
Absolute accuracy uncertainty, Non-linearities	Precision static Cal facility	1-2%
Long term stability	On board cal. source	<1%
Instrument Temp. effects	Laboratory cal.	<1%
Velocity effects	Beam cal., Wind sensor	?
Angle effects	Beam calibration	<<1%
Non-ideal acc. chamber	Beam calibration	<<1%
Time response	Beam calibration	~0.01 sec
Outgassing	UHV materials, Flag, RPA	-
Electron multiplier gain drift	Overlapping electrometer	-
Atomic Oxygen surface effects	Flag, RPA, Beam cal.	1% ?
Viscous effects	Insure molecular flow regime	



ADS Absolute Density Mass Spectrometer

ADS Absolute Density Mass Spectrometer

Testing and Verification:

- * Response to atomic oxygen beams
 - Produce correct number density and velocities to simulate spacecraft environment.
- * Dynamic response to a neutral beam
 - Measure angular, spatial, and velocity effects
 - Determine effectiveness of accommodation chamber
- * Static calibration
 - Determine absolute measurement accuracy
 - Verify reproducibility and time stability

Summary

- * Some of the primary error sources in the mass spectrometric measurement have been identified.
- * Methods to mitigate these errors exist -- primarily high quality static and dynamic calibration and instrument design.
- * Absolute measurement accuracies of better than 5% are attainable.

In Situ Measurements Of The Neutral Wind And Their Application To The ADS Mission

(D. C. Kayser, The Aerospace Corporation)

The upper atmosphere composition spectrometer (UACS) was flown on the Department of Defense Space Test Program mission S85-1. UACS was designed to measure neutral composition, temperature, and the in-track wind component in the lower thermosphere. In the high inclination orbit of S85-1, UACS measured the meridional component of wind at all but the highest latitudes. A general discussion of UACS can be found in Kayser, et al. [1986]. A later paper [Kayser, 1988] is devoted to a description of the specific instrumental technique which is used to derive the in-track component of the neutral wind.

As part of the ADS mission, UACS has been renamed CADS (for composition and density sensor) and will contribute to the coordinated measurement of density and composition. Its special contribution will be in the area of temperature and wind measurements. Later in this discussion it will be shown that measurements of the in-track wind component must be used in the analysis of density and composition data if the goal of 5% accuracy is to be reached. Also, in-track wind in combination with cross-track wind measured by the accelerometer prescribes the horizontal neutral wind field. These data can be compared with the output of dynamical models, thus contributing to improvements in the formulation of such models.

Briefly, in-track neutral wind is measured by CADS as an energy offset of the retarding potential analysis (RPA) curve. Figure 1 is an example of such a curve, and shows the normalized detector signal (data are circles) for molecular nitrogen versus retarding potential voltage. The position in volts of the 50% point on the curve corresponds approximately to the average energy of a molecule as seen in the satellite (~ 8 km s⁻¹) reference frame. An in-track wind component, if it is present, will shift the RPA curve to higher (head wind) or lower (tail wind) energies. In the figure a best-fit curve is shown along with two curves which are displaced 0.1 V either side of the best-fit voltage. These curves are calculated from the neutral gas distribution function which is convoluted with the instrument response function.

Table 1 shows the theoretical change in position for the 50% point on the RPA curve for a range of head-wind velocity, W . With ~ 44 m/s corresponding to an easily detected 0.1 volt, winds of this magnitude or less can be readily measured. Sensitivity varies by gas specie (Table 2), due to the mass dependence of kinetic energy. In terms of millivolts energy shift per m/s of wind, heavier gases give greater sensitivity. Abundance of each specie is also important however, as the sensor output signal is proportional ambient density. Combined, these considerations make molecular nitrogen the best gas specie to use in the lower thermosphere, with atomic oxygen a possible candidate for higher altitudes.

The wind measurements on S85-1 were obtained from analysis of the nitrogen signal. The experiment obtained a small but significant set of wind data for 2 days in July 1984 at altitudes between 200 and 235 km, at local solar times of 1030 and 2230 hours. The measured winds compare favorably with published results from ground-based incoherent scatter radar and Fabry-Perot interferometer experiments and with satellite-based cross-track measurements of the meridional wind: In Figure 2 the new data have been averaged into 2-degree latitude bins and plotted using (+) symbols. Also plotted are combined data sets of the nighttime meridional wind for the period corresponding to summer in the northern hemisphere. Letters, and letters with vertical bars, are previously published data from the AE-E satellite and a variety of ground stations. As much as possible the data shown are associated with solar minimum conditions. Winds to the north are positive. The same format is used in Figure 3 except that the combined data sets are for the daytime meridional wind. S85-1 measurements are plotted using dashes and circles. Overall, these favorable comparisons provide assurance that the RPA technique can be used effectively to measure neutral wind under typical thermospheric conditions.

Some additional comments can be made regarding the accuracy of in-track wind measurements: Table 3 summarizes the error levels realized on the S85-1 mission employing the RPA technique. Using only 4% of the available signal, UACS provided wind data with estimated point errors of 16-21 m/s in the 200-225 km altitude range. If those errors are adjusted to obtain consistency with along-the-track scatter, values of 20-28 m/s are calculated. Using typical density (hence signal) changes between 225 and 300 km, one can estimate an adjusted error of 130 m/s at 300 km. Had 100 % of the

nitrogen signal been used, projected errors of 4, 6, and 26 m/s are obtained for altitudes of 200, 225, and 300 km respectively. Thus, a sensor optimized for the task could in principle produce highly competitive wind measurements.

The extent to which density and composition measurements are affected by wind depends on the specific measurement technique employed. Table 4 summarizes the wind dependence which is implicit in each of the 3 common techniques: Drag techniques sense vehicle drag (A) which is a function of the B-factor, the mass density, and the square of the sum of satellite velocity plus in-track wind. Thus, the fractional error in density due to wind is equal to 2 times the ratio W/V . A mass spectrometer run in normal mode produces a signal S which is a product of a calibration factor C, the ambient composition N, and the sum of satellite velocity plus in-track wind. The fractional error in composition due to wind is therefore W/V . A mass spectrometer run in RPA mode produces a signal which to first order is independent of velocity and wind and is proportional to ambient composition. A measurement using this technique is, however, difficult to calibrate and gives lower sensitivity for the determination of composition.

Table 5 gives the measurement error in percent for drag and normal-mode mass - spectrometer measurements in the presence of in-track winds from 10 to 500 m/s. Roughly speaking, if an accuracy of 5% or better is required from drag measurements then winds over 50 m/s need to be known and corrected for in the data analysis. The equivalent level for mass-spectrometers is 100 m/s. Thus, it is anticipated that CADS can easily provide wind data of sufficient accuracy to remove this source of error from concurrent measurements of composition and density. In the auroral zones, where winds of over 500 m/s are routinely experienced, this capability is especially important.

References

Kayser, D. C., W. T. Chater, C. K. Howey, and J. B. Pranke, "The Upper Atmosphere Composition Spectrometer", *Journal of Spacecraft and Rockets*, 23, 336-341, May-June 1986.

Kayser, D. C., "Measurements of the Thermospheric Meridional Wind from the S85-1 Spacecraft", *Journal of Geophysical Research*, 93, 9979-9986, September 1988.

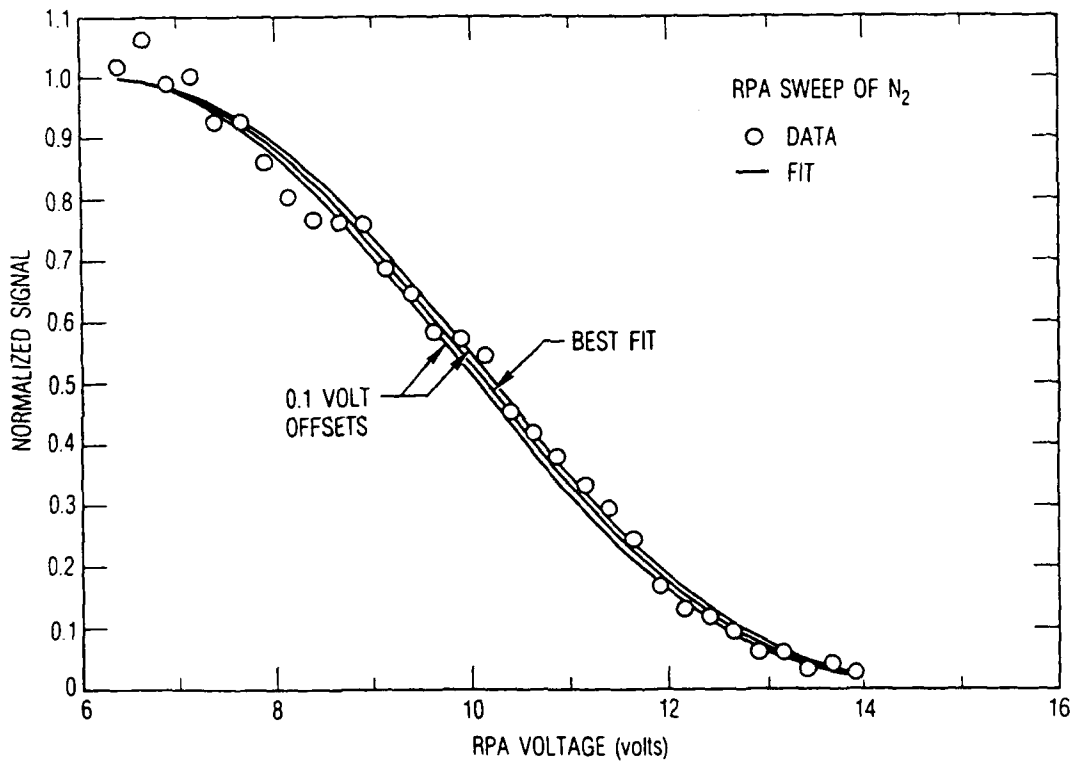


Figure 1. A retarding potential analysis curve.

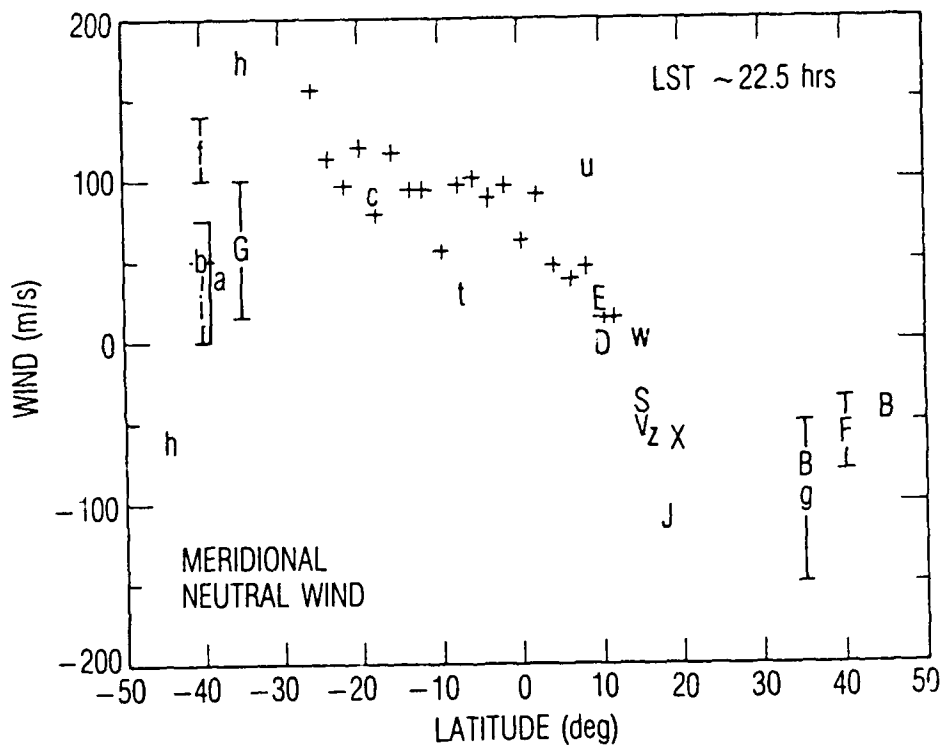


Figure 2. S85-1 wind data compared to other techniques. Nighttime meridional winds.

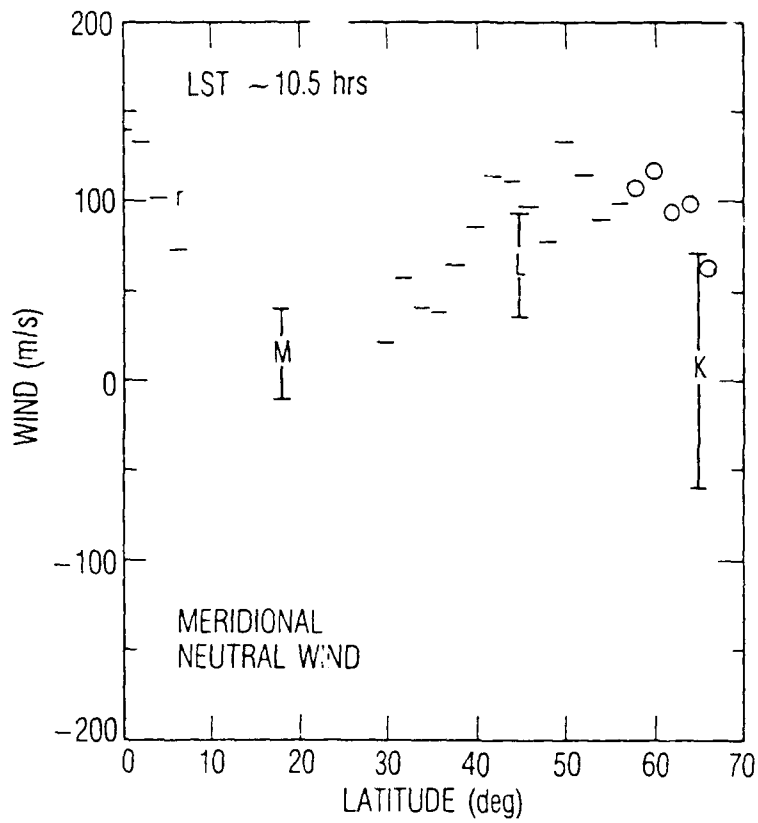


Figure 3. S85-1 wind data compared to other techniques. Daytime meridional winds.

Table 1. Retarding potential voltage shift for a range of typical neutral wind values.

<u>W (m/s)</u>	<u>V_R (VOLTS)</u>
0	8.9
44.0	9.0
87.5	9.1
130.7	9.2
216.5	9.4
427.1	9.9

(GAS IS N₂ , V_S = 7800 m/s)

Table 2. RPA sensitivity using various gases.

<u>GAS</u>	<u>M.W.</u>	<u>SENSITIVITY</u> <u>mV/(m/s)</u>
O	16	1.3
N ₂	28	2.3
AR	40	3.3

($V_S = 7800$ m/s)

Table 3. In-track wind component measurement errors (given in m/s).

ACCURACY OF S85-1 MEASUREMENTS, WHICH USED 4% OF SIGNAL:

	<u>200 KM</u>	<u>225 KM</u>	<u>EST.</u> <u>300 KM</u>
ERRORS FROM SWEEP ANALYSIS	16	21	104
ERRORS ADJUSTED FOR ALONG-THE-TRACK CONSISTENCY	20	28	130

PROJECTED ACCURACY FOR SENSOR USING 100% OF N₂ SIGNAL:

	<u>200 KM</u>	<u>225 KM</u>	<u>300 KM</u>
FUTURE SENSOR	4	6	26

Table 4. Density and composition measurement error due to an in-track wind.

(V- SATELLITE VELOCITY, W- IN-TRACK WIND)

DENSITY FROM DRAG:

$$A = 1/2 B \rho (v+w)^2$$

$$d\rho/\rho \sim 2 w/v$$

COMPOSITION FROM MASS SPECTROMETER (NORMAL MODE):

$$S = C N (v+w)$$

$$dN/N \sim w/v$$

COMPOSITION FROM MASS SPECTROMETER (RPA MODE):

$$S = C N$$

$$dN/N \sim 0$$

Table 5. Density and composition measurement error as a function of wind speed.

TECHNIQUE	IN-TRACK WIND (M/S)					
	10	20	50	100	200	500
DRAG	0.25	0.5	1.25	2.5	5.0	12.5
MASS-SPEC (NORMAL MODE)	0.13	0.25	0.63	1.25	2.5	6.3

MEASUREMENT ERROR IN PERCENT

4.13 FABRY-PEROT INTERFEROMETER FOR ADS

T. L. Killeen
Space Physics Research Laboratory
University of Michigan

The Fabry-Perot Interferometer, FPI, measures the intensity and spectral location of visible atmospheric emissions in altitude regions centered at ~98, 185 and 225 km. From these measurements the primary FPI state variables, winds and temperatures, can be calculated to better than ± 5 m/s. Secondary measurements are metastable atom densities to $\pm 10\%$. Density profiles can be obtained by using measured temperature profiles and the hydrostatic approximation, together with an in-situ observation of density to normalize the profile. Since FPI is a remote sensing instrument, measurements can be made continuously, however data will degrade at the higher altitudes of an elliptical orbit. The FPI was flown successfully on Dynamics Explorer 2 (Hays et al., 1984). Since the FPI is an instrument that has not been flown previously on an Air Force spacecraft and since it provides critical wind and temperature information needed for the modeling efforts, we discuss the instrument in greater detail than the in situ sensors described above.

FPI Instrument Description

The instrument is composed of three basic elements: the interferometer, an electronics package and the telescope sub-assembly. A schematic of the optical path of the instrument designed to meet the requirements discussed above is shown in figure 1 and the telescopes are shown in figure 2. The basic simplicity of the instrument is evident here. Also, shown is the IPD Photometer which will be discussed in the following section.

Incoming light passes through both fore and aft telescopes. The telescopes are oriented at $\sim 45^\circ$ with respect to the satellite velocity vector. The two look directions provide two vector wind components and, since vertical winds are normally small compared to horizontal winds, this permits the measurement of the vector winds. A simple scan mirror in each look direction chooses the altitude. A fore/aft selector chooses which telescope signal will be passed through a simple relay optics system to the interferometer. The telescopes are copies of the DE-FPI design.

Two line-to-circle convertors provide entry to the FPI/IPDPH. The line input matches the need to provide a narrow, horizontal sample of the horizon. In this way, good vertical resolution can be obtained while retaining good sensitivity using a broader horizontal field of view. The line shape is then converted to the circular input required by both the FPI and the IPDPH. Additionally the line inputs can be located close enough together such that they can share telescopes and operate simultaneously, sampling slightly different altitude regimes.

The light from the line-to-circle convertor is then partially collimated to pass through a dielectric interference filter mounted in a filter wheel. The interferometer light beam is then expanded and further collimated to meet theoretical requirements of the fixed-gap, high-resolution etalon. The etalon objective telescope then images the light, which now contains spectral information in an axially concentric pattern, onto the image plane detector. Figure 3 shows the basic interferometer output in the form of a high resolution 12 channel spectrogram which contains the wind, temperature and brightness information.

The optical throughput or etendue is held constant throughout the optical system to maximize sensitivity and minimize size. The etendue is controlled by the spectral resolution and instrument size constraints. Folded optics are used to minimize size as well as to avoid mechanical and thermal distortions.

Fabry-Perot Interferometer

The heart of the FPI is the Fabry-Perot interferometer that performs the high resolution spectral analysis of light emitted from the earth's atmosphere. The interferometer is a single, fixed gap etalon system with a folded optics objective telescope and a twelve-channel image plane detector. The interferometer section is made up entirely of flight-spare hardware and optics from the Dynamics Explorer program.

The etalon and etalon mount are the products of the development effort leading to the successful DE-FPI instrument. The etalon has three zerodur spacers glued to two fused silica end plates on whose inner surfaces

are deposited the semi-reflecting dielectric coatings. The etalon is mounted in a fully kinematic mount designed to provide isolation from stresses due to temperature gradients, etc., while maintaining optical alignment and instrumental ruggedness. (Killeen et al., 1982).

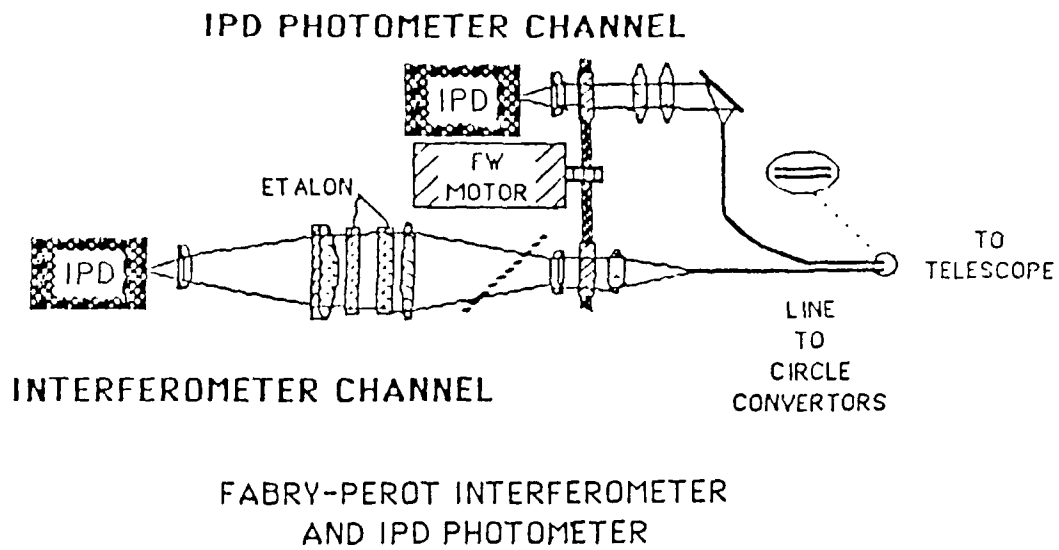


Figure 1. Optical schematic of ADS Fabry-Perot interferometer

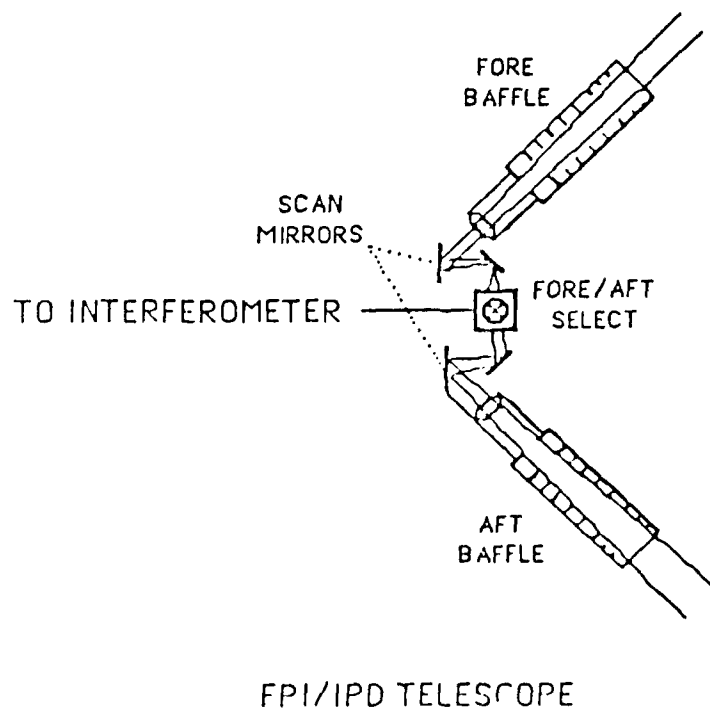


Figure 2. Baffle schematic for ADS Fabry-Perot interferometer

INTERFEROGRAMS OBTAINED WITH THE HE/NE LASER AND DE ETALON AND DETECTOR. A PRESSURE STEP WAS TAKEN TO SIMULATE A 100 M/S NEUTRAL WIND.

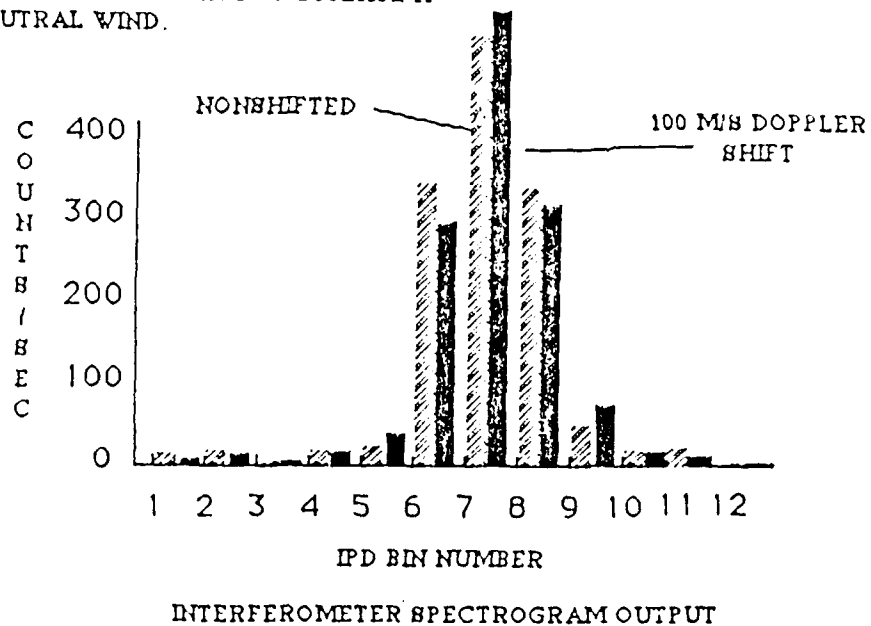


Figure 3. ADS Fabry-Perot interferometer spectrogram output. The peak detected by the multichannel IPD contains the Doppler information necessary to calculate winds, temperature and volume emission rates. The effect of a 100 m/sec wind on the spectrum is illustrated.

The image plane detector (IPD) is similarly a product of the DE development program and is a 12 channel concentric ring anode device incorporating a micro-channel plate electron multiplication stage and an S-20 photocathode. Each anode ring is single photon counting and measures one spectral element. The IPD effectively "scans" the etalon in angle without the need to mechanically change any etalon parameter. It also detects light in all spectral elements simultaneously, thereby enhancing instrument sensitivity over conventionally scanned interferometers. The IPD is identical to that used successfully on DE-FPI (Killeen et al., 1983).

Scanning telescope optical design.

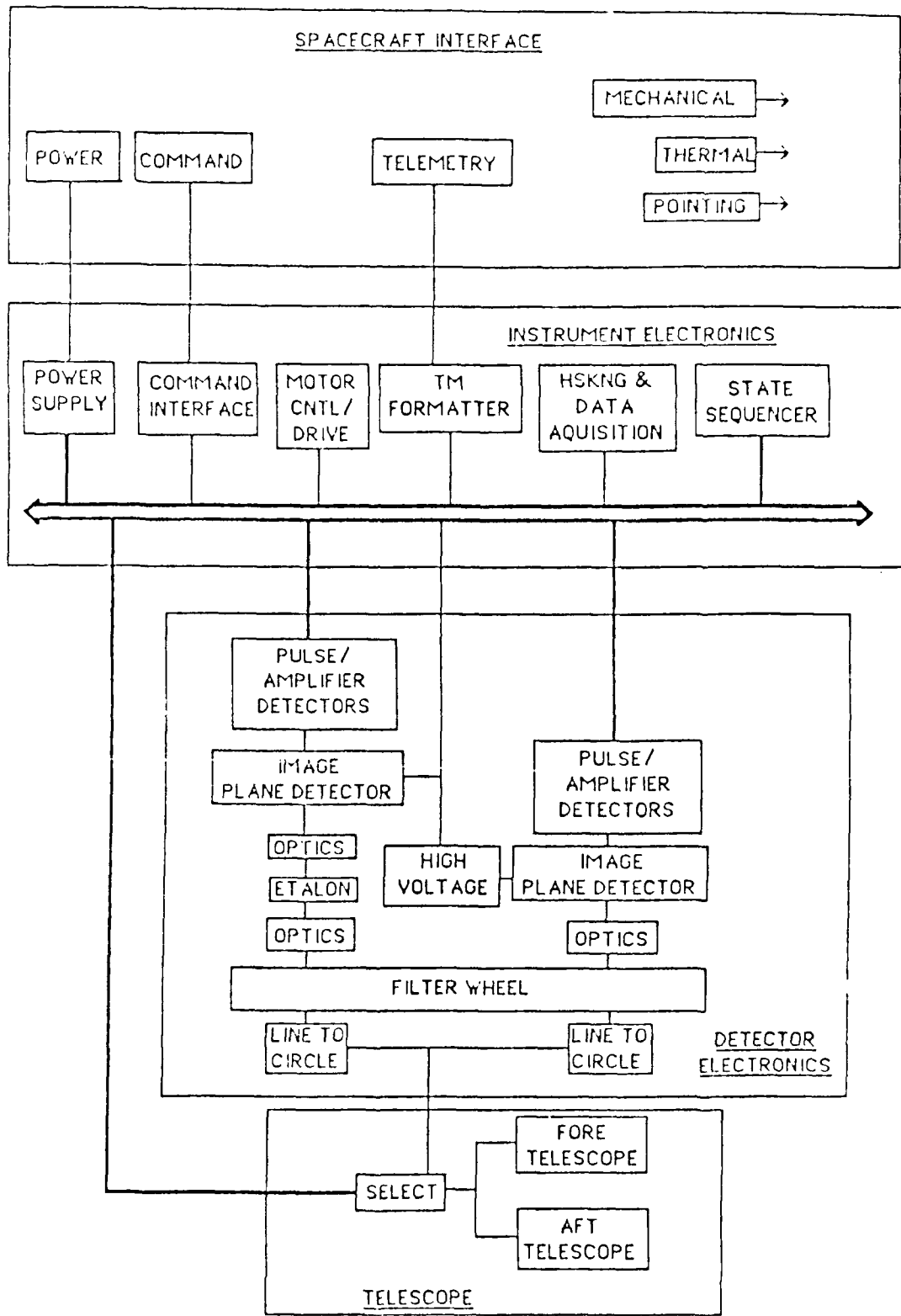
The telescope is shown schematically in figure 2. Two look directions at 45° with respect to the velocity vector are provided to obtain full vector wind measurements. The basic telescope design is the same as DE-FPI consisting of a protective cover, light shielding baffle, and horizon scan mirror. For this mission, an optical switch selects fore and aft views.

Electronics

The electronics block diagram is shown in figure 4. The instrument is functionally divided into four sections: telescope, detector, instrument electronics and satellite interface. The telescope drive consists of two stepper motors for horizon scan and another stepper motor for fore and aft selection. Scan will be controlled by a state sequencer similar to that flown on DE-FPI. The detector electronics are a basic copy of those flown on DE-FPI and consist of a HV supply for the IPD, 12 channels of analog and pulse detection of the IPD output signals, calibration sources and filter wheel drive and position. The IPDPH detector electronics are identical to the FPI detector electronics. The instrument electronics sub-system distributes supply voltages, commands and timing signals to the other instrument blocks. Instrument monitors such as temperature measurements, high voltage monitors, scan position decoder outputs etc., enter this section for transmission to the telemetry stream. The satellite interface section is designed to provide simple interfaces to facilitate testing, integration and flight operations and to minimize interconnects. The electronics design is almost entirely a carryover from the DE-FPI, AE-VAE systems with minor updates from the HRDI/UARS currently in final assembly and test.

FPI Sensitivity

The Low Altitude Doppler interferometer instrument described in the previous sections has the inherent high throughput of the Fabry-Perot interferometer and has the spectral selectivity to measure winds and temperatures in the earth's atmosphere. The basic instrument sensitivity is tabulated in Table 1.



FPI ELECTRONICS BLOCK DIAGRAM

Figure 4 Electronic functional block diagram for the ADS Fabry-Perot interferometer.

TABLE 1
ADS-FPI Instrument Sensitivity

System transmission, T_0 (all elements coated)	0.1
Quantum efficiency, Q_e	0.1
Etendue ($A\Omega$)	$1.815 \times 10^{-3} \text{ cm}^2 \text{ ster}$
$\Delta\nu(\text{ring})$	$0.045 \text{ cm}^{-1} (5577\text{\AA})$ $0.0327 \text{ cm}^{-1} (7650\text{\AA})$
Spectral response:	
C_i (counts per sample)	
$\frac{A\Omega}{4\pi} T_0 Q_e \times 10^6 \Delta t \int_0^\infty T_{FP}(\nu) R(R/\text{cm}) d\nu$	
5200 \AA	$0.22 \Delta t R_i$
5577 \AA	$0.20 \Delta t R_i$
5896 \AA	$0.14 \Delta t R_i$
6300 \AA	$0.10 \Delta t R_i$
7650 \AA	$0.03 \Delta t R_i$

FPI Error Analysis

Statistical Errors

Statistical errors in the measurements of winds, temperatures and emission line brightnesses are dependent on the integration time period and the brightness of the given emission. We have modified the full DE-FPI simulator computer program to calculate statistical measurement precisions for the ADS-FPI. These calculations involved the simulation of spectrograms using a measured instrument function and the analysis of the spectrograms using the DE-FPI flight analysis routines. The accuracies are depicted in figure

5. It can be seen that for typical daytime brightnesses for the 5577 \AA emission, accuracies of 5m/sec and 10 ° K are obtained with integration periods of 1 second. For typical nighttime brightnesses, these accuracies are degraded to 20 m/sec and 50 ° respectively. These errors are sufficiently small to enable the generation of vector altitude profiles as required for the proposed investigations.

ADS-FPI: TYPICAL 'ONE SHOT' INTEGRATION
TIMES FOR SPECIFIED ACCURACY

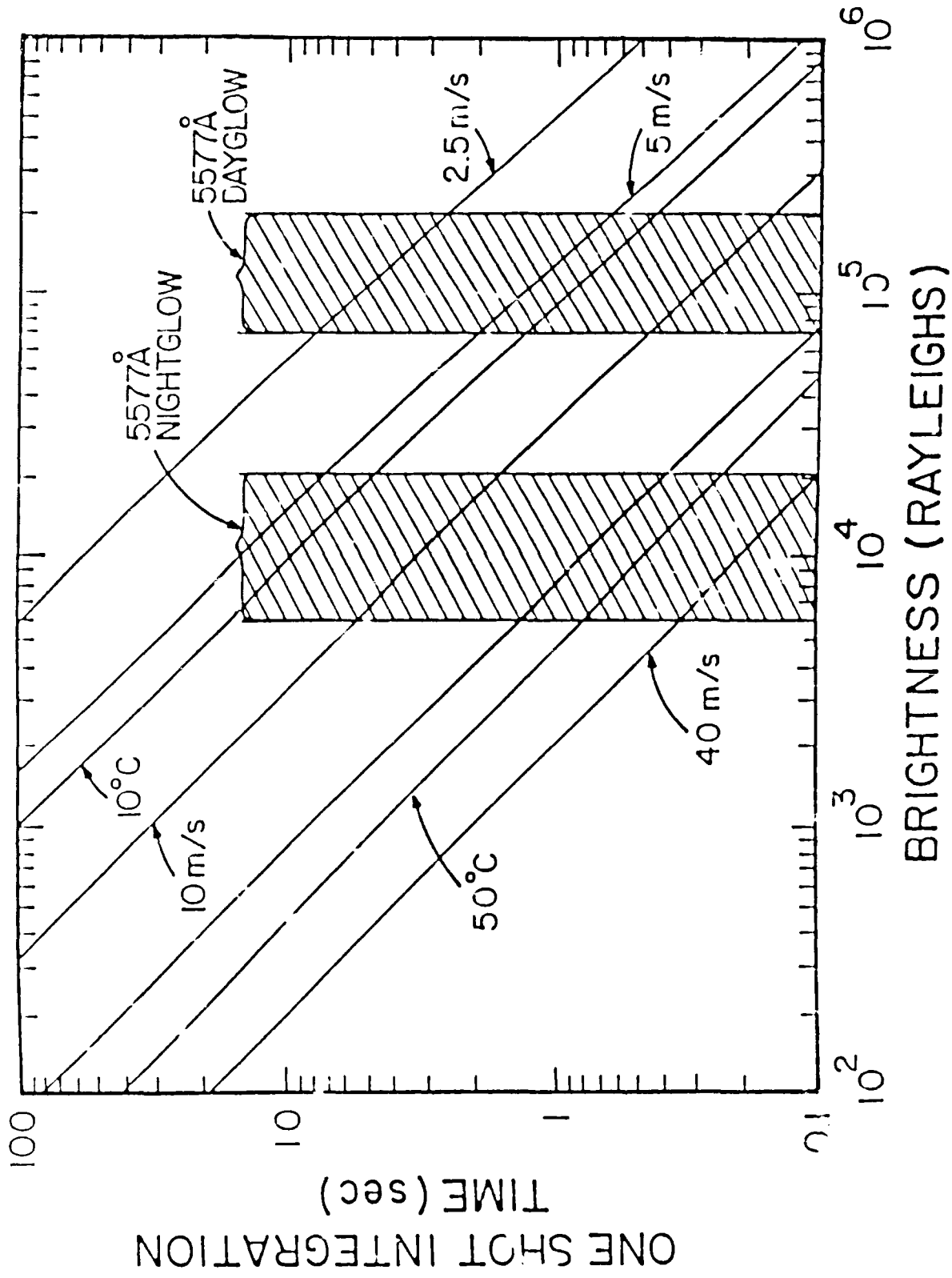


Figure 5 Errors on derived winds and temperatures for the ADS Fabry-Perot interferometer.

Systematic Errors

Possible systematic errors can occur due to instrument spectral drift. Experience with exhaustive laboratory calibrations and spaceflight for the DE-FPI have indicated that a combination of continuous etalon temperature measurements to 0.01° and periodic in-flight spectral calibrations are sufficient to provide knowledge of instrument drifts to $\sim 1\text{m/sec}$. Two further types of systematic error are of importance. These are due to uncertainties in the attitude and velocity of the instrument with respect to the earth and due to calibration uncertainties in the instrument discussed below.

The spacecraft has an inherent orbital velocity of about 7 km/sec which appears as a large DC background shift on any spectral signal attached to the earth. In our worst case, looking at 45° with respect to the spacecraft one finds that an attitude uncertainty of 0.05° leads to a 5m/sec error in the deduced wind. This is a very important point and clearly the wind measurements become degraded for large uncertainties in the attitude. The accuracy of the post-flight knowledge of attitude is therefore a matter of importance to the wind measurement and is of greater concern than errors in the determination of the satellite velocity itself. Several considerations, however, mitigate the negative impact of large attitude errors on the proposed science.

1) It is straightforward to use the Rayleigh scattered light signal from the lower atmosphere during the day and the 5577\AA emission during the night to provide for a rapid and accurate in-flight determination of the instrument zenith angle using simple discrimination electronics to optimize the field of view.

2) The volume emission rate altitude profiles and the kinetic and rotational altitude profiles are insensitive to errors in attitude and much of the science is therefore unaffected.

3) Many of the interesting science problems related to the dynamics of the mesosphere/lower thermosphere involve "AC" rather than "DC" wind systems (e.g. gravity waves, eddies etc.) and therefore relative measurements of winds, which are largely unaffected by attitude errors, are sufficient for many purposes.

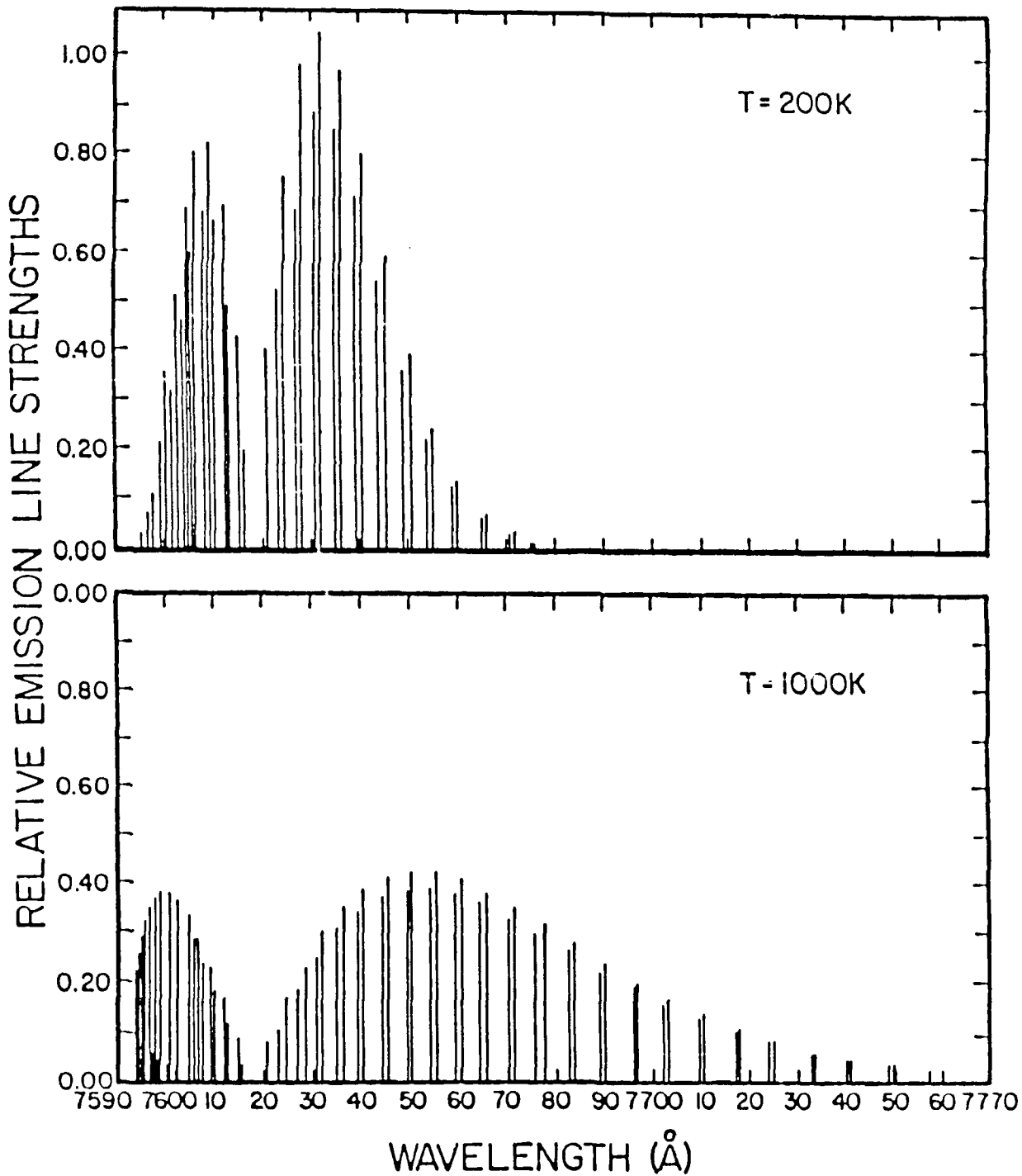
4) The wind measurements themselves (for example in the upper thermosphere at low latitudes where the wind field is known to be smoothly varying) will provide an in-flight indication of the magnitude of the attitude drift for later comparison.

IPDPH

The Image Plane Detector Photometer, IPDPH, is shown in figure 5.1. The IPDPH is an integral part of the ADS-FPI package which shares the telescope, filter wheel and many of its electronics with the FPI. Also, the IPD and its electronics are direct copies of the DE-FPI IPD. Additional elements are a second line to circle convertor and three simple lenses. The IPDPH complements the measurement package by providing for accurate rotational temperature measurements from $90\text{-}120\text{ km}$ using the O_2 (0-0) atmospheric band emission and direct O_2 density measurements from $60\text{ to }120\text{ km}$ using the method of oxygen fluorescence. Rotational temperature measurements are obtained to very high precision by detecting the spectral changes

in the shape of the O₂ atmospheric band (Figure 6). Figure 7 illustrates the accuracies with which rotational temperatures can be measured as a function of altitude in the daytime thermosphere by using a combination of the observations from the FPI and IPDPH channels of the ADS remote sensing instrument. As can be seen, rapid measurements of the temperature profile to accuracies of $\sim 1^\circ$ can be obtained in the altitude region 90 - 120 km. The technique is limited below 90 km by the increasing optical depth of the (0-0) emission and above 120 km by the fall off in O₂ density. In this region, however, the hydrostatic law can be used to derive O₂ density profiles.

O₂ ATMOSPHERIC (0-0) BAND



Temperature Dependence of the O₂ (0-0) atmospheric molecular emission band as seen from orbit (P-branch)

Figure 6 Changes in spectral signature of the O₂ (0-0) atmospheric band due to changes in rotational temperature. The rotational temperature can be measured by using two relatively low spectral resolution measurements with the FPI and IDPPH channels.

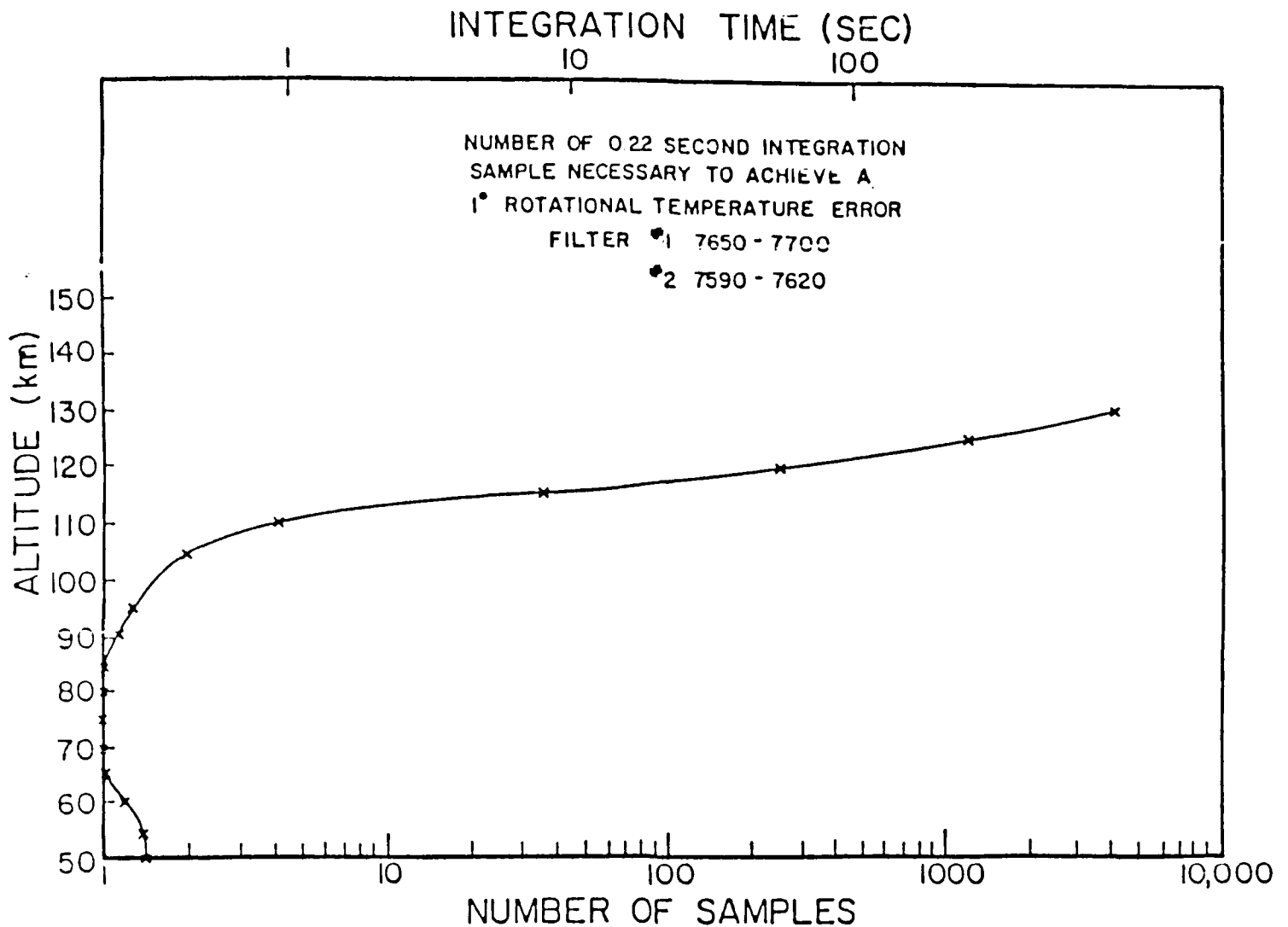


Figure 7 Number of 0.22 seconds integration times necessary to achieve a 1° rotational temperature error in the daytime thermosphere as a function of altitude using the ADS-FPI.

ADS-FPI Sample time and integration period for a statistical error of one degree on a measurement of rotational temperature from the O₂ (0-0) atmospheric band. Below ~70km, the optical depth² of the emission limits the measurement (although the technique can be somewhat extended into the optically deep region using algorithms such as those developed for the UARS/HRDI program, Hays, Private communication)

REFERENCES

- Hays, P. B., T. L. Killeen, N. W. Spencer, L. E. Wharton, R. G. Roble, B. E. Emery, T. J. Fuller-Rowell, D. Rees, L. A. Frank, and J. D. Craven, Observations of the dynamics of the polar thermosphere, *J. Geophys. Res.*, 89, 5597-5612, 1984.
- Killeen, T.L., P.B. Hays, B.C. Kennedy, D. Rees, Stable and rugged etalon for the Dynamics Explorer Fabry-Perot interferometer, 2. Performance. *Applied Optics*, 21, 3903-3912, 1982.
- Killeen, T.L., B.C. Kennedy, P.B. Hays, D.A. Symanow and D.H. Ceckowski, An image plane detector for the Dynamics Explorer Fabry-Perot interferometer, *Applied Optics*, 22, 3503-3513, 1983.

4.14

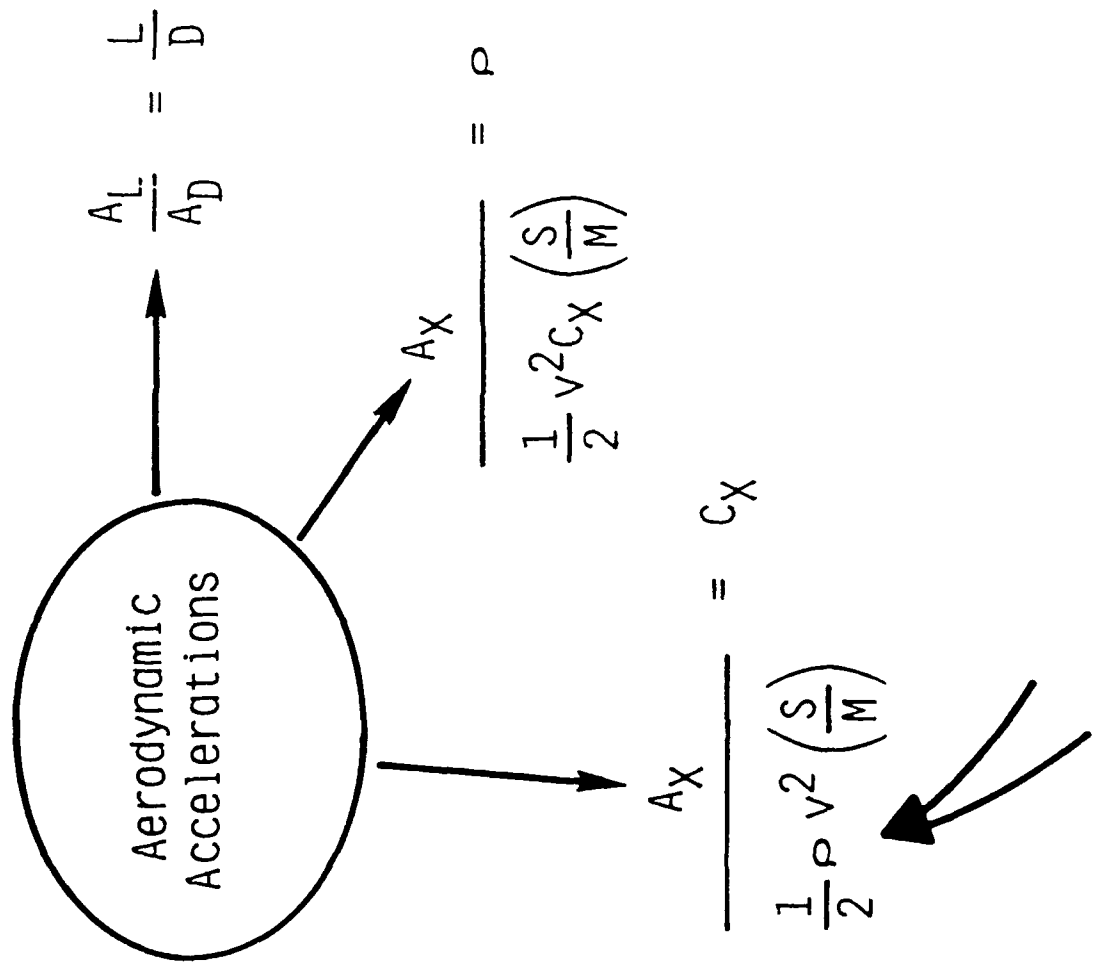
**SHUTTLE REENTRY DENSITY
MEASUREMENTS
(Between 60 and 160 km)**

**ATMOSPHERIC DENSITY AND AERODYNAMIC DRAG
MODELS FOR AIR FORCE OPERATIONS
AFGL WORKSHOP**

October 20 - 22, 1987

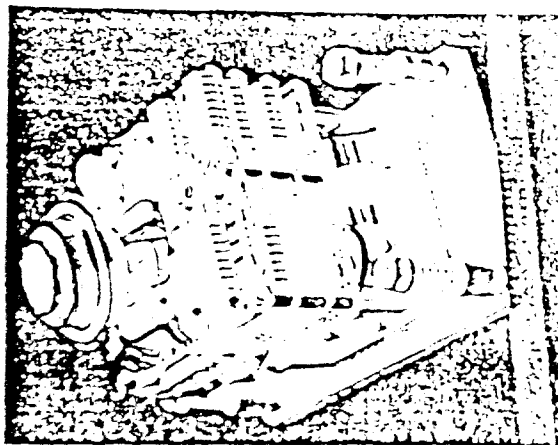
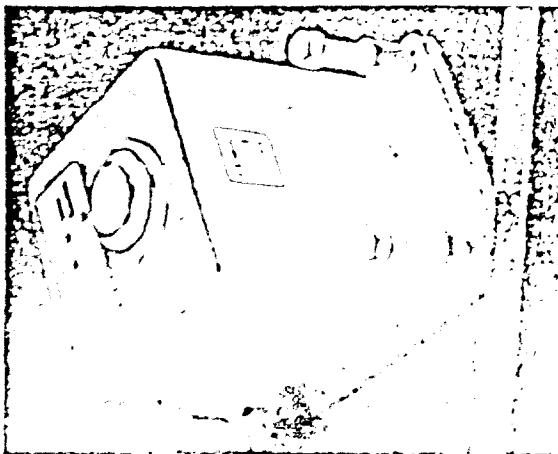
**R. Blanchard
E. Hinson
J. Nickolson**

ACCELEROMETER EXPERIMENT CONCEPTS



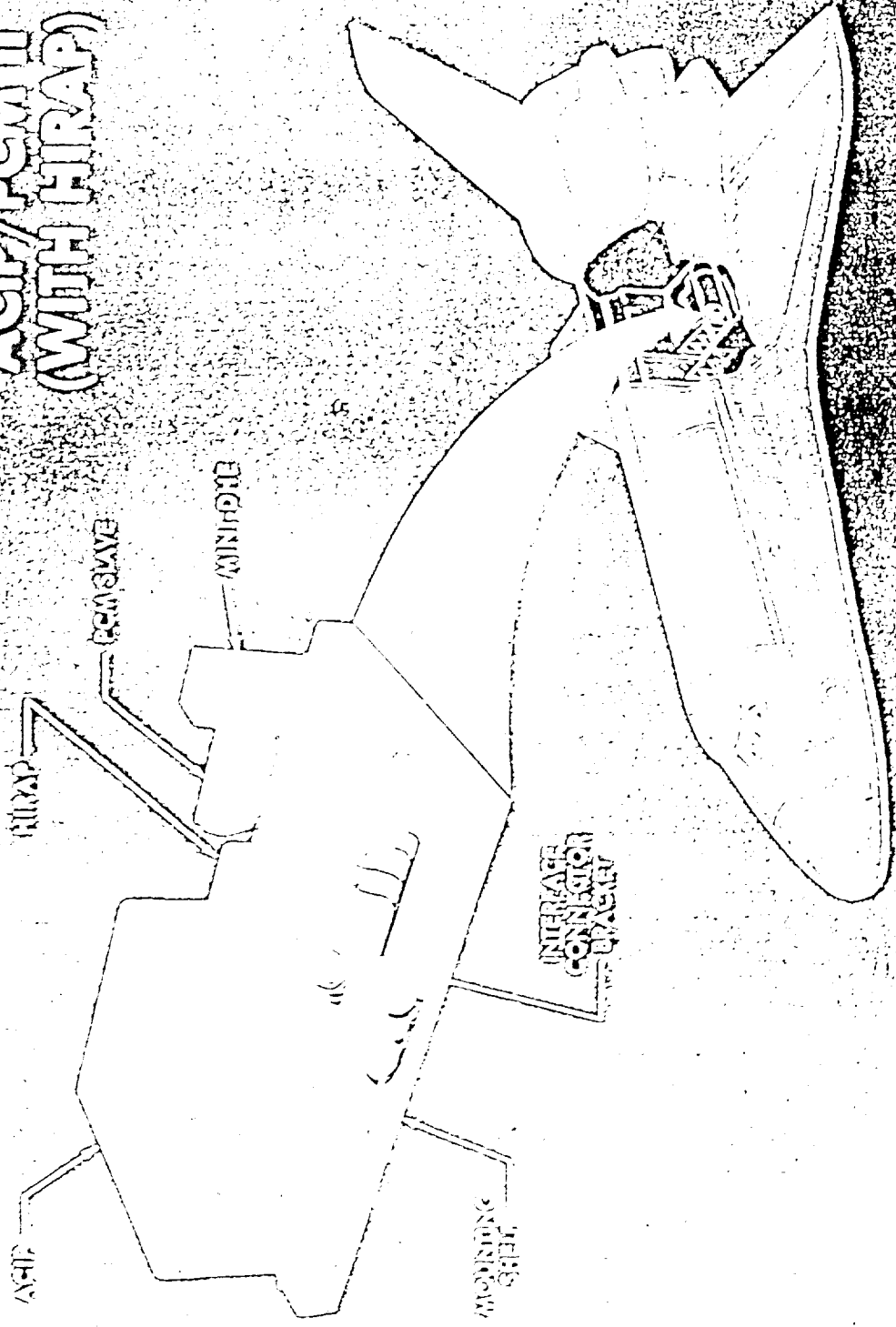
HIRAP DESIGN SPECIFICATIONS

SENSORS:	THREE ORTHOGONAL ACCELEROMETERS PENDULOUS TYPE (GAS DAMPED)
RANGE:	±8000 MICRO-G
RESOLUTION:	1.0 MICRO-G
ACCURACY:	2.0 MICRO-G (AFTER CALIBRATION)
SAMPLE RATE:	174 SAMPLES/SEC
SIZE:	8.89 CM x 12.7 CM x 10.16 CM (3.5" x 5" x 4")
WEIGHT:	1.134 KG (2.5 LBS)
POWER:	5 WATTS

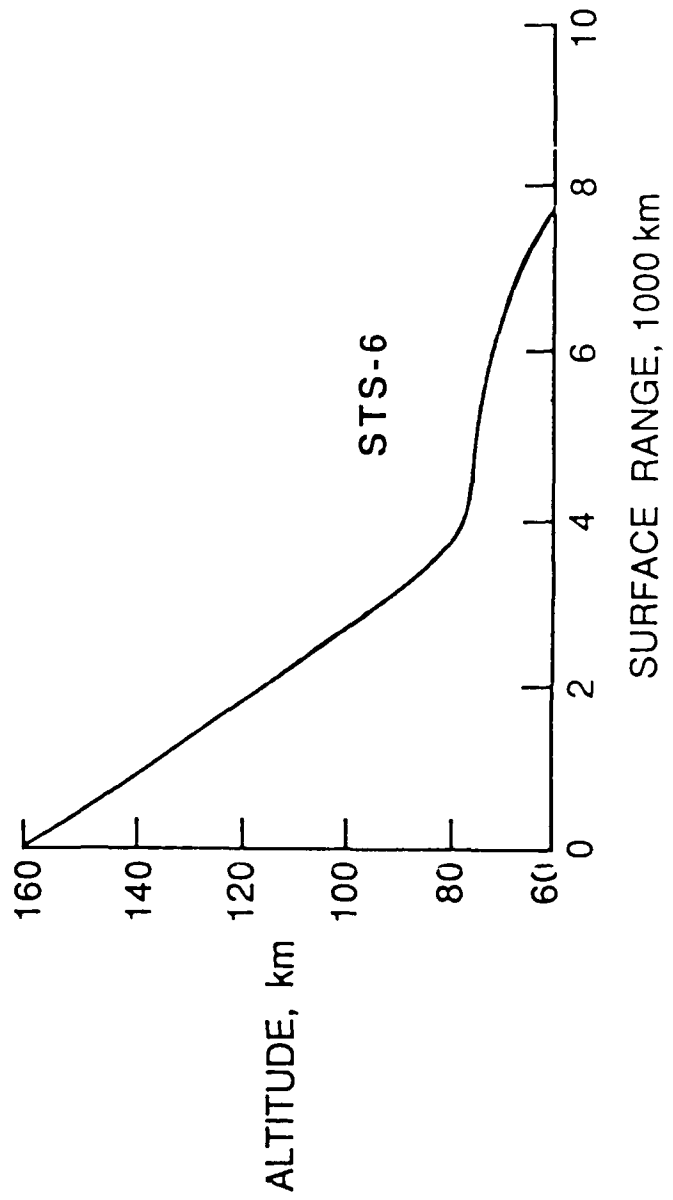


HIRAP FLIGHT UNIT (S/N 002)

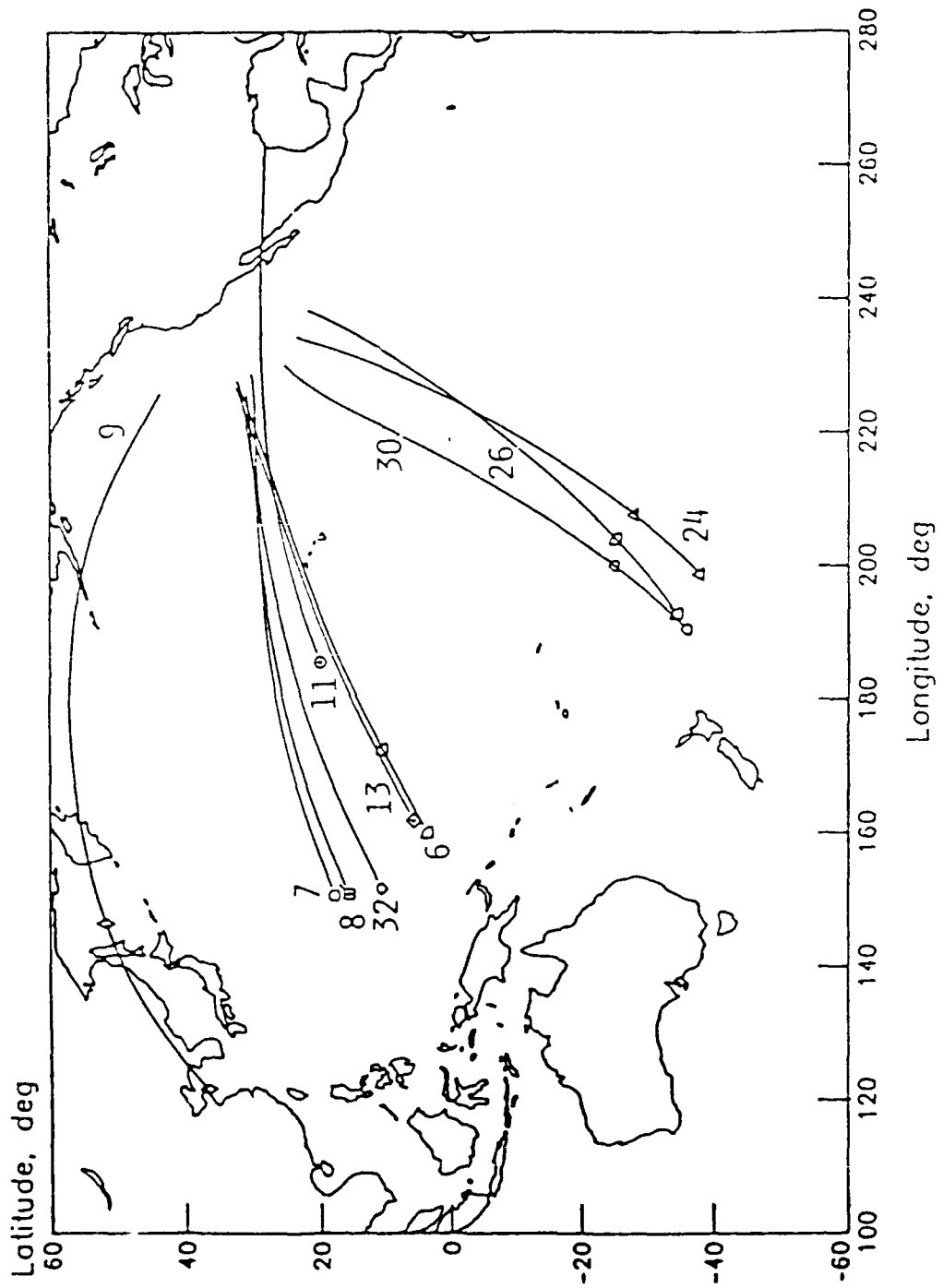
ACIP/PCM II (WITH HIRAP)



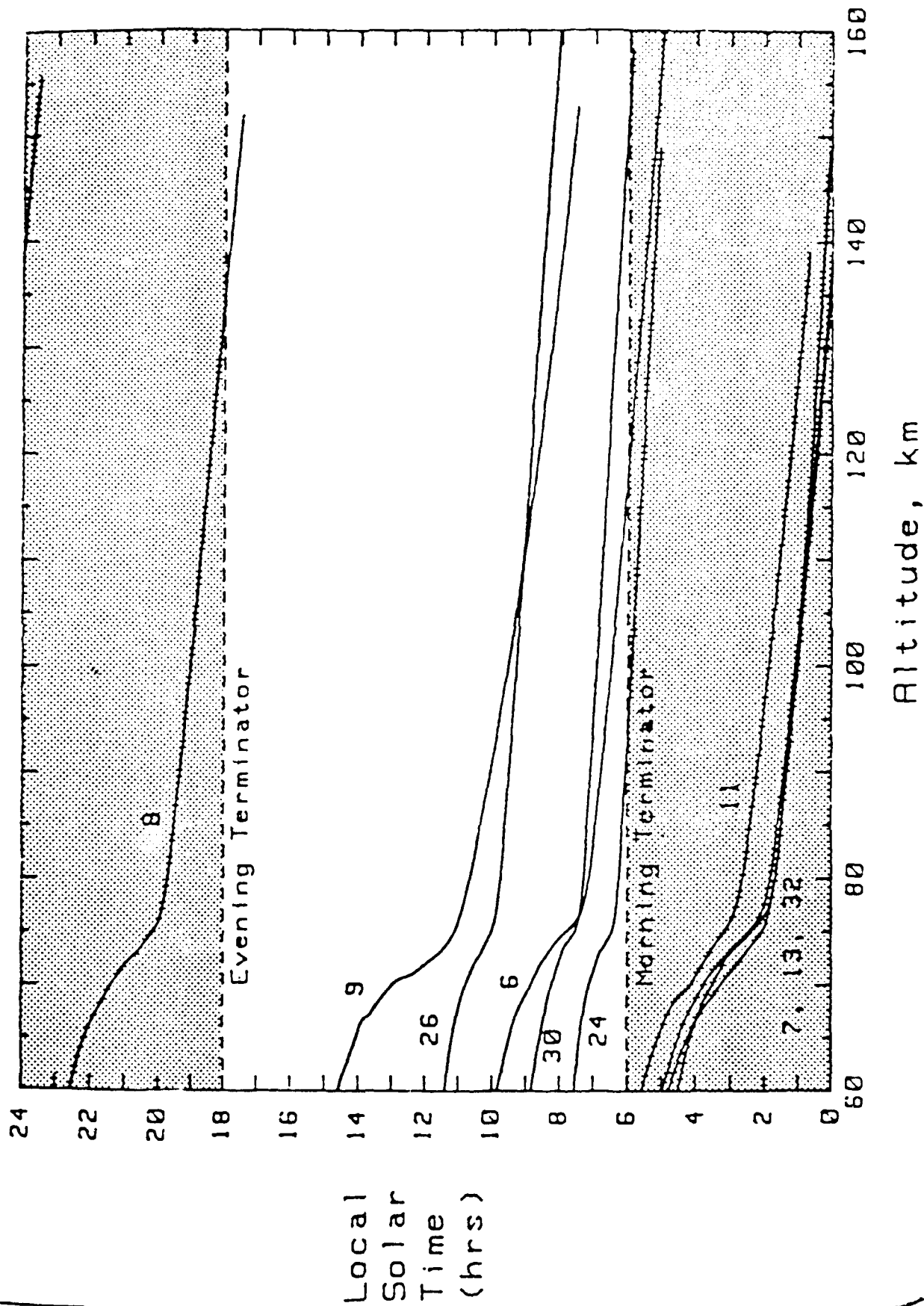
TYPICAL SPATIAL COVERAGE DURING SHUTTLE REENTRY



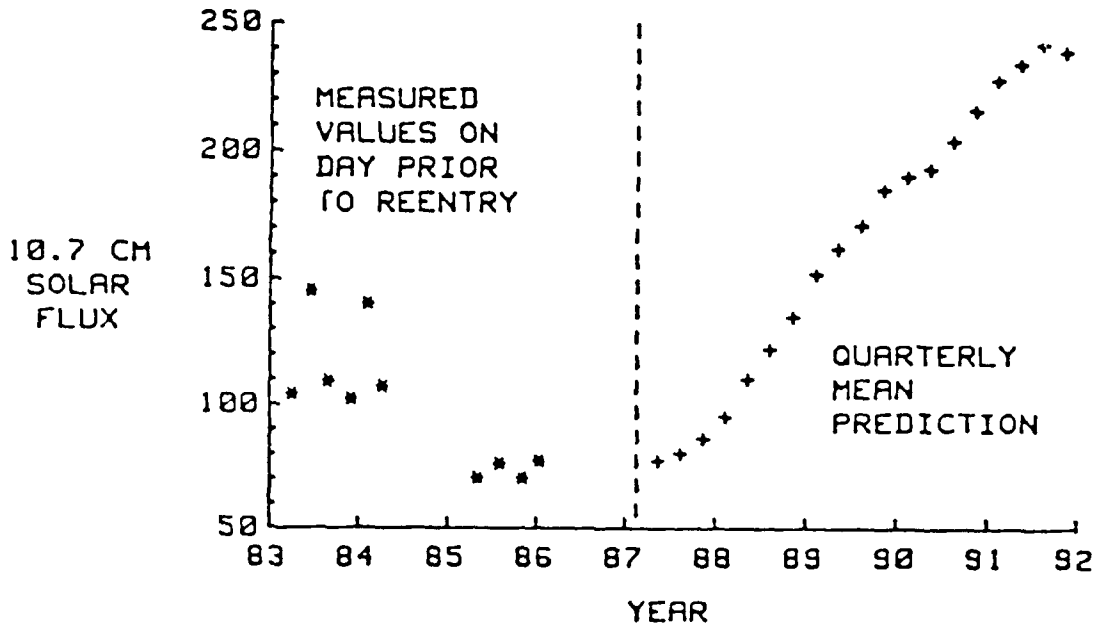
REENTRY GROUND TRACKS BETWEEN 160 AND 60 km



LOCAL SOLAR TIME COVERAGE

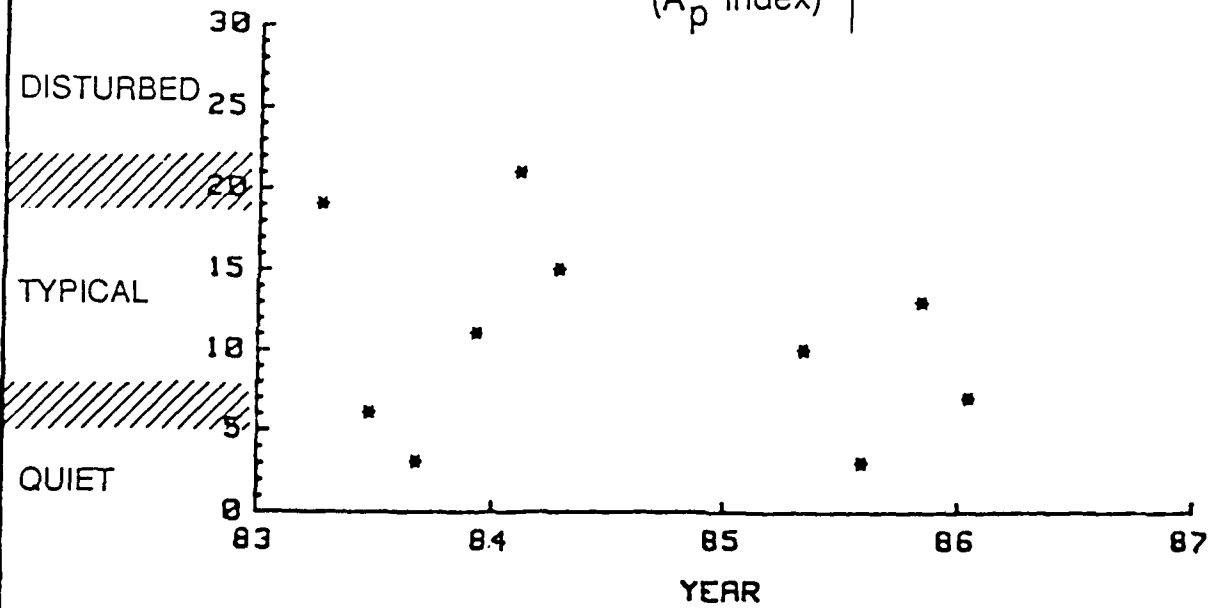


SOLAR FLUX COVERAGE

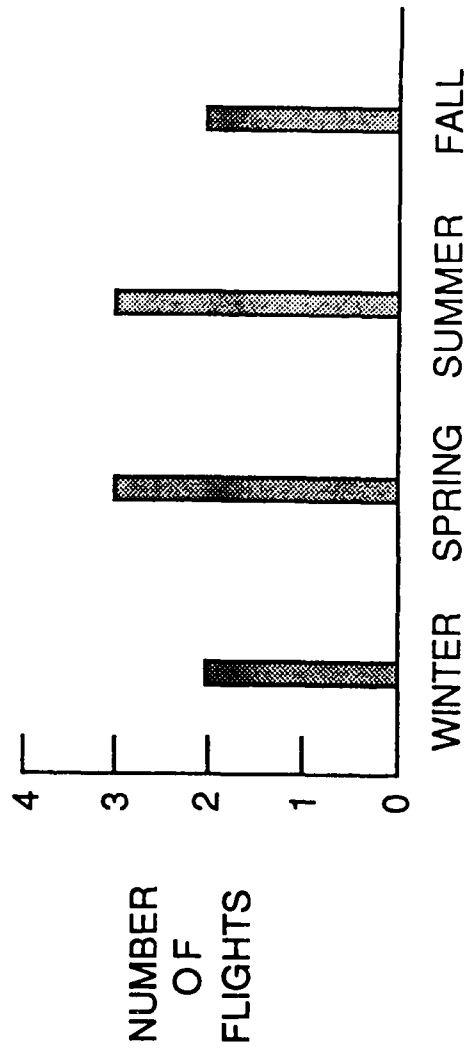


GEOMAGNETIC ACTIVITY COVERAGE

(A_p Index)



SEASONAL DISTRIBUTION OF HIRAP FLIGHTS

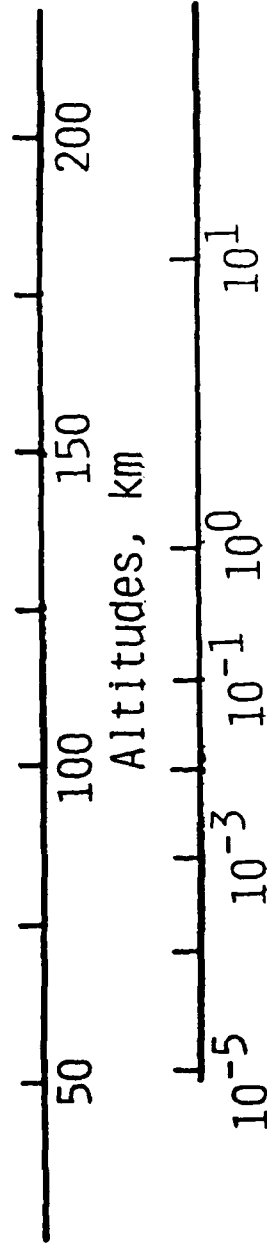
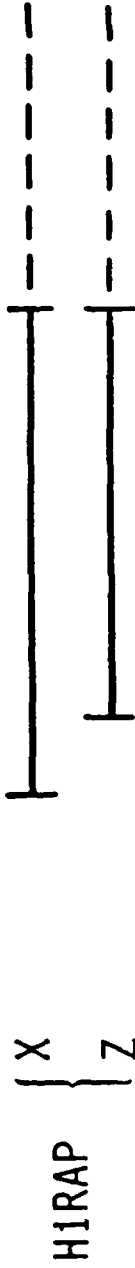


APPROXIMATE ORBITER ACCELEROMETER RANGES

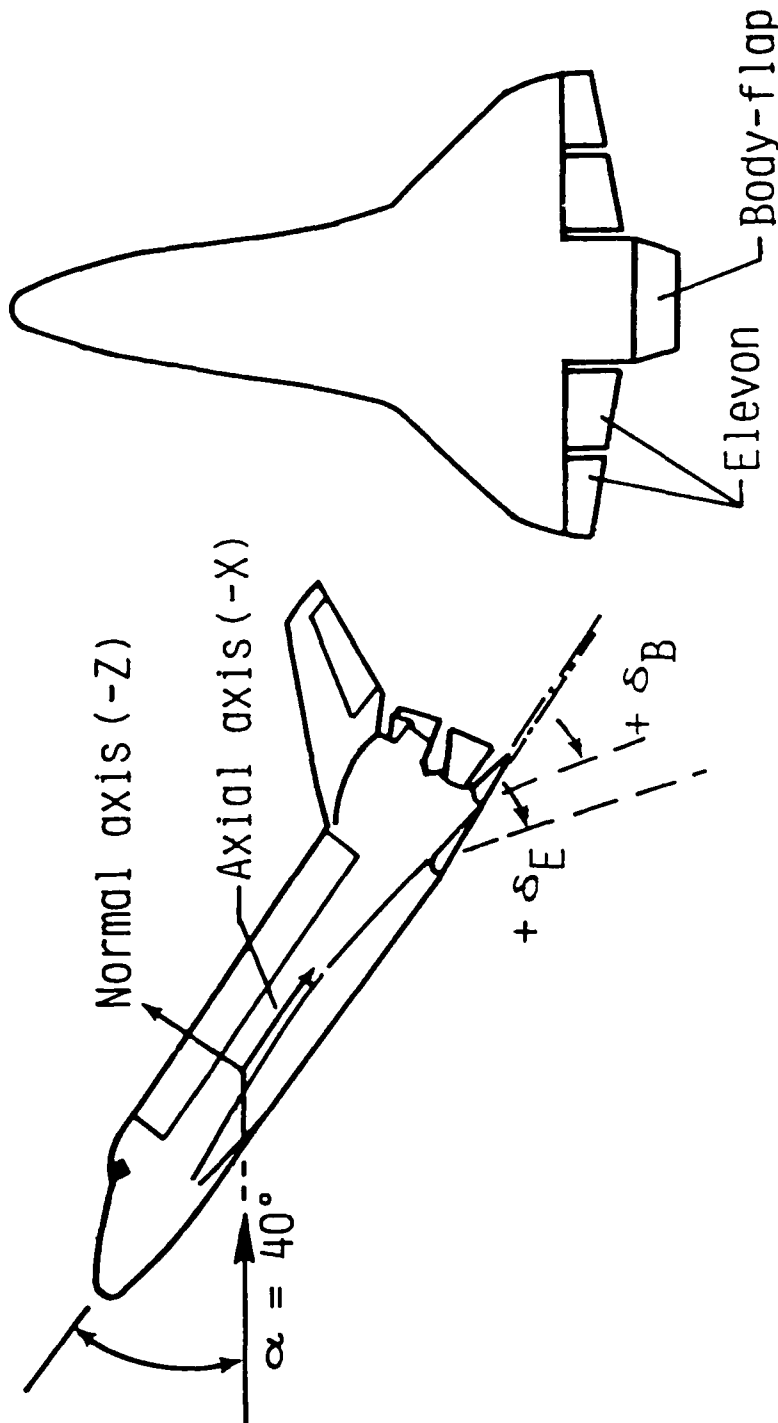
AXIS



* $R_L = 12.0609m$ (MAC)
1976 U.S. Standard



BODY-AXIS COORDINATE SYSTEM AND LOCATION OF CONTROL SURFACES



AERODYNAMIC MODEL

$$C_{I_j} = C_{I_{j0}} + [C_{I_{jF}} - C_{I_{jC}}] \bar{C}_{I_j} \quad j = N, A$$

Where $C_{I_j} = C_{I_{j0}} + \Delta C_{I_{jE}} + \Delta C_{I_{jB}} \quad j = C, F$

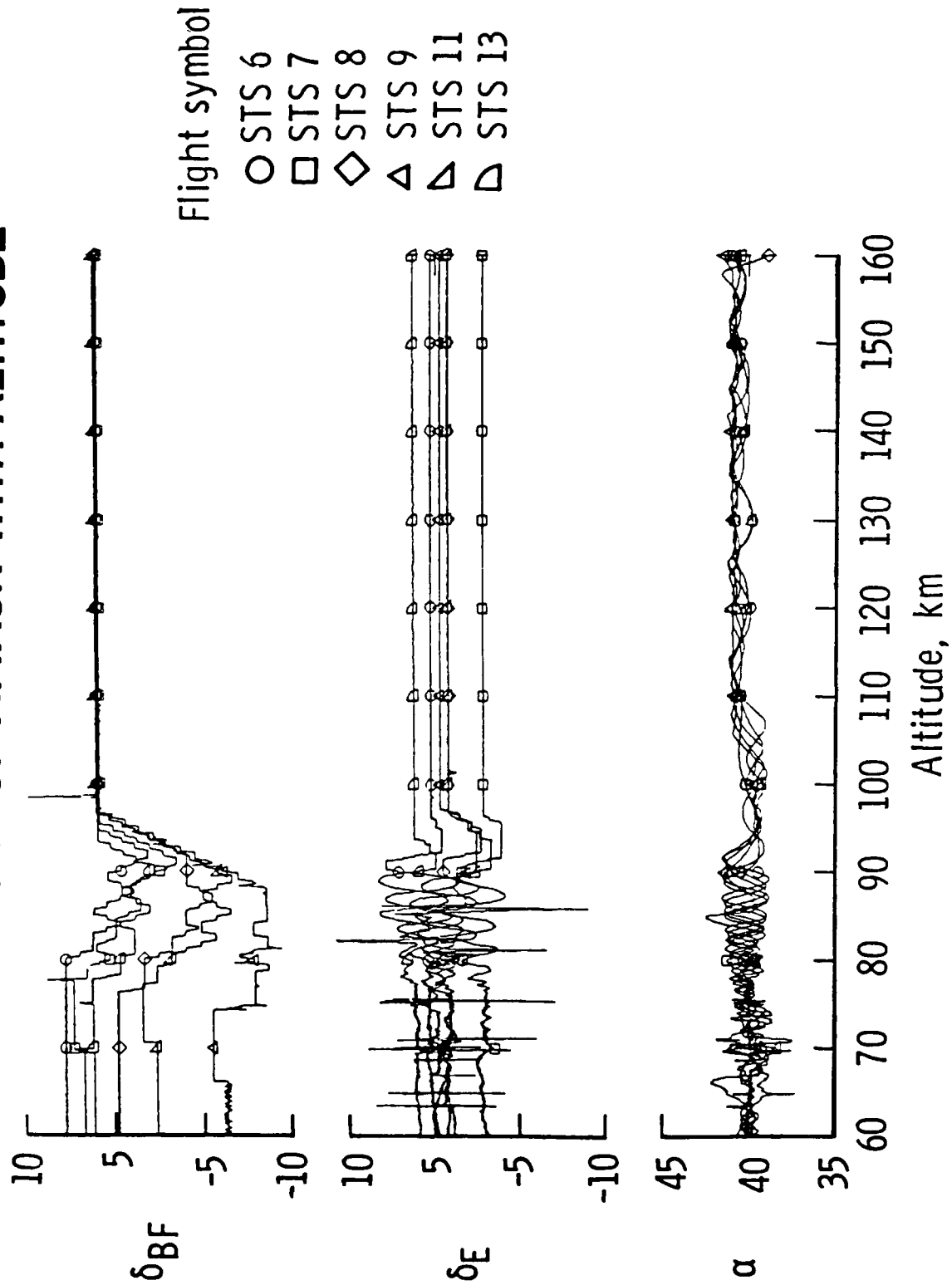
\bar{C}_{I_j} = Rarefied-flow normalized coefficients

Then
$$\frac{L}{D} = \frac{C_N - \tan \alpha}{1 + \frac{C_N}{C_A} \tan \alpha}$$

Match measurements

$$\frac{C_N}{C_A} = \frac{A_Z}{A_X}$$

CONTROL SURFACE DEFLECTIONS AND ANGLE OF ATTACK WITH ALTITUDE



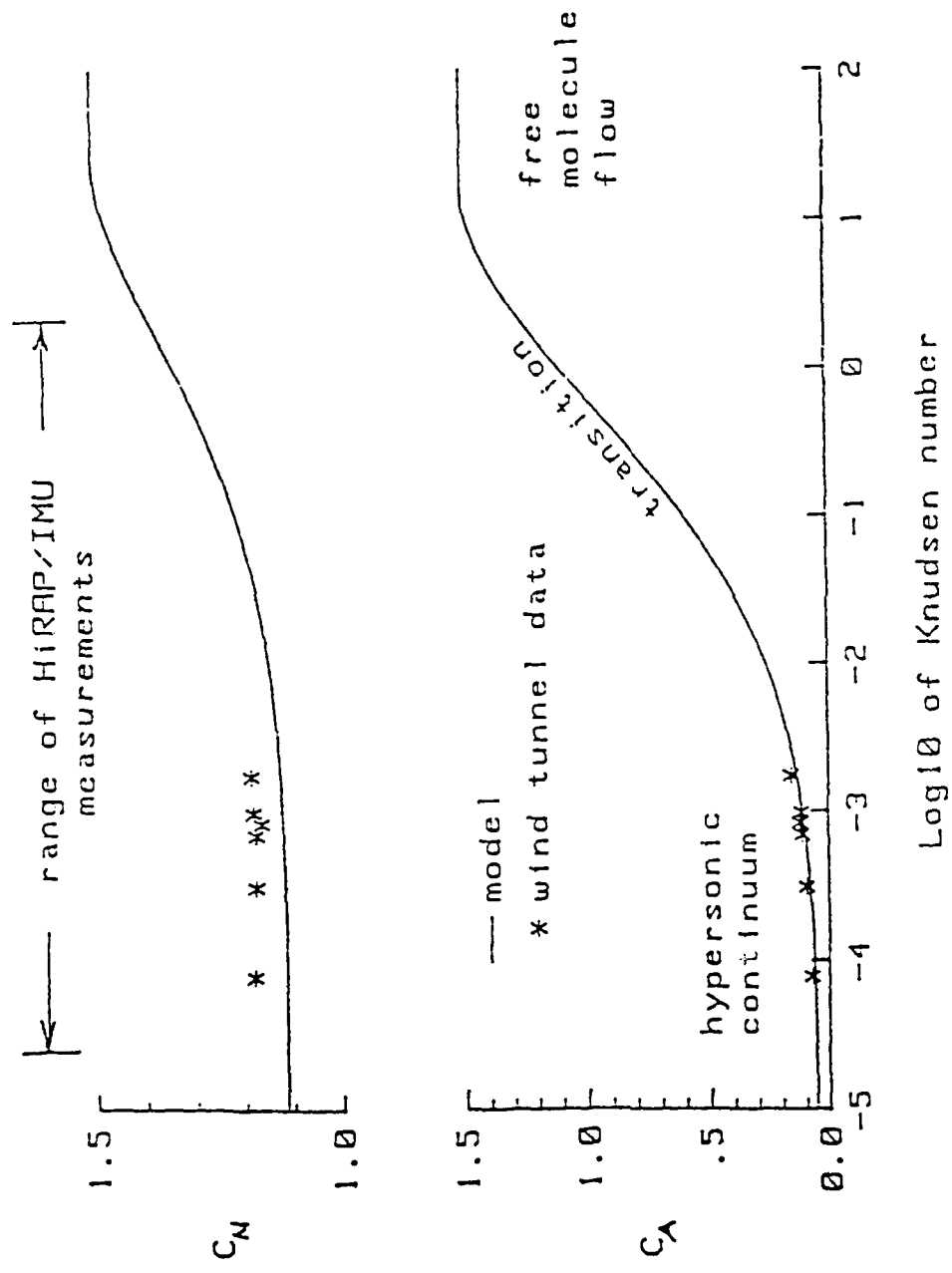
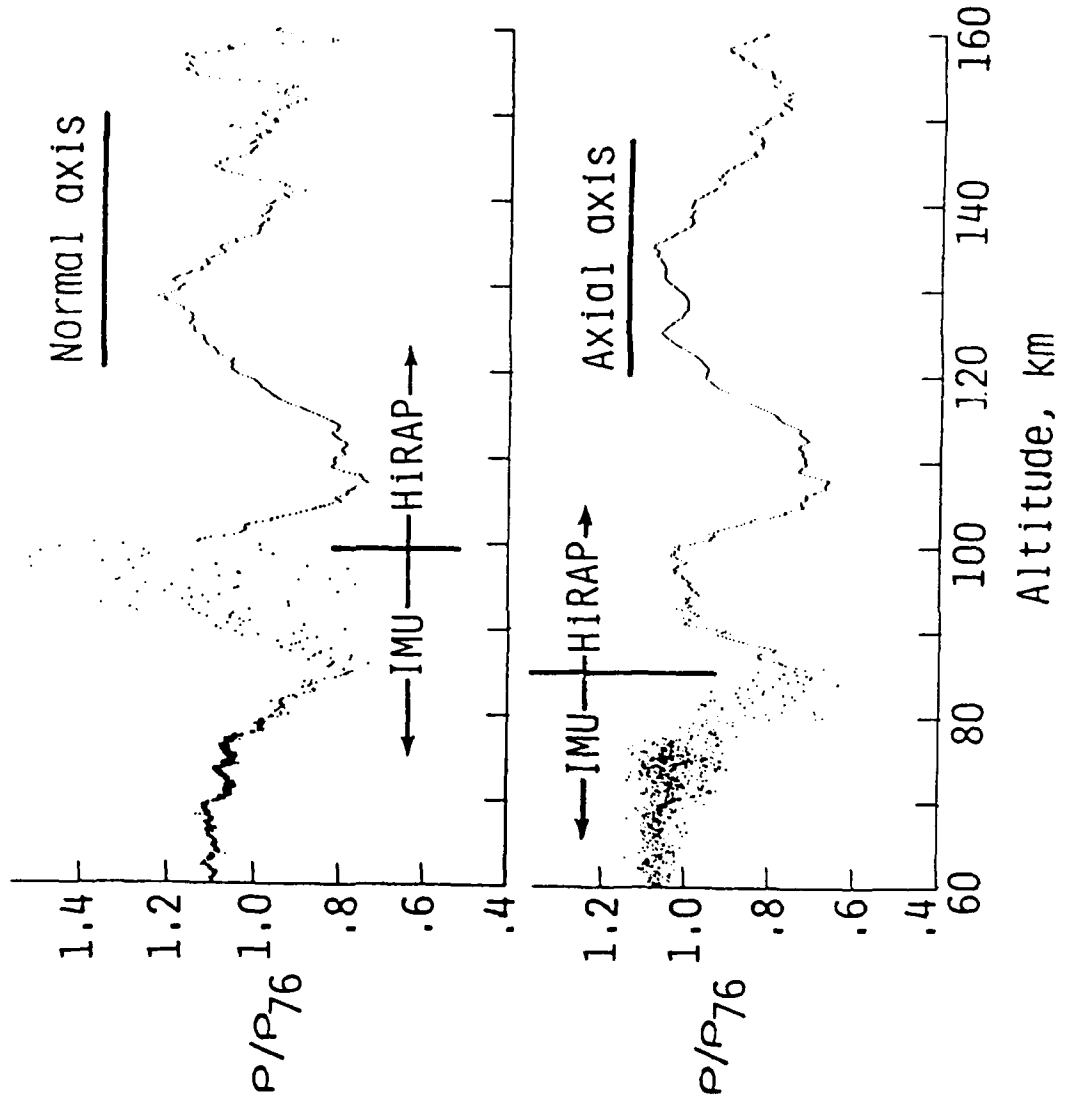
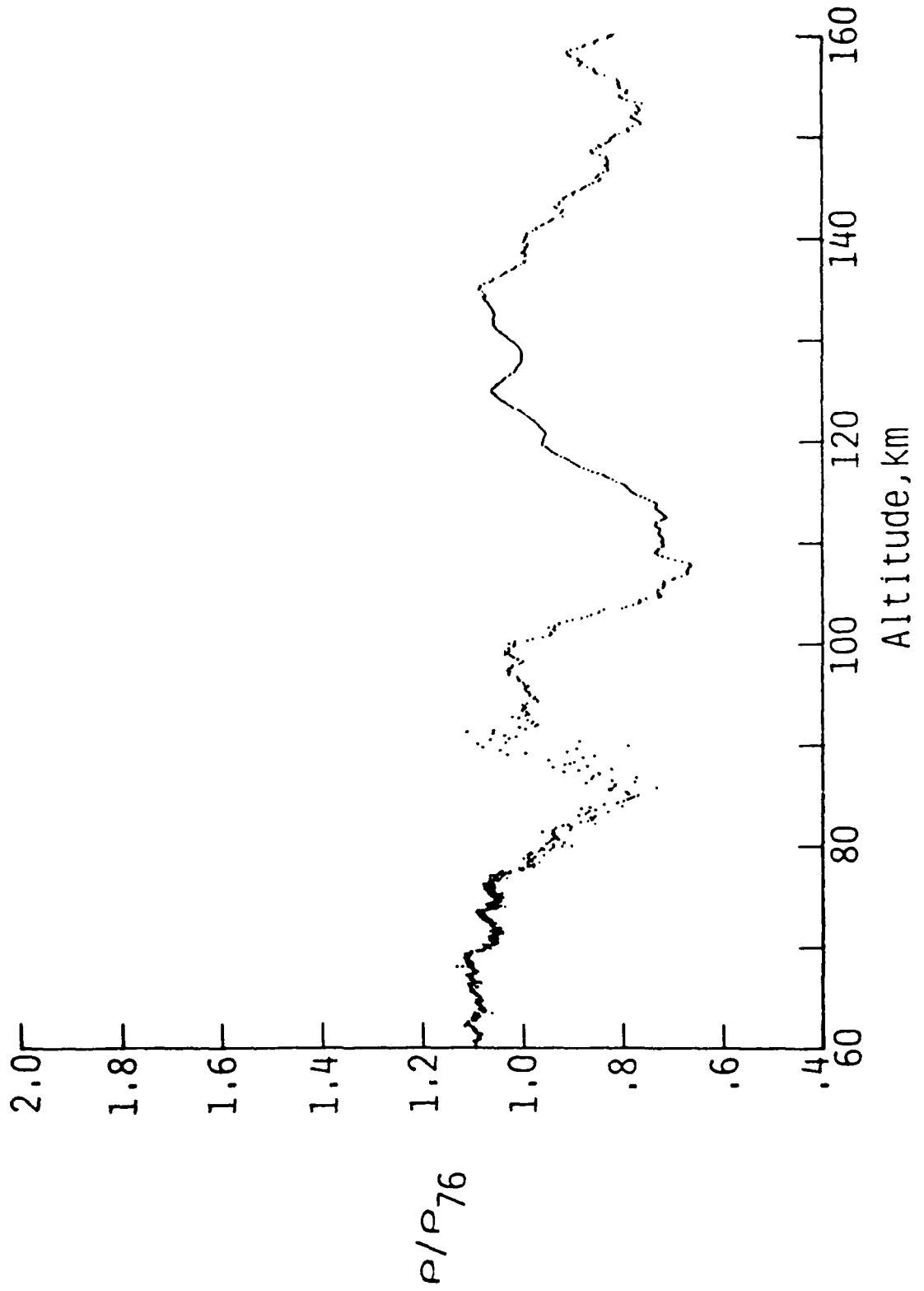


Fig. 3 Variation of normal and axial force coefficients

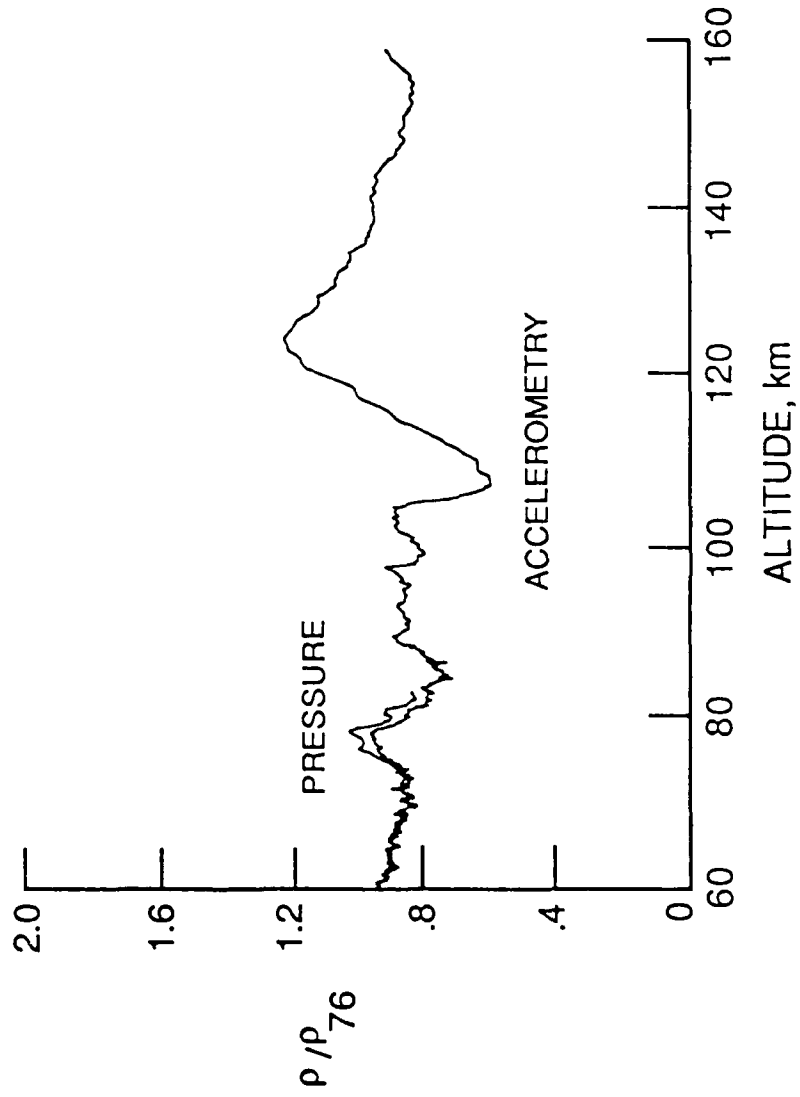
COMPONENT DENSITY DERIVED FROM ACCELEROMETRY (STS-6)



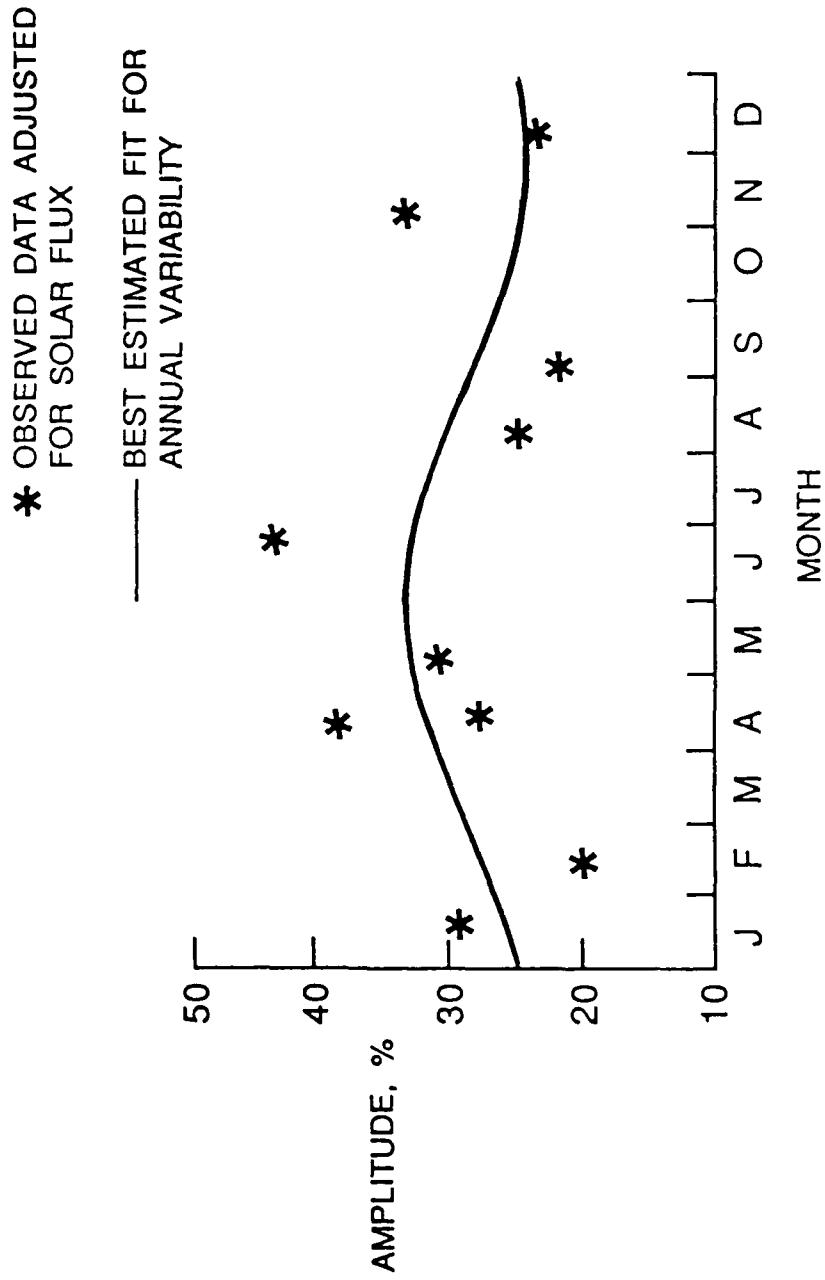
NORMALIZED DENSITY MEASUREMENTS FROM STS-6



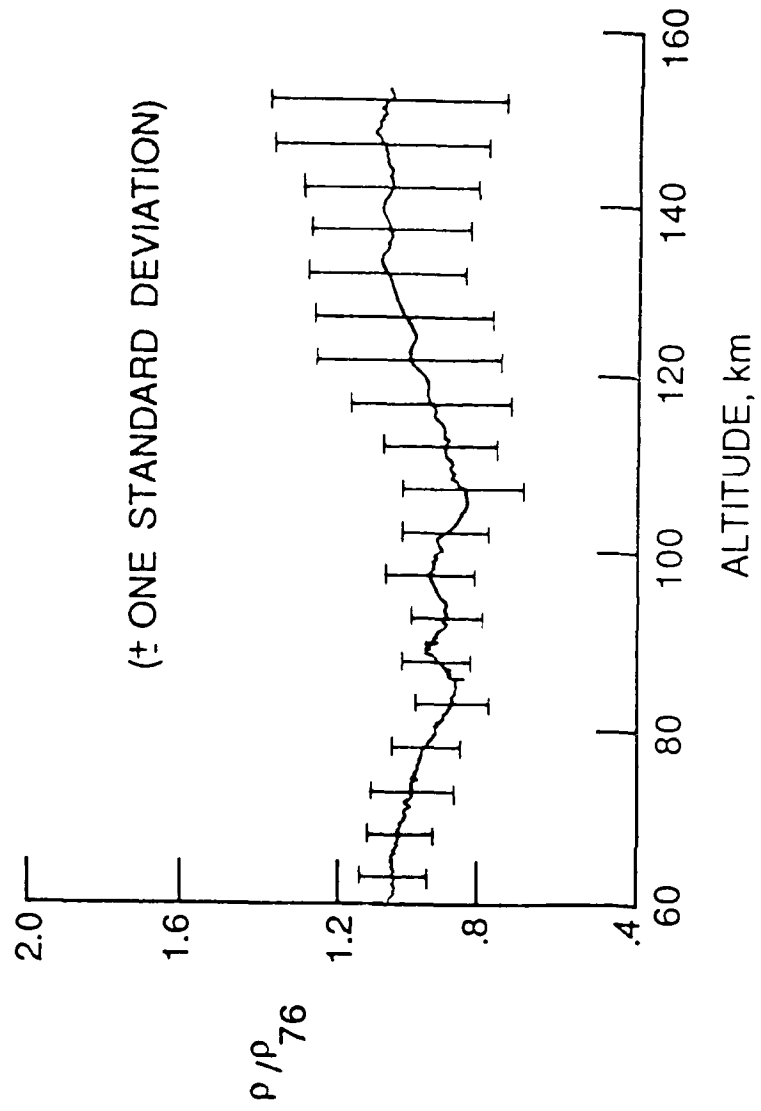
COMPARISON OF ACCELEROMETRY AND PRESSURE DERIVED DENSITIES FROM STS-32 MISSION



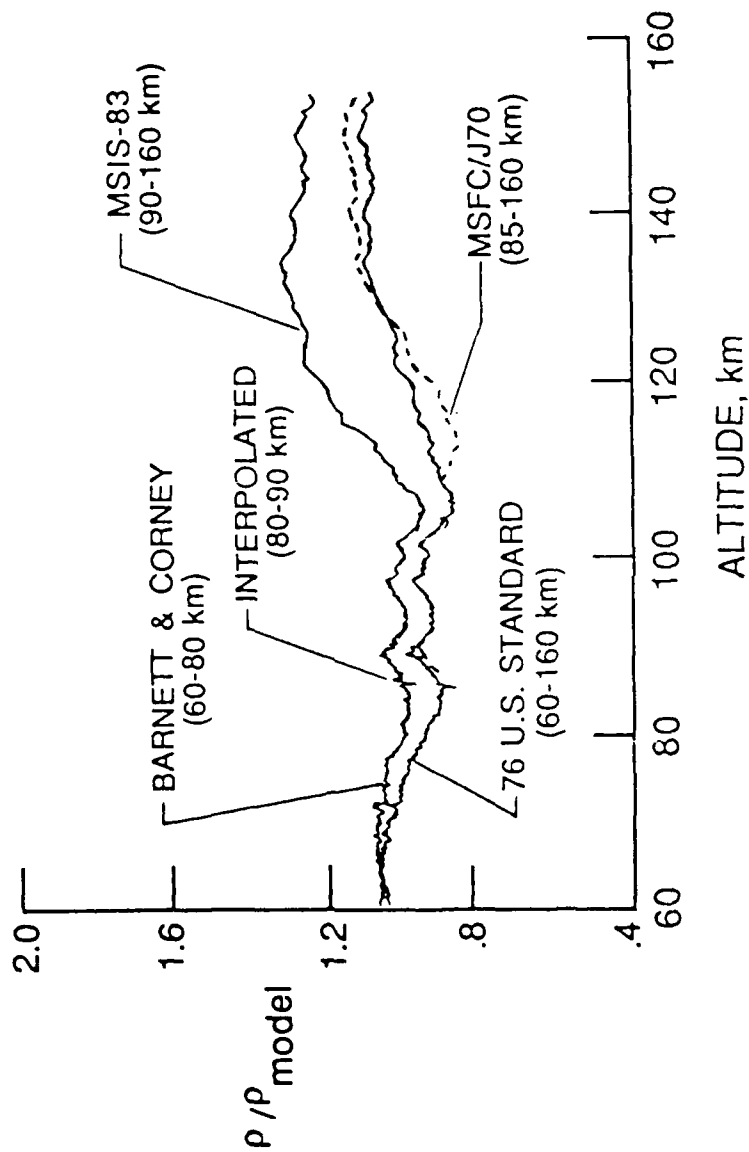
ANNUAL VARIABILITY IN THE AMPLITUDE OF THE NORMALIZED DENSITY (ρ/ρ_{76}) BETWEEN 80-115 km



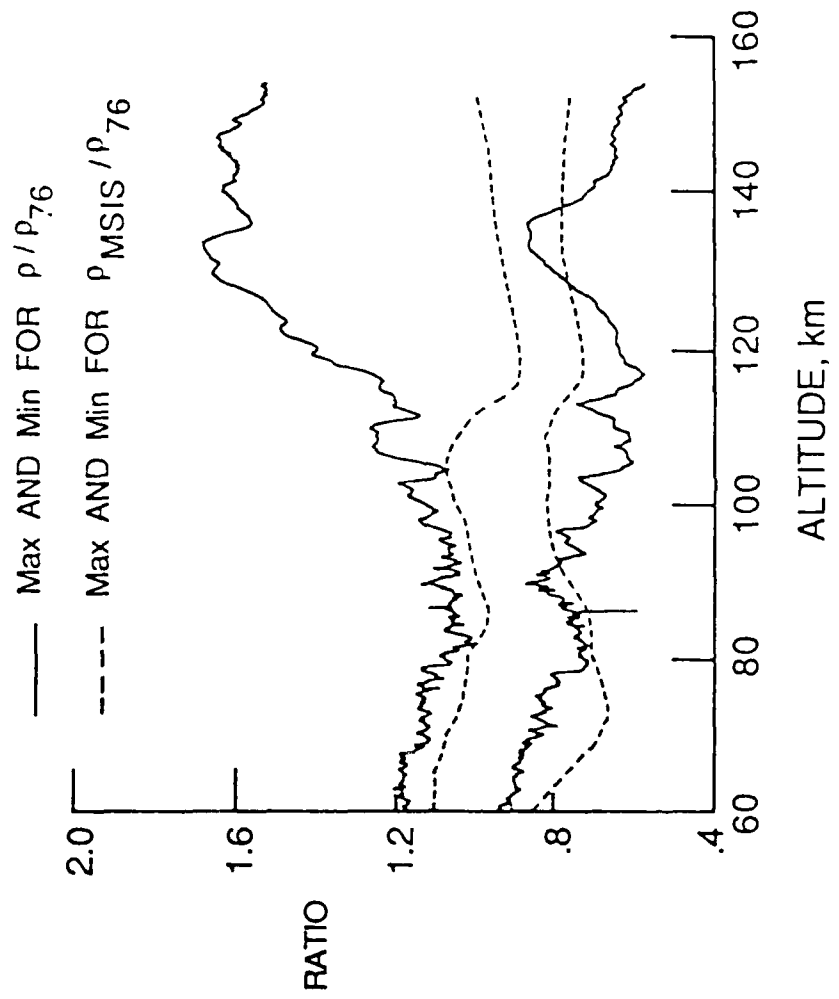
AVERAGE NORMALIZED DENSITY MEASUREMENTS FOR TEN HiRAP FLIGHTS



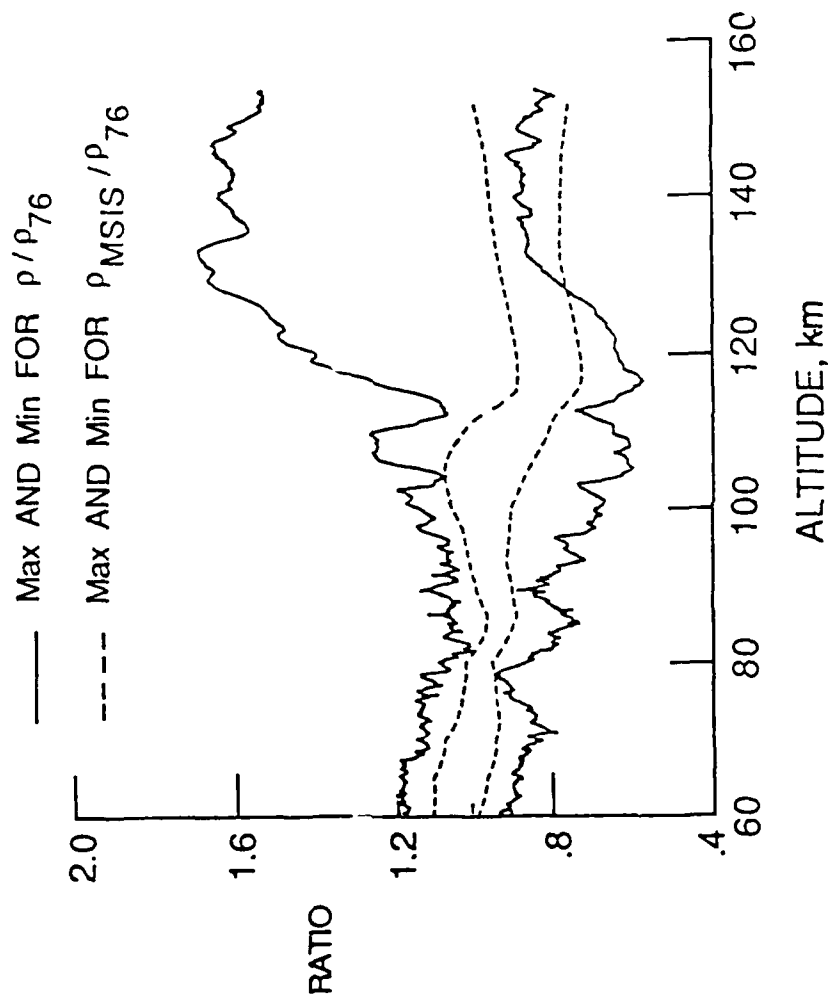
COMPARISON OF AVERAGE MEASURED DENSITY NORMALIZED TO VARIOUS ATMOSPHERE MODELS



ENVELOPE OF MAXIMUM AND MINIMUM DENSITY RATIOS (ALL HIRAP FLIGHTS)



ENVELOPE OF MAXIMUM AND MINIMUM DENSITY RATIOS (STS-9 OMITTED)



SUMMARY

- Obtained 10 Flights of Acceleration Measurements Over 3 Years
 - Updated component aerodynamic models, matching
 - average measured acceleration ratio
 - STS-32 flight pressure measurements
 - wind-tunnel data
 - Calculated inferred atmospheric densities ($60 \leq h \leq 160$ km)
 - considerable spread of solar activity, local solar time, and latitude
 - good seasonal distribution of measurements
 - densities compared to models show wave-like features
- Shuttle Accelerometers Provide Unique Density Measurements
 - Horizontal slice
 - Altitude region not frequently accessed